UNIVERSITÀ DEGLI STUDI DI PAVIA
DOTTORATO DI RICERCA IN FISICA – XXX CICLO

Generation of Nonclassical States of Light in Integrated Structures

Matteo Menotti

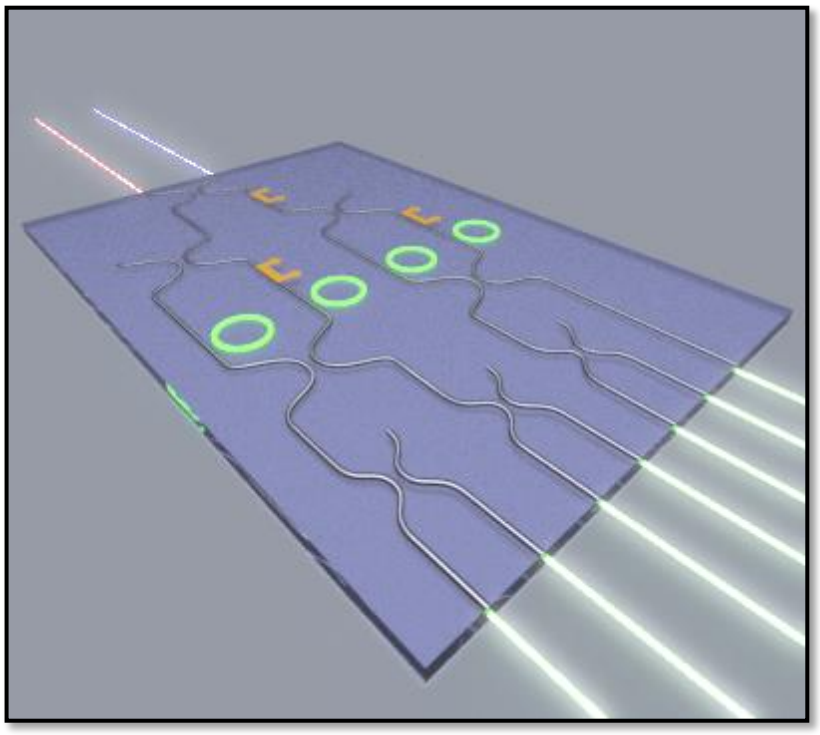

Tesi per il conseguimento del titolo

Università degli Studi di Pavia
Dipartimento di Fisica

DOTTORATO DI RICERCA IN FISICA – XXX CICLO

Generation of Nonclassical States of Light in Integrated Structures

Matteo Menotti

Submitted to the Graduate School of Physics in partial fulfillment of the requirements for the degree of

DOTTORE DI RICERCA IN FISICA
DOCTOR OF PHYLOSOPHY IN PHYSICS
at the
University of Pavia

Adviser: Prof. Marco Liscidini

Cover: Rendering of an integrated optical circuit designed for the generation of path-encoded tripartite Greenberger-Horne-Zeilinger states.

Generation of Nonclassical States of Light in Integrated Structures
Matteo Menotti
PhD thesis - University of Pavia
Pavia, Italy, November 2017

Preface

This document embodies the final relation of the three-years-long PhD course the author has endured in the Physics Department of the University of Pavia under the supervision of Prof. Marco Liscidini, in collaboration both with the nanophotonics group and with various research groups in external institutions. The author's effort is to produce a document that is as nimble and synthetic as possible, directly conveying the crucial take-home messages but also leaving some space for discussing the physical arguments and the numerical derivations that lead to those results.

Although the present work is intended for readers who possess a basic background in integrated quantum photonics and quantum information theory, we nonetheless provide some introductory sections. On the one hand this strategy is timely for recalling the fundamental concepts and ideas which are then implicitly assumed throughout the rest of the document, and on the other hand it clarifies the mathematical vest and provides some fundamental formulas, which reveal as convenient starting points for subsequent derivations. In the author's intent, some of the essential and most of the ancillary mathematical calculations are left to the Appendices, whenever the main body discussions allows for.

The results presented in this work are mostly theoretical and have been recently published in peer-reviewed journals. In our *modus operandi*, one of the primary requirement we constantly keep in mind is the practical feasibility of our theoretical proposals, for a rapid and accessible implementation and consequent experimental verification. Indeed, wherever this goal has not been accomplished yet, we set ongoing collaborations for the future to come.

Contents

Introduction

Starting in 2018 the European Commission will initiate a €1-billion flagship-scale initiative in the framework of the European Horizon 2020 research program, focused on Quantum Technologies. This is one of the major research initiatives endured by the EU, on the same scale as the previous ones on Graphene and the Human Brain Project. The goal of this agenda is "*to place Europe at the forefront of the second*[1] *quantum revolution now unfolding worldwide, bringing transformative advances to science, industry and society* [1]".

Quantum Technologies can be regarded as the field of physics and engineering that creates a bridge between theoretical research on quantum mechanics and the implementation of its unique features, such as quantum entanglement and quantum superposition, into practical applications and commercial devices [2]. With the upcoming flagship, the EU is investing in research on Quantum Technologies aiming at the lead of this "second quantum revolution", profiting from the consequent long-term industrial, scientific, and societal benefits. The expected impact on current technologies would be vast, bringing considerable benefits and advances to several areas, but particularly in the fields of (i) Communications, allowing for the unconditionally secure transmission of cryptographic keys [3, 4, 5, 6]; (ii) Computation, with quantum computers providing unprecedented resources for some specific and demanding tasks [7, 8, 9]; (iii) Simulations of quantum mechanical systems, as remarkably conveyed by the famous quote by Richard Feynman "*Nature isn't classical, dammit, and if you want to make a simulation of nature, you'd better make it quantum mechanical*"; (iv) Sensing/Metrology, where the use of quantum states is boosting the accuracy of time and length measurements [10, 11].

Luckily, many physical platforms are today rivaling to be the choice for the implementation of Quantum Technologies, stimulating competitive research on the one hand, and providing complementary solutions on the other. Among

[1] The expression "first quantum revolution" is typically associated with the scientific and technological breakthroughs occurred in the last decades of the 20th century, originated from the very first quantum theories on the blackbody radiation or the wave-particle duality. In this framework, we can include the invention and development of devices such as the laser systems, semiconductor and transistors, and MRI imagers.

the most promising physical implementations we recall *superconducting circuits* [12, 13] and *trapped ions* [14, 15], which have proved particularly fit for quantum computation and simulations, and *quantum states of light* [16], which are extensively used for quantum communications [17, 6, 18, 19] and quantum sensing/metrology [10, 20, 21], but they have also demonstrated an increasing potential for quantum computations as well [7, 19, 22, 9].

In the present work, we are particularly concerned with the use of photons for applications in Quantum Technologies, mostly for devising quantum communication protocols. The advantage of photons in this field is indisputable, given their exceptionally long coherence length and the possibility to propagate in existing optical networks with minimal losses [23].

The expression "quantum states of light" broadly refers to the electromagnetic radiation that cannot be adequately described by Maxwell's equations [24, 19]. Under this umbrella we could list a large variety of quantum states, yet in the present work we are only concerned with Fock states (particularly, single photons and entangled photon pairs), squeezed vacuum states, and multipartite entangled states. The generation and manipulation of these states of light is today extremely challenging, owing to the weakness of the processes commonly employed for their production, the unavoidable presence of losses with the consequent degradation of the quantum state purity, and the fragile nature of their quantum correlations. Nonetheless, in the last decades a plethora of solutions for their production and manipulation has been proposed, driven both by the scientific curiosity and by the promise of potential implementations in commercial devices. This interest is today ever-growing, as testified by the abundant scientific production and the private and public funding schemes, such as the EU flagship on Quantum Technologies.

Multiple platforms for the generation of nonclassical states of the radiation have been considered, including (i) *quantum dots* [25, 26, 27], nanometer-sized semiconductor particles which can be pictured as "artificial atoms" emitting single photons upon an exciton recombination, (ii) point defects in diamond [28, 29, 30] (*N-V centers* and *Si-V centers*), electronic spin systems with ground and excited states located in the diamond bandgap, and (iii) *parametric fluorescence* [24, 31], which takes advantage of the nonlinear optical response of media. This thesis deals with integrated sources based on this last approach for the generation of nonclassical states of light, focusing on entangled photon pairs and multipartite entangled states.

The integrated design and the use of resonant structures allows one for the tight confinement of the electromagnetic field in a microscopic interaction volume for relatively long time-scales, enhancing the light-matter interaction and ultimately increasing the source generation rate. Even more importantly, integrated solutions grant a precise control over the flow of light and enable the tailoring the quantum state properties [32, 33, 34]. Moreover, in the view of industrial-scale production, integrated devices have a vast margin for improvement in cost reduction, scalability and energy efficiency, following an historical evolution similar to that of semiconductor microelectronics.

Compared to the other above-mentioned platforms, the use of parametric

phenomena allows for a simpler design and fabrication of the device, often profiting from the existing fabrication techniques and infrastructure developed for microelectronics. Moreover, cryogenic temperature operation is not required, as frequently occurs with other devices such as quantum dots and superconducting circuits, yielding looser experimental constraints. Yet, one of the most detrimental drawbacks of sources based on parametric fluorescence is probably represented by their stochastic nature. Such intrinsic characteristic is highly inconvenient in the development of an on-demand source of quantum states of light, as it is typically the case. However, this limitation can be mitigated with strategies such as heralding [35, 36] and space/time source multiplexing [37]. The first approach, typically implemented for the design of single photon sources, consists of the production of a photon pair by parametric fluorescence, followed by the spatial separation of the two particles; the detection of one photon in the first spatial mode "heralds" the presence of the other photon in the second spatial mode. For the heralded photon to be in a pure quantum state, the generated photon pair must be completely unentangled [38, 39, 40]. Then, multiplexing aims at reducing the temporal delay between heralded photons by paralleling multiple sources, with the help of delay lines and controllable optical switches.

In this work, we present and characterize four integrated sources based on parametric fluorescence in nonlinear materials, for the generation of nonclassical states of light. One of the key premises we have kept in mind from the very beginning is the practical feasibility of our design, for a prompt fabrication in photonic integrated circuits. Indeed, where these sources have not been already experimentally verified, we set ongoing collaborations for their fabrication in the near future.

In the first chapter we introduce most of the fundamental background needed, and the mathematical tools we will employ recurrently throughout the rest of the document. This common ground includes a brief discussion of the concept of qubit, essential for dealing with quantum protocols. Since the quantum information can be encoded into different photonic degrees of freedom — a virtue from which we profit especially in Chapters 5 and 6 — we also recall the most common encoding schemes for qubits. In the same chapter we provide some elements of nonlinear optics and discuss the enhancement of the light-matter interaction granted by light confinement in integrated resonant structures, specifically focusing on microring resonators. The mathematical formalism used ubiquitously throughout this work is the asymptotic fields approach [41, 42]: we briefly summarize its main results, since they constitute both the starting point and the *language* of all the subsequent calculations.

In Chapter 2 we discuss the most common silicon-based material choices for the fabrication of integrated quantum optics. We place particular emphasis on the case of porous silicon, presenting the first observation of stimulated four-wave mixing in porous silicon microring resonators. This platform is particularly appealing for the relatively simple and cost-efficient fabrication technique of the source, which nonetheless maintains a quality factor high enough to observe appreciable third-order nonlinear phenomena. Moreover, the porous nature of

the material allows for the infiltration of highly-nonlinear media with minor effects on the light confinement, or a more efficient sensing of molecules and bacteria [43], which can penetrate deeply inside the waveguide where the field is more intense, ultimately boosting the sensing accuracy.

In Chapters 3 and 4 we present and analyze two sources of photon pairs based on spontaneous four-wave mixing in integrated microring resonators. This platform has been theoretically investigated for its potential to tailor the quantum correlation of the photon pairs, ranging from highly entangled to nearly unentangled, by tuning the pump pulse duration [44, 34, 40, 45]. The observation of such response and the source characterization have been achieved with the help of the Stimulated Emission Tomography [46], which exploits the classical counterpart of spontaneous four wave mixing to reconstruct the pair Joint Spectral Density with an accuracy unparalleled by standard approaches. Yet, the production of truly unentangled photon pairs, particularly relevant for the design of heralded single photon sources, cannot be achieved with a simple side-coupled microring resonator without filtering [38, 39], as we discuss later on. To address this issue, in Chapter 4 we propose a microring-based source which takes advantage of an interferometric coupling scheme [47, 48] to generate truly unentangled photon pairs.

As we saw, entangled states composed of two subsystems (*bipartite states*), such as photon pairs, are fundamental for Quantum Technologies and are today well-understood theoretically and experimentally. However, when entanglement is shared among more than two parties (*multipartite states*), the description the system becomes considerably more intricate. In Chapters 5 and 6 we discuss the phenomenology displayed by the simplest photonic multipartite states, namely the case of tripartite entanglement, pointing out the most successful strategies for their production, and some major applications to quantum communication protocols. Two inequivalent classes of tripartite entangled states were identified [49]: *W states* [50, 51, 52] and *GHZ states* [53, 18, 54]. Their generation using entangled photons relies on polarization-encoding schemes in bulk optical setups [50, 51, 52, 18, 55, 56], which does not easily fit in the paradigm of integrated quantum optics. Hence, in Chapters 5 and 6 we propose two novel integrated source designs for the production of tripartite W and GHZ states using alternative degrees of freedom: energy-encoding and path-encoding, respectively. Aside from allowing the source miniaturization, our design is expected to significantly increase the generation rate with respect to the previous demonstrations, thanks to the enhancement of the light-matter interaction proper of integrated devices.

Chapter 1

Elements of quantum photonics

1.1 The Qubit and the Qubit encoding

In classical communications and computation the standard unit of information is the *bit*, a logic variable which can only assume the values 0 and 1. In computation, for instance, it is physically represented by a voltage: when its value is below or above a given threshold — typically less than 1 V — the bit assumes the value 0 or 1, respectively. In quantum communications and quantum computation we can define a comparable fundamental unit of quantum information: the *qubit*. The states $|0\rangle$ and $|1\rangle$ are still reasonable values for a qubit, but now they just represent two instances out of an infinite number of possible values. Indeed, thanks to the principle of superposition proper of quantum mechanical systems, the generic state of a qubit is expressed as the linear combination

$$|\psi\rangle = \alpha\,|0\rangle + \beta\,|1\rangle\,, \tag{1.1}$$

where α and β are complex numbers whose squared modulus represents the probability of revealing the system in state $|0\rangle$ or $|1\rangle$, respectively, upon a measurement. The normalization condition on the quantum states (1.1) entails $|\alpha|^2 + |\beta|^2 = 1$. The orthonormal states $|0\rangle$ and $|1\rangle$ constitute the so-called *computational basis*: in this regard, the qubit can be envisioned as a unit vector in a two-dimensional complex plane. Yet, a more eloquent pictorial representation of the qubit (1.1) is provided by the *Bloch sphere*. Thanks to the normalization condition, we can recast Eq. (1.1) as

$$|\psi\rangle = \cos(\frac{\theta}{2})\,|0\rangle + e^{i\phi}\sin(\frac{\theta}{2})\,|1\rangle\,, \tag{1.2}$$

where now $\theta \in [0;\pi]$ and $\phi \in [0;2\pi]$ can be interpreted as the colatitude and longitude angles defining a point on the surface of a unit-radius three-dimensional sphere. Such sphere, represented in Fig. 1.1, is referred to as the Bloch sphere.

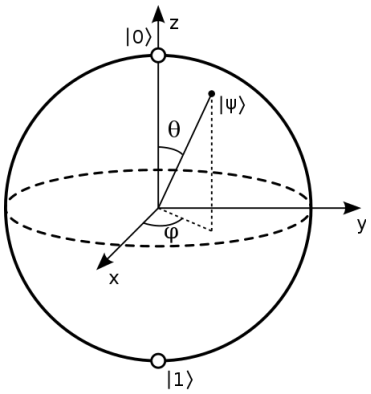

Figure 1.1: Representation of the Bloch sphere. The generic pure qubit state $|\psi\rangle$ is univocally identified by the angles (θ, ϕ), and the computational basis states are reported at the antipodes of the sphere.

The simple introduction of the qubit we recalled so far is not complete, for it applies only to *pure* quantum states. Indeed, from fundamental quantum mechanics we know that a state or a superposition of states can be either *pure* or *mixed*, and the most comprehensive characterization is through its *density operator*, or *density matrix*, ρ. This description is required whenever we don't possess the complete knowledge of the state, and we forced to consider it as a statistical mixture of all its possible outcomes, weighted by their correspondent probability p_i. Naturally, when we have a single possible outcome with unit probability, we go back to the degenerate case of a pure state. The density matrix is defined as

$$\rho = \sum_i p_i \left|\psi_i\right\rangle \left\langle\psi_i\right|, \tag{1.3}$$

where $p_i \in [0, 1]$ is the probability associated with the state $|\psi_i\rangle$. The defining properties of the density matrix are the unitarity of its trace, and its positiveness. The evolution of a system subject to the unitary transformation U is simply described in terms of the density matrix as $\rho = U\rho U^\dagger$, and the probability of obtaining the value m upon a measurement described by the *measurement operator* M_m is

$$p(m) = Tr[M_m^\dagger M_m \rho] \tag{1.4}$$

so that, right after the measurement, the mixed state ρ takes the form

$$\rho_m = \frac{M_m \rho M_m^\dagger}{Tr[M_m^\dagger M_m \rho]}. \tag{1.5}$$

With respect to the pictorial representation of Fig. 1.1, a mixed state is given by a point *inside* the sphere. This becomes evident when we recast the arbitrary density matrix (1.3) as

$$\rho = \frac{I + \vec{r} \cdot \vec{\sigma}}{2}, \tag{1.6}$$

where I is the identity matrix, $\vec{r}$ is a real three-dimensional vector such that $|r| \leq 1$, and $\vec{\sigma}$ is the vector of Pauli matrices $\vec{\sigma} = (\sigma_1, \sigma_2, \sigma_3)$ with

$$\sigma_1 \equiv \sigma_x = \begin{pmatrix} 0 & 1 \\ 1 & 0 \end{pmatrix} \tag{1.7}$$

$$\sigma_2 \equiv \sigma_y = \begin{pmatrix} 0 & -i \\ i & 0 \end{pmatrix} \tag{1.8}$$

$$\sigma_3 \equiv \sigma_z = \begin{pmatrix} 1 & 0 \\ 0 & -1 \end{pmatrix}. \tag{1.9}$$

Naturally, when the mixed state degenerates into a pure state, $|r| = 1$ and we return to our original description of the qubit.

In most communication or computation protocols we are concerned with the generation and evolution of complex quantum states composed of multiple qubits. The generalization of the previous introduction to the multi-qubit case is straightforward, and we assign an independent Hilbert space for each qubit. The most general pure two-qubit state is thus represented by

$$\begin{aligned} |\psi\rangle &= \alpha\,|0\rangle \otimes |0\rangle + \beta\,|0\rangle \otimes |1\rangle \\ &\quad + \gamma\,|1\rangle \otimes |0\rangle + \delta\,|1\rangle \otimes |1\rangle \\ &\equiv \alpha\,|00\rangle + \beta\,|01\rangle + \gamma\,|10\rangle + \delta\,|11\rangle\,, \end{aligned} \tag{1.10}$$

which is formally analogous to Eq. (1.1). Unfortunately, in this case there is no convenient pictorial representation of the two-qubit state, although there have been some attempts in this sense [57]. Among all the possible states encompassed by (1.10), some of the most relevant and meaningful are the *Bell states*

$$|\Phi^+\rangle = \frac{1}{\sqrt{2}}(|00\rangle + |11\rangle) \tag{1.11}$$

$$|\Phi^-\rangle = \frac{1}{\sqrt{2}}(|00\rangle - |11\rangle) \tag{1.12}$$

$$|\Psi^+\rangle = \frac{1}{\sqrt{2}}(|01\rangle + |10\rangle) \tag{1.13}$$

$$|\Psi^-\rangle = \frac{1}{\sqrt{2}}(|01\rangle - |10\rangle). \tag{1.14}$$

This set of two-photon states constitutes a basis for the $\mathcal{H}^{\otimes 2}$ space and are of fundamental practical and theoretical importance. In the former instance, the generation of Bell states using photons is the starting point for countless protocols in quantum communications — consider, for example, the famous E91 protocol for QKD [4] or the protocols for superdense coding [58] — and for

quantum metrology — in this context the states $|\Psi^{\pm}\rangle$ are usually referred to as *NOON states* with $N = 2$, and grant a N-fold measurement accuracy over classical counterparts [10]. In the latter instance, using Bell states it is possible to demonstrate some fundamental features of quantum mechanics, such as the principle of *nonlocality*, through the violation of the so-called Bell inequalities [59].

Commonly, it becomes necessary to measure just a subsection of a multipartite system, to access information on a particle and, for instance, perform a unitary operation on the unmeasured subsystem. This operation can be mathematically described in the framework of the density operators thanks to the reduced density matrix formalism. Let us consider, as before, a bipartite composed of a physical system A living in the Hilbert space $\mathcal{H}^A$ and a physical system B living in the Hilbert space $\mathcal{H}^B$. If we label the density matrix of the whole system ρ_{AB}, the reduced density matrices corresponding to the two subsystems A and B, respectively, are given by

$$\begin{aligned} \rho_A &= Tr_B[\rho_{AB}] \\ \rho_B &= Tr_A[\rho_{AB}], \end{aligned} \tag{1.15}$$

where $Tr_{A,B}[\rho_{AB}]$ indicated the partial trace on one of the Hilbert subspaces. Strictly speaking, the reduced density matrix on the subsystem B does not provide the the correct description of the state of the system A: this operation will just grant the correct measurement statistics on that subsystem. For instance, the reduced density matrix of the the Bell state $|\Phi^+\rangle$ on the second qubit produces the reduced density matrix $\rho_A = I/2$, which is a mixed state. The absolute knowledge of a bipartite state (pure) does not grant the complete knowledge on its subsystems individually (mixed). Nonetheless, the formalism of the reduced density matrices is a fundamental tool for the description of quantum entangled multipartite states, particularly for performing the *Quantum State Tomography* [60, 61, 62] on a multipartite system. This operation consists in the reconstruction of every element of the density matrix associated with a given quantum state, yielding its most complete description attainable. The protocol for Quantum State Tomography depends on the specific physical implementation of the qubit, and it might require vast number of measurements and nonlinear operations. For this reason, the reconstruction can be imprecise and maximum likelihood techniques should be adopted [60, 63].

The concept of qubit we introduced in the opening of this chapter is purely mathematical, but quantum protocols are crafted to operate in very real experimental setups and commercial devices. So, how can a qubit by physically realized? The basic requirement, common to every implementations, is having a system with two accessible orthonormal states, such as an atom in the ground or excited states, or simply the vacuum/occupation of an energy level. Here we restrict our discussion to the case of photonic systems, and in the following we describe the most common choices for the qubit encoding, pointing out the benefits and drawbacks of each solution.

1.1.1 Polarization encoding

Polarization is perhaps the most recurrent choice for a photonic qubit encoding. This variable is indeed naturally dihcotomic so that we can, for instance, assign the states $|0\rangle$ and $|1\rangle$ to the vertical and horizontal polarization of the photon, respectively (See Fig. 1.1.1).

Moreover, the generation of polarization-encoded photons is today routinely performed in laboratories through parametric processes in nonlinear crystals such as beta-Barium Borate (BBO) and Potassium Dihydrogen-Phosphate (KDP). While we leave a more comprehensive description of the physical principles behind parametric fluorescence to Section 1.2, we want to recall a common and explicative strategy adopted for the generation of polarization-encoded photon pairs. The scheme is that originally proposed in 1999 by P. Kwiat et al. [64], and it is schematically represented in Fig. 1.3.

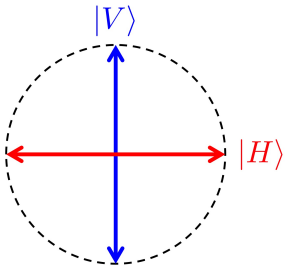

Figure 1.2: Polarization-encoding scheme for a photonic qubit.

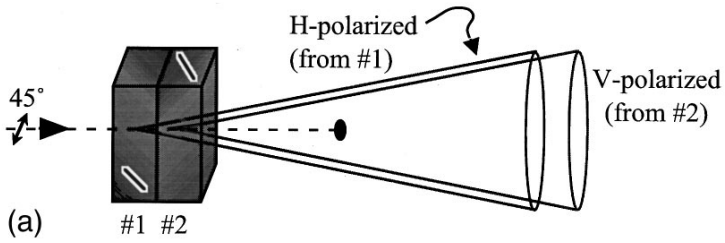

Figure 1.3: Sketch of the "sandwich source" presented in [64] for the generation of polarization-encoded photon pairs through Type I SPDC.

The source is composed of two identical, orthogonally oriented nonlinear crystals, an arrangement sometimes referred to as a "sandwich source". The photons coming from a strong pump laser pulse shined on the crystal can undergo type I Spontaneous Parametric Down-Conversion (SPDC), a process in which a pump photon is scattered into two daughter photons with equal polarization state, opposite to that of the original photon, obeying energy and momentum conservation. The generation of the photon pair occurs simultaneously and, if one assumes to polarize the laser pump at a 45° with respect to the optical axis of the crystals, the pump state is

$$|\psi_{pump}\rangle = \frac{1}{\sqrt{2}}(|H\rangle + e^{i\phi}|V\rangle), \tag{1.16}$$

and gives rise to the down-converted photon pair

$$|\psi_{pair}\rangle = \frac{1}{\sqrt{2}}(|VV\rangle + e^{i\phi'}\,|HH\rangle), \tag{1.17}$$

where the phase ϕ' depends on the pump and crystal parameters. The pair state (1.17) is a $|\Phi^+\rangle$ Bell state in polarization-encoding, and it can now be used for implementing quantum protocols. In this simplified scheme the quantum correlation comes from the uncertainty around the nonlinear crystal responsible for the pair generation, a circumstance that holds as long as the pump photon coherence length is much wider than the nonlinear crystal itself: otherwise, depending on the photon arrival time, one could access the information of which crystal actually generated the pair. It is worth to stress that the source of Fig. 1.3 should be complemented with additional elements to erase the small walks-off originated in the crystals, and the time difference between the two output channels, but this discussion is not relevant to the present introduction.

Other approaches for the generation of polarization-entangled photon pairs have been proposed and demonstrated, for instance using atomic cascade, i.e. the emission of entangled photon pairs upon the decay process of an atom with initial zero angular momentum [65], or using type II SPDC [66, 19] in which the daughter photons are created with orthogonal polarizations. Yet, in both these instances more stringent experimental constraints are required, and the source efficiency is considerably reduced.

After the polarization-encoded state is generated and possibly manipulated in an optical circuit, it is paramount to reconstruct the output state of such circuit through quantum state tomography. In polarization-encoding schemes it is possible to devise a simple protocol for the exact reconstruction of the density matrix of a qubit via a sequence of three linearly independent measurements [61, 67]. The standard scheme to perform such operations, reported in Fig. 1.4(a), is composed of a Quarter Wave Plate (QWP), followed by a Half Wave Plate (HWP) and a Polarizing Beam Splitter (PBS).

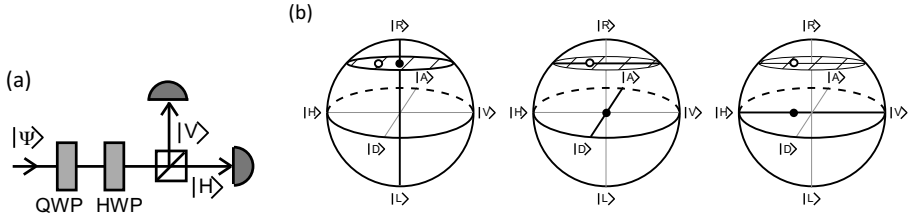

Figure 1.4: Schematic representation of (a) the basic setup for performing a complete quantum state tomography on a polarization-encoded qubit, and (b) the effect of the three projections in pin-pointing the coordinates of a qubit state on the Bloch sphere (adapted from [61]).

As it is schematically represented in Fig 1.4(b), each measurement with a suitable choice for the rotation angles of each wave-plate pins down one of the

free parameters of the state, pictured as the cartesian coordinates of the point representing the qubit state inside the Bloch sphere. When the quantum state is composed of multiple polarization-encoded qubits, the setup of Fig. 1.4(a) is applied at the output of each qubit, counting coincidences.

Polarization-entangled photons are typically involved in free-space experiments, where the polarization state is easily preserved upon propagation thanks to the uniformity and homogeneity of the air/vacuum, and it is manipulated using standard optical elements. Unfortunately, this is not the case for photonic integrated circuits where waveguides are typically asymmetric, and thus the vertical and horizontal polarizations — the TM- and TE-like modes, in this context — experience dissimilar propagation losses. Moreover, although feasible in principle [68, 69], the rotation of polarization-encoded states in integrated optics can be very challenging. The propagation of polarization-encoded states in existing optical networks poses constraints too, since polarization-maintaining fibers (such as Panda fibers of Bow-tie fibers) are not traditionally employed for long-distance communications, Dense Wavelength Division Multiplexing (DWDM) systems being preferred today.

1.1.2 Time-bin encoding

A photonic qubit can also encode information in the relative time of arrival, or *time-bin*, on a detector. Time-bin encoding is particularly useful for quantum communications, for it is a robust scheme against decoherence, yet it has also been proposed for the realization of universal quantum computation with fiber loops and switches [70]. The emission of a photon pair by parametric fluoresce in a nonlinear crystal is approximately instantaneous, so the photons are generated in a precise moment. Let us focus on one of the photons: its time of arrival depends on the route which separates it from the detector, and whenever multiple paths are present, the photon can be thought as passing through all of them with a correspondent probability. The simplest setup to create a time-bin encoded photon is an unbalanced Mach-Zehnder Interferometer (MZI), like the one reported in Fig. 1.5.

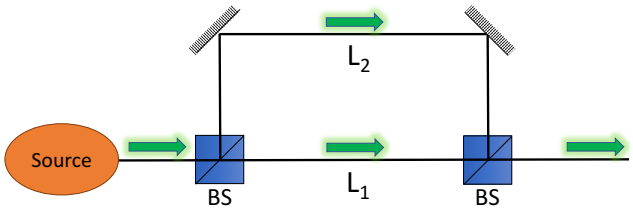

Figure 1.5: Representation of an unbalanced Mach-Zehnder Interferometer for the creation of time-bin encoded photonic qubits.

The incoming photon can equivalently take the lower or the upper arm of

the MZI. Provided that the difference in the arm length $L_2 - L_1$ is much larger then the coherence length of the photon, so that the branch taken can be unambiguously distinguished, the photon state at the output can be written

$$|\psi\rangle = \frac{1}{\sqrt{2}}(|0\rangle + e^{i\phi}|1\rangle), \tag{1.18}$$

where we assign the state $|0\rangle$ to the photon if it took the lower (shorter) arm of the MZI, and the state $|1\rangle$ if it took the upper (longer) arm, and ϕ is the extra phase accumulated by the photon in the upper arm.

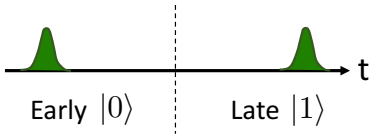

Figure 1.6: Time-bin encoding scheme for a photonic qubit.

Finally, the measurement in performed in the time domain. Naturally, if the photon took the longer path it will have accumulated a delay with respect to a photon traveling in the shorter path. Thus, at the detector, the state (1.18) can be expressed as

$$|\psi\rangle = \frac{1}{\sqrt{2}}(|E\rangle + e^{i\phi}|L\rangle), \tag{1.19}$$

where $|E\rangle$ is an "early" photon, and $|L\rangle$ is a "late" photon. The conceptual scheme of time-bin encoding is reported in Fig. 1.1.2.

1.1.3 *Color* encoding

When we consider the generation of photon pairs by parametric fluorescence in a nonlinear crystal pumped with a CW laser, the energy conservation constraint imposes a strong correlation on the energies of the converted photons. Naturally, the absolute value of their energy is undetermined, but the sum must equal the incident energy. We can exploit this constraint to devise a different scheme for qubit encoding, referred to as *frequency-bin encoding*, or *color encoding* [71], which uses discrete orthogonal modes in the frequency domain rather than spatial modes or the photon polarization.

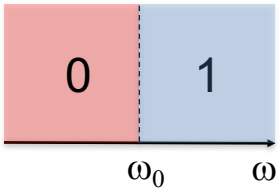

Figure 1.7: Energy-encoding scheme for a photonic qubit.

Quantum information can benefit from multi-frequency encoding in much the same way as classical communication has from the introduction of frequency multiplexing. The simplest case of color encoding of a qubit is represented in Fig. 1.1.3, where only two frequency-bin are considered. The $|0\rangle$ state correspond to a photon whose frequency is red-detuned with respect to a central value ω_0 (the central frequency of the pump), while the state $|1\rangle$ is physically represented by a photon whose frequency

is blue-detuned with respect to the central frequency. We will adopt this encoding scheme for the generation of energy-entangled W states in Chapter 5. Multiple sources of frequency-encoded photon pairs have been proposed at present, including birefringent optical fibers [40], integrated silicon microdisks [72] and integrated silicon microrings [44]. The quantum state tomography of a system of color-encoded photons in general requires nonlinear processes, for creating the superposition of $|0\rangle$ and $|1\rangle$ states would otherwise violate energy conservation. Nonetheless, as we discuss in Chapter 5, in particular circumstances one can take advantage of other degrees of freedom, such as the photon polarization [71] or path, to avoid the need for nonlinear processes and obtain a full tomography of the color-encoded qubits.

1.1.4 Path-encoding

Path encoding is another very natural encoding scheme for photonic qubits. Here, regardless the photon polarization or energy, we are mostly concerned with the spatial distribution of the field associated with the photon. Since the qubit lives in a two-dimensional Hilbert space, let us consider an encoding scheme with two independent waveguides, as schematically represented in Fig. 1.1.4: the photon can propagate either in the upper or the lower waveguide, and we assign the qubit state $|1\rangle$ and $|0\rangle$ to each state, respectively.

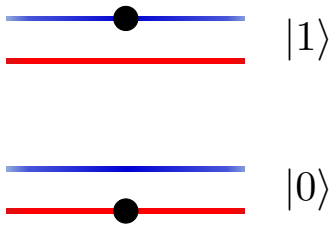

Figure 1.8: Path-encoding scheme for a photonic qubit.

Path-encoding is particularly suited for integrated quantum photonics, for photon pairs are often generated directly inside the waveguide by means of parametric processes, and remain thereon confined thanks to the refractive index contrast — in simple waveguides — or the Photonic Band Gap mechanism — in photonic crystal waveguides. Moreover, it is relatively easy to implement any unitary operation on the path-encoded qubit, simply by spatially rearranging or moving the waveguides closer to each other, and exploiting the evanescent coupling between the two modes in directional couplers. We will show how a variety of unitary transformations can be implemented with path-encoding in the opening of Chapter 6. On-chip solutions for the generation of path-encoded photon pairs have been proposed in multiple platforms [73], including silica-on-silicon [74], silicon on insulator [75], and lithium niobate [76]. Moreover, it has also been demonstrated the possibility to translate path-entanglement to polarization-entanglement by using specifically designed grating couplers [77].

Quantum state tomography on a path-encoded qubit is fundamental for a full reconstruction of the quantum state, and it has been demonstrated on-chip

with reconfigurable phase delays [75, 73], and with a static chip configuration exploiting on-chip "quantum walks" [78]. In the former instance, the standard configuration of an analyzing integrated circuit for a path-encoded qubit is reported in Fig. 1.9.

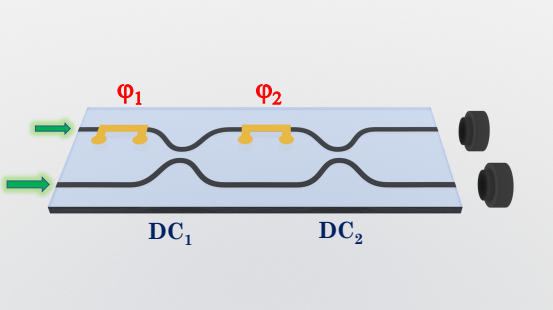

Figure 1.9: Sketch of a standard photonic integrated circuit for performing quantum state tomography on a path-encoded qubit.

The integrated circuit is composed of a MZI with two tunable phases, implemented through directional couplers and heaters. By adjusting the phases in three measurements it is possible to pin-point the state in the Bloch sphere, following the same strategy we discussed above for the tomographic reconstruction of a polarization-encoded qubit.

1.2 Nonlinear optics

In the Introduction we have recalled some of the widespread physical platforms for the generation of nonclassical states of light, including quantum dots, color centers in diamond, and parametric fluorescence. Here, we restrict our discussion to the latter solution and, in particular, we focus on the material third-order nonlinear response to generate photon pairs. Such photons can be subsequently manipulated in specifically designed optical circuits to yield a variety of nonclassical states of the radiation, as we do in the following Chapters. Parametric fluorescence is one of the most recurrent processes, and several materials have been considered and characterized for their intense nonlinear response. Throughout this Chapter we want to briefly recall the properties of nonlinear media, particularly focusing on the third-order nonlinear response and the phenomenon of four-wave mixing. Although this effect is rather feeble, the appropriate use of light confinement can overcome this limitation and vastly enhance the nonlinear response of materials.

1.2.1 Material nonlinearity

Regardless its atomic composition, structural arrangement, or external stimuli applied, every medium displays a nonlinear response when excited by an elec-

tromagnetic field. This effect roots back to the nonlinear functional relation between the incident electric field $\mathbf{E}(\mathbf{r},t)$ and the induced polarization $\mathbf{P}(\mathbf{r},t)$ in the medium, which can be Taylor-expanded as

$$\begin{aligned} P^i(\mathbf{r},t) = \epsilon_0 \chi^{ij}(\mathbf{r}) E^j(\mathbf{r},t) + \chi_2^{ijk}(\mathbf{r}) E^j(\mathbf{r},t) E^k(\mathbf{r},t) \\ + \epsilon_0 \chi_3^{ijkl}(\mathbf{r}) E^j(\mathbf{r},t) E^k(\mathbf{r},t) E^l(\mathbf{r},t) + \dots, \end{aligned} \tag{1.20}$$

where $\chi_2^{ijk}(\mathbf{r})$ and $\chi_3^{ijkl}(\mathbf{r})$ are the second- and third-order nonlinear optical susceptibility tensors and the Einstein's rule for summation over repeated indices applies. These quantities are typically small, of the order of $\chi_2 \approx 10^{-12}$ m/V and $\chi_3 \approx 10^{-24}$ m^2/V^2.

The second-order susceptibility is responsible for numerous nonlinear phenomena, including

- *Optical Rectification* (OR), the occurrence of a static polarization caused by the passage of an intense optical beam in the material.
- *Second-Harmonic Generation* (SHG) and, more generally, *Sum-Frequency Generation* (SFG), which consist in the inelastic scattering of two incident photons into a single photon whose frequency is the sum or the of that of the original photons. In the former case the impinging photons are identical, while in the latter they can have an arbitrary frequency.
- *Difference-Frequency Generation* (DFG), the generation of photons with a frequency that is the difference between that of two photons impinging on the nonlinear region.
- *Spontaneous Parametric Down-Conversion* (SPDC), which consists in the spontaneous "fission" of a photon in two daughter photons, respecting energy and momentum conservation.

Thanks to these processes it is possible to realize *Optical Parametric Amplifiers* (OPA) and *Optical Parametric Oscillators* (OPO, essentially an OPA in an optical cavity), which can produce down-converted photons in squeezed states with high efficiencies [79, 80]. Among the most common materials used for second-order nonlinear quantum optics we must consider Lithium Niobate ($LiNbO_3$) [81, 82, 83], KTP [84, 83] and BBO [85, 83] crystals, and III-V semiconductors, such as Indium Gallium Arsenide (InGaAs) [86, 87], Indium Phosphide (InP) [88], and Gallium Nitride (GaN) [89].

Unfortunately, not all of the optical media possess a second-order nonlinear response, and thus cannot give rise to the above-mentioned effects. This is indeed the case of bulk centrosymmetric crystalline structures, whose $\chi_2 = 0$ (and any other even-order nonlinear susceptibility) due to the particular crystal symmetry. One of the centrosymmetric materials that is most relevant to our discussion is silicon: as we will discuss further in details in Chapter 2.1, it is typically used for its high third-order nonlinear response and the well-established fabrication and lithography processes. Other notable platforms for the third-order nonlinear optics include Silicon Nitride (SiN) [71, 90, 91], Silicon Carbide (SiC) [92, 93], and

porous silicon [94, 95, 96]. The third-order nonlinear susceptibility is responsible for several nonlinear effects, including

- *Optical Kerr Effect* and *Self-Focusing*, the former being the field intensity-dependent variation of the refractive index by a quantity $\Delta n = n_2 I$, where n_2 is the so-called nonlinear refractive index and I is the incident field intensity; the latter is related to the Kerr effect and consists of the spontaneous focusing of a nonuniform wavefront to the highest intensity regions, led by the increased refractive index.

- *Third Harmonic Generation* (THG, or *frequency tripling*), which can be pictured as the fission of a photon into three down-converted photons.

- *Stimulated Raman Scattering* (SRS), the inelastic scattering of photons with the optical rotational, vibrational, and roto-vibrational modes of molecules.

- *Stimulate Brillouin Scattering* (SBS), the inelastic scattering of photons with the optical vibrational quasi-excitations of a crystal (phonons).

- *Four-Wave Mixing* (FWM), which consists in the inelastic scattering of two photons into a newly generated frequency-converted photon pair. This process can be *stimulated* by the presence of another incident photon, or otherwise *spontaneous*.

Throughout the rest of this work, we will always consider FWM processes for the generation of nonclassical states of light; for this reason, in the following sections we discuss more in details this particular third-order nonlinear phenomenon.

1.2.2 Stimulated and Spontaneous Four-Wave Mixing

As the name suggests, the FWM process involves the presence of four electromagnetic fields whose interaction is mediated by the third-order nonlinear susceptibility. We can distinguish between a "classical" and "quantum" FWM processes, typically referred to as *stimulated FWM* and *Spontaneous FWM (SFWM)*, respectively.

In stimulated FWM, two *pump* photons impinge on a nonlinear region, as sketched in Fig. 1.10, and originate a new photon pair composed of *signal* and an *idler* photon. The generation of photon pairs with the particular signal-idler energy (and wave-vector) combination is *stimulated* by the presence of another signal photon simultaneously fed into the nonlinear region. Ultimately, in this process the signal photon is not directly involved in the transition, and it is found in the output.

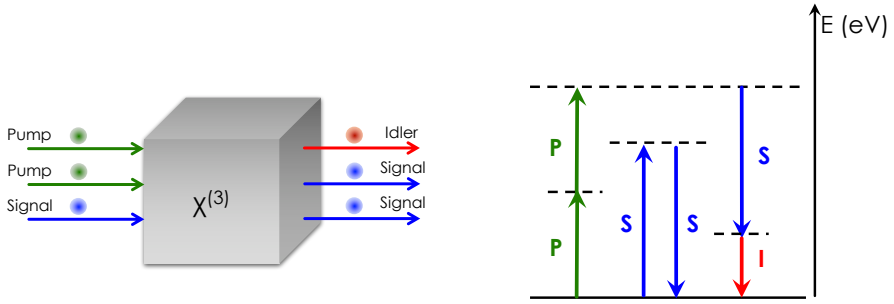

Figure 1.10: Pictorial representation of a FWM process in a third-order nonlinear material.

Naturally, the energy and momentum conservation must be enforces, so that

$$\omega_4 = \omega_1 \pm \omega_2 \pm \omega_3 \tag{1.21}$$
$$\mathbf{k}_4 = \mathbf{k}_1 \pm \mathbf{k}_2 \pm \mathbf{k}_3, \tag{1.22}$$

where ω_1, ω_2, and ω_3 are the frequency of the incoming waves and ω_4 is the frequency of the newly generated optical wave. Similar labelling is adopted for the wave vectors. It is worth to note that the condition (1.21) is easily satisfied and does not imply condition (1.22) (usually referred to as the *phase-matching* condition), for the material is dispersive. Hence, care must be taken to ensure that both Eq. (1.21) and (1.22) are satisfied; there are many strategies to fulfill such requirements, including the use of birefringent materials, the engineering of the material dispersion, the adoption of quasi phase-matching. For the moment we will consider these conditions to be both satisfied. Expressing the electric field for each mode involved in the nonlinear process as

$$\mathbf{E}(\mathbf{r}, t) = \frac{1}{2} A(\mathbf{r}) e^{i(\omega t - \mathbf{k}\cdot\mathbf{r})} + \text{c.c.} \tag{1.23}$$

where $\mathbf{A}(\mathbf{r})$ is the field amplitude, and using Eq. (1.20) we obtain, among the other terms,

$$\begin{aligned} P^i(\mathbf{r}, t) &= 3\chi_3^{ijkl} A_1^j(\mathbf{r}) A_2^k(\mathbf{r}) [A_3^l(\mathbf{r})]^* e^{i[(\omega_1+\omega_2-\omega_3)t + (\mathbf{k_1}+\mathbf{k_2}-\mathbf{k_3})\cdot\mathbf{r}]} + \text{c.c.} \\ &\equiv 3\chi_3^{ijkl} A_1^j(\mathbf{r}) A_2^k(\mathbf{r}) [A_3^l(\mathbf{r})]^* e^{i(\omega_4 t + \mathbf{k_4}\cdot\mathbf{r})} + \text{c.c.} \end{aligned} \tag{1.24}$$

where one of the conditions (1.21) and (1.22) emerges naturally. For simplicity, we can consider the degenerate case in which $\omega_1 = \omega_2 \equiv \omega_p$ are the pump photons, while the photon at ω_3 is the signal, and the resulting photon at ω_4 is the idler.

The SFWM process is the quantum counterpart of FWM, and it can be pictured as the inelastic scattering of two pump photons into a signal and an

idler photon, conserving energy and momentum in the frequency conversion. Such process is schematically depicted in Fig. (1.11).

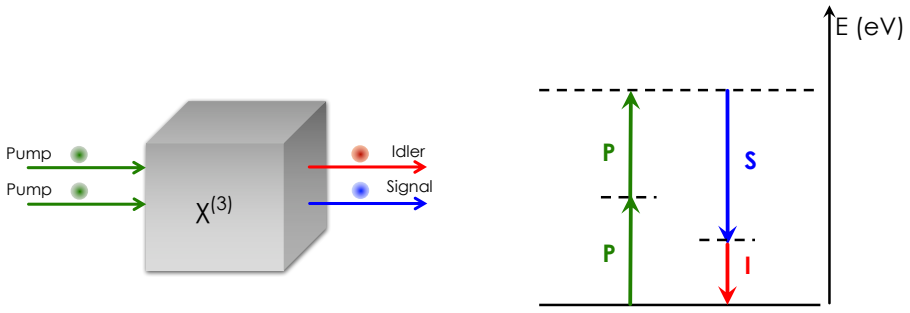

Figure 1.11: Sketch of a SFWM phenomenon occurring in a χ_3 material, with the corresponding process in the energy diagram.

The difference with respect to stimulated FWM is clearly the absence of input signal photons. From a quantum mechanical point of view, we can envision the frequency conversion as stimulated by vacuum fluctuations. It should be noticed that all these processes are *parametric*, meaning that there is no exchange of energy or momentum between the incoming fields and the nonlinear medium: the transition can be viewed as occurring between virtual energy levels, it is considered to be instantaneous, and the quantum state of the material is not modified by the interaction [97].

1.2.3 Enhancement of the nonlinear light-matter interaction

The generation rate of photon pairs by SFWM in a bulk nonlinear medium is affected by the weakness of the third-order response of most materials, yet the response of a nonlinear device can be dramatically enhanced by tailoring the confinement of light inside the nonlinear region. Indeed, looking back at Eq. (1.20), the medium polarization depends both on the nonlinear susceptibility and on the electric field amplitude. While the former is essentially set by the material with little space for improvement under external influences, there is a large margin for improvement on the latter factor.

The simplest way to increase the light-matter interaction and thus the third-order nonlinear response, is by confining the electromagnetic field in the transversal plane with respect to its propagation direction. This is typically implemented through integrated waveguides. We can identify two basic physical mechanisms for attaining light confinement: Total Internal Reflection (TIR) and the Photonic Band Gap (PBG) [98, 99].

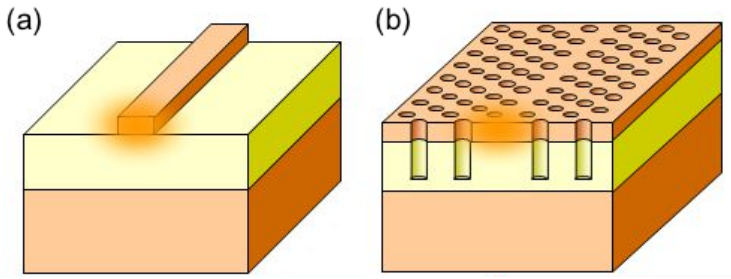

Figure 1.12: Schematic examples of waveguide structures, where the high-refractive index material is orange and the low refractive index material is yellow. (a) simple ridge waveguide, where light confinement is obtained by TIR; (b) PhC waveguide, where light confinement is obtained by a combination of TIR and the PBG mechanism.

The former simply refers to the existence of a critical angle above which light is totally reflected at the interface from the high-index medium to the low-index medium. Based on this approach we have multiple design for integrated optical waveguides, including *ridge waveguides*, *rib waveguides*, and *buried-channel waveguides* (see Fig. 1.12(a)) [99]. The second approach can be interpreted as a destructive interference effect, arising from the semi-infinite periodicity of the confining structure, a *Photonic Crystal* (PhC). In this framework, the Bloch-Floquet theorem applies and from the calculation of the band structure of the systems we note the presence of *photonic band gaps*, similarly to what occurs to electrons in a crystalline structure. Notably, this is the same basic principle of operation for a *Distributed Bragg Reflector* (DBR), so that a *PhC waveguide* can be pictured as a high-index region surrounded by DBR mirrors for light confinement (see Fig 1.12(b)). We can introduce an *effective area* A_{eff} that represents the effective interaction cross section, weighted on the nonlinear region alone, for the process occurring in the waveguide. Integrated optical waveguides can enhance the nonlinear response of optical media significantly thanks to the 2D confinement of light, but the interaction time τ is limited by the finite propagation length L_{prop} (limited by losses) or the physical length L of the waveguide to $\tau = L_{(prop)}/v_g$.

To further improve the light confinement, the simplest solution consists in the use of *optical resonators*, structures in which light is — ideally — confined in three dimensions. This can be achieved by means of metallic or dielectric mirrors, by producing a defect in a 3D photonic crystal, or simply by bending a waveguide onto itself in a circular shape. Once more, we can identify multiple instances of photonic resonators based on a combination of TIR and PBG, including *micropillar resonators*, *microdisks resonators* based on the so-called *whispering gallery modes* [99, 66], *PhC resonators* [98], and simple *microring resonators* [99]. In the following we will focus on the latter resonant structure alone, for this is the fundamental block at the basis of all the sources of nonclassical states of light we discuss in this work.

A microring resonator can be straightforwardly pictured as ridge waveguide

bent in a closed circular shape with radius R, as we schematically represent in Fig. 1.13.

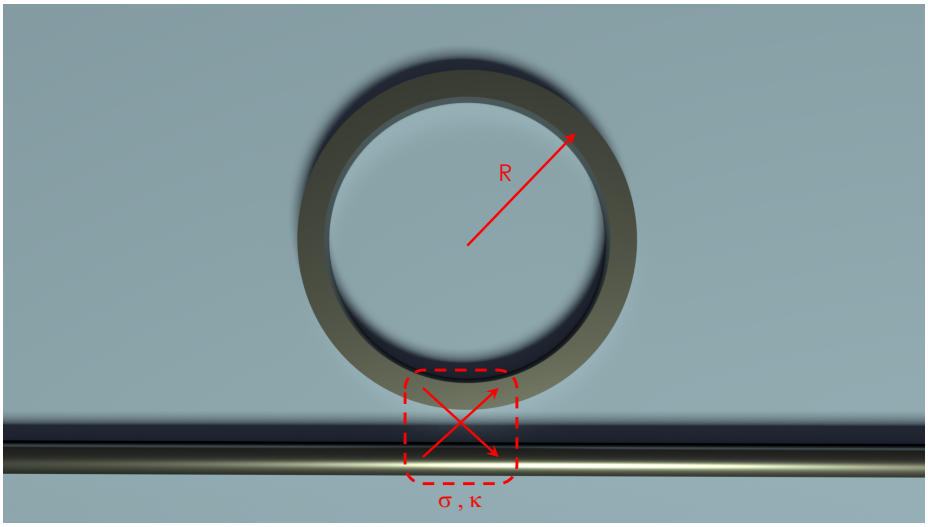

Figure 1.13: Schematic representation of a side-coupled microring resonator.

The optical excitation of the microresonator can be achieved by evanescent side-coupling to an external waveguide, referred to as the *bus waveguide*. The coupling strength depends on the distance d between the ring and the bus waveguide, and it can be selected upon design or tuned to a given extent in a finished structure with heaters, by thermal expansion effect. For most purposes, the bus-ring coupling is represented in terms of a real-valued self-coupling constant σ and a real-valued cross-coupling constant κ such that, referring to Fig. 1.13, we have

$$\begin{aligned} E_1 &= \sigma E_2 + i\kappa E_{in} \\ E_{out} &= i\kappa E_2 + \sigma E_{in}, \end{aligned} \tag{1.25}$$

and assuming the coupling to be reciprocal, we have $\sigma^2 + \kappa^2 = 1$. Light propagating in the microring is subject to various sorts of losses, including absorption, scattering and bending losses; their effect can be conveyed in a unique loss coefficient $\alpha \in [0, 1]$, so that

$$E_2 = \alpha E_1 e^{ik(\omega)L}, \tag{1.26}$$

where $\alpha = 1$ corresponds to the lossless scenario and $L = 2\pi R$ is the round trip distance. It should be noticed that the coefficient α includes all of the possible sources of loss in the system, wether represented by scattering and absorption, or by other output channels, regarded as a means of energy depletion from the

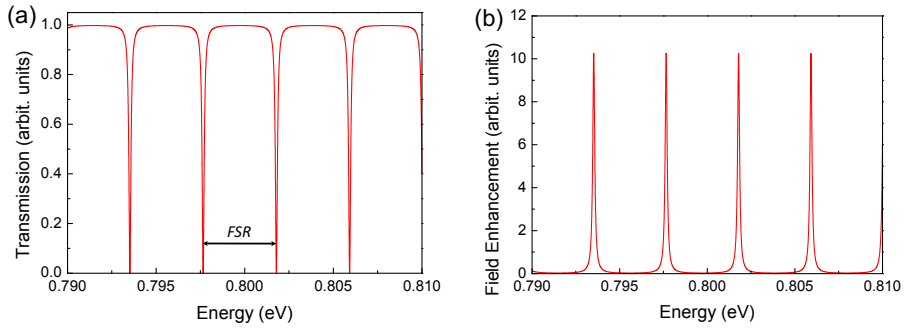

Figure 1.14: (a) Transmission spectrum of a side-coupled microring resonator ($R = 20\ \mu m$, $\sigma = \alpha = 0.95$) at the critical coupling condition. (b) Field Enhancement in the same ring resonator as a function of the energy, showing the nearly periodical lorentzian resonances.

resonator. The material dispersion comes here into play remembering that in general

$$k(\omega) = \frac{\omega_0}{c} n + \frac{1}{v_g}(\omega - \omega_0) + \frac{1}{2} GVD(\omega - \omega_0)^2 + \ldots, \tag{1.27}$$

where ω_0 is a central frequency around which $k(\omega)$ is Taylor expanded, n is the refractive index at ω_0, v_g is the group velocity at ω_0, and GVD is the group velocity dispersion at ω_0. Using Eq. (1.26) in Eq. (1.25) we can express the transmitted field amplitude as

$$\frac{E_{out}}{E_{in}} = \frac{\sigma - \alpha e^{ik(\omega)L}}{1 - \sigma\alpha e^{ik(\omega)L}}, \tag{1.28}$$

and thus the intensity transmission is (see Fig. 1.14(a))

$$T(\omega) \equiv \left|\frac{E_{out}}{E_{in}}\right|^2 = \frac{\sigma^2 + \alpha^2 - 2\sigma\alpha\cos(k(\omega)L)}{1 + \sigma^2\alpha^2 - 2\sigma\alpha\cos(k(\omega)L)}. \tag{1.29}$$

The condition for constructive interference for an electromagnetic wave propagating in the ring is given by $k(\omega)L = 2\pi m$ with $m \in \mathbb{Z}$. This condition is evident both from Eq. (1.26) , when we impose the in-phase sum of the fields, but also from Eq. (1.29), where the transmission minima correspond to resonant frequencies. The distance between adjacent resonances is the so-called *Free Spectral Range* (FSR), which in frequency is given by

$$\mathrm{FSR}_\nu = \frac{c}{2\pi R n_g}, \tag{1.30}$$

and in wavelength is approximately given by

$$\mathrm{FSR}_\lambda \approx \frac{\lambda_0^2}{n_g L} \tag{1.31}$$

where λ_0 is the central wavelength between the adjacent resonances, and $n_g = c/v_g$ is the group index which can be conveniently measured from the transmission spectrum of the resonator. When the microring is excited precisely at one of its resonances ω_{res} , the transmitted light intensity is

$$T(\omega_{\text{res}}) = \frac{(\sigma - \alpha)^2}{(1 - \sigma\alpha)^2}, \tag{1.32}$$

a quantity that vanishes whenever $\sigma = \alpha$. This condition is known as *critical coupling*, and it is the desired working point in most experiments, although it was recently demonstrated this is not the optimal coupling condition for heralded single photon sources [100].

Again using Eq. (1.26) in Eq. (1.25), we can express the field amplitude in the ring resonator, refereed to as the *Field Enhancement* (FE) as

$$\mathcal{F}(\omega) = \frac{E_1}{E_{\text{in}}} = \frac{i\kappa}{1 - \sigma\alpha e^{ik(\omega)L}}. \tag{1.33}$$

When calculated in the proximity of a resonant frequency ω_{res} and in the limit $\kappa \ll \sigma \approx 1$, the FE becomes

$$\mathcal{F}(\omega) \propto \frac{\Delta/2}{(\omega - \omega_{\text{res}}) + i(\Delta/2)}, \tag{1.34}$$

which is a Lorentzian function (see Fig 1.14(b)) centered around ω_{res} and with FWHM

$$\Delta = \frac{2(1 - \sigma\alpha)v_g}{L\sigma\alpha}. \tag{1.35}$$

We can finally point out some of the most relevant figures of merit for microrings resonators, starting from the *Quality factor* Q. This is a measure of the time-averaged energy stored in the ring divided by the power dissipated per optical cycle, so that

$$Q = \omega_{\text{res}} < \frac{\text{energy stored}}{\text{power loss}} >, \tag{1.36}$$

but more intuitively it can be pictured as the number of oscillations of the field before the field intensity drops to $1/e$ of the original value. Thus, the quality factor conveys the effectiveness of the resonator in 3D-confining an electromagnetic wave. The coupling to the bus waveguide represents a "loss" channel, and thus we can first express the so-called *intrinsic* or *bare quality factor* Q_{int}, which is essentially determined by intrinsic absorption, scattering, and bending losses as

$$Q_{\text{int}} = \frac{2\pi n_g}{\lambda_{\text{res}} a}, \tag{1.37}$$

where λ_{res} is the resonance wavelength, and a is the loss coefficient expressed as the inverse of a length. When the ring is coupled to the bus waveguide, we can decompose the ring quality factor as

$$\frac{1}{Q} = \frac{1}{Q_{\text{coupling}}} + \frac{1}{Q_{\text{int}}}, \tag{1.38}$$

where Q_{coupling} is the ring quality factor accounting for the coupling losses alone. The quality factor Q can be obtained directly from the transmission spectrum of the microring, as

$$Q = \frac{\omega_{\text{res}}}{\Delta}, \tag{1.39}$$

and using Eq. (1.35) we have

$$Q = \frac{\omega_{\text{res}} L \sigma \alpha}{2(1-\sigma\alpha) v_g}. \tag{1.40}$$

Using the previous expressions, the FE for a given resonance can also be expressed as

$$\mathcal{F}(\omega_{\text{res}}) = \sqrt{\frac{4 v_g}{L \omega_{\text{res}}} \frac{Q^2}{Q_{\text{coupling}}}}, \tag{1.41}$$

which, at the critical coupling becomes

$$\mathcal{F}(\omega_{\text{res}}) = \sqrt{\frac{2 v_g Q}{L \omega_{\text{res}}}}. \tag{1.42}$$

Another recurrent figure of merit for resonators is the *Finesse* F, defined as

$$F = \frac{\text{FSR}}{\Delta} = \frac{\lambda_{\text{res}}}{n_g L} Q, \tag{1.43}$$

which is directly linked to the quality factor, and measures the width of the resonances with respect to their separation.

Microring resonators are today widely used in photonic integrated circuits, both in the simple configuration of Fig. 1.13 and in more sophisticated arrangements, such as Add-Drop filters, double ring resonators, microring Coupled Resonator Optical Waveguides (CROWs) [99, 66], and more complex geometries.

1.3 Quantization of the electromagnetic field in an integrated device

The goal of this Chapter is to introduce the basic formalism we will adopt throughout the thesis. This discussion will provide the key to interpret how we tackle an electromagnetic problem in an integrated device, and introduce the mathematical garment. It will be the common starting point and the vocabulary of most of the following chapters and sections, so we believe it is convenient to discuss the basic strategy here, and simply recall it later.

We adopt the quantization of the electromagnetic field presented by Liscidini et al. in [41, 42], referred to as the *asymptotic fields approach*, which was inspired

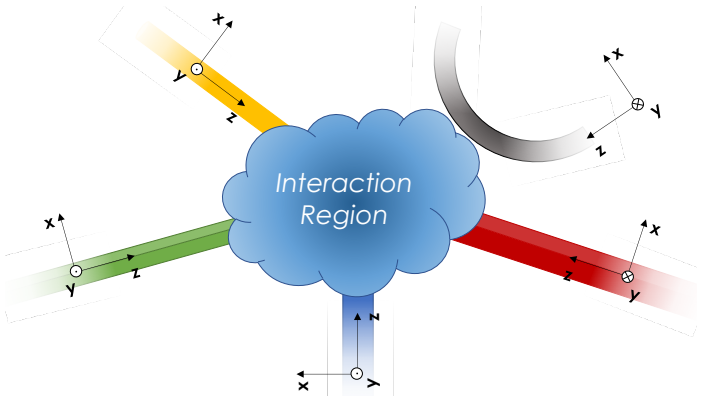

Figure 1.15: Sketch of the typical structure considered in the framework of the asymptotic states approach. An interaction region (e.g. a nonlinear medium) is directly connected or evanescently coupled to different in/out channels; each of the channels is associated with an independent reference frame with the z axis directed toward the interaction region so that incoming fields are related to positive wave vectors, while outgoing fields have negative wave vectors.

by the theory of scattering in quantum mechanics [101]. In this approach the electromagnetic field in an integrated structure can be expanded on the basis of *asymptotic-in* and *asymptotic-out* modes, solutions of the linear Maxwell equations inside the device. Since these modes constitute an orthogonal basis, they can be adopted for treating both the linear and the nonlinear propagation of light in the structure, when the nonlinearity is regarded as an effective "scattering center". Asymptotic-in states can be envisioned as fields, existing everywhere is space, whose superposition for $t \to -\infty$ results in a wave packet incident on the integrated structure; similarly, the superposition of asymptotic-out states results in a wave packet exiting the structure for $t \to +\infty$. To better visualize these concept one can refer to Fig. 1.15, where we schematically represented an integrated device as an "interaction region" surrounded by all the possible input and output channels to access or leave the structure. Please note that even absorption losses can be modeled as a "phantom channel" within this model [102]. Following this interpretation, the electric displacement and the magnetic field operators in any point of the structure are given by

$$\mathbf{D}(\mathbf{r}) = \sum_{n,I} \int_0^\infty dk \, \sqrt{\frac{\hbar\omega_{nIk}}{2}} a_{nIk} \mathbf{D}_{nIk}^{asy-in}(\mathbf{r}) + H.c. \tag{1.44}$$

$$\mathbf{B}(\mathbf{r}) = \sum_{n,I} \int_0^\infty dk \, \sqrt{\frac{\hbar\omega_{nIk}}{2}} a_{nIk} \mathbf{B}_{nIk}^{asy-in}(\mathbf{r}) + H.c.$$

where n labels the channel, I labels the particular propagating mode supported by channel n, k is the wave vector of such mode, a_{nIk} is the destruction operator

for asymptotic-in states characterized by

$$[a_{nIk}, a_{n'I'k'}] = 0 \tag{1.45}$$
$$[a_{nIk}, a^{\dagger}_{n'I'k'}] = \delta_{nn'}\delta_{II'}\delta(k-k'),$$

and $\mathbf{D}^{asy-in}_{nIk}(\mathbf{r})$ and $\mathbf{B}^{asy-in}_{nIk}(\mathbf{r})$ are the asymptotic-in states are, whose definition is

$$\mathbf{D}^{asy-in}_{nIk}(\mathbf{r}) \approx \mathbf{D}_{nIk}(\mathbf{r}_n) + \sum_{n'I'}\int_0^{\infty} dk'\ T^{out}_{nI,n'I'}(k,k')\mathbf{D}_{n'I'(-k')}(\mathbf{r}_{n'}) \tag{1.46}$$
$$\mathbf{B}^{asy-in}_{nIk}(\mathbf{r}) \approx \mathbf{B}_{nIk}(\mathbf{r}_n) + \sum_{n'I'}\int_0^{\infty} dk'\ T^{out}_{nI,n'I'}(k,k')\mathbf{B}_{n'I'(-k')}(\mathbf{r}_{n'}).$$

Eq. (1.46) clearly translates the verbal definition of asymptotic-in state we provided earlier. Here, $\mathbf{D}_{nIk}(\mathbf{r}_n)$ represents the electric displacement vector in the isolated input channel n, propagating in mode I with wave vector k, and $T^{out}_{nI,n'I'}(k,k')$ is the matrix that connects the fields in channel n, mode I, to the fields in all the other channels n', modes I'. If we consider Eq. (1.44) in the limit $t \to -\infty$ it can be demonstrated that, from Eq. (1.46), the outgoing contributions cancel out and the resulting field operators become

$$\mathbf{D}(\mathbf{r}) \to_{t\to-\infty} \sum_{n,I}\int_0^{\infty} dk\ \sqrt{\frac{\hbar\omega_{nIk}}{2}}a_{nIk}\mathbf{D}_{nIk}(\mathbf{r}) + H.c. \tag{1.47}$$
$$\mathbf{B}(\mathbf{r}) \to_{t\to-\infty} \sum_{n,I}\int_0^{\infty} dk\ \sqrt{\frac{\hbar\omega_{nIk}}{2}}a_{nIk}\mathbf{B}_{nIk}(\mathbf{r}) + H.c.,$$

which are the superposition of incoming fields from the isolated input channels, as expected.

Parallel to the introduction of asymptotic-in states, we can now briefly recall the concept of asymptotic-out states. This is an alternative basis for the expansion of field operators, and thus, similarly to Eq. (1.44) we have

$$\mathbf{D}(\mathbf{r}) = \sum_{n,I}\int_0^{\infty} dk\ \sqrt{\frac{\hbar\omega_{nIk}}{2}}b_{nIk}\mathbf{D}^{asy-out}_{nIk}(\mathbf{r}) + H.c. \tag{1.48}$$
$$\mathbf{B}(\mathbf{r}) = \sum_{n,I}\int_0^{\infty} dk\ \sqrt{\frac{\hbar\omega_{nIk}}{2}}b_{nIk}\mathbf{B}^{asy-out}_{nIk}(\mathbf{r}) + H.c.,$$

where the destruction operator for asymptotic-out states is now labelled b_{nIk} just for clarity, and the asymptotic-out states are defined as

$$\mathbf{D}^{asy-out}_{nIk}(\mathbf{r}) \approx \mathbf{D}_{nI(-k)}(\mathbf{r}_n) + \sum_{n'I'}\int_0^{\infty} dk'\ T^{in}_{nI,n'I'}(k,k')\mathbf{D}_{n'I'k'}(\mathbf{r}_{n'}) \tag{1.49}$$
$$\mathbf{B}^{asy-out}_{nIk}(\mathbf{r}) \approx \mathbf{B}_{nI(-k)}(\mathbf{r}_n) + \sum_{n'I'}\int_0^{\infty} dk'\ T^{in}_{nI,n'I'}(k,k')\mathbf{B}_{n'I'k'}(\mathbf{r}_{n'})$$

the matrix $T^{in}_{nI,n'I'}(k,k')$ now relating the output fields to the input ones. Once more, Eq. (1.49) truly reflects mathematically the definition of asymptotic-out states: indeed, if we let $t \to +\infty$ and look at the field operator as superposition of asymptotic-out states in Eq. (1.48), we obtain

$$\begin{aligned}\mathbf{D}(\mathbf{r}) &\to_{t\to+\infty} \sum_{n,I} \int_0^\infty dk \, \sqrt{\frac{\hbar\omega_{nIk}}{2}} b_{nI(-k)} \mathbf{D}_{nI(-k)}(\mathbf{r}) + H.c. \\ \mathbf{B}(\mathbf{r}) &\to_{t\to+\infty} \sum_{n,I} \int_0^\infty dk \, \sqrt{\frac{\hbar\omega_{nIk}}{2}} b_{nI(-k)} \mathbf{B}_{nI(-k)}(\mathbf{r}) + H.c.,\end{aligned} \tag{1.50}$$

which are the superposition of outgoing fields in the isolated output channels, as expected.

The two asymptotic states bases are clearly not independent, and can be linked by noting that

$$\begin{aligned}\mathbf{D}^{asy-out}_{nIk}(\mathbf{r}) &= [\mathbf{D}^{asy-in}_{nIk}(\mathbf{r})]^* \\ \mathbf{B}^{asy-out}_{nIk}(\mathbf{r}) &= [\mathbf{B}^{asy-in}_{nIk}(\mathbf{r})]^*,\end{aligned} \tag{1.51}$$

and, from the completeness of the basis, that

$$\begin{aligned}\mathbf{D}^{asy-out}_{nIk}(\mathbf{r}) &= \sum_{n'I'} \int_0^\infty dk' \; T^{in}_{nI,n'I'}(k,k') \mathbf{D}^{asy-in}_{n'I'k'}(\mathbf{r}) \\ \mathbf{D}^{asy-in}_{nIk}(\mathbf{r}) &= \sum_{n'I'} \int_0^\infty dk' \; T^{out}_{nI,n'I'}(k,k') \mathbf{D}^{asy-out}_{n'I'k'}(\mathbf{r}),\end{aligned} \tag{1.52}$$

and similarly for the magnetic field asymptotic state. It is now evident the physical interpretation of $T^{in}_{nI,n'I'}(k,k')$ as the scattering matrix $S_{nI,n'I'}(k,k')$ of the integrated structure. The interpretation of the other matrix we introduced for the asymptotic-in states, $T^{out}_{nI,n'I'}(k,k')$, follows directly from recognizing its connection to $T^{in}_{nI,n'I'}(k,k')$ thanks to Eq. (1.51) and (1.52)

$$T^{out}_{nI,n'I'}(k,k') = [T^{in}_{nI,n'I'}(k,k')]^* = S^*_{nI,n'I'}(k,k'). \tag{1.53}$$

From these relations it is finally possible to express the connection between the destruction operators for asymptotic-in and -out states

$$\begin{aligned}a_{nIk} &= \sum_{n'I'} \int_0^\infty dk' \; T^{in}_{nI,n'I'}(k,k') b_{n'I'k'} \\ b_{nIk} &= \sum_{n'I'} \int_0^\infty dk' \; T^{out}_{nI,n'I'}(k,k') a_{n'I'k'}.\end{aligned} \tag{1.54}$$

With these relations it will be possible to connect the creation operators in the input channels to the correspondent operators in the output channels, and gather immediately the output state for any integrated circuit.

Let us now show how the use of the asymptotic fields can facilitate the solution of a linear or nonlinear problem in integrated quantum optics. This brief discussion is based on the backward Heisenberg picture approach, presented in details in [41] for the case of SPDC, and in [103] for SFWM. Since the exhaustive derivation of all the formulas involved is not instrumental to the rest of the present thesis, we redirect the interested reader to those publications.

We envision a situation very close to that represented in Fig. 1.15, where we have linear channels entering and exiting from a restricted region, where the nonlinear interaction takes place. Our goal is to express the relation between a state impinging on the structure from the input channels at $t = t_0 \ll 0$, labelled $|\psi(t_0\rangle$, to an output state exiting the structure from the output channels at $t = t_1 \gg 0$, labelled $|\psi(t_1)\rangle$. The evolution is governed by both the linear and the nonlinear Hamiltonians

$$\begin{aligned} H_L &= \sum_n \int_0^\infty dk\ \hbar\omega_{n,k} a^\dagger_{n,k} a_{n,k} \\ H_{NL} &= -\frac{1}{4\epsilon_0} \int d\mathbf{r}\ \Gamma_3^{ijkl} D^i(\mathbf{r}) D^j(\mathbf{r}) D^k(\mathbf{r}) D^l(\mathbf{r}), \end{aligned} \tag{1.55}$$

where we have neglected the zero-point energy, and considered only the third-order nonlinear response, which will be the our only focus in the following chapters. Now, if we let $t_0 \to -\infty$, the energy of the incoming electromagnetic field can be regarded as completely localized in the isolated input channels. This condition can be envisioned as the limit for $t \to -\infty$ of an asymptotic-in state, as we described in (1.47). Therefore, we can regard the input state as evolving into the asymptotic-in state at $t = 0$, through the linear Hamiltonian H_L

$$|\psi_{in}\rangle = e^{-iH_L(0-t_0)/\hbar} |\psi(t_0)\rangle = e^{iH_L t_0/\hbar} |\psi(t_0)\rangle\,, \tag{1.56}$$

where $|\psi_{in}\rangle$ is the asymptotic-in state. Similarly, we consider the output state $|\psi(t_1)\rangle$, in the limit $t_1 \to +\infty$, as that evolving from an asymptotic-out state $|\psi_{out}\rangle$ at $t = 0$ (see (1.50)), subject to the linear Hamiltonian H_L

$$|\psi(t_1)\rangle = e^{-iH_L(t_1-0)/\hbar} |\psi_{out}\rangle = e^{-iH_L t_1/\hbar} |\psi_{out}\rangle\,. \tag{1.57}$$

This situation can be better understood from the sketch in Fig. 1.16.

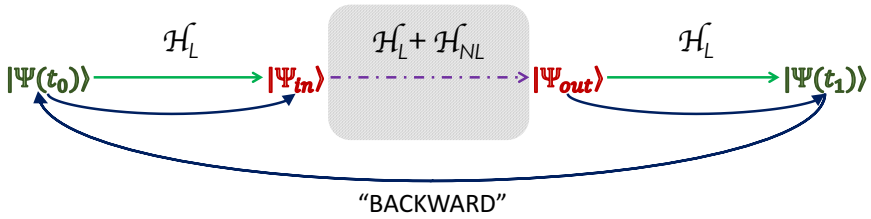

Figure 1.16: Schematic representation of the idea behind the backward Heisenberg picture approach used for calculating the asymptotic states of an arbitrary nonlinear structure.

The underlying intent of the previous discussion is to carry out a shift in the point of view: now we are no longer interested in finding directly the relation between generic input and output states, but we look for the connection between the asymptotic-in and -out states. Indeed, we moved from searching the solution of the problem

$$|\psi(t_1)\rangle = e^{-i(H_L+H_{NL})(t_1-t_0)/\hbar}\,|\psi(t_0)\rangle \tag{1.58}$$

to solving

$$\begin{aligned} |\psi_{out}\rangle &= e^{iH_L t_1/\hbar} e^{-i(H_L+H_{NL})(t_1-t_0)/\hbar} e^{-iH_L t_0/\hbar}\,|\psi_{in}\rangle \\ &\equiv U(t_1,t_0)\,|\psi_{in}\rangle\,. \end{aligned} \tag{1.59}$$

Let us consider, for a moment, the particular case of a completely linear evolution of the fields, namely $H_{NL} = 0$. Hence, Eq. (1.59) leads us to

$$|\psi_{out}\rangle = e^{iH_L(t_1-t_0)/\hbar}\,|\psi_{in}\rangle\,, \tag{1.60}$$

and considering that the asymptotic-in and -out states are just functions of the creation and destruction operators $F\{a^\dagger_{nIk}, a_{nIk}\}$ and $G\{b^\dagger_{nIk}, b_{nIk}\}$ respectively, then Eq. (1.60) reduces to a simple change in the basis from asymptotic-in to asymptotic-out modes, governed by Eq. (1.54)

$$G\{b^\dagger_{nIk}, b_{nIk}\}\,|vac\rangle = e^{iH_L(t_1-t_0)/\hbar} F\{a^\dagger_{nIk}, a_{nIk}\}\,|vac\rangle\,. \tag{1.61}$$

Going back to the more interesting case of a non-vanishing nonlinear interaction, let us assume that the asymptotic-in state is in the form

$$|\psi_{in}\rangle = e^{O}\,|vac\rangle\,, \tag{1.62}$$

and thus also the asymptotic-out state can be expressed as

$$\begin{aligned} |\psi_{out}\rangle &= U(t_1,t_0)\,|\psi_{in}\rangle = U(t_1,t_0)e^{O}\,|vac\rangle \\ &= U(t_1,t_0)e^{O}U^\dagger(t_1,t_0)\,|vac\rangle \equiv e^{\bar{O}}\,|vac\rangle\,, \end{aligned} \tag{1.63}$$

since $U^\dagger(t_1,t_0)\,|vac\rangle = |vac\rangle$. Note that from the comparison between Eq. (1.62) and Eq. (1.63) it is clear that we are currently working in the Heisenberg picture representation. The operator $\bar{O}$ satisfies the time-evolution differential equation

$$i\hbar\frac{d\bar{O}(t)}{dt} = [\bar{O}(t), \hat{V}(t)] \tag{1.64}$$

subject to the condition $\bar{O}(t_1) = O$ (this also clarifies the definition "backward"), and where

$$\hat{V}(t) = U(t_1,t)e^{iH_Lt/\hbar}H_{NL}e^{-iH_Lt/\hbar}U^\dagger(t_1,t). \tag{1.65}$$

Once we have specified the explicit form of the nonlinear Hamiltonian and we have integrated Eq. (1.64) we can find the relation between the operators $\bar{O}$ and O, which embodies the relation between the input and output asymptotic states. First, recalling Eq. (1.44) and keeping solely the energy-conserving terms associated with SFWM, the nonlinear Hamiltonian becomes

$$H_{NL} = -\sum_{n_1,n_2,n_3,n_4}\sum_{I_1,I_2,I_3,I_4}\int_{\Omega_{SI}}dk_1dk_2\int_{\Omega_P}dk_3dk_4\;S_{n_1,n_2,n_3,n_4}(k_1,k_2,k_3,k_4) \tag{1.66}$$
$$\times b^\dagger_{n_1I_1k_1}b^\dagger_{n_2I_2k_2}a_{n_3I_3k_3}a_{n_4I_4k_4} + H.c.,$$

where the integrals are carried out over the pump and signal/idler wave vector intervals Ω_P and Ω_{SI}, respectively, and

$$S_{n_1,n_2,n_3,n_4}(k_1,k_2,k_3,k_4) = \tag{1.67}$$
$$= \frac{3}{2\epsilon_0}\sqrt{\frac{\hbar\omega_{n_1I_1k_1}\hbar\omega_{n_2I_2k_2}\hbar\omega_{n_3I_3k_3}\hbar\omega_{n_4I_4k_4}}{16}}$$
$$\times\int d\mathbf{r}\Gamma_3^{ijkl}(\mathbf{r})[D^{i,asy-out}_{n_1I_1k_1}(\mathbf{r})]^*[D^{j,asy-out}_{n_2I_2k_2}(\mathbf{r})]^*D^{k,asy-in}_{n_3I_3k_3}(\mathbf{r})D^{l,asy-in}_{n_4I_4k_4}(\mathbf{r}).$$

With such nonlinear Hamiltonian, the operator $\hat{V}(t)$ becomes

$$\hat{V}(t) = \sum_{n_1,n_2,n_3,n_4}\sum_{I_1,I_2,I_3,I_4}\int_{\Omega_{SI}}dk_1dk_2\int_{\Omega_P}dk_3dk_4\;S_{n_1,n_2,n_3,n_4}(k_1,k_2,k_3,k_4;t) \tag{1.68}$$
$$\times\bar{b}^\dagger_{n_1I_1k_1}(t)\bar{b}^\dagger_{n_2I_2k_2}(t)\bar{a}_{n_3I_3k_3}(t)\bar{a}_{n_4I_4k_4}(t) + H.c.,$$

with

$$S_{n_1,n_2,n_3,n_4}(k_1,k_2,k_3,k_4;t) = \tag{1.69}$$
$$S_{n_1,n_2,n_3,n_4}(k_1,k_2,k_3,k_4)e^{i(\omega_{n_1I_1k_1}+\omega_{n_2I_2k_2}-\omega_{n_3I_3k_3}-\omega_{n_4I_4k_4})t},$$

and

$$i\frac{d\bar{b}_k^\dagger(t)}{dt} = \int dk_1 dk_2 \; S(k_1,k_2,k;t)\bar{c}_{k_1}^\dagger(t)\bar{c}_{k_2}^\dagger(t), \tag{1.70}$$

and a similar definition holds for the barred operators $\bar{a}_k^\dagger$. Assuming that the input field, referred to as the pump, is a coherent state, namely

$$O = \alpha A^\dagger - H.c. \tag{1.71}$$

with $|\alpha|^2$ the expected number of photons in the pump pulse,

$$A^\dagger = \int dk \; \phi_P(k) a_k^\dagger \tag{1.72}$$

and $\phi_P(k)$ the normalized pump spectrum, then from integrating Eq. (1.64) subject to the undepleted pump approximation, and limiting ourselves to only the first order corrections in the Taylor expansion of the solution (see [41, 103] for further details), we obtain the squeezed vacuum state

$$|\psi_{out}\rangle = e^{\bar{O}}\,|vac\rangle = e^{\alpha A^\dagger + \beta C_{II}^\dagger - H.c.}\,|vac\rangle\,, \tag{1.73}$$

where

$$C_{II}^\dagger = \frac{1}{\sqrt{2}}\sum_{n_1,n_2}\sum_{I_1,I_2}\int dk_1 dk_2 \; \phi_{n_1,n_2}(k_1,k_2) b_{n_1,I_1,k_1}^\dagger b_{n_2,I_2,k_2}^\dagger \tag{1.74}$$

is the creation operator for a photon pair, and

$$\begin{aligned}\phi_{n_1,n_2}(k_1,k_2) = {} & \frac{3\sqrt{2}i\pi\alpha^2\hbar}{4\beta\epsilon_0}\int dk_3 \; \phi_P(k_3)\phi_P(k_1+k_2-k_3) \\ & \times\sqrt{\omega_{n_1 I_1 k_1}\omega_{n_2 I_2 k_2}\omega_{n_3 I_3 k_3}\omega_{n_4 I_4 (k_1+k_2-k_3)}} \\ & \times\int d\mathbf{r}\; \Gamma_3^{ijkl}(\mathbf{r}) D_{n_1 I_1 k_1}^{i,asy-in}(\mathbf{r}) D_{n_2 I_2 k_2}^{j,asy-in}(\mathbf{r}) D_{n_3 I_3 k_3}^{k,asy-in}(\mathbf{r}) D_{n_4 I_4 (k_1+k_2-k_3)}^{l,asy-in}(\mathbf{r})\end{aligned} \tag{1.75}$$

is the so-called *Biphoton Wave Function* (BWF). In Eq. (1.73) and (1.75) the coefficient β represents the average number of photon pairs generated by SFWM in the limit of low generation probability, and it can be obtained simply by imposing the normalization on the BWF. Under the same conditions, Eq. (1.73) can be written as [104]

$$|\psi_{out}\rangle = \left(1+\mathcal{O}(|\beta|^2)\right)|\text{vac}\rangle + \beta C_{II}^\dagger\,|\text{vac}\rangle + \frac{1}{2}\left[\beta C_{II}^\dagger\right]^2|\text{vac}\rangle + \ldots, \tag{1.76}$$

where now it should be noticed that the state (1.76) is not normalized. Since in the next chapters of this thesis we will be interested in the generation of single photon pairs and double photon pairs, it is more convenient to normalize the single states appearing in (1.76). In particular, given the definition of $C_{II}^\dagger$ in (1.74), we can identify the state associated with a converted photon pair as $|II\rangle \equiv C_{II}^\dagger\,|vac\rangle$; similarly, the state representing two photon pairs generated

by the nonlinear interaction is given by $|IV\rangle \equiv (C_{II}^{\dagger})^2 |vac\rangle$. The state $|II\rangle$ is already normalized, no matter which is the source geometry. The same property does not hold for the state $|IV\rangle$, whose normalization depends on the particular source design (we further discuss these properties in Appendices A.1 and B.2). From these considerations, the output state (1.76) can be written as

$$|\psi_{out}\rangle = \left(1 + \mathcal{O}(|\beta|^2)\right) |\text{vac}\rangle + \beta |II\rangle + \frac{\beta^2}{\sqrt{N}} |IV\rangle + \dots, \tag{1.77}$$

where N is the appropriate normalization constant.

Finally, we now possess all the theoretical support needed to deal with the topics presented in the following chapters. As the reader will notice, we will adopt the asymptotic-in and -out fields formalism recurrently for both linear and nonlinear propagation of electromagnetic fields in an integrated structure, and whenever we will rely on parametric fluorescence for the generation of photon pairs, the backward Heisenberg picture approach recalled in this section will provide us the quantum state produced by the source.

Chapter 2

Nonlinear response in silicon-based integrated devices

2.1 Silicon-based materials for nonlinear optics

A wide range of materials are today under investigation for their relatively high nonlinear response, exploiting both second- and third-oder processes. As we recalled before, III-V semiconductors, $LiNbO_3$, BBO or KTP crystals are commonly employed for second-order parametric processes but, since here we focus our attention of SFWM as the reference phenomenon for the generation of non-classical light, we need to move our discussion to the most common solution, which is represented by silicon-based (Si-based) materials. Before proceeding with a general introduction on these platforms, we want to emphasize that, despite their prevalence, Si-based materials do not represent the sole material choice for integrated quantum optics: for instance, a remarkable example is given by silica-on-silicon waveguides [74]. In this case, an optical waveguide is fabricated inside a silica slab by controlling the refractive index through a low level of doping; such structure is grown with a bottom-up approach, starting from a Si substrate. The resulting waveguide is characterized by low propagation losses, in the order of 10^{-1} dB/cm or less depending on the geometry [105, 106], mostly ascribed to residual hydrogen bondings and tunneling of light into the Si substrate. However, the material third-order nonlinearity is low (in the order of 10^{-22} m^2/V^2 [107]) and the small index mismatch between the core and the cladding region, typically around 0.5%, asks for very large silica substrates and bending radii. Other examples of non-Si-based materials can be considered, but in the context of this work we will be mostly concerned with Si-based materials.

Silicon-On-Insulator (SOI) is today one of the preferred platforms for integrated quantum photonics, owing to the large benefits it brings in terms of nonlinearity and fabrication technology; yet, a number of alternatives emerged recently in order to overcome some of the drawbacks associated with crystalline

silicon waveguides, and to ease the fabrication processes. Among these, we we are interested in discussing the properties of Silicon Nitride and Porous Silicon.

The SOI platform

Silicon is the dominant crystalline material for exploiting third-order nonlinear phenomena. Such prevalence is granted by the many benefits it bring in all areas, from the physical properties to the fabrication infrastructure. Indeed, silicon is probably not the absolute best-performing material in most of those areas, but considering the overall balance it emerges as the preferable choice. The crystalline structure of silicon, sketched in Fig. 2.1, is centrosymmetric and thus an ideal bulk silicon crystal has null second-order nonlinear response (although it is still possible to obtain an "effective" non-vanishing χ_2, by straining silicon mechanically or electrically [108, 109], a strategy also used for silicon nitride waveguides [91]). Yet, the third-order nonlinear susceptibility is particularly high, more than 100 times that of silica [110]. The silicon band structure is characterized by an energy gap of 1.12 eV and low intrinsic carrier concentration, allowing the material to be transparent to wavelengths above 1.1 μm including, most notably, the bandwidths commonly used for optical telecommunications, around 1.55 μm and 1.3 μm: this feature is particularly convenient for the integration of SOI platforms into the current optical network without the need for frequency-conversions. Another fundamental characteristic of silicon for integrated quantum optics is represented by its high refractive index, around $n_{Si} \approx 3.48$ at $\lambda = 1.55$ μm. Indeed, the refractive index mismatch between the core of the waveguide and its cladding determines how tightly the electromagnetic field can be confined, and thus the field enhancement. In SOI platforms, the substrate beneath the waveguide is made of silica ($n_{SiO_2} \approx 1.45$ at $\lambda = 1.55$ μm), which is typically the same material as the top and lateral cladding (simply air is another possibility), and thus a very strong index contrast can be achieved, reducing the bending radius by a factor of 10^3 compared to silica-on-silicon waveguides, and boosting the nonlinear response of the waveguide. In summary, the combination of strong third-order nonlinear response and high field enhancement due to the large refractive index makes silicon one of the most natural choices for integrated quantum optics.

Unfortunately, the propagation losses experienced by light in a SOI device can be relatively high in the framework of quantum optics, depending on the waveguide geometry and the fabrication technique. Considering a standard SOI ridge waveguide with 500 nm $\times$ 220 nm cross section, typical losses can be measured around $2-3$ dB/cm, and they are mainly ascribed to the scattering of light induced by the roughness of the waveguide sidewall. This technological issue can limit the convenience of SOI platforms whenever very high quality factor resonators are required, or large multipartite quantum states should be generated and propagated on a chip. Another detrimental feature of the SOI platform, and nonetheless common to all the silicon-based materials, is the lack of a bright integrated laser source. Indeed, crystalline silicon has an indirect bandgap (i.e. the maximum of the valence band has a different lattice wave vector then the mini-

mum of the conduction band), which makes it a poor light-emitting material: an electronic transition should always be mediated by a phonon to provide the missing momentum. Several strategies have been tested to create a silicon laser for integrated optics, yet today the source pumping is still commonly implemented with strong external lasers. A notable exception to this solution is represented by the hybrid integration of non-Si-based laser sources by wafer bonding on a silicon substrate [111]. Finally, we need to emphasize that whenever a relatively high optical power is propagated in a SOI waveguide (in the order of a few mW) one can observe the rise of other nonlinear phenomena which, to our goal, constitute a source of noise. For instance, we can recall Self- and Cross-Phase Modulation (SPM and XPM), which originate from the real part of the nonlinear susceptibility; Stimulated Brillouin Scattering (SBS), Stimulated Raman Scattering (SRS), and Two-Photon-Absorption (TPA), which originate from the imaginary part of the nonlinear susceptibility. This latter effect is particularly relevant for SOI platforms working at wavelengths approximately below 2 μm, and it consists of the simultaneous absorption of two incident photons allowing an electron to transition from the valence to the conduction band of silicon. Hence, it affects the light propagation twice, both by the direct absorption of photons to promote electrons, and by increasing the free electron concentration, leading to higher Free Carrier Absorption (FCA) of photons. From a practical point of view, the pump intensity coupled to a SOI for the generation of photons by SFWM should me maintained below a certain threshold.

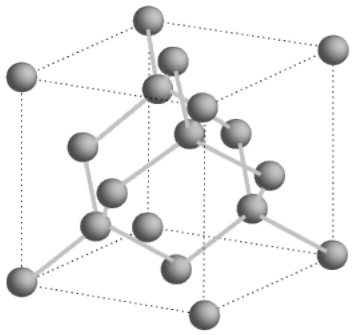

Figure 2.1: Representation of the crystalline structure of silicon.

Despite the possible disadvantages we listed above, the SOI platform is today the widespread platform for integrated quantum photonics. This is mostly due to the technological advances and the industrial environment associated with the production of CMOS (Complementary Metal-Oxide Semiconductor) devices. Indeed, for other physical reasons, silicon is the dominant material of microelectronic industry, and therefore the lithographic processes are well-established, the purity of the material is extremely high, and the overall chip production is much cheaper with respect to all the competing alternatives. Moreover, since the control of the dynamic response of a photonic integrated circuit is usually achieved by heaters and electro-optic modulators, the SOI platforms permits a straightforward integration and interoperability of these components, ultimately delivering a complete electronic-optical circuit.

Silicon Nitride

The linear and nonlinear (TPA-related) losses experienced by photons traveling in silicon waveguides can be relatively high, as we recalled above, and this can lead to poor generation rates and reduced quantum state purity for sources of nonclassical states of light. These effects are particularly significant in the telecommunication bands, where many devices are intended to operate and where the infrastructure for quantum communications is already being developed. Therefore, a variety of materials have been investigated for their nonlinear response and their performances in light confinement. Recently, Silicon Nitride (Si_3N_4) was demonstrated as a promising candidate for integrated nonlinear optics [112, 90, 113, 114]. Similarly to SOI structures, silicon nitride is CMOS compatible and it can benefit from the fabrication technologies and infrastructure we already discussed.

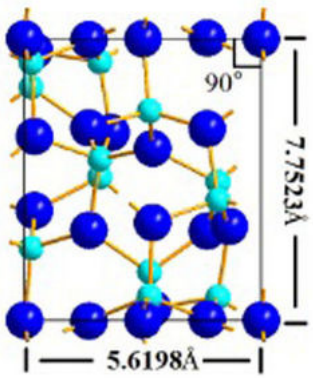

Figure 2.2: Representation of the crystalline structure of silicon nitride (Si_3N_4, adapted from [115]).

Different techniques are today adopted to produce silicon nitride, such as Low Pressure Chemical Vapour Deposition (LPCVD) at high temperature or Plasma Enhanced Chemical Vapour Deposition (PECVD) at low temperature. The former method guarantees results closer to the correct stoichiometric ratio, and the resulting silicon nitride is highly strained characterized by high homogeneity of material index and thickness. Nonetheless, given the strained nature of silicon nitride, historically it has been technologically challenging to realize layers with thickness above a few hundreds of microns, yet recent advances in the fabrication techniques have produced silicon nitride layers more than 500 nm thick [112, 116]. Through PECVD, silicon nitride composition can be strongly tailored by tuning the deposition conditions, obtaining a range of results from silicon-rich (with a higher refractive index) to nitrogen-rich (with a lower refractive index). The crystalline structure of stoichiometric Si_3N_4 is depicted in Fig. 2.2, and it shares most of the properties of crystalline silicon, including the the centrosymmetry (averaged, in the case of non-stoichiometric silicon nitride), and the indirect bandgap, which separates the valence and conduction bands by $\approx$ 5 eV. The resulting refractive index is $n_{Si_3N_4} = 2$ at $\lambda = 1.55$ μm, a much lower value compared to the SOI platform. However, it should be noticed that a higher refractive index contrast (with a silica cladding, for instance) can be both beneficial and detrimental, for it enhances every form of light matter interaction, including scattering. On the one hand, the nonlinear

third-order response of silicon is stronger than silicon nitride (typically by a factor 10^{-2} for an identical waveguide geometry), but on the other hand the propagation losses are extremely reduced [117, 118, 90], even down to ~ 0.13 dB/m [119]. The reduced refractive index contrast asks for the design of larger footprint integrated circuits, with a minimal bending radius attainable around 40 μm, but the low-loss propagation allows for the realization of record-high quality factor ring resonators, very recently achieving $Q = 67 \cdot 10^6$ [119]. In addition to those impressive features, it is fundamental to emphasize that, given the high bandgap of silicon nitride, TPA is a negligible effect at telecom wavelengths.

In synthesis, silicon nitride waveguides are characterized by drastically reduced linear and nonlinear losses with respect to SOI waveguides, at the expense of a weaker third-order nonlinear response and a poorer field confinement.

Porous Silicon

Although the optical properties of porous silicon (pSi) have not been thoroughly explored, this material shows some interesting features which can make it a potential alternative, for some specific applications, to the well-established Si-based platforms such as silicon or silicon nitride we introduced above. Thanks to its peculiar structural features and the fabrication processes, pSi is today being investigated for its linear and nonlinear response, and the realization of optical elements such as waveguides and resonators has already been demonstrated [120, 121, 122, 123].

Porous silicon is fabricated by electrochemical etching of crystalline silicon, resulting in a nanoporous skeleton comprised of silicon and air (see an example in Fig. 2.3).

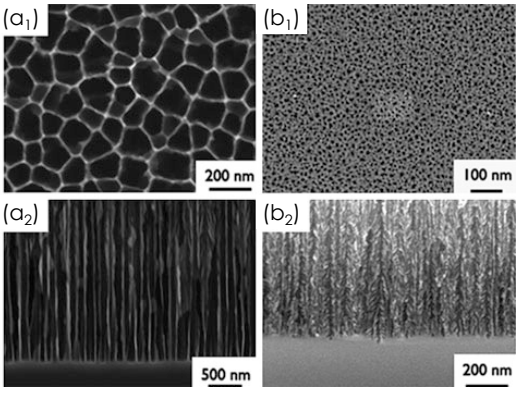

Figure 2.3: Examples of pSi structures, from the top and cross-section perspectives (adapted from [120]): (a) medium-scale pores ($\sim$ 120 nm) and (b) meso-scale pores ($\sim$ 20 nm).

Thanks to its porous nature, this material has been considered primarily for the fabrication of optical sensors for biochemical analysis. The average diameter

of the pores typically ranges from 5 nm to more than 100 nm, depending on the fabrication process the electrochemical current density applied [124], and since the pores are much smaller than the wavelength of light used for sensing, the material is well approximated by a Bruggeman effective index model [125]. The sponge-like architecture of pSi, when properly functionalized, can host analytes deep into the optical waveguide, where the field intensity is highest, yielding sensitivities as low as 10^{-6}/RIU (Refractive Index Units) [126].

The propagation losses in standard pSi waveguides are much higher compared to those of silicon — and silicon nitride — waveguides, as it is expected from the inhomogeneous and rough interfaces of pSi, and they typically range between 10 and 20 dB/cm. Multiple studies have been performed examining the nature of those losses and determined that their most significant origins are scattering due to interface roughness and porosity fluctuations and material absorption [127, 128, 129]. Yet, through oxidization of the pSi waveguide, it is still possible to achieve very low losses, down to 0.5 dB/cm near $\lambda = 1.55$ μm [126], albeit giving away the possibility to infiltrate the material for sensing purposes.

Despite the relatively high losses of the pSi, numerous linear optical devices have been demonstrated, including optical filters [130], microcavities [131, 123], and sensors [132]. Yet, the nonlinear optical response of pSi has been poorly investigated, even though pSi displays some interesting and unique characteristics in this respect. For instance, the large internal surface area of pSi increases the surface recombination rate, which dramatically reduces the free-carrier lifetime [94]. A few studies on the third-order nonlinear response of pSi have been performed in the wavelengths below 1064 nm [95, 133], thus far from the telecom wavelengths, and a more recent characterization of the nonlinear effects at $\lambda = 1.55$ μm was performed by Apiratikul et al. [94], finding that the instantaneous nonlinearities (TPA and SPM) in pSi are comparable to crystalline silicon. And while the increased surface-to-volume ratio of pSi has not proved to yield any enhancement of the surface χ_2 nonlinearity, it is still a conceivable and interesting idea to leverage the porous nature of pSi to infiltrate the material with high-nonlinearity media. This solution would increase the effective third-order response while impacting minimally on the linear properties of the device.

2.2 FWM and SFWM in porous silicon ring resonators

In this section we investigate more deeply the performance of porous silicon as a possible low-cost material for integrated nonlinear optics. Originally, the long-term goal of this research was to demonstrate SFWM in a pSi-based source, but this proved to be an exceedingly hard task, mainly due to the high propagation losses observed experimentally. Nonetheless, this material revealed a remarkably high nonlinear parameter γ that, together with the distinctive properties of pSi such as the large internal surface area and the possibility to infiltrate with other materials, boosts the interest for applications in low-power integrated nonlinear optics. We have investigated theoretically the nonlinear response of a pSi

integrated device, predicting a strong nonlinearity such that it was possible to observe photon pairs generated by stimulated FWM even with a continuous wave (CW) low-power pump. Our analysis was complemented by the sample fabrication and experimental characterization, provided by the nanophotonics group in Pavia in a collaboration with the Vanderbilt University. From the results of the classical experiment we could finally compute the expected production rate of photon pairs by SFWM.

We investigated the response of a pSi microring resonator in a CW low-power stimulated FWM experiment [96]. The choice of the source is motivated by the recent demonstration of pSi microrings with quality factors up to 10^4, which could enable the observation of classical an quantum nonlinear phenomena, such as stimulated and spontaneous FWM [123]. Moreover, as we recalled in the introduction, microrings are some of the most appealing platforms for nonlinear optics, for they guarantee large field enhancement and a relatively small mode volume.

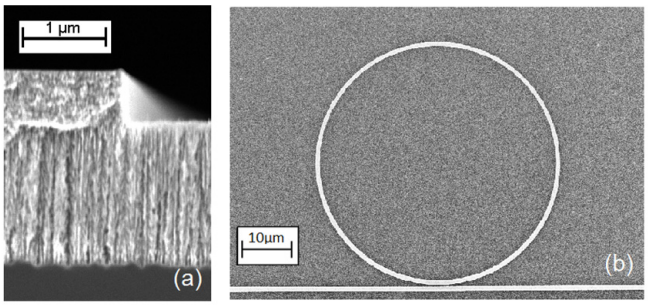

Figure 2.4: SEM image of the pSi waveguide cross section (a) and top view of the pSi microring resonator (b) [96].

Our pSi source was fabricated at Vanderbilt University, in a collaboration with the group led by Prof. Sharon Weiss. It is made of a single-channel microring resonator fabricated in a pSi slab waveguide on top of a crystalline silicon substrate, as shown in Fig. 2.4(a). The slab waveguide consists of a higher index guiding layer ($n = 1.79$) and a lower index cladding ($n = 1.24$), with thicknesses of 0.6 μm and 1.4 μm, respectively, on a silicon substrate, where the refractive index is controlled by engineering the silicon fraction in the porous material. The pSi layers are realized by means of electrochemical etching in a HF-based electrolyte, followed by soaking in KOH for pore widening and annealing in air at 500°C for surface passivation. Finally, the ridge waveguide and microring are fabricated by means of standard Electron Beam Lithography (EBL) and Reactive Ion Etching (RIE) on top of the guiding layer. A Scanning Electron Microscopy (SEM) image of the top view of the sample is shown in Fig. 2.4(b). The bus waveguide is 1.2 μm wide and critically coupled to a 25 μm radius microring with a gap distance of 200 nm. The cross section of the bus and the ring waveguides are identical.

The field profile of the fundamental TE mode supported by the waveguide, as computed by a Finite Difference Eigenmode (FDE) solver and by an effective index method (EIM, see Ref. [134]), is reported in Fig. 2.5(a) and 2.5(b). As it clearly appears from Fig. 2.5, the agreement between the calculations with the two independent models is very good, and it confirms that the EIMs are valid tools for a rapid and reliable estimate of the field characteristics in a ridge waveguide (see also [135]).While propagation losses associated with the material roughness have a typical value of $\alpha = 2.75$ dB/mm, the overall losses were measured in the order of 30 dB around the central wavelength $\lambda_0 = 1.55$ μm. These are mainly due to the poor in-out coupling efficiency. In Fig. 2.6 we show the transmission spectra of the microring around the resonances involved in the FWM experiment.

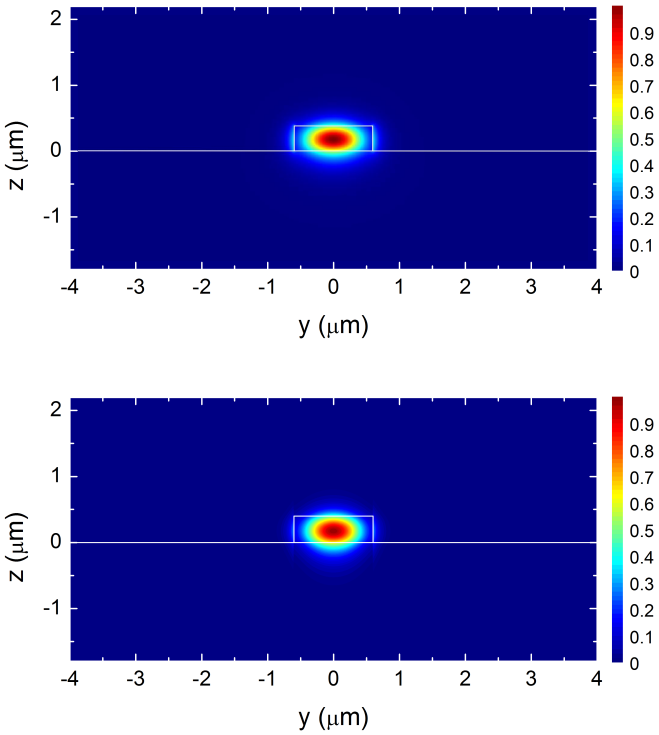

Figure 2.5: Comparison between the field profile of the TE mode supported by the pSi waveguide, as computed numerically using (a) a FDE solver and (b) an EIM [96]. In the first instance, the waveguide is found to be monomodal at $\lambda_0 = 1.55$ μm and the computed TE mode effective refractive index is $n_{FDE} = 1.39495$; in the second calculation, more approximate but faster, the Vertical EIM was adopted (See Ref. [134]), which led to a TE mode effective refractive index $n_{VEIM} = 1.4189$. The index n_{VEIM} is found 1.72% higher than the index n_{FDE}, a slight difference that can be attributed to the intrinsic approximations defining the EIM methods and the mesh discretization in the FDE simulation.

Assuming the theoretical Lorentzian shape of the transmission dip (see Sec. 1.2), the resonances have quality factors Q of several thousands ($Q_I = 5800$ and $\lambda_I = 1571.6$ nm, $Q_P = 5900$ and $\lambda_P = 1578.58$ nm, and $Q_S = 4200$ and $\lambda_S = 1585.57$ nm). It should be noticed that the experimental estimate of the quality factors agrees with with the theoretical prediction, under the assumption of a nearly-critically coupled microring and negligible dispersion. Indeed, the intrinsic quality factor Q_{int} of an isolated ring is given by

$$Q_{int} = \frac{2\pi n_g}{\lambda_0 \alpha}, \tag{2.1}$$

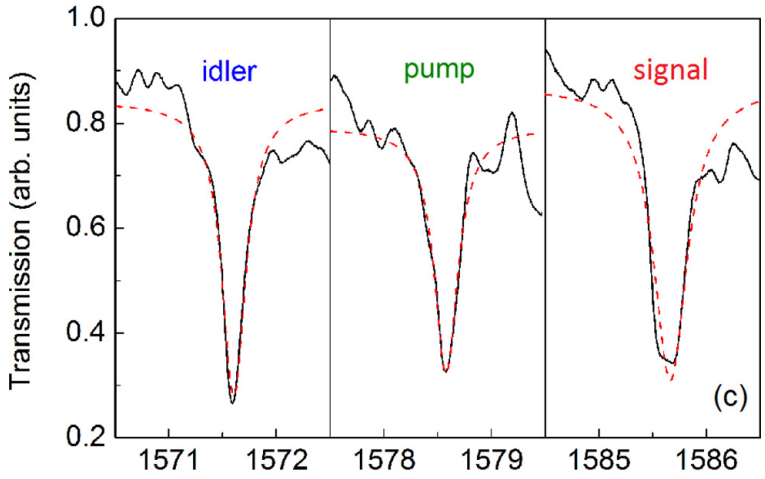

Figure 2.6: Transmission spectrum obtained by exciting the pSi microring with a CW tunable infrared laser. The spectra show the idler, pump, and signal resonances we use for the FWM experiment. The solid lines represent the measured transmission, while the dashed red lines correspond to the best Lorentzian fit for each resonance, which reveal quality factors $Q \approx 5000$ [96].

where λ_0 is the wavelength in vacuum and n_g is the mode group index. When we take $\alpha = 6.33\,\mathrm{cm}^{-1}$ (i.e., 2.75 dB/mm) and $n = 1.51$ (simulated numerically with the effective index method), the quality factor is expected to be $Q = Q_{int}/2 \approx 4800$. The higher values that were found from the linear characterization indicate a slight undercoupling.

The FWM spectrum obtained with a pump power of 650 μW and a signal power of 60 μW is reported in Fig. 2.7. Note that all these powers are estimated already inside the bus waveguide. The main peak in the spectrum shown in Fig. 2.7 corresponds to the idler field generated by FWM, which is located at the idler resonance as expected from energy conservation. The weaker peaks on the right are the residual pump and signal inputs, which have been highly suppressed by the filtering stage. The peak power is about 0.6 pW, which is quite remarkable given the high fraction (around 60%) of air in the ridge. In particular, despite the fact that pSi is characterized by an intrinsic roughness, the quality factor of our ring is sufficiently high to observe FWM at low power.

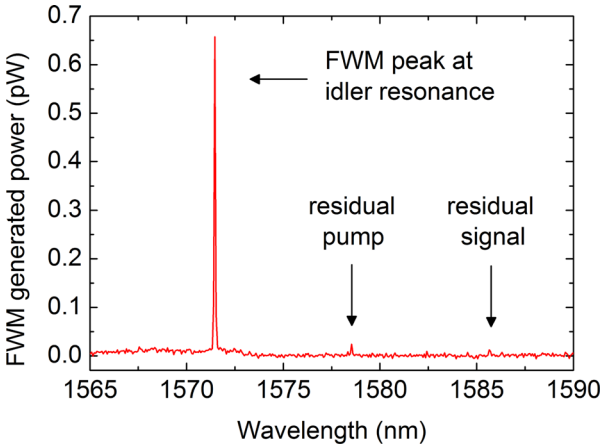

Figure 2.7: Transmission spectrum obtained in a FWM experiment where the pump power is 650 μW and the signal power is 60 μW, highlighting the presence of a FWM peak at the idler resonance. The peaks corresponding to the pump and the signal resonances are highly suppressed by off-chip filtering [96].

From the theory of stimulated FWM and in the limit of an undepleted pump, the expected idler power generated in the bus waveguide is [103]

$$P_I = (\gamma 2\pi R)^2 \Big(\frac{Q v_g}{\omega_P \pi R}\Big)^4 P_S P_P^2, \tag{2.2}$$

where R is the radius of the ring, Q is the quality factor of the resonances, v_g is the group velocity, ω_P is the pump frequency, and γ is the nonlinear waveguide parameter, defined as $\gamma = \frac{\omega_P n_2}{c A_{eff}}$. Here, n_2 is the nonlinear refractive index, A_{eff} is the effective area of the waveguide, and c is the speed of light. From Eq. (2.2) we see that P_I scales quadratically with P_P and linearly with P_S; this trend was experimentally verified (see Fig. 2.8), for this is a direct proof that the peak observed in the output spectrum in Fig. 2.7 is due to FWM taking place in the ring resonator.

Now, from the experimental data on the transmitted power as a function of the input pump power, it is possible to estimate the nonlinear parameter of the waveguide γ. Inverting Eq. (2.2), we have

$$\gamma = \Big(\frac{2\pi R c}{\lambda_P v_g}\Big)^2 \frac{\pi}{2RQ_P P_P \sqrt{Q_I Q_S}} \sqrt{\frac{P_I}{P_S}}, \tag{2.3}$$

where the group velocity v_g is given by $v_g = FSR \cdot 2\pi R$, assuming that group velocity dispersion is negligible in the wavelength range considered here. The experimental estimate of our waveguide nonlinear parameter is $\gamma = (20 \pm 2)\ \mathrm{m^{-1}W^{-1}}$. This value is intermediate between that of semiconductors (e.g. for silicon nanowires $\gamma_{Si} \sim 200\ \mathrm{m^{-1}W^{-1}}$) and that oxides (e.g. for Hydex nanowires $\gamma_{Hy} \sim 0.2\ \mathrm{m^{-1}W^{-1}}$)[136, 137].

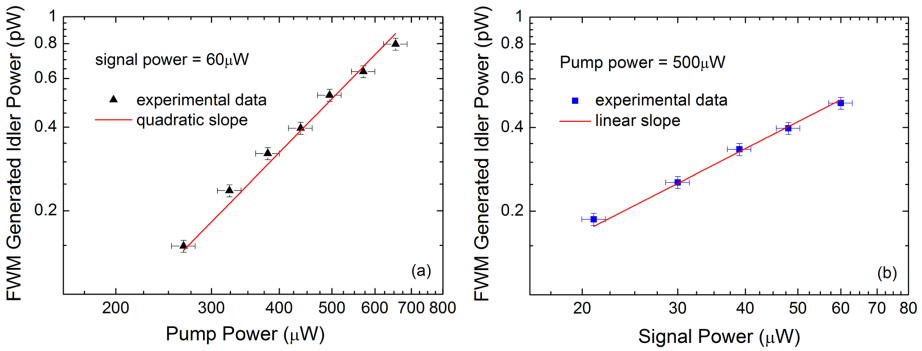

Figure 2.8: Power generated by FWM at the idler frequency as a function of the input pump and signal powers. In (a) we verify the quadratic dependance of the output with respect to the pump intensity. The signal power is fixed at 60 μW, while the pump power is increased. The experimental data (black triangles) is well interpolated by a quadratic trend. Similarly, in (b) the pump is fixed at 500 μW, while the signal power is increased. In this case, the experimental data (blue squares) are well fit by a linear trend, as expected. These behavior indicate, within the experimental error, that FWM is taking place in the pSi microring [96].

We can go a bit further with the characterization of pSi and estimate an upper bound for the n_2 coefficient of pSi in the assumption that the nonlinearity is restricted to the ridge region and in the hypothesis of weak confinement. This calculation, although affected by more assumptions and uncertainties, is very interesting since the n_2 index is solely related to the bulk material properties of pSi, independently on the guiding geometry (as it is for of the waveguide nonlinear parameter γ). The effective area is given by

$$A_{eff}^{-1} = \frac{\int d\mathbf{r}_\perp \; \Gamma_3^{ijkl}(\mathbf{r}_\perp) D^i_{\omega_1}(\mathbf{r}_\perp) D^j_{\omega_2}(\mathbf{r}_\perp) D^k_{\omega_3}(\mathbf{r}_\perp) D^l_{\omega_4}(\mathbf{r}_\perp)}{\sqrt{\int d\mathbf{r}_\perp \; D_{\omega_1}(\mathbf{r}_\perp) \int d\mathbf{r}_\perp \; D_{\omega_2}(\mathbf{r}_\perp) \int d\mathbf{r}_\perp \; D_{\omega_3}(\mathbf{r}_\perp) \int d\mathbf{r}_\perp \; D_{\omega_4}(\mathbf{r}_\perp)}}, \quad (2.4)$$

where $\Gamma_3^{ijkl}(\mathbf{r}_\perp)$ is the nonlinear susceptibility tensor, and $D_\omega(\mathbf{r}_\perp)$ is the normalized displacement vector at the frequency ω. We have calculated numerically the effective area by using a commercial FDE solver, obtaining $A_{eff} = 0.86$ μm^2. From the standard definition of γ and using our previous estimate, we obtain the nonlinear refractive index of porous silicon $n_2 = 4.26 \cdot 10^{-18}$ m^2/W. This result is in good agreement with previous works [94] and is comparable with that of crystalline silicon.

Finally we want to stress that, as discussed in details in [103], the idler power generated in a spontaneous nonlinear phenomenon is directly related to that generated by the stimulated counterpart. Based on this result and restricting

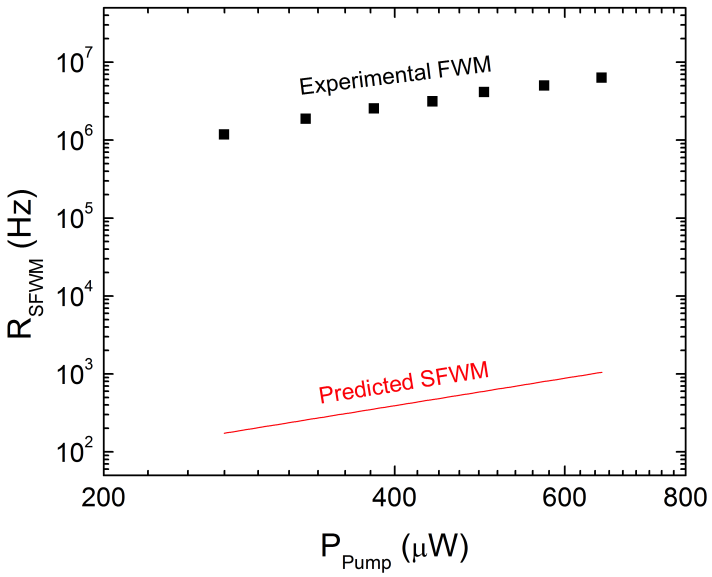

Figure 2.9: Comparison between the experimental generation rate for the stimulated FWM process and the predicted SFWM generation rate, based on Eq. (2.6).

our focus on the case of a third-order resonant process, we have

$$\frac{P_{I,Sp}}{P_{I,St}} = \frac{1}{4Q}\frac{\hbar\omega_P^2}{P_S}, \tag{2.5}$$

and thus we can estimate the generation rate of photon pairs by SFWM in our microring resonator, obtaining

$$R_{SFWM} = \frac{P_I}{P_S}\frac{\pi c \lambda_I}{2Q_S\lambda_P^2}. \tag{2.6}$$

In Fig. 2.9 we report the comparison between the stimulated FWM experimental data, and our predicted SFWM generation rate, based on Eq. (2.6).

From Fig. 2.9 we can conclude that increasing the pump power it will be possible to observe photons produced by SFWM with kHz generation rates. This is indeed an attractive proposal, since it has never been reported in literature of a source of entangled photon pairs fabricated in porous silicon. Moreover, this would pave the way for exploiting the unique features of pSi: for example, it would be possible to study the response of this device when the pSi waveguide is infiltrated with a variety of highly nonlinear materials. These would improve the generation rate with a slight impact on the lateral confinement of light, thus boosting the waveguide nonlinear parameter. Once more, we stress that such results are in reach thanks to the relatively high quality factor of the pSi ring resonator, which enhances the electromagnetic field to the limit where spontaneous nonlinear effects became appreciable.

In conclusion, in this Chapter we have discussed the performance of pSi as a low-cost material for nonlinear integrated optics, and possibly for parametric fluorescence. The results we have presented were possible only thanks to the use of integrated resonators for the amplification of the light-matter interaction. In the following chapters we will develop with this strategy further, focusing on a well-established platform for integrated optics: Silicon-On-Insultaor (SOI) Photonic Integrated Circuits (PICs). Specifically, we will discuss the generation of spectrally correlated to truly uncorrelated photon pairs by SFWM in integrated microring resonators, two opposite regimes which can be accessed by carefully engineering the source dynamical response and its geometrical design. As we recalled in the opening of this introductory part of the present work, the ability to produce these nonclassical states of light is paramount for the development of photonic quantum technologies.

Spectral correlations of photon pairs generated by ring resonators

As we discussed in the previous Chapters 1 and 2, spontaneous nonlinear phenomena such as SFWM are very weak processes, due to the small nonlinear susceptibility displayed by most materials. For this reason, the realization of efficient sources of nonclassical states of light apparently cannot rely on parametric fluorescence. Yet, this impression has proven wrong, particularly in the development of integrated sources. We can identify the intuitive reason by looking at Eq. (1.75): the average number of generated photons β is determined both by the magnitude of the nonlinear susceptibility $\Gamma_3^{ijkl}(\mathbf{r})$, and by how intensely the field is confined in the nonlinear region, as represented by the overlap integral. As a matter of fact, the generation of entangled photon pairs by parametric processes can be obtained *efficiently* once a strong enhancement of the light-matter interaction is guaranteed by a properly designed optical device.

Across the literature there are multiple instances of confinement strategies, as we recalled in Sec. 1.2 : Simple waveguides — usually referred to as nanowires — where the light is confined in the plane perpendicular to the propagation direction by TIR; PhC waveguides, which are waveguides relying on both TIR and the PBG mechanism, engineered to take advantage of the so-called *Slow Light* effect which increases the interaction time; Optical cavities and optical resonators, where light is confined in three dimensions by a combination of TIR and PBG, depending on the device design. This is not by far an exhaustive list of the strategies adopted for confining light and increasing the nonlinear response of a device (spirals, mixed PhC waveguides and resonators, ...), but certainly it groups some of the most common solutions.

In the following we will limit our attention to optical resonators, and specifically to the generation of photon pairs by SFWM in integrated microrings. The goal of the next Chapters is analyzing the spectral correlations of the produced photon pairs, examining the possible outcomes, and discussing a few strategies to engineer such sources to produce the desired quantum correlations. Specifically, in Sec. 3 we will study the simplest case of a side-coupled microring resonator,

while in Sec. 4 we will present a novel approach for the generation of completely unentangled photon pairs using microring resonators.

Chapter 3

Energy-entangled photon pairs generated in a side-coupled microring resonator

Let us consider the simple case of a side-coupled microring resonator, as sketched in Fig. 3.1. We imagine to couple the pump from the In channel, and collect the photon pairs generated by SFWM in the Out channel. Given the constraints on energy and momentum conservation implied in SFWM, when we pump in correspondence of one of the ring resonances we expect to observe photon pairs generated in equally spaced nearby resonances. For the sake of simplicity, we assume to collect photons only from the resonances closer to the one we choose for pumping. We label the red-shifted and blue-shifted photons as *signal* and *idler*, respectively.

Taking advantage of the asymptotic field formalism we recalled in Sec. 1.3 it is possible to predict the spectral properties of the photons generated by SFWM, as well as the source generation rate. All these informations are embedded in the BWF. Recalling Eq. (1.75), for a generic two ports system we have

$$\begin{aligned}\phi_{Out,Out}(k_1,k_2) = \frac{3\sqrt{2}i\pi\alpha^2\hbar}{4\beta\epsilon_0}\int dk_3\ \phi_P(k_3)\phi_P(k_1+k_2-k_3) \\ \times\sqrt{\omega_{Out,k_1}\omega_{Out,k_2}\omega_{In,k_3}\omega_{In,(k_1+k_2-k_3)}} \\ \times\int d\mathbf{r}\ \Gamma_3^{ijkl}(\mathbf{r})D^{i,asy-in}_{Out,k_1}(\mathbf{r})D^{j,asy-in}_{Out,k_2}(\mathbf{r}) \\ \times D^{k,asy-in}_{In,k_3}(\mathbf{r})D^{l,asy-in}_{In,k_1+k_2-k_3}(\mathbf{r}),\end{aligned} \tag{3.1}$$

where we suppressed the mode index I since we suppose, for simplicity, to deal with a mono-modal waveguide. Under the further assumption of having a single-valued dispersion relation, we can recast the BWF in the frequency domain as

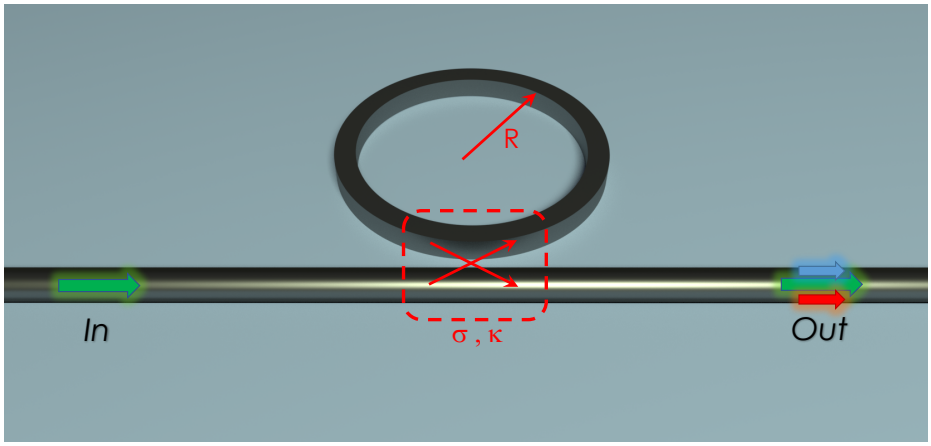

Figure 3.1: Schematic representation of a side-coupled ring resonator for the generation of entangled photon pairs by SFWM. The pump is injected in the In channel, coupled to the ring resonator where the spontaneous fluorescence takes place. The residual pump together with the newly generated signal and idler photons finally exit the source from the Out channel.

$$\begin{aligned}\phi_{Out,Out}(\omega_1,\omega_2) = \frac{3\sqrt{2}i\pi\alpha^2\hbar}{4\beta\epsilon_0}\int d\omega_3\ \phi_P(\omega_3)\phi_P(\omega_1+\omega_2-\omega_3) \\ \times\sqrt{\frac{\omega_1\omega_2\omega_3(\omega_1+\omega_2-\omega_3)}{v_g(\omega_1)v_g(\omega_2)v_g(\omega_3)v_g(\omega_1+\omega_2-\omega_3)}} \\ \times\int d\mathbf{r}\ \Gamma_3^{ijkl}(\mathbf{r})D^{i,asy-in}_{Out,k(\omega_1)}(\mathbf{r})D^{j,asy-in}_{Out,k(\omega_2)}(\mathbf{r}) \\ \times D^{k,asy-in}_{In,k(\omega_3)}(\mathbf{r})D^{l,asy-in}_{In,k(\omega_1+\omega_2-\omega_3)}(\mathbf{r}),\end{aligned} \tag{3.2}$$

where we labelled $\omega_{1,2} \equiv \omega_{Out,k(\omega_{1,2})}$ and $\omega_{3,4} \equiv \omega_{In,k(\omega_{3,4})}$, and $v_g(\omega)$ is the group velocity. The field overlap integral in Eq. (3.2) is depending on the nonlinear parameter $\Gamma_3^{ijkl}(\mathbf{r})$, but we can recast it in a more familiar form, using the third order nonlinear susceptibility $\chi_3^{ijkl}(\mathbf{r})$. Assuming a simple linear response, so that $D^i(\mathbf{r},t) = \epsilon_0\epsilon E^i(\mathbf{r},t) = \epsilon_0 n^2(\mathbf{r};\omega)E^i(\mathbf{r},t)$, we can apply the substitution

$$\Gamma_3^{ijkl}(\mathbf{r}) \to \frac{\chi_3^{ijkl}(\mathbf{r})}{\epsilon_0^2 n^2(\mathbf{r}_\perp;\omega_1)n^2(\mathbf{r}_\perp;\omega_2)n^2(\mathbf{r}_\perp;\omega_3)n^2(\mathbf{r}_\perp;\omega_1+\omega_2-\omega_3)}, \tag{3.3}$$

where we have also included the material dispersion. Hence, Eq. (3.2) becomes

$$\phi_{Out,Out}(\omega_1,\omega_2) = \frac{3\sqrt{2}i\pi\alpha^2\hbar}{4\beta\epsilon_0}\int d\omega_3\ \phi_P(\omega_3)\phi_P(\omega_1+\omega_2-\omega_3) \tag{3.4}$$
$$\times\sqrt{\frac{\omega_1\omega_2\omega_3(\omega_1+\omega_2-\omega_3)}{v_g(\omega_1)v_g(\omega_2)v_g(\omega_3)v_g(\omega_1+\omega_2-\omega_3)}}$$
$$\times\int d\mathbf{r}\ \frac{\chi_3^{ijkl}(\mathbf{r})}{\epsilon_0^2 n^2(\mathbf{r}_\perp;\omega_1)n^2(\mathbf{r}_\perp;\omega_2)n^2(\mathbf{r}_\perp;\omega_3)n^2(\mathbf{r}_\perp;\omega_1+\omega_2-\omega_3)}$$
$$\times D^{i,asy-in}_{Out,k(\omega_1)}(\mathbf{r})D^{j,asy-in}_{Out,k(\omega_2)}(\mathbf{r})D^{k,asy-in}_{In,k(\omega_3)}(\mathbf{r})D^{l,asy-in}_{In,k(\omega_1+\omega_2-\omega_3)}(\mathbf{r}).$$

Now we can work out the explicit form of the asymptotic states, and plug them into Eq. (3.4) to obtain the final expression of the BWF. The field inside our mono-modal waveguide is given by

$$\mathbf{D}_{nk(\omega)}(\mathbf{r}) = \frac{\mathbf{d}_{nk(\omega)}(\mathbf{r})}{\sqrt{2\pi}}e^{ik(\omega)z}, \tag{3.5}$$

where, again, n labels the channel. Then the asymptotic-in field from the In channel is

$$D^{i,asy-in}_{In,k(\omega)}(\mathbf{r}) = \begin{cases} \frac{d^i_{k(\omega)}(\mathbf{r}_\perp)}{\sqrt{2\pi}}e^{ik(\omega)z} & z<0 \\ T(k(\omega))\frac{d^i_{k(\omega)}(\mathbf{r}_\perp)}{\sqrt{2\pi}}e^{ik(\omega)z} & z>0 \\ D^{i,ring}_{In,k(\omega)}(\mathbf{r}) & \text{in the ring} \end{cases}, \tag{3.6}$$

where $T(k(\omega))$ is the transmission coefficient of the ring (see Eq. (1.29)), and

$$D^{i,ring}_{In,k(\omega)}(\mathbf{r}) = \frac{i\kappa(\omega)}{1-\sigma(\omega)e^{ik(\omega)l}}\frac{d^i_{k(\omega)}(\mathbf{r}_\perp,\zeta/R)}{\sqrt{2\pi}}e^{ik(\omega)\zeta}, \tag{3.7}$$

where ζ is the coordinate in the counterclockwise direction in the ring, $\sigma(\omega)$ and $\kappa(\omega)$ are the self- and cross-coupling coefficients, and $l = 2\pi R$ where R is the ring radius. A similar expression for the asymptotic-in field from the Out channel can be easily obtained.

The only term that is relevant in the calculation of the nonlinear response of the structure is that involving the ring itself, where the field is enhanced at the resonances. For this reason, the leading contribution to the overlap integral comes from the field in the ring, and we can neglect the generation of photon pairs in the waveguide. Hence, Eq. 3.4 becomes

$$\phi_{Out,Out}(\omega_1,\omega_2) = \frac{3\sqrt{2}i\alpha^2\hbar}{16\pi\beta\epsilon_0}\int d\omega_3\ \phi_P(\omega_3)\phi_P(\omega_1+\omega_2-\omega_3) \tag{3.8}$$
$$\times\sqrt{\frac{\omega_1\omega_2\omega_3(\omega_1+\omega_2-\omega_3)}{v_g(\omega_1)v_g(\omega_2)v_g(\omega_3)v_g(\omega_1+\omega_2-\omega_3)}}$$
$$\times\frac{i\kappa(\omega_1)}{1-\sigma(\omega_1)e^{-ik(\omega_1)l}}\frac{i\kappa(\omega_2)}{1-\sigma(\omega_2)e^{-ik(\omega_2)l}}\frac{i\kappa(\omega_3)}{1-\sigma(\omega_3)e^{ik(\omega_3)l}}$$
$$\times\frac{i\kappa(\omega_1+\omega_2-\omega_3)}{1-\sigma(\omega_1+\omega_2-\omega_3)e^{ik(\omega_1+\omega_2-\omega_3)l}}$$
$$\times\int d\mathbf{r}\ \frac{\chi_3^{ijkl}(\mathbf{r})}{\epsilon_0^2 n^2(\mathbf{r}_\perp;\omega_1)n^2(\mathbf{r}_\perp;\omega_2)n^2(\mathbf{r}_\perp;\omega_3)n^2(\mathbf{r}_\perp;\omega_1+\omega_2-\omega_3)}$$
$$\times[d^i_{k(\omega_1)}(\mathbf{r}_\perp,\zeta/R)d^j_{k(\omega_2)}(\mathbf{r}_\perp,\zeta/R)d^k_{k(\omega_3)}(\mathbf{r}_\perp,\zeta/R)$$
$$\times d^l_{k(\omega_1+\omega_2-\omega_3)}(\mathbf{r}_\perp,\zeta/R)e^{i(k(\omega_3)+k(\omega_1+\omega_2-\omega_3)-k(\omega_1)-k(\omega_2))\zeta}].$$

Under some very minor assumption, we can now provide a simple interpretation of Eq. (3.8). If we suppose that the field profile in the ring is independent on the radial component, apart from the phase delay, we have $d^\alpha_k(\mathbf{r}_\perp,\zeta/R)\equiv d^\alpha_k(\mathbf{r}_\perp)$ with $\alpha = x,y,z$. Moreover, grouping out of the integral an average nonlinear susceptibility $\bar{\chi}_3$, the BWF becomes

$$\phi_{Out,Out}(\omega_1,\omega_2) = \frac{3\sqrt{2}i\alpha^2\hbar\bar{\chi}_3}{16\pi\beta\epsilon_0}\sqrt{\frac{\omega_1\omega_2}{v_g(\omega_1)v_g(\omega_2)}}\mathcal{F}^*(\omega_1)\mathcal{F}^*(\omega_2) \tag{3.9}$$
$$\times\int d\omega_3\ \phi_P(\omega_3)\phi_P(\omega_1+\omega_2-\omega_3)$$
$$\times\sqrt{\frac{\omega_3(\omega_1+\omega_2-\omega_3)}{v_g(\omega_3)v_g(\omega_1+\omega_2-\omega_3)}}\mathcal{F}(\omega_3)\mathcal{F}(\omega_1+\omega_2-\omega_3)$$
$$\times\frac{e^{i\phi(\omega_1,\omega_2,\omega_3,\omega_1+\omega_2-\omega_3)}}{\sqrt{A(\omega_1,\omega_2,\omega_3,\omega_1+\omega_2-\omega_3)}}e^{i\pi R\Delta k}\mathrm{sinc}(\pi R\Delta k),$$

where

$$\mathcal{F}(\omega) = \frac{i\kappa(\omega)}{1-\sigma(\omega)e^{ik(\omega)l}} \tag{3.10}$$

is the FE in the ring resonator (see Eq. (1.33)), the quantity

$$\frac{e^{i\phi(\omega_1,\omega_2,\omega_3,\omega_1+\omega_2-\omega_3)}}{\sqrt{A(\omega_1,\omega_2,\omega_3,\omega_1+\omega_2-\omega_3)}} = \tag{3.11}$$
$$\int d\mathbf{r}_\perp\ \frac{\chi_3^{ijkl}(\mathbf{r})}{\bar{\chi}_3}\frac{1}{\epsilon_0^2 n^2(\mathbf{r}_\perp;\omega_1)n^2(\mathbf{r}_\perp;\omega_2)n^2(\mathbf{r}_\perp;\omega_3)n^2(\mathbf{r}_\perp;\omega_1+\omega_2-\omega_3)}\times$$
$$d^i_{-k(\omega_1)}(\mathbf{r}_\perp,\zeta/R)d^j_{-k(\omega_2)}(\mathbf{r}_\perp,\zeta/R)d^k_{k(\omega_3)}(\mathbf{r}_\perp,\zeta/R)d^l_{k(\omega_1+\omega_2-\omega_3)}(\mathbf{r}_\perp,\zeta/R)$$

is proportional to the inverse of the square root of an area, which can be interpreted as an effective transverse coupling area between the modes involved, and $\Delta k \equiv k(\omega_3)+k(\omega_1+\omega_2-\omega_3)-k(\omega_1)-k(\omega_2)$. The average number of generated photons β is obtained imposing the normalization condition

$$\int d\omega_1 d\omega_2 \ |\phi_{Out,Out}(\omega_1,\omega_2)|^2 = 1. \tag{3.12}$$

This is related to the nonlinear susceptibility, but also — and critically — to the FE in the ring resonator as well as the lateral confinement $A(\omega_1,\omega_2,\omega_3,\omega_1+\omega_2-\omega_3)$, as it is now clear from Eq. (3.9). It is paramount to highlight that the spectral profile of the pump $\phi_P(\omega)$ is another key parameter that contributes to determine the shape of the BWF. The field confinement and the nonlinear susceptibility are essentially bound to geometrical and material characteristics, which can be chosen and engineered solely in the design stage; the pump profile, on the contrary, is a dynamical parameter which it can be adjusted during operation, by tuning the pump pulse duration. As a consequence, the quantum correlations exhibited by photon pairs produced by SFWM in an integrated ring resonator can be tailored "on-the-fly" by adjusting the pump temporal profile. In the following, we will discuss two opposite pumping regimes, namely the *short* and the *long pump pulse regime*, analyzing how each scenario impacts the quantum correlations of the photon pairs.

Although the generation of entangled photon pairs by SFWM in integrated microrings can be quite efficient, reaching 10^7 pairs/s with a coupled pump power of 1 mW [44], the frequency range over which photons can be generated spans the complete idler and signal resonances. Therefore, to capture every fine detail of the Joint Spectral Density (JSD) — the square modulus of the BWF, and the easiest accessible experimentally — very long integration times would be required. Unfortunately, a compromise on the JSD resolution impacts severely on the quality of the reconstruction of the JSD, leading to large uncertainties in the measurement of the quantum correlations. Yet, it was recently proposed by Liscidini et al. [46] that the characterization of a source based on SFWM can be achieved much more efficiently by exploiting the corresponding stimulated nonlinear process, which is FWM. This technique is referred to as *Stimulated Emission Tomography* (SET). Since the stimulated process is intrinsically much more intense and yields very high signal-to-noise ratios, taking advantage of the SET it is possible to reconstruct every detail of the JSD.

We consider a silicon microring resonator with radius $R = 15$ μm, side coupled to a 500 nm wide $\times$ 220 nm high silicon bus waveguide; the entire structure is embedded in silica. In Fig. 3.2(a) we report the measured transmission spectrum of the structure along with that of a reference waveguide. It should be noticed that the bell shape of the transmission is due to the spectral response of the grating coupler [138].

In Fig. 3.2(b–d) we plot the transmission spectra of the signal, pump and idler resonances, respectively, used in the SFWM and FWM experiments. From Fig. 3.2(b-d) we can conclude that the ring resonator is essentially critically coupled, and that the three Lorentzian resonances have similar full width at half

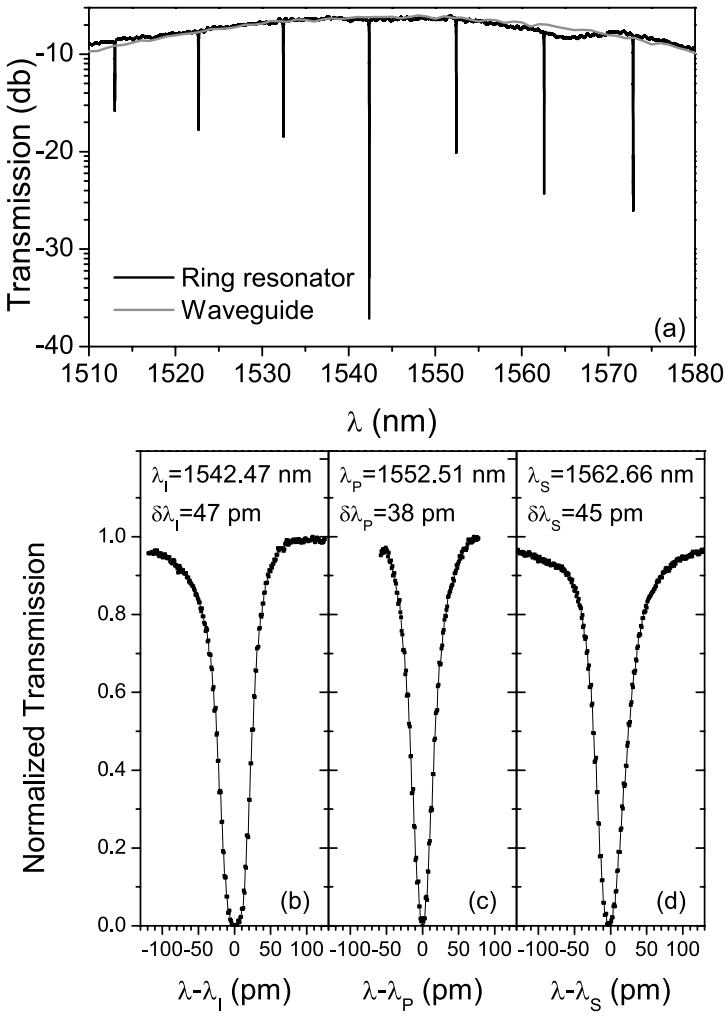

Figure 3.2: Measured transmission spectra from our sample microring resonator. (a) A lower resolution transmission spectrum covering multiple resonances and including the spectral response of the grating coupler; (b-d) High resolution characterization of the pump, signal, and idler resonances we consider for the SFWM and the FWM experiments.

maxima ($\delta\lambda_i$) corresponding to a Q factor of about 40000. We are particularly interested in the pump resonance quality factor, $Q_P = 40800 \pm 2000$, which corresponds to a coherence time $\tau_p = 1/\Delta\omega$ 33 ± 2 ps. This value represents the minimum pump pulse duration we are keen to consider in our discussion. Indeed, the pump laser coupled to the In channel is spectrally filtered by the ring resonator. Even if we imagine to reduce the pump pulse duration, the larger pump spectrum coupled to the bus waveguide will be filtered by the ring, and the resulting pump spectrum will correspond to the pump resonance itself: every effort to shorten the pump duration would be fruitless.

When the microring is pumped with a laser centered on the pump resonance we can observe, as expected, the emission of signal and idler photons due to SFWM, as reported in Fig. 3.3; note that here the pump photons have been filtered.

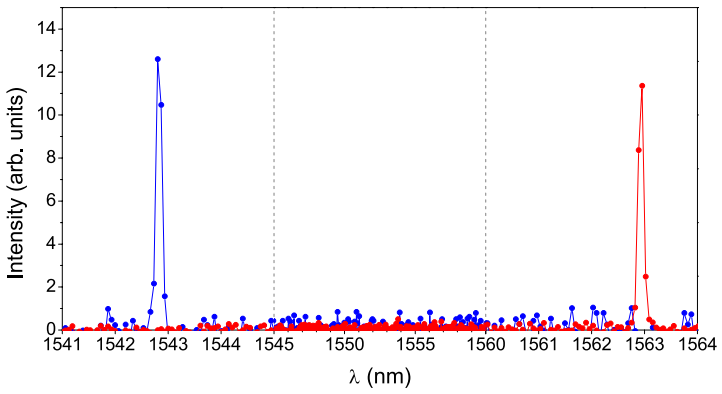

Figure 3.3: Example SFWM spectrum obtained with a pulsed pump, proving the generation of signal and idler photons. The pump photons have been filtered outside the chip.

The reconstruction of the JSD is performed using the above-mentioned SET technique. To this end, a CW tunable signal laser is coupled into the structure together with the pulsed pump laser, and the idler photons exiting the structure pass through a filter narrow enough to resolve the idler resonance. For each signal frequency, the idler resonance is completely scanned. With this double sweep it is possible to reconstruct the full JSD within the experimental resolution, which in this case is 2 pm.

Now we can finally investigate the response of our source as a function of the pump pulse duration, from a minimum threshold of ≈ 33 ps when the pulse is filtered by the pump resonance, up to the CW limit. In order to quantify the energy-entanglement of the generated pairs, we rely on the Schmidt number K. This quantity represents the "effective" number of superpositions of factorizable states needed to reconstruct the original quantum state [139, 140]. To grasp the reason why an "effective" number of states should be considered, and the consequent explicit expression of the Schmidt number, one needs to consider a

pure state $|\psi\rangle$ and its Schmidt decomposition as in J. H. Eberly [139]

$$\begin{aligned} |\psi\rangle &= \sum_n \sum_\nu C(n,\nu)\,|n\rangle \otimes |\nu\rangle \\ &= \sum_s \sqrt{\lambda_s}\,|F^s\rangle \otimes |\Phi^s\rangle\,, \end{aligned} \tag{3.13}$$

where $C(n,\nu)$ is the so-called entanglement amplitude, $|n\rangle$ and $|\nu\rangle$ are arbitrary basis states and, essentially through the singular value decomposition theorem, one obtains the same state expressed as a superposition of Schmidt modes $|F^s\rangle$ and $|\Phi^s\rangle$, orthogonal bases in the respective Hilbert spaces $\mathcal{H}_1$ and $\mathcal{H}_2$ of the two photons. Notably, in the final expression we have a single summation. The coefficients λ_s are the eigenvalues of the reduced density matrices $\rho_1 \equiv \sum_\mu \langle\mu|(|\psi\rangle\langle\psi|)|\mu\rangle$ and $\rho_2 \equiv \sum_\gamma \langle\gamma|(|\psi\rangle\langle\psi|)|\gamma\rangle$, with certain orthonormal bases $\{|\mu\rangle\}$ and $\{|\gamma\rangle\}$.

Naturally, since the Schmidt modes constitute orthogonal bases, a state whose reconstruction requires more than one Schmidt mode cannot necessary be factored, and thus it is entangled. On the contrary, if the reconstruction of a state is achieved through only one Schmidt mode, the state is factorable and therefore not entangled. From this simple discussion, it appears that the simple count of the number of Schmidt modes required to reconstruct an original quantum states is a good indicator of its degree of entanglement, and some authors actually accept this as the definition of Schmidt number. However, the simple count of the Schmidt modes completely neglects the relative weight of each term into the sum (3.13). For instance, if a single Schmidt mode accounts for the vast majority of the state decomposition leaving just vanishing corrections to other few modes, one would expect to identify a nearly-factorable state, with a Schmidt number close to unity, but this is not the case. Hence, a preferable definition of the Schmidt number invokes a weighted average of the number of Schmidt modes, the weights being represented by the eigenvalues λ_s. As in J. H. Eberly [139], the Schmidt number is defined as

$$K \equiv \frac{1}{\sum \lambda_n^2}, \tag{3.14}$$

which is also the inverse of the state purity of either one of the reduces states, since $\frac{1}{\sum \lambda_n^2} = \frac{1}{Tr[(\rho_1)^2]} = \frac{1}{Tr[(\rho_2)^2]}$. Following Eq. (3.14), a pure separable state has $K = 1$, while any entangled state is characterized by a real-valued Schmidt number $K > 1$. It should be noticed that the Schmidt number is not the only quantity for the measuring entanglement: other indicators, such as the Von Neumann entropy or the Concurrence could be adopted equivalently [141].

Let us now consider and discuss two limiting pumping regimes, namely the *short* and the *long pump pulse* regime.

3.1 Short pump pulse regime

When the microring resonator is pumped with a short pulse laser, we can express the pump spectrum in the Gaussian approximation as

$$\phi_P(\omega) = \frac{1}{\sqrt{2\pi}\sigma_P} e^{-\frac{1}{2}\frac{(\omega-\omega_P)^2}{\sigma_P^2}}, \tag{3.15}$$

where

$$\sigma_P = \frac{1}{2\tau_P\sqrt{2\ln(2)}}, \tag{3.16}$$

τ_P is the pump pulse duration and ω_p is the pump resonance central frequency. Using the pump spectrum (3.15) in the theoretical result (3.9) and assuming that the variation of the transversal mode profile with frequency is negligible, we can numerically compute the expected JSD. In our calculation we model the coupling coefficient $\sigma(\omega)$ so that the resulting resonator quality factors match those experimentally observed; this allows us to effectively include in our quantum model the losses experienced by the light in the resonator. In Fig. 3.4(a) we report the theoretical JSD considering a pump pulse duration $\tau_P = 33$ ps, and waveguide effective index $n_{eff} = 2.54$, group velocity $v_g = 116$ μm/ps, and Group Velocity Dispersion GVD = 1.84 μm^2/ps. These are obtained by means of a numerical calculation of the BWF and the normalized JSD starting from Eq. (3.9). No a priori assumption on the resonances' spectral profile has been implied and, in the estimation of the Schmidt number, the computation is progressively refined in the frequency discretization till convergence of the output. Clearly, since the BWF is symmetric under the exchange of the idler/signal wavelengths, Fig. 3.4 only shows half of the complete BWF, the remaining part being symmetrically positioned with respect to the $\lambda_1 = \lambda_2$ line.

This result can be compared to the experimental outcome, reported in Fig. 3.4(b). From the JSDs we can then estimate the correspondent Schmidt Numbers K, under the assumption to deal with pure states. We obtain $K_{theory} = 1.09$ for the theoretical calculation, and $K_{bound} = 1.03 \pm 0.1$ for the experimental result. The theoretical Schmidt Number is in good agreement with the experimental one, yet a few significant remarks should be pointed out:

1. The experimental Schmidt Number represents an upper bound on the "true" Schmidt Number: indeed, our setup is capable of reconstructing only the real part of the BWF. A more complex experimental setup is required for a phase-sensitive reconstruction of the BWF [142].

2. Our theoretical model does not take into account other nonlinear phenomena, such as TPA, which broaden the pump resonance;

3. The experimental JSD resolution affects the calculation of K_{bound}, resulting in a Schmidt Number smaller than the theoretical one. This effect is clearly related to the finite experimental resolution, for K_{theory} is the minimum value realizable with a side-coupled ring resonator (we will discuss other approaches for lowering this value in Chapter (4)).

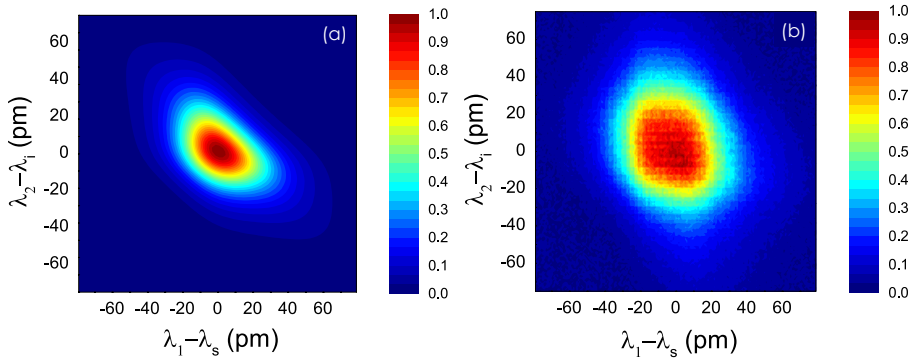

Figure 3.4: Theoretical calculation (a) and experimental measurement (b) of the JSD of the nearly uncorrelated photon pairs produced by SFWM in the short pump pulsing regime ($\tau_P = 33$ ps). The slight asymmetry in (a) is introduced by taking explicitly into account the waveguide group velocity dispersion.

In conclusion, the photons generated by SFWM in our microring resonator in the short pump pulse scheme are *nearly uncorrelated*, as it is expected in this system when the pump pulse duration is equal or shorter than the dwelling time of the photons in the ring [44]. Actually, it is not possible to further reduce the Schmidt Number by shortening the temporal duration of the pump pulse: although this would correspond to a wider pump frequency spectrum, it will inevitably be filtered by the fixed microring resonance linewidth. Therefore, in a side-coupled microring resonator the minimal correlation between the photons can already be obtained when the pump temporal duration is equal to the photon dwelling time in the ring, and the integrand in Eq. (3.9) will encompass the product of four identical — as the pump, signal, and idler resonances are — lorentzian-shaped function, which leads to $K = 1.09$.

3.2 Long pump pulse regime

We now consider the pump pulse duration τ_P is much longer that the dwelling time of the photons in the ring, close to the limit of CW pumping. Under these conditions, the generation of entangled photon pairs is expected, and has been recently demonstrated [44].

Once more, the theoretical and the experimental JSD are reported next to each other in Fig. 3.5, assuming a pump pulse duration $\tau_P = 1$ μs, and performing the numerical evaluation following the same prescriptions discussed in the previous section. The elongated shape of both the JSDs indicates spectral correlations, and the lower bound of the Schmidt number calculated from the data is indeed $K_{bound} = 3.93$. This value is very far from the theoretical result, $K_{theory} = 37038$, but it is clear from Fig. 3.5 that in order to grasp the fine details of the theoretical JSD, an extremely high experimental resolution would be required. Nonetheless, we are still able to discriminate between the generation of

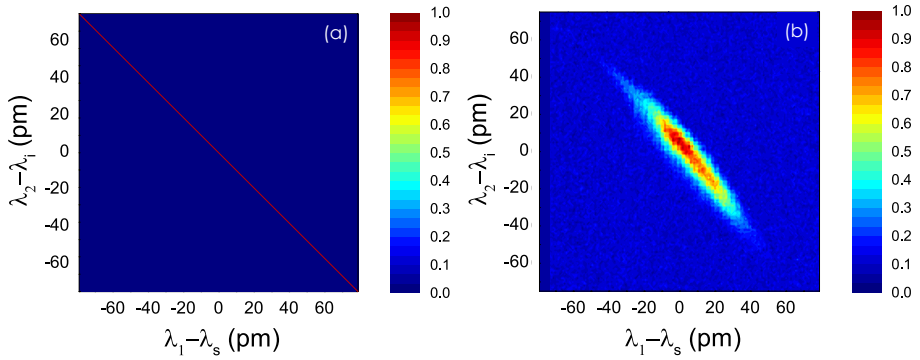

Figure 3.5: Sketch (a) and experimental measurement (b) of the JSD of the highly energy-entangled photon pairs produced by SFWM in the long pump pulsing regime ($\tau_P = 1\ \mu s$).

correlated and nearly uncorrelated photons. In the present case this would not be possible with state-of-the-art techniques based on coincidence measurements, which have a resolution of hundreds of pm, (i.e. the typical pixel is larger than the whole Fig. 3.4(b) or 3.5).

From the discussion of these antithetical cases, it is clear that a microring resonator integrated on a silicon chip can be driven to emit nearly uncorrelated or time-energy entangled photon pairs depending on the pump pulse duration. These theoretical predictions are well confirmed by the experimental outcomes, obtained taking advantage of the SET technique for reducing the measurement time and dramatically increasing the JSD resolution. Thanks to this dynamical behavior of microrings it is possible to design sources of nonclassical states of light with tunable quantum correlations, which is a powerful enabling tool for quantum information technologies.

Yet, as we recalled above, the use of standard side-coupled microring resonators cannot produce truly uncorrelated photons without resorting to optical filters (the maximum Schmidt number being $K = 1.09$). This can be a quite severe limitation, for instance in the case of single photon sources based on heralding, where a completely pure and separable state is mandatory. We will address this issue in the following Chapter, discussing a novel scheme for coupling microring resonators which is capable of breaking these constraints.

Chapter 4

Truly unentangled photon pairs without spectral filtering

In the previous chapters we discussed the generation of energy-entangled photon pairs by SFWM in a side-coupled microring resonator showing that, by adjusting the pump pulse duration, it is possible to tailor the quantum correlations of the photon pairs, from strongly correlated to nearly uncorrelated. But as we pointed out, the minimum Schmidt number one can obtain from such a device is $K = 1.09$, where a truly separable state corresponds to Schmidt number $K = 1$.

Since, as we demonstrated in the previous chapters, the properties of a BWF can be engineered by changing the pump pulse and/or the geometrical outlook of the device, it is natural to wonder if it is possible to come up with a source design which yields photon pairs with unitary Schmidt number. This will be the main goal of this chapter. To find an answer to this question, we can investigate more in details the expression of the BWF generated by the side-coupled microring resonator, to highlight the factors limiting the state separability. Omitting proportionality factors not essential in our discussion, we can recast the BWF of Eq. (3.9) in the minimal form

$$\phi_{Out,Out}(\omega_1, \omega_2) \propto \mathcal{F}(\omega_1)\mathcal{F}(\omega_2)\mathcal{L}(\omega_1 + \omega_2), \tag{4.1}$$

where

$$\mathcal{L}(\omega) = \int d\omega_3 \ \phi_P(\omega_3)\phi_P(\omega - \omega_3)\mathcal{F}(\omega_3)\mathcal{F}(\omega - \omega_3), \tag{4.2}$$

$\mathcal{F}(\omega)$ is the FE in the ring resonator, and $\phi_P(\omega)$ is the pump spectrum. We have already demonstrated in Chapter 3 that in the long pump pulse regime $\mathcal{L}(\omega)$ is narrowly peaked about $\omega = 0$ leading to a function $|\mathcal{L}(\omega_1 + \omega_2)|^2$ which has support only along the line $\omega_2 = -\omega_1$. The corresponding JSD is associated with highly energy anti-correlated photons (see Fig. 3.5). This extreme lack of separability of the BWF can be mitigated by broadening $\mathcal{L}(\omega)$ by an amount

sufficient to make $|\mathcal{L}(\omega_1+\omega_2)|^2$ nearly uniform over the domain defined by the Lorentzian factors in (4.1). Indeed, if the factor $\mathcal{L}(\omega_1+\omega_2)$ is nearly constant, the BWF (4.1) becomes clearly separable. This is actually the strategy we followed in the previous Chapter while discussing the short pump pulse regime, which corresponds to a broader pump spectrum. As clearly visible in Fig. 3.4, under these conditions the correlation of the generated photon energies to the central frequency of the pump pulse is relaxed. However, the filtering of the pump light as it enters the resonator, represented by the Lorentzian factors $\mathcal{F}(\omega_3)\mathcal{F}(\omega-\omega_3)$ in the integrand of (4.2), means that the spectrum of the pump photons available for conversion *cannot be arbitrarily increased by broadening the injected pump*, and rather is fundamentally limited by the linewidth of the pump resonance. This is the ultimate reason for the unachievable complete separability of the photon pairs produced by SFWM in side-coupled microring resonators. Yet, this insight provided by Eq. (4.1) and (4.2) is also the key for devising a different approach to the generation of truly unentangled photon pairs: the pump resonance linewidth must be significantly broader than those of the signal and idler or, equivalently, the pump resonance quality factor must be much smaller than those of the signal and idler resonances.

Most examples in the literature of microring-based SFWM have used devices with nearly equal resonance linewidths for the pump, signal and idler, yielding BWFs that display residual correlations even when pumped by a pulse with an arbitrarily broad spectrum [75, 33, 45]. In those instances, the generation of unentangled photon pairs is achieved by spectrally filtering the resulting BWF [38, 143], a simpler approach which nonetheless sacrifices the source luminescence, or, as very recently proposed, by an appropriate spectral engineering of the pump pulse [144]. Both this approaches have been theoretically demonstrated as viable routes to the generation of completely unentangled photon pairs. However, in the first instance the introduction of filters inevitably lowers the number of usable photon pairs, either because the frequency of one — or both — of the generated photons is found outside of the filter transparency window, or because of the loss introduced by the filter itself. Moreover, as pointed out in [38], spectral filtering of the photon pairs can significantly affect the heralding efficiency, a key feature for quantum technologies. Finally, in view of the integration of the complete setup on-chip, this approach would require integrated hard-edge filters with strong rejection, a feature that is presently out of reach. Even in a bulk approach, it has been shown that the purity of the heralded quantum state rapidly degrades with the decreasing sharpness of the filter transparency window. In the second instance, which considers the use of a properly engineered pump spectrum, a more complex pumping scheme is required and the temporal distance between the pump pulses (in a double-pulse configuration) increases with the resonator quality factor, which makes the experiment more challenging. Moreover, since the resonances posses a nearly-identical quality factor, the same issue with heralding efficiency pointed out in [100] is encountered.

In the following, we present an interferometric coupling scheme for a ring resonator in the configuration of an add-drop filter, and we demonstrate how this geometry can yield truly unentangled photon pairs. This design is inspired

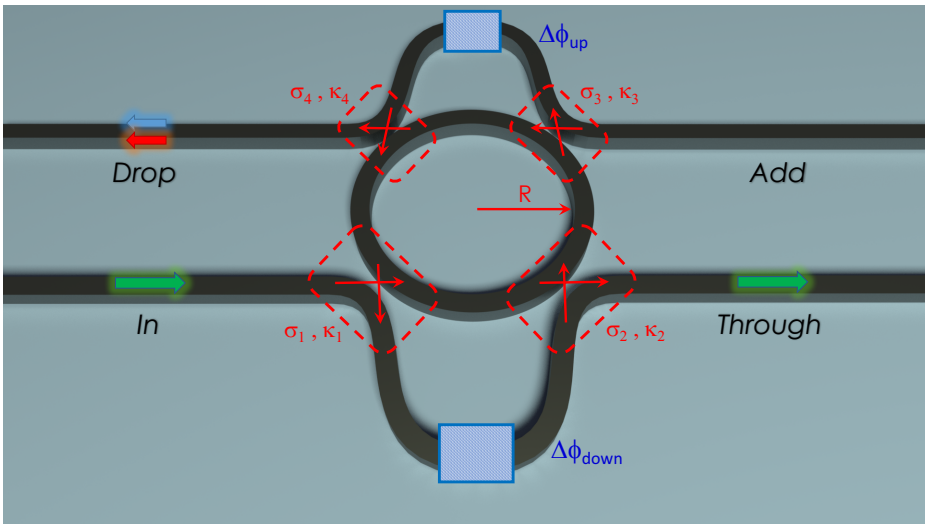

Figure 4.1: Sketch of an integrated microring resonator, with two MZI couplings to bus waveguides. Each physical coupling point is characterized by a self- and a cross-coupling coefficient (σ_i and κ_i). The pump pulse is injected through the *In* channel, and with a proper choice of the MZI geometry, it will leave the structure mostly from the *Through* channel, while the Signal and Idler photons generated by SFWM will leave the structure from the *Drop* channel.

by the work of Gentry et al. [47] and of Chen et al. [48], where the authors show that two coupling points between the bus waveguide and the ring provide a precise control over the individual quality factors of the ring resonances, and therefore also over the quantum properties of the generated light. The presence of two coupling points establishes a MZI that can be used to gain control on the interference between the light in the ring and that in the bus waveguide by using microheaters mounted on the device. Such interferometric coupling overcomes the limitation, typical in microresonator systems, represented by the lack of independent control over different resonances.

The integrated circuit we propose is sketched in Fig. 4.1 and it is composed of a microring add-drop filter with two identical and tunable dual MZI couplers.

By appropriately tuning the MZIs, the system can be configured such that the bottom channel only couples to the pump mode in the resonator, while the top channel only couples to the signal and idler modes. Increasing the coupling strength of the bottom channel then decreases the quality factor of the pump resonance without significantly affecting the properties of the signal and idler resonances, allowing pump light with a much larger bandwidth to couple into the ring.

4.1 A quick estimate of the heralded state purity

Let us reconsider the approximate expressions (4.1) and (4.2). For convenience, we can recast the FE $\mathcal{F}(\omega)$ of any given resonance as a function of its central frequency ω_j and quality factor Q_j

$$\mathcal{F}(\omega) \approx \frac{1}{-i(\omega - \omega_j) + \frac{\omega_j}{2Q_j}}. \tag{4.3}$$

It is paramount to emphasize that Eq. (4.3) is an approximation which comes from assuming simple frequency-independent point-couplings for each resonance. The complete expression of the FE in the ring is reported in the next section. Nonetheless, the quantity $\mathcal{F}(\omega_j)$ is still a good Lorentzian approximation of the FE in the ring, and Eq. (4.3) has the merit of explicitly introducing the the loaded quality factor Q_j in the expression of the BWF. Finally, it should be noticed that Eq. (4.3) will also differ from Eq. (3.10), for here we are dealing with an add-drop filter.

At this point, we can imagine to adjust the phase delays in the MZIs to tune the coupling strength of each resonance, almost independently. As we will demonstrate in the following with the full numerical calculation, this is indeed a feasible operation. Since we aim at a pump resonance much broader than the that of the signal and idler, the relevant figure of merit we should define is the ratio Q_{SI}/Q_P, where $Q_{SI} = \min(Q_S, Q_I)$. In each configuration, we can then compute the Schmidt number or, equivalently, the purity of the heralded state, defined as $\gamma = 1/K$.

To estimate the Schmidt number, and hence the purity of the heralded state, first we need to construct the BWF following Eq. (4.1) and (4.3) for a given choice of the resonances quality factors. Then, by projecting the state onto the Hilbert spaces associated with each photon in the pair, we can reconstruct the reduced density operators

$$\rho_1(\omega_2) = \int d\omega_k \ \phi(\omega_k, \omega_2)\phi^*(\omega_k, \omega_2) \tag{4.4}$$

and

$$\rho_2(\omega_1) = \int d\omega_k \ \phi(\omega_1, \omega_k)\phi^*(\omega_1, \omega_k). \tag{4.5}$$

Finally, when the BWF is computed with a sufficiently fine frequency discretization, Eq.s (4.4) and (4.5) reduce to correspondent finite sums, and it is possible to calculate the eigenvalues of $\rho_1(\omega_2)$ and $\rho_2(\omega_1)$. From these estimates we can finally obtain the Schmidt number K as discussed previously, as [139, 145, 140, 146]

$$K = \frac{1}{Tr[(\rho_1)^2]} = \frac{1}{Tr[(\rho_2)^2]} \equiv \frac{1}{\sum_n \lambda_n^2}. \tag{4.6}$$

Following this approach, we have considered a range of Q_{SI}/Q_P ratios, and computed the expected purity of the generated photon pairs. The result is reported in Fig. 4.2.

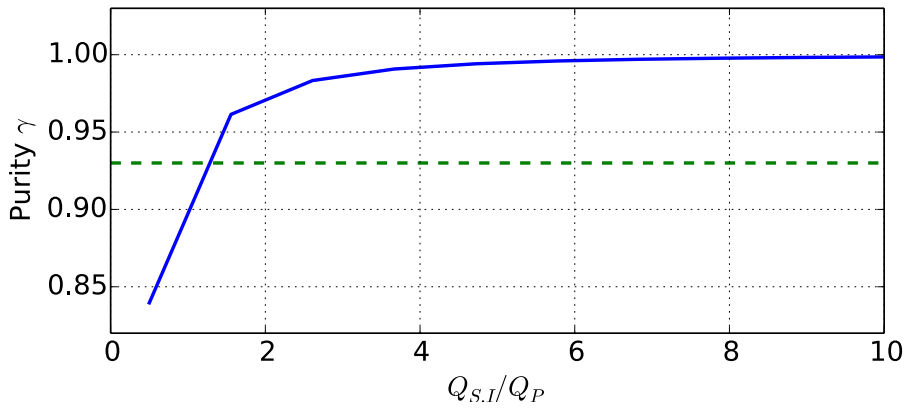

Figure 4.2: Maximum heralded state purity γ as a function of the Q_{SI}/Q_P ratio, as predicted by the theoretical effective point-coupling model. The dashed line represents the upper bound of 91.7% purity for a system with equal quality factors, which is clearly exceeded with the proposed strategy.

As expected, when the ratio Q_{SI}/Q_P is unitary (i.e. in the simple side-coupled ring scenario), we obtain a purity γ around 91.7%, which is consistent with our previous conclusions. With lower Q_{SI}/Q_P ratios, the purity diminishes, indicating stronger quantum correlations between the generated photons. More interestingly, when the ratio Q_{SI}/Q_P exceeds unity, the purity asymptotically approaches 100%, and the photon pairs generated can be safely considered as truly unentangled.

Once more, we stress that such result is crucial for the development of sources of heralded single photons, for it produces true separable photon pairs efficiently without resorting to any spectral filtering. Yet, the conclusions we reached in this Section are based on the premise that we can engineer the dual MZI couplers to resemble a simple frequency-dependent point coupler, and that the resulting FE in the ring would sill be Lorentzian. In the following Section, we will provide a more detailed insight into the structure of Fig. 4.1, demonstrating that our assumptions are indeed correct.

4.2 Numerical calculation of the heralded state purity

In this Section we apply the Asymptotic field formalism presented in Sec. 1.3 to calculate the BFW and thus the spectral purity of the photon pairs generated by the source depicted in Fig. 4.1. As customary, we start from the complete BWF (3.4), which we report here for convenience

$$\phi_{Drop,Drop}(\omega_1,\omega_2) = \frac{3\sqrt{2}i\pi\alpha^2\hbar}{4\beta\epsilon_0}\int d\omega_3\ \phi_P(\omega_3)\phi_P(\omega_1+\omega_2-\omega_3) \tag{4.7}$$
$$\times\sqrt{\frac{\omega_1\omega_2\omega_3(\omega_1+\omega_2-\omega_3)}{v_g(\omega_1)v_g(\omega_2)v_g(\omega_3)v_g(\omega_1+\omega_2-\omega_3)}}$$
$$\times\int d\mathbf{r}\ \frac{\chi_3^{ijkl}(\mathbf{r})}{\epsilon_0^2 n^2(\mathbf{r}_\perp;\omega_1)n^2(\mathbf{r}_\perp;\omega_2)n^2(\mathbf{r}_\perp;\omega_3)n^2(\mathbf{r}_\perp;\omega_1+\omega_2-\omega_3)}$$
$$\times D^{i,asy-in}_{Drop,k(\omega_1)}(\mathbf{r})D^{j,asy-in}_{Drop,k(\omega_2)}(\mathbf{r})D^{k,asy-in}_{In,k(\omega_3)}(\mathbf{r})D^{l,asy-in}_{In,k(\omega_1+\omega_2-\omega_3)}(\mathbf{r}),$$

remembering that, for the present structure, we look for the BWF of the Signal and Idler photons exiting from the *Drop* channel, while the pump incomes from the *In* channel (see Fig. 4.1). Similarly to what we did in Sec. 3, we now move on to compute the expression of the asymptotic-in fields from channels *In* and *Drop*.

Asymptotic-in fields from channels *In* and *Add*

Let us consider a schematic representation of the source, as depicted in Fig. 4.3(a-b).

We consider the general case in which the pump field comes from the *In* and *Add* channels, traveling counter-clockwise in the ring resonator. Using the labels indicated in the sketch we can express the field amplitude in each point of the structure as

$$\begin{cases} A = i\kappa_1 In + \sigma_1 H \\ B = e^{ik(\omega)L_1}A \\ C = i\kappa_2 L + \sigma_2 B \\ D = e^{ik(\omega)L_2}C \\ E = i\kappa_3 Add + \sigma_3 D \\ F = e^{ik(\omega)L_1}E \\ G = i\kappa_4 N + \sigma_4 F \end{cases} \qquad \begin{cases} H = e^{ik(\omega)L_2}G \\ I = i\kappa_1 H + \sigma_1 In \\ L = e^{ik(\omega)L_3}I \\ M = i\kappa_3 D + \sigma_3 Add \\ N = e^{ik(\omega)L_4}M \\ Through = i\kappa_2 B + \sigma_2 L \\ Drop = i\kappa_4 F + \sigma_4 N \end{cases} . \tag{4.8}$$

Solving the set of coupled equations we eventually obtain

$$Through = \tag{4.9}$$
$$\frac{(\sigma_1\sigma_2 e^{ik(\omega)L_3} - \kappa_1\kappa_2 e^{ik(\omega)L_1}) - e^{ik(\omega)(L_1+2L_2+L_3)}(\sigma_3\sigma_4 e^{ik(\omega)L_1} - \kappa_3\kappa_4 e^{ik(\omega)L_4})}{1 - e^{2ik(\omega)L_2}(\sigma_1\sigma_2 e^{ik(\omega)L_1} - \kappa_1\kappa_2 e^{ik(\omega)L_3})(\sigma_3\sigma_4 e^{ik(\omega)L_1} - \kappa_3\kappa_4 e^{ik(\omega)L_4})} In$$
$$-\frac{e^{ik(\omega)L_2}(\sigma_1\kappa_2 e^{ik(\omega)L_1} + \kappa_1\sigma_2 e^{ik(\omega)L_3})(\sigma_3\kappa_4 e^{ik(\omega)L_4} + \kappa_3\sigma_4 e^{ik(\omega)L_1})}{1 - e^{2ik(\omega)L_2}(\sigma_1\sigma_2 e^{ik(\omega)L_1} - \kappa_1\kappa_2 e^{ik(\omega)L_3})(\sigma_3\sigma_4 e^{ik(\omega)L_1} - \kappa_3\kappa_4 e^{ik(\omega)L_4})} Add$$

and

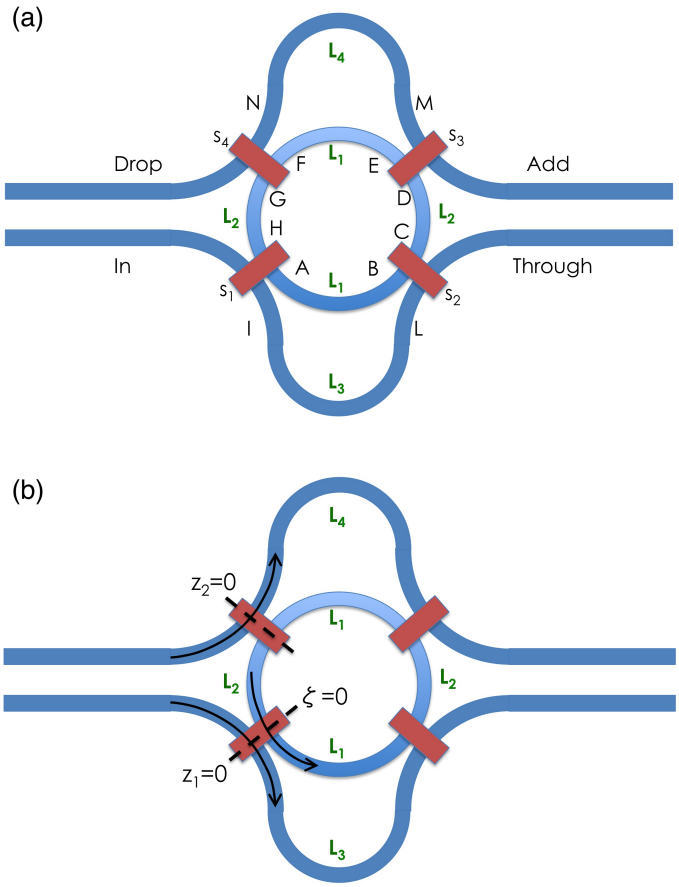

Figure 4.3: Schematic representation of the dual MZI ring resonator, with (a) all the relevant labels and (b) the explicit reference frames for light propagation in any part of the structure.

$$Drop = \tag{4.10}$$
$$-\frac{e^{ik(\omega)L_2}(\sigma_1\kappa_2 e^{ik(\omega)L_3}+\kappa_1\sigma_2 e^{ik(\omega)L_1})(\sigma_3\kappa_4 e^{ik(\omega)L_1}+\kappa_3\sigma_4 e^{ik(\omega)L_4})}{1-e^{2ik(\omega)L_2}(\sigma_1\sigma_2 e^{ik(\omega)L_1}-\kappa_1\kappa_2 e^{ik(\omega)L_3})(\sigma_3\sigma_4 e^{ik(\omega)L_1}-\kappa_3\kappa_4 e^{ik(\omega)L_4})}In$$
$$+\frac{(\sigma_3\sigma_4 e^{ik(\omega)L_4}-\kappa_3\kappa_4 e^{ik(\omega)L_1})-e^{ik(\omega)(L_1+2L_2+L_4)}(\sigma_1\sigma_2 e^{ik(\omega)L_1}-\kappa_1\kappa_2 e^{ik(\omega)L_3})}{1-e^{2ik(\omega)L_2}(\sigma_1\sigma_2 e^{ik(\omega)L_1}-\kappa_1\kappa_2 e^{ik(\omega)L_3})(\sigma_3\sigma_4 e^{ik(\omega)L_1}-\kappa_3\kappa_4 e^{ik(\omega)L_4})}Add$$

which are fundamental for the calculation of the transmission spectra. Yet, here we are most concerned about expressing the fields inside the ring and the MZI arms, for there the FE is boosting the generation of pairs by SFWM. The field amplitude in the lateral sections of the ring is

$$C = \tag{4.11}$$
$$\frac{i(\sigma_1\kappa_2 e^{ik(\omega)L_3}+\kappa_1\sigma_2 e^{ik(\omega)L_1})}{1-e^{2ik(\omega)L_2}(\sigma_1\sigma_2 e^{ik(\omega)L_1}-\kappa_1\kappa_2 e^{ik(\omega)L_3})(\sigma_3\sigma_4 e^{ik(\omega)L_1}-\kappa_3\kappa_4 e^{ik(\omega)L_4})}In$$
$$+\frac{ie^{ik(\omega)L_2}(\sigma_1\sigma_2 e^{ik(\omega)L_1}-\kappa_1\kappa_2 e^{ik(\omega)L_3})(\sigma_3\kappa_4 e^{ik(\omega)L_4}+\kappa_3\sigma_4 e^{ik(\omega)L_1})}{1-e^{2ik(\omega)L_2}(\sigma_1\sigma_2 e^{ik(\omega)L_1}-\kappa_1\kappa_2 e^{ik(\omega)L_3})(\sigma_3\sigma_4 e^{ik(\omega)L_1}-\kappa_3\kappa_4 e^{ik(\omega)L_4})}Add$$

and

$$G = \tag{4.12}$$
$$\frac{ie^{ik(\omega)L_2}(\sigma_1\kappa_2 e^{ik(\omega)L_3}+\kappa_1\sigma_2 e^{ik(\omega)L_1})(\sigma_3\sigma_4 e^{ik(\omega)L_1}-\kappa_3\kappa_4 e^{ik(\omega)L_4})}{1-e^{2ik(\omega)L_2}(\sigma_1\sigma_2 e^{ik(\omega)L_1}-\kappa_1\kappa_2 e^{ik(\omega)L_3})(\sigma_3\sigma_4 e^{ik(\omega)L_1}-\kappa_3\kappa_4 e^{ik(\omega)L_4})}In$$
$$+\frac{i(\sigma_3\kappa_4 e^{ik(\omega)L_4}+\kappa_3\sigma_4 e^{ik(\omega)L_1})}{1-e^{2ik(\omega)L_2}(\sigma_1\sigma_2 e^{ik(\omega)L_1}-\kappa_1\kappa_2 e^{ik(\omega)L_3})(\sigma_3\sigma_4 e^{ik(\omega)L_1}-\kappa_3\kappa_4 e^{ik(\omega)L_4})}Add,$$

while the field amplitude in the bottom and top sections of the ring is

$$A = \tag{4.13}$$
$$\frac{i\kappa_1+i\kappa_2 e^{ik(\omega)(2L_2+L_3)}(\sigma_3\sigma_4 e^{ik(\omega)L_1}-\kappa_3\kappa_4 e^{ik(\omega)L_4})}{1-e^{2ik(\omega)L_2}(\sigma_1\sigma_2 e^{ik(\omega)L_1}-\kappa_1\kappa_2 e^{ik(\omega)L_3})(\sigma_3\sigma_4 e^{ik(\omega)L_1}-\kappa_3\kappa_4 e^{ik(\omega)L_4})}In$$
$$+\frac{i\sigma_1 e^{ik(\omega)L_2}(\sigma_3\kappa_4 e^{ik(\omega)L_4}+\kappa_3\sigma_4 e^{ik(\omega)L_1})}{1-e^{2ik(\omega)L_2}(\sigma_1\sigma_2 e^{ik(\omega)L_1}-\kappa_1\kappa_2 e^{ik(\omega)L_3})(\sigma_3\sigma_4 e^{ik(\omega)L_1}-\kappa_3\kappa_4 e^{ik(\omega)L_4})}Add$$

and

$$E = \tag{4.14}$$
$$\frac{i\sigma_3 e^{ik(\omega)L_2}(\sigma_1\kappa_2 e^{ik(\omega)L_3}+\kappa_1\sigma_2 e^{ik(\omega)L_1})}{1-e^{2ik(\omega)L_2}(\sigma_1\sigma_2 e^{ik(\omega)L_1}-\kappa_1\kappa_2 e^{ik(\omega)L_3})(\sigma_3\sigma_4 e^{ik(\omega)L_1}-\kappa_3\kappa_4 e^{ik(\omega)L_4})}In$$
$$+\frac{i\kappa_3+i\kappa_4 e^{ik(\omega)(2L_2+L_4)}(\sigma_1\sigma_2 e^{ik(\omega)L_1}-\kappa_1\kappa_2 e^{ik(\omega)L_3})}{1-e^{2ik(\omega)L_2}(\sigma_1\sigma_2 e^{ik(\omega)L_1}-\kappa_1\kappa_2 e^{ik(\omega)L_3})(\sigma_3\sigma_4 e^{ik(\omega)L_1}-\kappa_3\kappa_4 e^{ik(\omega)L_4})}Add.$$

Finally, we can express the field amplitude in the bottom and top arm of the MZI couplers, as

$$I = \frac{\sigma_1 - \sigma_2 e^{ik(\omega)(L_1+2L_2)}\left(\sigma_3\sigma_4 e^{ik(\omega)L_1} - \kappa_3\kappa_4 e^{ik(\omega)L_4}\right)}{1 - e^{2ik(\omega)L_2}\left(\sigma_1\sigma_2 e^{ik(\omega)L_1} - \kappa_1\kappa_2 e^{ik(\omega)L_3}\right)\left(\sigma_3\sigma_4 e^{ik(\omega)L_1} - \kappa_3\kappa_4 e^{ik(\omega)L_4}\right)} In - \frac{\kappa_1 e^{ik(\omega)L_2}\left(\sigma_3\kappa_4 e^{ik(\omega)L_4} + \kappa_3\sigma_4 e^{ik(\omega)L_1}\right)}{1 - e^{2ik(\omega)L_2}\left(\sigma_1\sigma_2 e^{ik(\omega)L_1} - \kappa_1\kappa_2 e^{ik(\omega)L_3}\right)\left(\sigma_3\sigma_4 e^{ik(\omega)L_1} - \kappa_3\kappa_4 e^{ik(\omega)L_4}\right)} Add \tag{4.15}$$

$$N = -\frac{\kappa_3 e^{ik(\omega)(L_2+L_4)}\left(\sigma_1\kappa_2 e^{ik(\omega)L_3} + \kappa_1\sigma_2 e^{ik(\omega)L_1}\right)}{1 - e^{2ik(\omega)L_2}\left(\sigma_1\sigma_2 e^{ik(\omega)L_1} - \kappa_1\kappa_2 e^{ik(\omega)L_3}\right)\left(\sigma_3\sigma_4 e^{ik(\omega)L_1} - \kappa_3\kappa_4 e^{ik(\omega)L_4}\right)} In + \frac{\sigma_3 e^{ik(\omega)L_4} - \sigma_4 e^{ik(\omega)(L_1+2L_2+L_4)}\left(\sigma_1\sigma_2 e^{ik(\omega)L_1} - \kappa_1\kappa_2 e^{ik(\omega)L_3}\right)}{1 - e^{2ik(\omega)L_2}\left(\sigma_1\sigma_2 e^{ik(\omega)L_1} - \kappa_1\kappa_2 e^{ik(\omega)L_3}\right)\left(\sigma_3\sigma_4 e^{ik(\omega)L_1} - \kappa_3\kappa_4 e^{ik(\omega)L_4}\right)} Add. \tag{4.16}$$

We can now express the asymptotic-in fields $D^{asy-in}_{In,k(\omega)}(\mathbf{r})$ of Eq. (4.7) as

$$D^{i,asy-in}_{In,k(\omega)}(\mathbf{r}) = \begin{cases} \frac{d^i_k(\mathbf{r}_\perp)}{\sqrt{2\pi}} e^{ik(\omega)z_1} & z_1 \in [-\infty, 0] \\ Through \cdot \frac{d^i_k(\mathbf{r}_\perp)}{\sqrt{2\pi}} e^{ik(\omega)z_1} & z_1 \in [L_3, \infty] \\ Drop \cdot \frac{d^i_k(\mathbf{r}_\perp)}{\sqrt{2\pi}} e^{-ik(\omega)z_2} & z_2 \in [-\infty, 0] \\ A_{In} \cdot \frac{d^i_k(\mathbf{r}_\perp, \zeta/R)}{\sqrt{2\pi}} e^{ik\zeta} & \zeta \in [0, L_1] \\ C_{In} \cdot \frac{d^i_k(\mathbf{r}_\perp, \zeta/R)}{\sqrt{2\pi}} e^{ik(\zeta - L_1)} & \zeta \in [L_1, \pi R] \\ E_{In} \cdot \frac{d^i_k(\mathbf{r}_\perp, \zeta/R)}{\sqrt{2\pi}} e^{ik(\zeta - \pi R)} & \zeta \in [\pi R, \pi R + L_1] \\ G_{In} \cdot \frac{d^i_k(\mathbf{r}_\perp, \zeta/R)}{\sqrt{2\pi}} e^{ik(\zeta - \pi R - L_1)} & \zeta \in [\pi R + L_1, 2\pi R] \\ I_{In} \cdot \frac{d^i_k(\mathbf{r}_\perp)}{\sqrt{2\pi}} e^{ik(\omega)z_1} & z_1 \in [0, L_3] \\ N_{In} \cdot \frac{d^i_k(\mathbf{r}_\perp)}{\sqrt{2\pi}} e^{-ik(\omega)z_2} & z_2 \in [0, L_4] \end{cases} . \tag{4.17}$$

One can pursue a similar strategy to compute the asymptotic-in fields $D^{asy-in}_{Drop,k(\omega)}(\mathbf{r})$, as we briefly recall in the next section.

Asymptotic-in fields from channels *Drop* and *Through*

Let us refer to the same labelling and reference frames we adopted in the previous section and reported in Fig. (4.1). The field amplitude in each section of the circuit is given by

$$\begin{cases} F = i\kappa_4 Drop + \sigma_4 G \\ E = e^{ik(\omega)L_1} F \\ D = i\kappa_3 M + \sigma_3 E \\ C = e^{ik(\omega)L_2} D \\ B = i\kappa_2 Through + \sigma_2 C \\ A = e^{ik(\omega)L_1} B \\ H = i\kappa_1 I + \sigma_1 A \end{cases} \qquad \begin{cases} G = e^{ik(\omega)L_2} H \\ N = i\kappa_4 G + \sigma_4 Drop \\ M = e^{ik(\omega)L_4} N \\ L = i\kappa_2 C + \sigma_2 Through \\ I = e^{k(\omega)L_3} L \\ Add = i\kappa_3 E + \sigma_3 M \\ In = i\kappa_1 A + \sigma_1 I \end{cases} . \tag{4.18}$$

We can proceed with the same calculation as in the previous case but, comparing Eq. (4.18) and Eq. (4.8), one can notice they are equivalent, provided labels are properly interchanged. Such property is guaranteed by the symmetry enjoyed by our source geometry. Hence, when the substitutions

$$\begin{aligned} A &\leftrightarrow F \\ B &\leftrightarrow E \\ C &\leftrightarrow D \\ G &\leftrightarrow H \\ I &\leftrightarrow N \\ L &\leftrightarrow M \\ In &\leftrightarrow Drop \\ Add &\leftrightarrow Through \\ L_3 &\rightarrow L_4 \\ \sigma_1 &\rightarrow \sigma_4 \\ \sigma_2 &\rightarrow \sigma_3. \end{aligned} \tag{4.19}$$

are implemented in (4.8), we directly obtain the transmission amplitudes

$$Add = \tag{4.20}$$
$$\frac{(\sigma_3\sigma_4 e^{ik(\omega)L_4} - \kappa_3\kappa_4 e^{ik(\omega)L_1}) - e^{ik(\omega)(L_1+2L_2+L_4)}(\sigma_1\sigma_2 e^{ik(\omega)L_1} - \kappa_1\kappa_2 e^{ik(\omega)L_3})}{1 - e^{2ik(\omega)L_2}(\sigma_1\sigma_2 e^{ik(\omega)L_1} - \kappa_1\kappa_2 e^{ik(\omega)L_3})(\sigma_3\sigma_4 e^{ik(\omega)L_1} - \kappa_3\kappa_4 e^{ik(\omega)L_4})} Drop$$
$$- \frac{e^{ik(\omega)L_2}(\kappa_3\sigma_4 e^{ik(\omega)L_1} + \sigma_3\kappa_4 e^{ik(\omega)L_4})(\sigma_1\kappa_2 e^{ik(\omega)L_1} + \kappa_1\sigma_2 e^{ik(\omega)L_3})}{1 - e^{2ik(\omega)L_2}(\sigma_1\sigma_2 e^{ik(\omega)L_1} - \kappa_1\kappa_2 e^{ik(\omega)L_3})(\sigma_3\sigma_4 e^{ik(\omega)L_1} - \kappa_3\kappa_4 e^{ik(\omega)L_4})} Through$$

$$In = \tag{4.21}$$
$$- \frac{e^{ik(\omega)L_2}(\kappa_3\sigma_4 e^{ik(\omega)L_4} + \sigma_3\kappa_4 e^{ik(\omega)L_1})(\kappa_1\sigma_2 e^{ik(\omega)L_1} + \sigma_1\kappa_2 e^{ik(\omega)L_3})}{1 - e^{2ik(\omega)L_2}(\sigma_1\sigma_2 e^{ik(\omega)L_1} - \kappa_1\kappa_2 e^{ik(\omega)L_3})(\sigma_3\sigma_4 e^{ik(\omega)L_1} - \kappa_3\kappa_4 e^{ik(\omega)L_4})} Drop$$
$$+ \frac{(\sigma_1\sigma_2 e^{ik(\omega)L_3} - \kappa_1\kappa_2 e^{ik(\omega)L_1}) - e^{ik(\omega)(L_1+2L_2+L_3)}(\sigma_3\sigma_4 e^{ik(\omega)L_1} - \kappa_3\kappa_4 e^{ik(\omega)L_4})}{1 - e^{2ik(\omega)L_2}(\sigma_1\sigma_2 e^{ik(\omega)L_1} - \kappa_1\kappa_2 e^{ik(\omega)L_3})(\sigma_3\sigma_4 e^{ik(\omega)L_1} - \kappa_3\kappa_4 e^{ik(\omega)L_4})} Through,$$

and, with the help of (4.18), the field amplitudes in the each part of the ring

$$C = \frac{ie^{ik(\omega)L_2}\left(\sigma_3\kappa_4 e^{ik(\omega)L_1} + \kappa_3\sigma_4 e^{ik(\omega)L_4}\right)}{1 - e^{2ik(\omega)L_2}\left(\sigma_3\sigma_4 e^{ik(\omega)L_1} - \kappa_3\kappa_4 e^{ik(\omega)L_4}\right)\left(\sigma_1\sigma_2 e^{ik(\omega)L_1} - \kappa_1\kappa_2 e^{ik(\omega)L_3}\right)} Drop + \frac{ie^{2ik(\omega)L_2}\left(\sigma_3\sigma_4 e^{ik(\omega)L_1} - \kappa_3\kappa_4 e^{ik(\omega)L_4}\right)\left(\kappa_1\sigma_2 e^{ik(\omega)L_3} + \sigma_1\kappa_2 e^{ik(\omega)L_1}\right)}{1 - e^{2ik(\omega)L_2}\left(\sigma_3\sigma_4 e^{ik(\omega)L_1} - \kappa_3\kappa_4 e^{ik(\omega)L_4}\right)\left(\sigma_1\sigma_2 e^{ik(\omega)L_1} - \kappa_1\kappa_2 e^{ik(\omega)L_3}\right)} Through \tag{4.22}$$

$$G = \frac{ie^{2ik(\omega)L_2}\left(\sigma_1\sigma_2 e^{ik(\omega)L_1} - \kappa_1\kappa_2 e^{ik(\omega)L_3}\right)\left(\sigma_3\kappa_4 e^{ik(\omega)L_1} + \kappa_3\sigma_4 e^{ik(\omega)L_4}\right)}{1 - e^{2ik(\omega)L_2}\left(\sigma_1\sigma_2 e^{ik(\omega)L_1} - \kappa_1\kappa_2 e^{ik(\omega)L_3}\right)\left(\sigma_3\sigma_4 e^{ik(\omega)L_1} - \kappa_3\kappa_4 e^{ik(\omega)L_4}\right)} Drop + \frac{ie^{ik(\omega)L_2}\left(\sigma_1\kappa_2 e^{ik(\omega)L_1} + \kappa_1\sigma_2 e^{ik(\omega)L_3}\right)}{1 - e^{2ik(\omega)L_2}\left(\sigma_1\sigma_2 e^{ik(\omega)L_1} - \kappa_1\kappa_2 e^{ik(\omega)L_3}\right)\left(\sigma_3\sigma_4 e^{ik(\omega)L_1} - \kappa_3\kappa_4 e^{ik(\omega)L_4}\right)} Through \tag{4.23}$$

$$A = \frac{i\sigma_2 e^{ik(\omega)(L_1+L_2)}\left(\kappa_3\sigma_4 e^{ik(\omega)L_4} + \sigma_3\kappa_4 e^{ik(\omega)L_1}\right)}{1 - e^{2ik(\omega)L_2}\left(\sigma_1\sigma_2 e^{ik(\omega)L_1} - \kappa_1\kappa_2 e^{ik(\omega)L_3}\right)\left(\sigma_3\sigma_4 e^{ik(\omega)L_1} - \kappa_3\kappa_4 e^{ik(\omega)L_4}\right)} Drop + \frac{i\kappa_2 e^{ik(\omega)L_1} + i\kappa_1 e^{ik(\omega)(L_1+2L_2+L_3)}\left(\sigma_3\sigma_4 e^{ik(\omega)L_1} - \kappa_3\kappa_4 e^{ik(\omega)L_4}\right)}{1 - e^{2ik(\omega)L_2}\left(\sigma_1\sigma_2 e^{ik(\omega)L_1} - \kappa_1\kappa_2 e^{ik(\omega)L_3}\right)\left(\sigma_3\sigma_4 e^{ik(\omega)L_1} - \kappa_3\kappa_4 e^{ik(\omega)L_4}\right)} Through \tag{4.24}$$

$$E = \frac{i\kappa_4 e^{ik(\omega)L_1} + i\kappa_3 e^{ik(\omega)(L_1+2L_2+L_4)}\left(\sigma_1\sigma_2 e^{ik(\omega)L_1} - \kappa_1\kappa_2 e^{ik(\omega)L_3}\right)}{1 - e^{2ik(\omega)L_2}\left(\sigma_1\sigma_2 e^{ik(\omega)L_1} - \kappa_1\kappa_2 e^{ik(\omega)L_3}\right)\left(\sigma_3\sigma_4 e^{ik(\omega)L_1} - \kappa_3\kappa_4 e^{ik(\omega)L_4}\right)} Drop + \frac{i\sigma_4 e^{ik(\omega)(L_1+L_2)}\left(\sigma_1\kappa_2 e^{ik(\omega)L_1} + \kappa_1\sigma_2 e^{ik(\omega)L_3}\right)}{1 - e^{2ik(\omega)L_2}\left(\sigma_1\sigma_2 e^{ik(\omega)L_1} - \kappa_1\kappa_2 e^{ik(\omega)L_3}\right)\left(\sigma_3\sigma_4 e^{ik(\omega)L_1} - \kappa_3\kappa_4 e^{ik(\omega)L_4}\right)} Through, \tag{4.25}$$

and in the arms of the MZI couplers

$$I = -\frac{\kappa_2 e^{ik(\omega)(L_2+L_3)}\left(\sigma_3\kappa_4 e^{ik(\omega)L_1} + \kappa_3\sigma_4 e^{ik(\omega)L_4}\right)}{1 - e^{2ik(\omega)L_2}\left(\sigma_1\sigma_2 e^{ik(\omega)L_1} - \kappa_1\kappa_2 e^{ik(\omega)L_3}\right)\left(\sigma_3\sigma_4 e^{ik(\omega)L_1} - \kappa_3\kappa_4 e^{ik(\omega)L_4}\right)} Drop + \frac{\sigma_2 e^{ik(\omega)L_3} - \sigma_1 e^{ik(\omega)(L_1+2L_2+L_3)}\left(\sigma_3\sigma_4 e^{ik(\omega)L_1} - \kappa_3\kappa_4 e^{ik(\omega)L_4}\right)}{1 - e^{2ik(\omega)L_2}\left(\sigma_1\sigma_2 e^{ik(\omega)L_1} - \kappa_1\kappa_2 e^{ik(\omega)L_3}\right)\left(\sigma_3\sigma_4 e^{ik(\omega)L_1} - \kappa_3\kappa_4 e^{ik(\omega)L_4}\right)} Through \tag{4.26}$$

$$N = \frac{\sigma_4 - \sigma_3 e^{ik(\omega)(L_1+2L_2)}\left(\sigma_1\sigma_2 e^{ik(\omega)L_1} - \kappa_1\kappa_2 e^{ik(\omega)L_3}\right)}{1 - e^{2ik(\omega)L_2}\left(\sigma_1\sigma_2 e^{ik(\omega)L_1} - \kappa_1\kappa_2 e^{ik(\omega)L_3}\right)\left(\sigma_3\sigma_4 e^{ik(\omega)L_1} - \kappa_3\kappa_4 e^{ik(\omega)L_4}\right)} Drop - \frac{\kappa_4 e^{ik(\omega)L_2}\left(\kappa_1\sigma_2 e^{ik(\omega)L_3} + \sigma_1\kappa_2 e^{ik(\omega)L_1}\right)}{1 - e^{2ik(\omega)L_2}\left(\sigma_1\sigma_2 e^{ik(\omega)L_1} - \kappa_1\kappa_2 e^{ik(\omega)L_3}\right)\left(\sigma_3\sigma_4 e^{ik(\omega)L_1} - \kappa_3\kappa_4 e^{ik(\omega)L_4}\right)} Through. \tag{4.27}$$

Finally, we can express the asymptotic-in fields $D^{i,asy-in}_{Drop,k(\omega)}(\mathbf{r})$ of Eq. (4.7) as

$$D^{i,asy-in}_{Drop,k(\omega)}(\mathbf{r}) = \begin{cases} \frac{d^i_k(\mathbf{r}_\perp)}{\sqrt{2\pi}} e^{ik(\omega)z_2} & z_2 \in [-\infty, 0] \\ Add \cdot \frac{d^i_k(\mathbf{r}_\perp)}{\sqrt{2\pi}} e^{ik(\omega)z_2} & z_2 \in [L_4, \infty] \\ In \cdot \frac{d^i_k(\mathbf{r}_\perp)}{\sqrt{2\pi}} e^{-ik(\omega)z_1} & z_1 \in [-\infty, 0] \\ A_{Drop} \cdot \frac{d^i_k(\mathbf{r}_\perp, \zeta/R)}{\sqrt{2\pi}} e^{-ik\zeta} & \zeta \in [0, L_1] \\ C_{Drop} \cdot \frac{d^i_k(\mathbf{r}_\perp, \zeta/R)}{\sqrt{2\pi}} e^{-ik(\zeta - L_1)} & \zeta \in [L_1, \pi R] \\ E_{Drop} \cdot \frac{d^i_k(\mathbf{r}_\perp, \zeta/R)}{\sqrt{2\pi}} e^{-ik(\zeta - \pi R)} & \zeta \in [\pi R, \pi R + L_1] \\ G_{Drop} \cdot \frac{d^i_k(\mathbf{r}_\perp, \zeta/R)}{\sqrt{2\pi}} e^{-ik(\zeta - \pi R - L_1)} & \zeta \in [\pi R + L_1, 2\pi R] \\ I_{Drop} \cdot \frac{d^i_k(\mathbf{r}_\perp)}{\sqrt{2\pi}} e^{-ik(\omega)z_1} & z_1 \in [0, L_3] \\ N_{Drop} \cdot \frac{d^i_k(\mathbf{r}_\perp)}{\sqrt{2\pi}} e^{ik(\omega)z_2} & z_2 \in [0, L_4] \end{cases} . \tag{4.28}$$

Calculation of the BWF and the state purity

In the scenario discussed in the opening of this Section, we imagine to inject the pump through the *In* channel and look for frequency-converted photons in the *Drop* channel. Plugging the asymptotic-in fields we derived in Eq. (4.17) and (4.28)in the BWF expression (4.7), after a few manipulations we obtain

$$\begin{aligned} \phi_{Drop,Drop}(\omega_1, \omega_2) = \frac{3\sqrt{2} i \alpha^2 \bar{\chi}_3 \hbar}{16\pi\epsilon_0 \beta} \sqrt{\frac{\omega_1 \omega_2}{v_g(\omega_1) v_g(\omega_2)}} \\ \times \int d\omega_3 \Big[\phi_P(\omega_1 + \omega_2 - \omega_3) \phi_P(\omega_3) \sqrt{\frac{\omega_3(\omega_1 + \omega_2 - \omega_3)}{v_g(\omega_3) v_g(\omega_1 + \omega_2 - \omega_3)}} \\ \times \Big\{ I_{Drop,k(\omega_1)} I_{Drop,k(\omega_2)} I_{In,k(\omega_3)} I_{In,k(\omega_1+\omega_2-\omega_3)} L_3 e^{i\Delta k \frac{L_3}{2}} sinc(\frac{\Delta k L_3}{2}) \\ + N_{Drop,k(\omega_1)} N_{Drop,k(\omega_2)} N_{In,k(\omega_3)} N_{In,k(\omega_1+\omega_2-\omega_3)} L_4 e^{-i\Delta k \frac{L_4}{2}} sinc(\frac{\Delta k L_4}{2}) \\ + \Big[A_{Drop,k(\omega_1)} A_{Drop,k(\omega_2)} A_{In,k(\omega_3)} A_{In,k(\omega_1+\omega_2-\omega_3)} \\ + E_{Drop,k(\omega_1)} E_{Drop,k(\omega_2)} E_{In,k(\omega_3)} E_{In,k(\omega_1+\omega_2-\omega_3)} \Big] L_1 e^{i\Delta k \frac{L_1}{2}} sinc(\frac{\Delta k L_1}{2}) \\ + \Big[C_{Drop,k(\omega_1)} C_{Drop,k(\omega_2)} C_{In,k(\omega_3)} C_{In,k(\omega_1+\omega_2-\omega_3)} \\ + G_{Drop,k(\omega_1)} G_{Drop,k(\omega_2)} G_{In,k(\omega_3)} G_{In,k(\omega_1+\omega_2-\omega_3)} \Big] \\ \times (\pi R - L_1) e^{i\Delta k \frac{\pi R - L_1}{2}} sinc(\frac{\Delta k(\pi R - L_1)}{2}) \Big] . \end{aligned} \tag{4.29}$$

As one would expect, each segment of the structure intervenes in the final expression of the BWF, and the relative weight of each contribution is determined by the FE in the correspondent section of the circuit. We can immediately

point out a significant deviation from the approximated model we adopted in the opening of this chapter: photon pairs are not generated in the ring alone, but in the external arms of the MZI couplers as well. In general, this will affect the properties of the BWF, and the correspondent Schmidt number; yet, as we will discuss in the following, this contribution will be negligible for high Q_{SI}/Q_P ratios.

We now turn our attention to the development of a practical strategy for the control of the Q_{SI}/Q_P ratio. Let us simplify the problem by considering the four point couplings as identical, thus simply described by the coefficients σ and $\kappa = \sqrt{1-\sigma^2}$. We can regard the MZI coupler as an "effective" point coupler, as originally proposed by Chen et al. [48]. Referring to the usual labels reported in Fig. 4.4, we can write

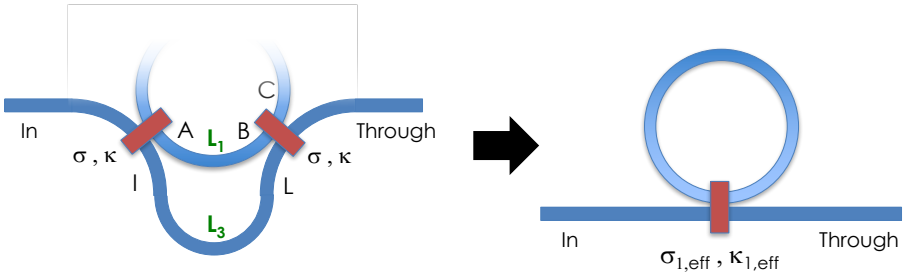

Figure 4.4: Analogy between the complete MZI coupling scheme, and the effective point-coupling approximation.

$$C = \kappa_{1,eff}(\omega) In = 2\kappa\sigma \cos\left(\frac{k(\omega)\Delta L_{31}}{2}\right) In, \tag{4.30}$$

where $\kappa_{1,eff}(\omega)$ is the effective frequency-dependent cross-coupling coefficient between the ring and the bottom bus waveguide, and $\Delta L_{31} \equiv L_3 - L_1$. In order to maximize the heralding efficiency [100] we would like to overcouple the pump resonance to the bottom bus waveguide and, at the same time, significantly undercouple the signal and idler modes to the same waveguide, redirecting the converted photons to the *Drop* port. Thus, we impose

$$\begin{aligned} \kappa^2_{1,eff}(\omega_{SI}) &= 0 \\ \kappa^2_{1,eff}(\omega_P) &= 4\kappa^2\sigma^2, \end{aligned} \tag{4.31}$$

where we assume that the first condition in (4.31) should be satisfied for, at least, one of the two modes, and we notice that the second coefficient is the maximum achievable, given the explicit form of $\kappa_{1,eff}(\omega)$. Eq. (4.31) leads us

to

$$\begin{aligned}\frac{\Delta L_{31} k_{SI}}{2} &= \frac{\pi}{2} + l_{SI}\pi \\ \frac{\Delta L_{31} k_P}{2} &= l_P \pi\end{aligned} \tag{4.32}$$

with $l_{SI,P} \in \mathbb{Z}$. This conditions can easily be met whenever the pump resonance number m_P is even and the signal and idler resonance numbers m_{SI} are odd. Thus, for instance we have $\Delta L_{31} = \frac{2l_P\pi}{k_P} = \frac{2l_p\pi R}{m_P}$, and choosing $l_P = m_P/2$ we have $\Delta L_{31} = \pi R$.

Recalling that the quality factor of a ring resonance can be expressed as

$$Q = \frac{\omega_{res} L}{2 v_g} \frac{1}{1 - \sigma\alpha}, \tag{4.33}$$

where α represents any form of loss in the ring resonator (as we stressed in Section 1.2) and $L = 2\pi R$, we can leverage the effective coupling model to express the Q factor as

$$\begin{aligned}Q &= \frac{\omega_{res} L}{2 v_g} \frac{1}{1 - \sqrt{1 - \kappa_{1,eff}^2(\omega_{res})}\sqrt{1 - \kappa_{2,eff}^2(\omega_{res})}} \\ &= \frac{\omega_{res} L}{2 v_g} \frac{1}{1 - \sqrt{1 - 4\sigma^2\kappa^2 \cos^2\left(\frac{k(\omega_{res})\Delta L_{31}}{2}\right)}\sqrt{1 - 4\sigma^2\kappa^2 \cos^2\left(\frac{k(\omega_{res})\Delta L_{41}}{2}\right)}},\end{aligned} \tag{4.34}$$

where $\Delta L_{41} \equiv L_4 - L_1$. With the proper choice of ΔL_{31} , the ratio Q_{SI}/Q_P as a function of ΔL_{41} is given by

$$\frac{Q_{SI}}{Q_P}(\Delta L_{41}) = \frac{\omega_{SI}}{\omega_P} \frac{1 - \sqrt{1 - 4\sigma^2\kappa^2}\sqrt{1 - 4\sigma^2\kappa^2 \cos^2\left(\frac{k(\omega_P)\Delta L_{41}}{2}\right)}}{1 - \sqrt{1 - 4\sigma^2\kappa^2 \cos^2\left(\frac{k(\omega_{SI})\Delta L_{41}}{2}\right)}} \tag{4.35}$$

and its trend is reported in Fig. 4.5 for $R = 20\ \mu m$, $\sigma = 0.95$ $m_P = 206$, and $m_{SI} = m_P \pm 1$.

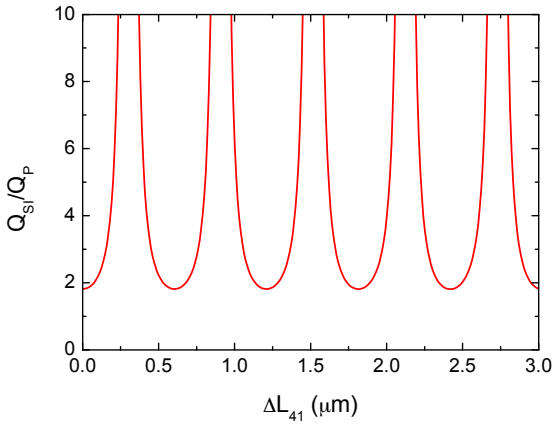

Figure 4.5: Expected Q_{SI}/Q_P ratio as a function of the path difference ΔL_{41} in the upper MZI coupler.

Once the desired Q_{SI}/Q_P ratio is chosen, all of the geometrical properties of the structure of Fig. 4.1 are set, and one can refer to Eq. (4.29) for the numerical calculation of the BWF, and to the strategy reported in (4.4)-(4.6) for the computation of the state purity. In Fig. 4.6 we report the same plot of Fig. 4.2, complemented with several points corresponding to the state purity computed numerically, starting from arbitrary ratios Q_{SI}/Q_p chosen from Fig. 4.5.

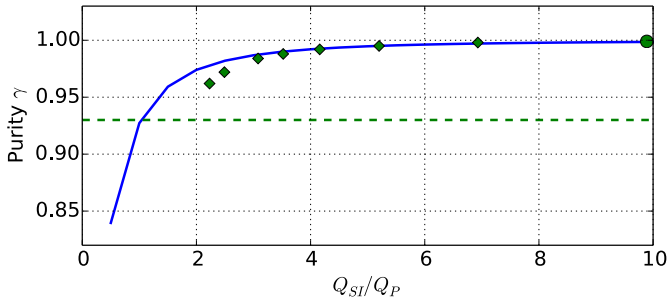

Figure 4.6: Maximum heralded state purity γ as a function of the Q_{SI}/Q_P ratio, as previously reported in Fig. 4.2. The green dots represent the result of the full numerical calculation, while the last circular marker corresponding to the JSD depicted in Fig. 4.9(b).

There is clearly a good agreement between the approximate model and the full numerical calculation, particularly for high purity photon pairs. When smaller Q_{SI}/Q_P ratios are considered, the theoretical model and the numerical calculations show a slightly poorer agreement. This issue could have multiple origins, but among the other we should point out that

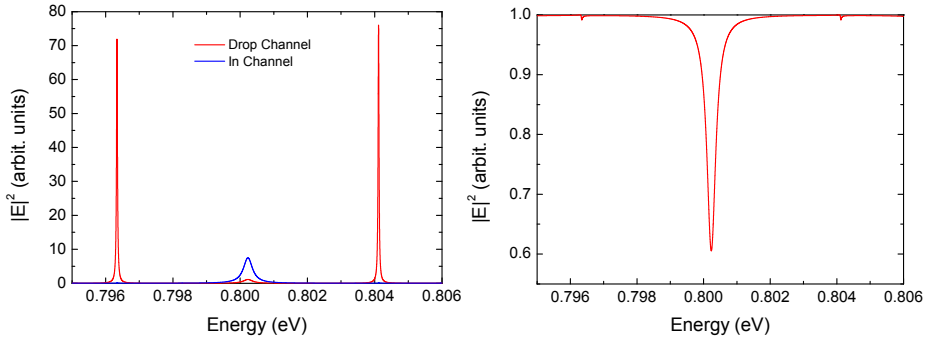

Figure 4.7: (a) Field intensity spectrum calculated in segment C of the dual MZI microring (see Fig. 4.1), when light is coupled from the In or the $Drop$ channel. The pump resonance — around 0.8 eV — is well coupled to the bottom MZI (blue line), and poorly coupled to the upper waveguide (red line). At the same time, the signal and idler resonances are strongly coupled to the upper MZI (red line), while vanishingly coupled to the bottom MZI (blue line). (b) Transmission spectrum as observed from channel $Through$ when light is coupled to the In channel, showing the poor coupling of signal/idler modes to the bottom bus waveguide.

1. The generation of photon pairs occurs in the arms of the MZI couplers as well as in the ring resonator. Hence, since the FE in the MZI arms is typically much smaller than that in the ring, we expect a "waveguide-like" contribution to the BWF, impacting the state purity. This effect naturally decreases when the ratio Q_{SI}/Q_P increases, for the "ring-like" contribution takes the lead.

2. The spectral profile of the ring resonances is not, in general, Lorentzian: this feature can be appreciated, for instance, by inspecting Eq. (4.11)-(4.14).

3. The position of the structure resonances is slightly offset with respect to those of a simple side-coupled microring. This deviation depends on ΔL_{31} and ΔL_{41}, and it can be ascribed to the interaction of multiple resonant "subsections" of the structure.

Finally, we can focus on the last point reported in Fig. 4.5 to analyze the transmission spectra and compare the shape of the resulting BWF with that of the previous Chapter. The ring we considered in the simulation has a radius $R = 20$ μm, identical coupling points with $\sigma = 0.95$, and $L_1 = 1$ μm, $L_3 = \pi R - L_1$ and $L_4 = 1.228$ μm. The resulting FE in the ring (segment C) and the transmission spectrum are reported in Fig. 4.7(a-b).

The linewidth of the pump resonance, when light is coupled from the In channel, is much broader than that of the signal and idler resonances, light being coupled from the $Drop$ channel. At the same time, the pump is poorly coupled

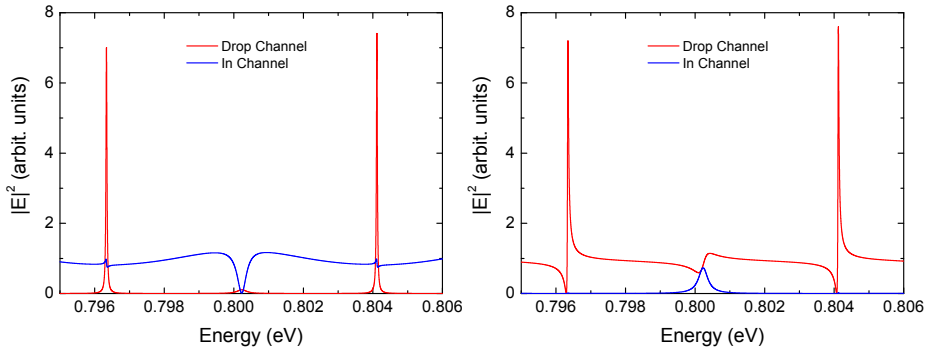

Figure 4.8: (a) Field intensity calculated in segment I of the dual MZI microring (see Fig. 4.1), when light is coupled from the In or the $Drop$ channel. By comparison to Fig. 4.7 we notice the considerably smaller FE at the signal/idler resonances, and the nearly absent pump resonance. (b) Field intensity calculated in segment N of the dual MZI microring (see Fig. 4.1), when light is coupled from the In or the $Drop$ channel. Here, the pump FE is an order of magnitude smaller than inside the ring (see Fig. 4.7), and both the signal and idler resonances display a sharp response which vanishes at the center.

to the upper bus waveguide, and we observe a vanishing coupling of the signal and idler resonances to the bottom bus waveguide. In Fig. 4.8 we also report the field intensity in the upper (a) and lower (b) external arms of the MZI microring resonator, corresponding to sections I and N of Fig. 4.1, respectively. Here, either the pump or the signal/idler resonances vanish at their central position, leading to a negligible contribution to the BWF (4.29).

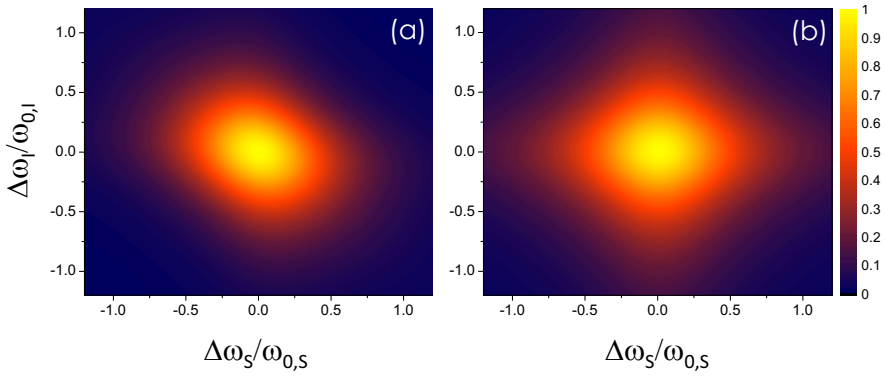

Figure 4.9: JSD of photon pairs generated in (a) a standard side-couple microring resonator, and (b) the dual MZI microring resonator of Fig. 4.1.

When a temporally short pump pulse (spectrally wider than the pump mode

resonance) is injected in the In channel, signal and idler photons generated by SFWM can be observed in the $Drop$ channel. Their JSD is reported in Fig 4.9(b), together with that of the nearly uncorrelated photon pairs, in Fig. 4.9(a), obtained when the ring is side-coupled to a single bus waveguide (similarly to what we have already discussed in Section 3). Once more, we stress that these results are obtained by a numerical computation starting from the BWF (4.29), with no a priori assumption on the shape of the resonances involved and a progressively refined frequency discretization till the simulation convergence.

As it is clear from Fig. 4.9(b), there is are no residual quantum correlations between the generated photons, and the pair can be considered as truly unentangled.

Beyond photon pair generation

In the previous chapters we have been focusing our attention on the generation of two particles, specifically photons, which can be spectrally entangled or completely unentangled. As we recalled , the quantum correlations displayed by a system composed of two parties, or *bipartite entangled state*, are well known and understood both theoretically [19, 141, 147] and experimentally [148, 149]. More recently, entangled states of composite systems involving more than two subsystems, or *multipartite entangled states*, were investigated [150, 151, 141, 152].

In general, the correlations they exhibit cannot be considered a trivial generalization of bipartite entanglement. It should be noticed that in this context it is customary to refer to generic "parties" rather than specifying the physical implementation: any subsystem can qualify as a party and, in any case, all the analysis and the conclusions do not hinge on a specific realization. Multipartite entangled states have been realized using a multitude of different physical systems such as photons [52, 150, 51, 50, 153], trapped ions [154], superconducting circuits [155, 156], and electronic spins [157].

Let us consider the simplest case of multipartite entanglement, namely a quantum state composed of three subsystems, or *tripartite entangled state*. It was demonstrated by Dür et al. [49] that pure tripartite states can be grouped into four inequivalent classes, as schematically represented in Fig. (4.10):

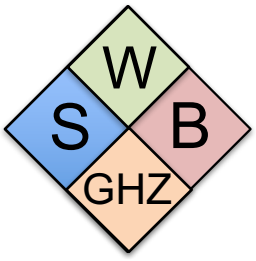

Figure 4.10: Schematic classification of tripartite entangled states.

1. **S**: Separable states, which are expressed as a convex sum of projectors on product vectors, e.g. $|\psi\rangle = |0\rangle \otimes |1\rangle \otimes |0\rangle$;
2. **B**: Biseparable states, which are expressed as a convex sum of projectors on product and bipartite entangled states, e.g. $|\psi\rangle = |0\rangle \otimes \frac{1}{\sqrt{2}}(|01\rangle + |10\rangle)$;

3. **GHZ**: Greenberger-Horne-Zeilinger states;

4. **W** states.

While the fully separable and biseparable states involve at least one tensor product of Hilbert spaces, the GHZ and W states are true tripartite entangled states, with entanglement shared between all the parties simultaneously. Moreover, GHZ and W states constitute inequivalent classes, which cannot be converted into each other using stochastic local operations and classical communication [49, 53, 150, 141, 152]. Both types of states display interesting features from the point of view of fundamental research and potential applications in quantum tasks.

In the following Chapters we will elaborate more on the properties of W and GHZ states, briefly recalling the state-of-the-art techniques and performances in their production. Most notably, in each section we will propose a novel approach for the generation of the correspondent tripartite state, based on the use of unconventional degrees of freedom [158, 54]. Please note that the schemes we provide can be fit either into a bulk optics experiment or in an integrated solution. However, considering the scope of this thesis, we will present the generation of W and GHZ states in integrated platforms.

Chapter 5

Generation of energy-entangled W states

The W states are a relatively recent research subject, at least compared to the well-established research area on GHZ states. Yet, they have proven as promising candidates for a large number of tasks, particularly in the field of quantum communications. The paradigmatic form of a W state is [49]

$$|W\rangle = \frac{1}{\sqrt{3}}\big(\,|001\rangle + |010\rangle + |100\rangle\,\big), \tag{5.1}$$

where $|0\rangle$ and $|1\rangle$ indicate orthogonal states of a qubit. Typically they refer to either "vacuum" and "occupation", or "ground state" and "excited state". In the former instance, (5.1) would involve only one particle. However, many protocols involving W states require the presence of three actual particles, such as ions or photons. This is a necessary condition, for instance, in tests of non-locality and to exploit the robustness of W states in quantum communications. The density matrix associated with the state is reported in Fig. (5.1).

One of the recurrent techniques for the generation of W states involves cooled atoms in a Paul trap [154]. Here, the qubit is represented by the excitation state of an atom. The main benefit of this platform is arguably the possibility to control each atom individually and with great accuracy by using focused narrow-band laser pulses, even allowing for the realization of controlled gates. On the other hand, these systems typically require delicate experimental conditions, working in high vacuum and very low temperatures. The other common technique for the generation of W states is using photon pairs obtained by parametric fluorescence in nonlinear media [52, 50, 51, 153]. Having in mind the use of W states for quantum communication protocols, the advantage of photons in this respect is evident. Since in this Chapter we are concerned with the generation of W states using photons, in the following paragraphs we will always assume to deal with such systems.

W states have attracted particular interest in the field of quantum communications, and they have shown to be promising candidates for the implementation of a range of protocols for multipartite Quantum Key Distribution (QKD), with secret keys shared safely among three parties [159]; dense coding, where the capacity of a transmission channel is increased by using quantum states of light [160]; teleportation [161]. One of the main reasons why W states are appealing for quantum communications is that they are more robust with respect to losses than GHZ states [52]. Indeed, when one of the photon is lost (for example, due to absorption or scattering in the communication link), the remaining photon pair still retains entanglement. This is evident when we partial trace the density matrix of a W state over one of the qubits (A)

$$\begin{aligned} Tr_A[\rho_W] &= \langle 0|\,\rho_W\,|0\rangle + \langle 1|\,\rho_W\,|1\rangle \\ &= \frac{1}{3}(|00\rangle\langle 00| + |01\rangle\langle 01| + |01\rangle\langle 10| + |10\rangle\langle 01| + |10\rangle\langle 10|), \end{aligned} \tag{5.2}$$

which is an entangled state.

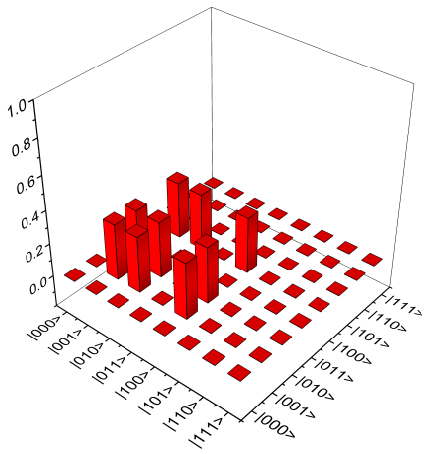

Figure 5.1: Real part of the density matrix associated with the standard form (5.1) of the W state.

When the physical carrier of a qubit is a photon, the quantum information can be encoded in different degrees of freedom, such as the photon polarization, the frequency, or the spatial mode distribution. At present, W states of photons have been generated solely exploiting the photon polarization [50, 51, 52]. This is probably due to the fact that (i) the polarization is a very natural choice for qubit encoding, (ii) bulk sources of polarization entangled photons, such as β-Barium-Borate (BBO) crystals are widely available in laboratories, and (iii) the management of polarization in free space is simple and reliable, and one can easily perform an arbitrary rotation of the qubit on the Bloch sphere. When polarization-encoding is considered, the W state might take the form

$$|W\rangle = \frac{1}{\sqrt{3}}\big(\,|HHV\rangle + |HVH\rangle + |VHH\rangle\,\big), \tag{5.3}$$

where H and V indicate horizontal and vertical polarization, respectively.

The experimental preparation of such states usually requires the simultaneous generation of two photon pairs by means of type-II spontaneous parametric down-conversion (SPDC) in a bulk nonlinear crystal [50, 51]. The photons then propagate in free space or in optical fibers, and one can perform operations on them by using optical elements such as beam splitters, polarization beam splitters, and wave-plates. A typical implementation, from Eibl et al. [50, 51], of a scheme for the generation of polarization-entangled W states is reported in Fig. (5.3).

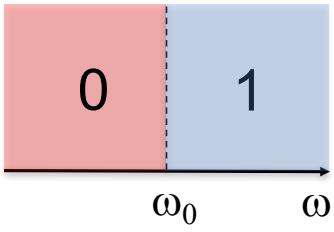

Figure 5.2: Schematic representation of the frequency-encoding adopted in Eq. (5.4) and (5.5).

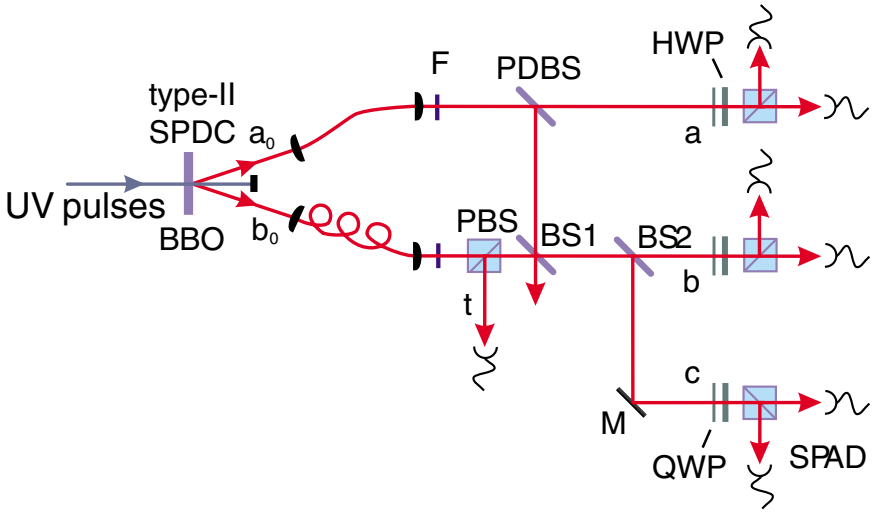

Figure 5.3: Example of an optical scheme for the generation of polarization-encoded W states [51]. Double photon pairs are generated by SPDC in the BBO crystal, and propagate in a bulk linear optical circuit composed of Polarization Beam Splitters (PBS), Polarization Dependent Beam Splitters (PDBS), and Beam Splitters (BS). When a target photon is detected by a Single Photon Avalanche Detector (SPAD) in channel t, one can observe the generation of a W state exiting from the other three channels a, b, and c. Finally, a proper quantum state tomography can be achieved by placing Half-Wave Plates (HWP) and Quarter-Wave Plates (QWP) after each output channel.

Yet the use of polarization can be problematic for long distance communication using optical fibers, where polarization can drift during propagation, and for the development of integrated quantum devices, where sophisticated solutions are required to control light polarization on a chip [68]. Thus, it is worth investigating the use of other degrees of freedom for the photonic implementations of W states.

We propose a strategy to generate W states that relies on energy-entanglement rather than polarization entanglement [158]. Our scheme can be implemented in an integrated optics platform, and thus has the advantages of scalability and efficiency [162, 163]. The source we propose is capable of preparing a W state either of the form

$$\frac{1}{\sqrt{3}}(|BBR\rangle + |BRB\rangle + |RBB\rangle) \tag{5.4}$$

or

$$\frac{1}{\sqrt{3}}(|RRB\rangle + |RBR\rangle + |BRR\rangle), \tag{5.5}$$

where $|B\rangle$ and $|R\rangle$ are photons that are blue and red detuned with respect to the pump (see Fig. 5.2).

Before presenting the specific structure we have in mind, it is worth to compare the bulk optical elements used to manipulate polarization-entangled states with the integrated optical elements used to manipulate energy-entangled states. This allows us to establish a correspondence, when possible, which is particularly useful in translating a polarization- to an energy-entanglement scheme for the generation of W states. This correspondence is shown in Fig. 5.4.

The sources commonly considered for the preparation of polarization-entangled photon pairs in bulk devices are nonlinear crystals such as BBO, in which type-II SPDC is used to generate the photons; instead a source for the preparation of energy-entangled photon pairs in an integrated structure is a silicon micro-ring resonator, in which spontaneous four-wave mixing (SFWM) is used to generate the photons [163]. Depending on their polarization, photons generated in a bulk crystal can be spatially separated using a polarization beam splitter (PBS); instead, photons generated in a micro-ring resonator can be spatially separated depending on their energy using a tunable add-drop filter [164]. Finally, the beam splitters commonly employed for photons generated in bulk optics can be replaced by directional couplers for photons generated in integrated structures [164].

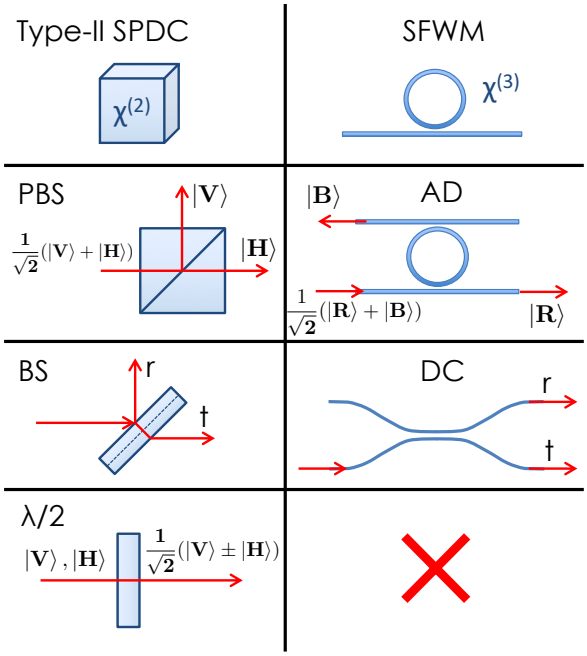

Figure 5.4: Analogies between optical elements employed in bulk optics for schemes involving polarization-entangled states (on the left) and the corresponding integrated optical elements for the scheme introduced here involving energy-entangled states (on the right). Note the absence of an analogue for the $\lambda/2$ waveplate.

However, not all of the elements in polarization-entanglement optics find a straightforward analog in energy-entanglement integrated optics. For example, in the work by Bouwmeester et al. [150] on the preparation of polarization-entangled GHZ states, a $\lambda/2$ plate is used to rotate the polarization. This element cannot be replaced with a linear component in an integrated optical scheme such as that proposed here, for it would require a change in the photon energy. Although this feature seems detrimental to the design of a source of energy-entangled photons, performing such operations is not strictly required to produce a W state. Moreover, we show in the following that this is not a necessary condition even to obtain a full reconstruction of the density matrix of the state.

5.1 Theoretical Proposal

Let us consider the scheme sketched in Fig. 5.5. It is composed of a silicon micro-ring resonator acting as the source (S) for the generation of photon pairs, two add-drop filters (AD_1 and AD_2) for the extraction of specific spectral components, and three cascaded directional couplers (referred to as DC_1, DC_2, and

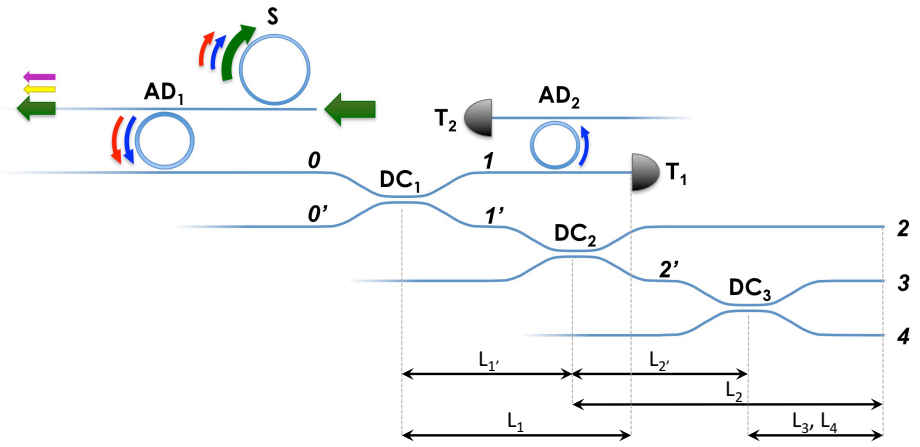

Figure 5.5: Scheme for generating energy-entangled W states. S) Micro-ring resonator for the production of photons pairs by SFWM. AD_1) Add-drop filter extracting only the red and blue photons. AD_2) Add-drop filter routing the red and blue photons to different target detectors. The DC_is are directional couplers, characterized by real-valued transmission and reflection coefficients t_i and r_i, respectively.

DC_3).

An intense pump pulse is injected into the silicon micro-ring resonator S, with the center frequency of the pulse chosen to equal that of one of the resonances of the micro-ring. As we discussed in details in Chapter 3, the small volume of the cavity and the build-up of the field due to constructive interference in the ring dramatically enhance the nonlinear response of the resonator [103]. We can safely assume that the pair generation takes place in the ring resonator alone, for it is the only resonant structure the pump photons will enter. As ubiquitous in this thesis, we assume that the generation rate is low and the undepleted pump approximation is assumed, so that the state produced by SFWM is in the usual form

$$|\psi\rangle = \left(1 - \mathcal{O}(|\beta|^2)\right)|\text{vac}\rangle + \beta C_{II}^{\dagger}|\text{vac}\rangle + \frac{1}{2}[\beta C_{II}^{\dagger}]^2|\text{vac}\rangle + \dots \tag{5.6}$$

Here have truncated the expansion (5.6) at the second order, which corresponds to the creation of two photon pairs, and we have assumed negligible time-ordering corrections [165]. We can recast the state (5.6) as

$$|\psi\rangle = \left(1 - \mathcal{O}(|\beta|^2)\right)|\text{vac}\rangle + \beta|\text{II}\rangle + \frac{\sqrt{6}}{2}\beta^2|\text{IV}\rangle + \dots \tag{5.7}$$

where the state $|\psi\rangle$, the photon pair state

$$|II\rangle = C_{II}^{\dagger}\,|vac\rangle = \frac{1}{\sqrt{2}}\int dk_1 dk_2\ \phi(k_1,k_2) b_{k_1}^{\dagger} b_{k_2}^{\dagger}\,|vac\rangle\,, \tag{5.8}$$

and the four-photon state

$$\begin{aligned} |IV\rangle &= \frac{1}{\sqrt{6}}(C_{II}^{\dagger})^2\,|vac\rangle \\ &= \frac{1}{2\sqrt{6}}\int dk_1 dk_2 dk_3 dk_4\ \phi(k_1,k_2)\phi(k_3,k_4) b_{k_1}^{\dagger} b_{k_2}^{\dagger} b_{k_3}^{\dagger} b_{k_4}^{\dagger}\,|vac\rangle \end{aligned} \tag{5.9}$$

are all normalized (see Appendix A.1).

In order to generate a W state we consider only the creation of two photon pairs; the probability of this event is $|\frac{\sqrt{6}}{2}\beta^2|^2$. In particular, here we consider SFWM in a ring resonator when one of the generated photons in each pair is centered at a resonant frequency below that of the pump, and one at a resonant frequency above. While pairs of photons can be generated at many different resonant frequencies, as long as the energy is conserved and the phase matching condition is satisfied, we focus on energy-entangled W states in which photons are generated via two particular resonances, that we will assume as our $|R\rangle$ and $|B\rangle$ photons. Therefore, here we are adopting the energy-encoding for qubits we have previously discussed in Section 1.1. We also imagine discarding every other photon that could enter the rest of the circuit.

To do this, one could simply place notch filters in front of each detector, but in the spirit of integration we consider using another ring resonator in the configuration of an add-drop filter (AD_2). The radius of this ring is chosen to guarantee the resonant condition only for red and blue photons; we can obtain this result by choosing a radius that is incommensurable with that of the ring S. Ideally, this solution should also remove the pump photons, but in practice an additional filtering stage may be necessary [166].

The photon pairs produced by SFWM in the microring resonator are generally correlated in energy, as we discussed in details in Chapter 3, and the Schmidt Number depends on the ring geometry, the coupling between the ring and the waveguide, the pump pulse shape and duration. These parameters can be tailored to generate a variety of states, ranging from strongly correlated to nearly uncorrelated photon pairs. For the generation of W states, we are not interested in the energy correlations within a single photon pair, but on the entanglement resulting from the manipulation of two identical photon pairs. To this goal, we can imagine to pump the ring S with very short pulses, or to adopt the coupling scheme we presented in Chapter 4. Under this conditions, the expression for the state produced by the nonlinear interaction in the microring becomes

$$|\psi\rangle = \frac{\sqrt{6}}{2}\beta^2 (b_{B,0}^{\dagger} b_{R,0}^{\dagger})^2\,|\mathrm{vac}\rangle\,, \tag{5.10}$$

where $a_{R,0}^{\dagger}$ and $a_{B,0}^{\dagger}$ are the creation operators for the red and blue photons, respectively, in channel 0.

Once this state is identified, we can calculate the output state following the linear propagation of the fields inside the structure by exploiting the asymptotic field approach discussed in Section 1.3. When the path between the ring and the detector is stabilized with the appropriate relative phase factors, we find the output state is (see Appendix A.2)

$$\begin{aligned} |\psi\rangle &= \eta\,|\Phi\rangle + 6\sqrt{2}ir_1t_1^3r_2t_2^2r_3t_3\beta^2e^{2iL_0(k_R+k_B)} \\ &\times \quad [e^{i\Gamma_1}b^\dagger_{R,1}\,|W_{T_1}\rangle + e^{i\Gamma_2}b^\dagger_{B,1}\,|W_{T_2}\rangle] \end{aligned} \tag{5.11}$$

where

$$\begin{aligned} &|W_{T_1}\rangle = \\ &= \frac{1}{\sqrt{3}}(b^\dagger_{B,2}b^\dagger_{B,3}b^\dagger_{R,4} + e^{-i\Delta k\Delta L_{34}}b^\dagger_{B,2}b^\dagger_{R,3}b^\dagger_{B,4} + e^{-i\Delta k\Delta L_{22'4}}b^\dagger_{R,2}b^\dagger_{B,3}b^\dagger_{B,4})\,|vac\rangle \\ &\equiv \frac{1}{\sqrt{3}}(|BBR\rangle + e^{-i\Delta k\Delta L_{34}}\,|BRB\rangle + e^{-i\Delta k\Delta L_{22'4}}\,|RBB\rangle) \end{aligned} \tag{5.12}$$

and

$$\begin{aligned} &|W_{T_2}\rangle = \\ &= \frac{1}{\sqrt{3}}(b^\dagger_{R,2}b^\dagger_{R,3}b^\dagger_{B,4} + e^{i\Delta k\Delta L_{34}}b^\dagger_{R,2}b^\dagger_{B,3}b^\dagger_{R,4} + e^{i\Delta k\Delta L_{22'4}}b^\dagger_{B,2}b^\dagger_{R,3}b^\dagger_{R,4})\,|vac\rangle \\ &\equiv \frac{1}{\sqrt{3}}(|RRB\rangle + e^{i\Delta k\Delta L_{34}}\,|RBR\rangle + e^{i\Delta k\Delta L_{22'4}}\,|BRR\rangle) \end{aligned} \tag{5.13}$$

are two normalized W states. In (5.11), the state vector $|\Phi\rangle$, occurring with probability $|\eta|^2$, includes all the terms that do not involve a single photon in each of the four output channels, r_i and t_i are real reflection and transmission coefficients of the directional coupler DC_i, satisfying $r_i^2 + t_i^2 = 1$, $b^\dagger_{R,i}$ and $b^\dagger_{B,i}$ are the photon creation operators in the output channel i, and

$$\begin{aligned} \Delta k &= k_B - k_R \\ \Delta L_{34} &= L_3 - L_4 \\ \Delta L_{22'4} &= L_2 - L_{2'} - L_4 \\ \Gamma_1 &= k_R(L_1 + L_{1'} + L_{2'} + L_4) + k_B(2L_{1'} + L_2 + L_{2'} + L_3), \\ \Gamma_2 &= k_R(2L_{1'} + L_2 + L_{2'} + L_3) + k_B(L_1 + L_{1'} + L_{2'} + L_4), \end{aligned} \tag{5.14}$$

L_i being the length of the i-th channel (see Fig. 5.5). The state obtained in (2,3,4) can be $|W_{T_1}\rangle$ or $|W_{T_2}\rangle$, depending on the energy of the photon in channel 1.

To discriminate between $|W_{T_1}\rangle$ and $|W_{T2}\rangle$, we introduce an add-drop filter (AD_2) that routes red and blue photons to different target detectors T_1 and T_2. The radius of the micro-ring resonator in the add-drop filter configuration is chosen to guarantee a resonance for the blue photons, and high transmission

probability for the red photons. In the present scheme we set the AD_2 microring radius to be 1/4 that of the radius of the S microring, so that the energy of a red photon is found in the middle of the free spectral range of the AD_2 ring. Both detection events occur with identical probability $|2\sqrt{3}\beta^2 r_1 t_1^3 r_2 t_2^2 r_3 t_3|^2$. The maximum is found for $r_1 = \frac{1}{2}$, $r_2 = \frac{1}{\sqrt{3}}$, and $r_3 = \frac{1}{\sqrt{2}}$, corresponding to a W state generation probability of $|\frac{3\sqrt{2}}{8}\beta^2|^2$.

It is worth to stress that the detection of a photon either in T_1 or in T_2 may arise from the generation of a single pair, and even when two photon pairs are generated, only a fraction of the detection events (those in which four detectors click) will correspond to a W state. Thus in our scheme the generation of W states relies on a post-selection, and there is no heralding. It should be noticed that this is not a limitation in a number of applications, for instance multipartite quantum key distribution, in which heralding is not requested.

Comparing the output state (5.12) to the expected state (5.4), one can notice the presence of two additional phases associated with the terms $|BRB\rangle$ and $|RBB\rangle$. For a reliable generation of energy-entangled W states it is crucial that these phases do not fluctuate significantly over time, and thus we must guarantee that

$$\begin{aligned} \Delta k \Delta L_{34} &\ll 2\pi, \\ \Delta k \Delta L_{22'4} &\ll 2\pi. \end{aligned} \tag{5.15}$$

To grasp the physical meaning and understand the experimental constraints entailed by (5.15), we can split Δk in its contributions

$$\begin{aligned} \Delta k &= \bar{k}_B - \bar{k}_R + \delta k_B - \delta k_R \\ &\equiv \Delta\bar{k} + \epsilon, \end{aligned} \tag{5.16}$$

where $\bar{k}_B$ and $\bar{k}_R$ are the central wave vectors or the blue and red photons (center of the corresponding resonances in the ring S), and ϵ is the "fluctuation" of the wave vector around its mean value, as dictated by the BWF. At this point, we can determine two main constraints on the generation of pure W states:

1. a *Coherence* constraint

$$\begin{aligned} \Delta L_{34} &\ll \frac{2\pi}{\epsilon}, \\ \Delta L_{22'4} &\ll \frac{2\pi}{\epsilon}, \end{aligned} \tag{5.17}$$

   which is a common requirement for any MZI operating at a fixed frequency,

2. a *Stability* constraint

$$\begin{aligned} n\Delta L_{34} &\ll \frac{2\pi}{\Delta\bar{k}}, \\ n\Delta L_{22'4} &\ll \frac{2\pi}{\Delta\bar{k}}, \end{aligned} \tag{5.18}$$

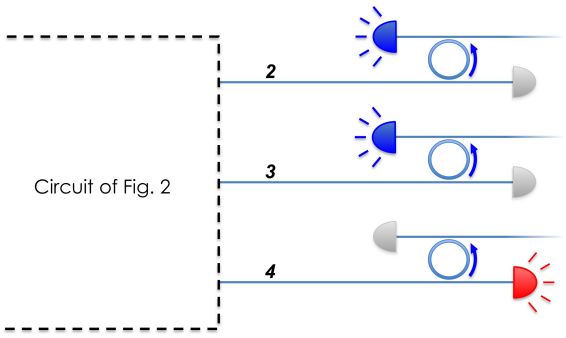

Figure 5.6: Schematic representation of the detection setup. Here, as an example, we sketch a threefold coincidence measurement revealing the $|BBR\rangle$ state in the output channels. All these measurements are subject to the simultaneous detection of a red photon by T_1 (see Fig. 5.5). Note that not all of the detectors represented are actually required: the density matrix of the state can be fully reconstructed using four detectors.

which is related to the phase delay between blue and red photons propagating with different phase velocities in the waveguides.

It should be noted that the stability constraint is much more stringent than the coherence constraint. Indeed, ϵ is naturally smaller than $\Delta\bar{k}$ and it can be furthermore reduced, for example by filtering the generated photon pairs, albeit reducing the luminosity of the source. On the contrary, $\Delta\bar{k}$ is determined by the FSR of the ring which it is typically much larger than the resonance FWHM (consider, for instance, high finesse resonators) and it is fixed with the source geometry. Nonetheless, with current bulk and integrated sources of entangled photon pairs the stability of the length difference should be limited to a few hundreds of nanometers, which is experimentally viable.

To demonstrate the generation of a W state, we can perform a series of measurements in the output channels 2, 3, and 4. Let us focus, for instance, on the demonstration of the W_{T_1} state in (5.12). We consider the post-selection of the event characterized by the simultaneous detection of a red photon in channel 1, and one photon in each channel 2, 3, and 4.

Since we need to evaluate the energy of the photons in the output channels, we can employ three add-drop filters identical to AD_2, one for each channel, as sketched in Fig. 5.6. Their role is to route the incoming photons on the basis of their energy to different frequency-independent detectors. Generally, the strategy to prove the generation of a particular quantum state is dual: either by means of a witness operator, or performing a full tomography of the state. The first solution only guarantees the creation of a quantum state belonging to the desired class without accessing all the details of its associated density matrix, a deeper insight provided by the second approach. While it is always

possible to construct a witness operator for the W state [167], here we want to propose a strategy for performing the full tomography of an energy-entangled tripartite state. We choose this approach because, to the best of our knowledge, it was never reported in literature and, most notably, because the strategy we propose does not require any nonlinear element. This can in fact be somewhat counterintuitive, for the ability to perform a full tomography hinges on the possibility to rotate a qubit on the Bloch sphere, and in our case this would imply a series of frequency conversions at the single photon level, which are in principle possible, are extremely demanding. Yet, the strategy we propose (discussed in details in Appendix A.3) takes advantage of the path degree of freedom to avoid the need for any nonlinear operation.

Very recently, Xin et al. [168] showed that it is possible to reconstruct the full density matrix of almost any tripartite state (including W states) by measuring its reduced density matrices. The first step toward proving the preparation of the W state (5.12) is to ensure that the states $|BBR\rangle$, $|BRB\rangle$, and $|RBB\rangle$ occur with the same $\frac{1}{3}$ probability. This can be proved by counting the coincidences in the three detectors in 2, 3, and 4. In the following we will assume that this condition has been verified. As pointed out by Acín et al. [169] and more recently by Eibl et al. [51], this is not enough to confirm the generation of a W state. Indeed, a variety of mixed states lead to the same statistics in the coincidence count, such as the incoherent mixture $\rho_S = \frac{1}{3}\{|BBR\rangle\langle BBR| + |BRB\rangle\langle BRB| + |RBB\rangle\langle RBB|\}$ and a mixture of biseparable states $\rho_B = \frac{1}{3}\{\rho_2 \otimes \rho_{34} + \rho_3 \otimes \rho_{24} + \rho_4 \otimes \rho_{23}\}$ where, for example, ρ_2 corresponds to a blue photon in channel 2, and ρ_{34} represents a Bell state in channels 3 and 4.

Whenever $|RRB\rangle$, $|RBR\rangle$, and $|BRR\rangle$ occur with equal probability, the density matrix describing a system composed of two blue photons and one red photon distributed in channels 2, 3, and 4 is

$$\rho_{234} = \begin{array}{c} \\ |BBR\rangle \\ |BRB\rangle \\ |RBB\rangle \end{array} \begin{array}{c} \begin{array}{ccc} \langle BBR| & \langle BRB| & \langle RBB| \end{array} \\ \begin{pmatrix} \frac{1}{3} & a & b \\ a^* & \frac{1}{3} & c \\ b^* & c^* & \frac{1}{3} \end{pmatrix} \end{array} \tag{5.19}$$

where we have specified the diagonal elements, and a, b, and c are complex numbers to be determined. To this end, we can evaluate the state of the photon pair in channels 3 and 4, subject to the detection of a blue photon in channel 2. Given the detection of a blue photon in channel 2, the density matrix associated with the photon pair in channels 3 and 4 is

$$\rho_{34} = \begin{array}{c} \\ |BR\rangle \\ |RB\rangle \end{array} \begin{array}{c} \begin{array}{cc} \langle BR| & \langle RB| \end{array} \\ \begin{pmatrix} \frac{1}{2} & \frac{3}{2}a \\ \frac{3}{2}a^* & \frac{1}{2} \end{pmatrix} \end{array}. \tag{5.20}$$

Of course, the general density matrix for two photons, each either red or blue, and one in each of two channels, is a 4×4 matrix. In our particular case, since the process creating the photons satisfies energy conservation, we expect only one blue and one red photon. Hence that larger 4×4 matrix must be of the form

$$\rho_{pair} = \begin{array}{c} \\ |BB\rangle \\ |BR\rangle \\ |RB\rangle \\ |RR\rangle \end{array} \begin{array}{c} \begin{array}{cccc} \langle BB| & \langle BR| & \langle RB| & \langle RR| \end{array} \\ \begin{pmatrix} 0 & 0 & 0 & 0 \\ 0 & \frac{1}{2} & \frac{3}{2}a & 0 \\ 0 & \frac{3}{2}a^* & \frac{1}{2} & 0 \\ 0 & 0 & 0 & 0 \end{pmatrix} \end{array}. \tag{5.21}$$

The energy correlation of the two photons responsible for the simple form of ρ_{pair} allows for the determination of a by performing tomography on the photon pairs in channels 3 and 4, as we report in details in the next Section. A similar approach was previously adopted by Ramelow et al. [71]. It should be noted that these schemes entail just simple interferometric measurements between the two modes, and no frequency conversion.

We can apply the same reasoning to the tomography on channels 2 and 4 subject to the detection of a blue photon in channel 3, which would lead to the determination of the complex coefficient b; and to the tomography on channels 2 and 3 subject to the detection of a blue photon in channel 4, which would lead to the determination of the complex coefficient c. This procedure allows us to reconstruct the density matrix (5.19) of the three-photon state, and prove the generation of a W_{T_1} state. The protocol to prove the generation of a W_{T_2} state is analogous.

In conclusion, we have proposed a design for a device capable of generating energy-entangled W states, relying on SFWM in a microring resonator and the linear propagation of light in an integrated optical circuit. All of the elements involved in the integrated structure we propose are feasible with current technology and have already been characterized individually. We have compared them with the elements used for the generation of polarization-entangled states using bulk optics, for establishing a simple scheme to translate polarization-encoded qubits to energy-encoded qubits. Finally, we have presented a feasible protocol to confirm that a W state is indeed generated when the two pairs of photons are initially produced.

In the following, we will discuss in further details the strategy we embrace for obtaining the full tomography of the quantum state generated by our optical circuit. To do so, we propose a simple bulk optics experimental setup we developed in a collaboration with the University of Illonois at Urbana-Champaign, where the experimental demonstration of out theoretical proposal is ongoing.

5.2 Towards a practical implementation

In the previous Section we have proposed a feasible protocol to obtain a full tomography of the energy-entangled W states generated by the circuit of Fig. 5.5. This is based on the reduced density matrix approach [168], which helps in reducing the dimension of the density matrix to be reconstructed. Yet, it is still required to work out a strategy for deriving the 2×2 reduced density matrix of an energy-encoded photon pair (Eq. (5.20), for instance). To this end, in the following we present a bulk optics setup equivalent to the integrated

circuit introduced above for the generation of energy-entangled W states; on that platform we propose a feasible strategy for the reconstruction of the 2×2 reduced density matrices, and the corresponding experimental setup and procedures for its completion.

It is worth to point out that, in this context, the implementation of our circuit in a bulk optics setup can bring a strategic advantage concerning the output state characterization. As we will discuss in the following, the tomographic procedure involves a large number of measurements in different experimental configurations; the reconfiguration of an integrated circuit from one setup to the other would involve a large number of heaters and tunable AD filters, likely resulting in a complex and unreliable procedure. The same tasks are typically less demanding in a bulk optics experiment, where optical elements can be included, removed and tuned manually. Nonetheless, when the W state source alone is required, the integrated approach would still be preferable, for less tuning will be necessary, and it can benefit from higher efficiency and stability.

Let us focus on the reconstruction of the reduced density matrix ρ_{34}, for which we introduce the experimental setup sketched in Fig. 5.7. We imagine to inject a short an intense pump pulse in a birefringent optical fiber, where energy-entangled photon pairs are generated by SFWM [40]. The residual pump and the converted photons propagate in free space to a series of three cascaded achromatic beam splitters, characterized by 25 : 75, 33 : 66, and 50 : 50 split ratio, respectively. The photons exiting from channel 1 of Fig. 5.7 reach a filter letting only blue photons to arrive at a frequency-independent detector. As for our integrated circuit, when such event occurs and we post-select on four-fold coincidences, we expect an energy-entangled W state to exit the source from channels 2, 3, and 4.

Following the reduced density matrix approach, the reconstruction of ρ_{34} requires post-selecting on a red photon detection in channel 2, too; thus, a red filter and another detector will be involved (see Fig. 5.8). Now we can finally analyze the properties of the photons exiting from channels 3 and 4. As already pointed out in Eq. (5.21), the generic density matrix for a system of two bicolored photons is 4×4. Although we will be interested only in the central submatrix thanks to post-selection, we nonetheless need to begin our discussion from the generic reduced density matrix

$$\rho_{34} = \begin{bmatrix} a_{11} & a_{12} & a_{13} & a_{14} \\ a_{12}^* & a_{22} & a_{23} & a_{24} \\ a_{13}^* & a_{23}^* & a_{33} & a_{34} \\ a_{14}^* & a_{24}^* & a_{34}^* & a_{44} \end{bmatrix}, \tag{5.22}$$

which should be Hermitian. To obtain a full tomography one has to determine 15 free parameters, since the unit trace condition must be observed.

The tomography procedure on ρ_{34} we propose involves a series of unitary operations on the photon pair, followed by detection and coincidence counts. We imagine that the structure responsible for the manipulation of the state is described, for the moment, by a generic frequency-dependent scattering matrix, as in Fig. 5.8, with

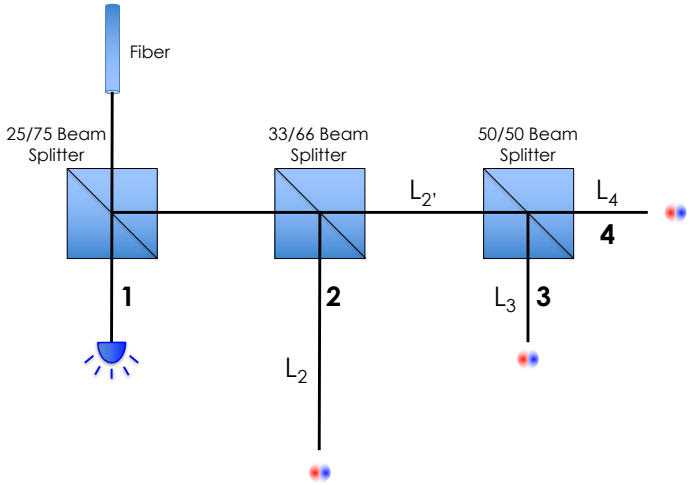

Figure 5.7: Sketch of a bulk optics experimental setup equivalent to the integrated circuit presented in Fig. 5.5.

$$S(\omega) = \begin{bmatrix} S_{11}(\omega) & S_{12}(\omega) \\ S_{21}(\omega) & S_{22}(\omega) \end{bmatrix} \tag{5.23}$$

so that

$$\begin{bmatrix} |R_5\rangle \\ |R_6\rangle \end{bmatrix} = S(R) \cdot \begin{bmatrix} |R_3\rangle \\ |R_4\rangle \end{bmatrix} \tag{5.24}$$

or

$$\begin{bmatrix} |B_5\rangle \\ |B_6\rangle \end{bmatrix} = S(B) \cdot \begin{bmatrix} |B_3\rangle \\ |B_4\rangle \end{bmatrix} \tag{5.25}$$

where the two channels exiting from the manipulation stage are labelled 5 and 6.

Given the properties of a scattering matrix and the asymptotic-in/out fields formalism we recalled in Sec. 1.3, we can express the photon creation operators in the output channels as

$$\begin{aligned} b^\dagger_{\omega,5} &= S_{11}(\omega) b^\dagger_{\omega,3} + S_{12}(\omega) b^\dagger_{\omega,4} \\ b^\dagger_{\omega,6} &= -\frac{S^*_{12}(\omega)}{det[S(\omega)]^*} b^\dagger_{\omega,3} + \frac{S^*_{11}(\omega)}{det[S(\omega)]^*} b^\dagger_{\omega,4} = S_{21} b^\dagger_{\omega,3} + S_{22} b^\dagger_{\omega,4}. \end{aligned} \tag{5.26}$$

Then, the single photon states at the structure output will be

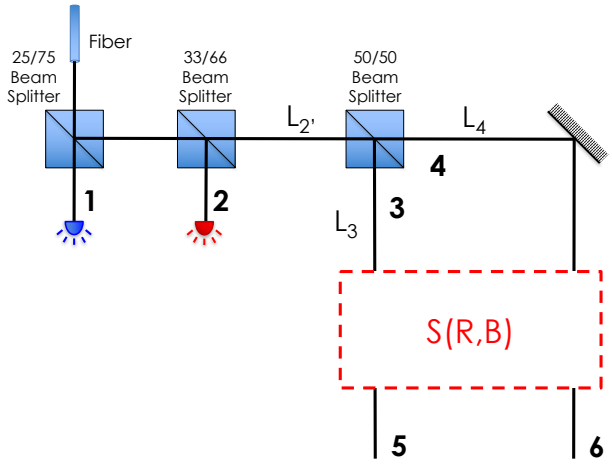

Figure 5.8: Sketch of the generic unitary operation on the photons exiting from channels 3 and 4, required for the characterization of the quantum state generated by the source. Suitable choices of the scattering matrix $S(R,B)$ lead to the reconstruction of all the different elements of the reduced density matrix ρ_{34}.

$$
\begin{aligned}
|R_5\rangle &= S_{11}(R)\,|R_3\rangle + S_{12}(R)\,|R_4\rangle \\
|R_6\rangle &= -\frac{S_{12}^*(R)}{(det[S(R)])^*}\,|R_3\rangle + \frac{S_{11}^*(R)}{(det[S(R)])^*}\,|R_4\rangle \\
|B_5\rangle &= S_{11}(B)\,|B_3\rangle + S_{12}(B)\,|B_4\rangle \\
|B_6\rangle &= -\frac{S_{12}^*(B)}{(det[S(B)])^*}\,|B_3\rangle + \frac{S_{11}^*(B)}{(det[S(B)])^*}\,|B_4\rangle\,,
\end{aligned}
\tag{5.27}
$$

and the two-photon states in the output ports $\{|w_i\rangle\} \equiv \{|R_5B_5\rangle\,, |R_5B_6\rangle\,, |R_6B_5\rangle\,, |R_6B_6\rangle\}$ are given by

$$
\begin{aligned}
|R_5B_5\rangle &= (S_{11}(R)\,|R_3\rangle + S_{12}(R)\,|R_4\rangle) \\
&\times\ (S_{11}(B)\,|B_3\rangle + S_{12}(B)\,|B_4\rangle) \\
&= S_{11}(R)S_{11}(B)\,|R_3B_3\rangle + S_{11}(R)S_{12}(B)\,|R_3B_4\rangle \\
&+\ S_{12}(R)S_{11}(B)\,|R_4B_3\rangle + S_{12}(R)S_{12}(B)\,|R_4B_4\rangle\,,
\end{aligned}
\tag{5.28}
$$

$$
\begin{aligned}
|R_5 B_6\rangle &= (S_{11}(R)\,|R_3\rangle + S_{12}(R)\,|R_4\rangle) \\
&\times \; (-\frac{S_{12}^*(B)}{(det[S(B)])^*}\,|B_3\rangle + \frac{S_{11}^*(B)}{(det[S(B)])^*}\,|B_4\rangle) \\
&= -\frac{S_{11}(R)S_{12}^*(B)}{(det[S(B)])^*}\,|R_3 B_3\rangle + \frac{S_{11}(R)S_{11}^*(B)}{(det[S(B)])^*}\,|R_3 B_4\rangle\,,
\end{aligned} \tag{5.29}
$$

$$
\begin{aligned}
|R_6 B_5\rangle &= (-\frac{S_{12}^*(R)}{(det[S(R)])^*}\,|R_3\rangle + \frac{S_{11}^*(R)}{(det[S(R)])^*}\,|R_4\rangle) \\
&\times \; (S_{11}(B)\,|B_3\rangle + S_{12}(B)\,|B_4\rangle) \\
&= -\frac{S_{12}^*(R)S_{11}(B)}{(det[S(R)])^*}\,|R_3 B_3\rangle - \frac{S_{12}^*(R)S_{12}(B)}{(det[S(R)])^*}\,|R_3 B_4\rangle \\
&+ \; \frac{S_{11}^*(R)S_{11}(B)}{(det[S(R)])^*}\,|R_4 B_3\rangle + \frac{S_{11}^*(R)S_{12}(B)}{(det[S(R)])^*}\,|R_4 B_4\rangle\,,
\end{aligned} \tag{5.30}
$$

and

$$
\begin{aligned}
|R_6 B_6\rangle &= (-\frac{S_{12}^*(R)}{(det[S(R)])^*}\,|R_3\rangle + \frac{S_{11}^*(R)}{(det[S(R)])^*}\,|R_4\rangle) \\
&\times \; (-\frac{S_{12}^*(B)}{(det[S(B)])^*}\,|B_3\rangle + \frac{S_{11}^*(B)}{(det[S(B)])^*}\,|B_4\rangle) \\
&= \frac{S_{12}^*(R)S_{12}^*(B)}{(det[S(R)])^*(det[S(B)])^*}\,|R_3 B_3\rangle - \frac{S_{12}^*(R)S_{11}^*(B)}{(det[S(R)])^*(det[S(B)])^*}\,|R_3 B_4\rangle \\
&- \; \frac{S_{11}^*(R)S_{12}^*(B)}{(det[S(R)])^*(det[S(B)])^*}\,|R_4 B_3\rangle + \frac{S_{11}^*(R)S_{11}^*(B)}{(det[S(R)])^*(det[S(B)])^*}\,|R_4 B_4\rangle\,.
\end{aligned} \tag{5.31}
$$

This allows us to express, in principle, every element of the density matrix in the asymptotic-in basis in terms of the asymptotic-out basis. We shall call the output density matrix

$$
\rho_{56} = \sum_{i,j} \tau_{ij}\,|w_i\rangle\,\langle w_j|\,. \tag{5.32}
$$

We can access the diagonal elements of ρ_{56} by placing detectors in channels 5 and 6. At a first glance this seems to necessitate the use of two frequency-dependent detectors in the same channel. Yet, such inconvenient can be overcome using a dichroic mirror in each output channel. In this configuration, the blue an red photons are routed to different output ports, and the experiments can be performed just using frequency-independent detectors.

As we state explicitly in Appendix A.3, from Eq. (5.28)-(5.31) and (5.32) one can express the diagonal elements of ρ_{56} as a function of the elements of ρ_{34}. For convenience, each type of coincidence measurement in channels 5 and 6 is referred to either as an X measurement, when both a red and a blue photon are detected in channel 5, a Y measurement, when the red photon is detected in channel 5 and the blue photon is detected in channel 6, or a Z measurement, when the blue photon is detected in channel 5 and the red photon is detected in channel 6. Conversely, each element of the reduced density matrix ρ_{34} can be reconstructed by performing a series of coincidence measurements X, Y, and Z, subject to selected scattering matrices.

We are particularly interested in the measuring the elements of the central submatrix of ρ_{34}, so we will focus on those alone. The same strategy we adopt in the following can be used for the calculation of all the other elements of the reduced density matrix. The reconstruction of the diagonal elements of ρ_{34} is straightforward and we report in Fig. 5.9 the optical setups for the measurement of a_{22} and a_{33}.

The reconstruction of the element a_{23} is considerably more demanding, and for this task we can refer to the optical setup represented in Fig. 5.10, where a Z measurement is shown, for example.

The scattering matrices $S(R, B)$ for the red and blue photons are

$$\begin{aligned} S(R) &= \frac{1}{\sqrt{2}} \begin{bmatrix} e^{ik_R L_5} & ie^{ik_R(L_6+L_7)+i\phi_R} \\ ie^{ik_R L_5} & e^{ik_R(L_6+L_7)+i\phi_R} \end{bmatrix} \\ S(B) &= \frac{1}{\sqrt{2}} \begin{bmatrix} e^{ik_B L_5} & ie^{ik_B(L_6+L_8)+i\phi_B} \\ ie^{ik_B L_5} & e^{ik_B(L_6+L_8)+i\phi_B} \end{bmatrix} \end{aligned} \tag{5.33}$$

The coincidence count in a Y measurement gives

$$\begin{aligned} Y(\phi_R, \phi_B) &= \frac{1}{4} - \frac{a_{12}^R + a_{34}^R}{2} \sin[k_B(L_5 - L_6 - L_8) - \phi_B] \\ &- \frac{a_{12}^I + a_{34}^I}{2} \cos[k_B(L_5 - L_6 - L_8) - \phi_B] \\ &+ \frac{a_{13}^R + a_{24}^R}{2} \sin[k_R(L_5 - L_6 - L_7) - \phi_R] \\ &+ \frac{a_{13}^I + a_{24}^I}{2} \cos[k_R(L_5 - L_6 - L_7) - \phi_R] \\ &+ \frac{1}{2} \cos[(k_R + k_B)(L_5 - L_6) - (k_R L_7 + k_B L_8) - (\phi_R + \phi_B)] a_{14}^R \\ &- \frac{1}{2} \cos[(k_R - k_B)(L_5 - L_6) - (k_R L_7 - k_B L_8) - (\phi_R - \phi_B)] a_{23}^R \\ &- \frac{1}{2} \sin[(k_R + k_B)(L_5 - L_6) - (k_R L_7 + k_B L_8) - (\phi_R + \phi_B)] a_{14}^I \\ &+ \frac{1}{2} \sin[(k_R - k_B)(L_5 - L_6) - (k_R L_7 - k_B L_8) - (\phi_R - \phi_B)] a_{23}^I. \end{aligned} \tag{5.34}$$

The same estimate for a Z measurement gives

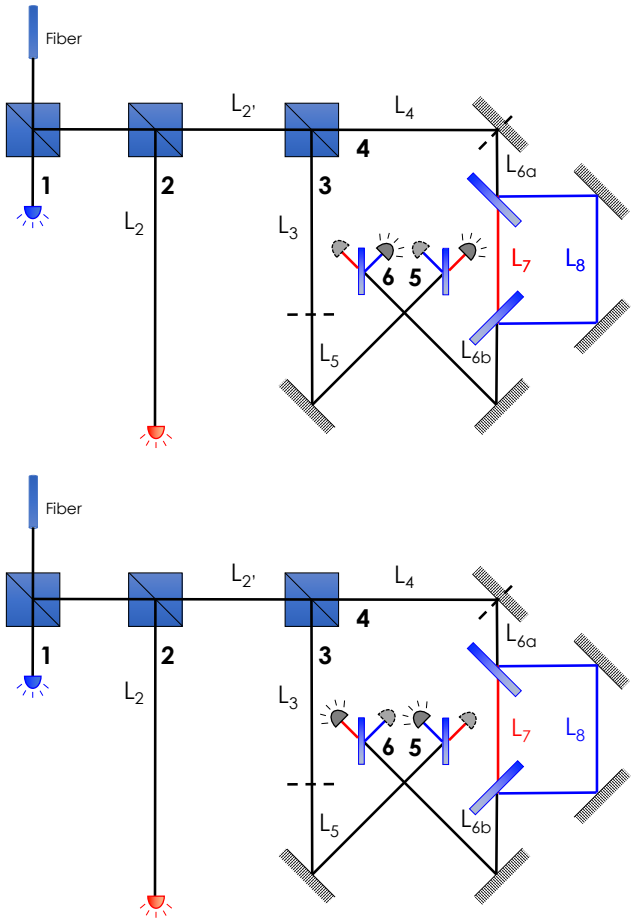

Figure 5.9: Experimental setup we envision for measuring the diagonal elements of the reduced density matrix ρ_{34}. In (a) we show the simultaneous detection of a red photon in channel 5 and a blue photon in channel 6; from the normalized count of the coincidences the element a_{22} can be accessed. The same setup is used in (b) for the simultaneous detection of a blue photon in channel 5 and a red photon in channel 6, whose normalized coincidence count reveals the element a_{33}.

$$
\begin{aligned}
Z(\phi_R,\phi_B) &= \frac{1}{4} + \frac{a_{12}^R + a_{34}^R}{2}\sin[k_B(L_5 - L_6 - L_8) - \phi_B] \\
&+ \frac{a_{12}^I + a_{34}^I}{2}\cos[k_B(L_5 - L_6 - L_8) - \phi_B] \\
&- \frac{a_{13}^R + a_{24}^R}{2}\sin[k_R(L_5 - L_6 - L_7) - \phi_R] \\
&- \frac{a_{13}^I + a_{24}^I}{2}\cos[k_R(L_5 - L_6 - L_7) - \phi_R] \\
&+ \frac{1}{2}\cos[(k_R + k_B)(L_5 - L_6) - (k_R L_7 + k_B L_8) - (\phi_R + \phi_B)]a_{14}^R \\
&- \frac{1}{2}\sin[(k_R + k_B)(L_5 - L_6) - (k_R L_7 + k_B L_8) - (\phi_R + \phi_B)]a_{14}^I \\
&- \frac{1}{2}\cos[(k_R - k_B)(L_5 - L_6) - (k_R L_7 - k_B L_8) - (\phi_R - \phi_B)]a_{23}^R \\
&+ \frac{1}{2}\sin[(k_R - k_B)(L_5 - L_6) - (k_R L_7 - k_B L_8) - (\phi_R - \phi_B)]a_{23}^I .
\end{aligned}
\tag{5.35}
$$

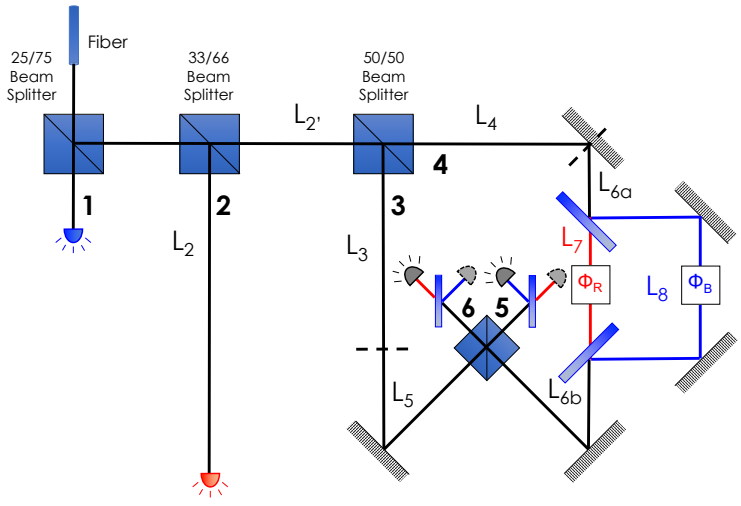

Figure 5.10: Scheme of the experimental setup we propose for the reconstruction of the diagonal element a_{23} of the reduced density matrix ρ_{34}.

The sum of the coincidence counts in the Y and Z measurement is

$$\begin{aligned} Y(\phi_R,\phi_B)+Z(\phi_R,\phi_B) &= \frac{1}{2}+\cos(\xi_+-\phi_+)a_{14}^R-\cos(\xi_--\phi_-)a_{23}^R \\ &- \sin(\xi_+-\phi_+)a_{14}^I+\sin(\xi_--\phi_-)a_{23}^I \\ &= \frac{1}{2}+\cos(\xi_+)\cos(\phi_+)a_{14}^R+\sin(\xi_+)\sin(\phi_+)a_{14}^R \\ &- \cos(\xi_-)\cos(\phi_-)a_{23}^R-\sin(\xi_-)\sin(\phi_-)a_{23}^R \\ &- \sin(\xi_+)\cos(\phi_+)a_{14}^I+\cos(\xi_+)\sin(\phi_+)a_{14}^I \\ &+ \sin(\xi_-)\cos(\phi_-)a_{23}^I-\cos(\xi_-)\sin(\phi_-)a_{23}^I, \end{aligned} \tag{5.36}$$

where

$$\begin{aligned} \xi_+ &\equiv (k_R+k_B)(L_5-L_6)-(k_RL_7+k_BL_8) \\ \xi_- &\equiv (k_R-k_B)(L_5-L_6)-(k_RL_7-k_BL_8) \\ \phi_+ &\equiv (\phi_R+\phi_B) \\ \phi_- &\equiv (\phi_R-\phi_B). \end{aligned} \tag{5.37}$$

We can consider some particular configurations, such as

$$\begin{aligned} Y(0,0)+Z(0,0) &= \frac{1}{2}+\cos(\xi_+)a_{14}^R-\cos(\xi_-)a_{23}^R \\ &- \sin(\xi_+)a_{14}^I+\sin(\xi_-)a_{23}^I \\ Y(\frac{\pi}{2},\frac{\pi}{2})+Z(\frac{\pi}{2},\frac{\pi}{2}) &= \frac{1}{2}-\cos(\xi_+)a_{14}^R-\cos(\xi_-)a_{23}^R \\ &+ \sin(\xi_+)a_{14}^I+\sin(\xi_-)a_{23}^I \\ Y(0,\frac{\pi}{2})+Z(0,\frac{\pi}{2}) &= \frac{1}{2}+\sin(\xi_+)a_{14}^R+\sin(\xi_-)a_{23}^R \\ &+ \cos(\xi_+)a_{14}^I+\cos(\xi_-)a_{23}^I \\ Y(\frac{\pi}{2},0)+Z(\frac{\pi}{2},0) &= \frac{1}{2}+\sin(\xi_+)a_{14}^R-\sin(\xi_-)a_{23}^R \\ &+ \cos(\xi_+)a_{14}^I-\cos(\xi_-)a_{23}^I \end{aligned} \tag{5.38}$$

that, combining the results, provide us

$$\begin{aligned} Y(0,0)+Z(0,0)+Y(\frac{\pi}{2},\frac{\pi}{2})+Z(\frac{\pi}{2},\frac{\pi}{2}) = \\ = 1-2\cos(\xi_-)a_{23}^R+2\sin(\xi_-)a_{23}^I \end{aligned} \tag{5.39}$$

$$\begin{aligned} Y(0,\frac{\pi}{2})+Z(0,\frac{\pi}{2})-Y(\frac{\pi}{2},0)-Z(\frac{\pi}{2},0) = \\ = 2\sin(\xi_-)a_{23}^R+2\cos(\xi_-)a_{23}^I, \end{aligned}$$

and finally

$$\begin{aligned} a_{23}^{R} &= \frac{1}{2}\cos(\xi_{-})[1 - Y(0,0) - Z(0,0) - Y(\frac{\pi}{2},\frac{\pi}{2}) - Z(\frac{\pi}{2},\frac{\pi}{2})] \\ &+ \frac{1}{2}\sin(\xi_{-})[Y(0,\frac{\pi}{2}) + Z(0,\frac{\pi}{2}) - Y(\frac{\pi}{2},0) - Z(\frac{\pi}{2},0)] \\ a_{23}^{I} &= \frac{1}{2}\sin(\xi_{-})[Y(0,0) + Z(0,0) + Y(\frac{\pi}{2},\frac{\pi}{2}) + Z(\frac{\pi}{2},\frac{\pi}{2}) - 1] \\ &+ \frac{1}{2}\cos(\xi_{-})[Y(0,\frac{\pi}{2}) + Z(0,\frac{\pi}{2}) - Y(\frac{\pi}{2},0) - Z(\frac{\pi}{2},0)]. \end{aligned} \tag{5.40}$$

Once the value of ξ_{-} is obtained, by classical measurements, one can reconstruct the complex diagonal element a_{23}.

In conclusion, by performing 6 coincidence measurements in different configurations and combining the results, it is possible to reconstruct the internal submatrix of the reduced density matrix ρ_{34}. Such approach can then be iterated for the characterization of the density matrices ρ_{23} and ρ_{24}, yielding the three reduced density matrices required for the full reconstruction of tripartite quantum state produced by our structure, and experimentally demonstrate the generation of energy-entangled W states.

We now move on to discuss the case of another tripartite entangled state, namely the GHZ state, which is particularly interesting for its possible applications in a multitude of quantum information processes. In analogy with the present Chapter, we will provide a novel approach for the generation of such quantum state, which is particularly helpful in the view of enhancing the source efficiency and for a simpler integration on a PIC.

Chapter 6

Generation of path-encoded GHZ states

First introduced in 1989 by D. M. Greenberger, M. A. Horne and A. Zeilinger [53], GHZ states have since attracted an ever-growing interest, thanks to their effectiveness in testing fundamental aspects of quantum mechanics and their use in quantum protocols for communication and metrology. The simplest form of a GHZ states is

$$|GHZ\rangle = \frac{1}{\sqrt{3}}(|000\rangle + |111\rangle), \tag{6.1}$$

where $|0\rangle$ and $|1\rangle$ represent the orthogonal states of a qubit which, as we discussed above, can be implemented using different degrees of freedom, such as polarization, energy, or mode spatial distribution. The density matrix of the GHZ state (6.1) state is reported in Fig. 6.1.

GHZ states have been applied in tests of local realism [55], where the use of tripartite states allows for a demonstration of its conflict with quantum mechanics even in a definite measurement, as opposed to such tests using bipartite states which rely on the statistics of a large number of measurements. They have also been used to devise quantum communication protocols, such as multipartite QKD [56], dense coding [170], and entanglement swapping [171].

The first experimental evidence of GHZ states was provided by Bouwmeester et al. [150] using polarization-entangled photon pairs produced by SPDC in a nonlinear crystal. The scheme adopted by the authors is reported in Fig. **??**.

As we already argued in the previous Chapter on W states, when photons are used to produce a multipartite state, the choice of polarization as the entangled degree of freedom is typical and, at present, the sole reported in literature. Yet the use of polarization poses several constraints, especially aiming for an integrated source, and for long distance communications. In the former instance, the manipulation of a photon polarization on-chip is complicated by any asymmetry in the waveguide geometry, and by the fabrication complexity, the footprint,

and the bandwidth requirements of integrated polarization rotators [172, 69]; in the latter instance, we must recall that the current optical network is composed of polarization-insensitive fibers, and therefore any fluctuation in the birefringence would have a damaging impact on the GHZ state. Once more, the use of other degrees of freedom in photonic implementations of GHZ states is worth investigating.

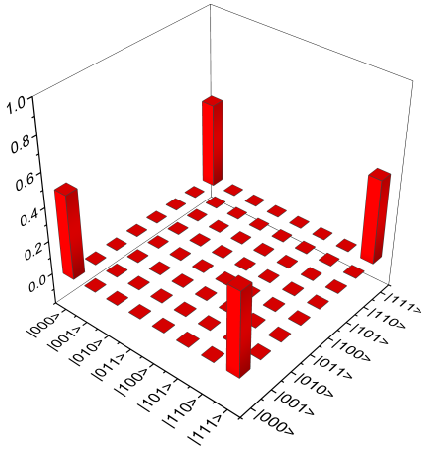

Figure 6.1: Real part of the density matrix associated with the standard form (6.1) of the GHZ state.

In the following we demonstrate the possibility to prepare GHZ states with the generated photons entangled in the path degree of freedom [54]; the states $|0\rangle$ and $|1\rangle$ here refer to the photon being in different spatial modes [173], regardless any other degree of freedom. Given the scope of this thesis, we envision the generation of GHZ states in a photonic integrated circuit (PIC) in which **two photon pairs** are generated by SFWM in a $\chi^{(3)}$ material, but we stress that a similar approach would be device-independent. The scheme we propose allows us to take advantage of the enhancement of the generation rate provided by integrated microresonators, and to drastically reduce the footprint of the source [136]. Note that, in principle, it would be possible to design optical schemes that manipulate path-encoded states and subsequently translate and output them in the polarization representation. This has been proposed recently to achieve chip-to-chip quantum communication [77]. However, here we are mainly interested in both the manipulation and output of path-encoded states on optical chips.

We envision the situation depicted in Fig. 6.3: four photons are generated in an integrated device, of which one is used as a target and three are used as qubits. For each qubit there are two paths, each path associated with a basis state. The three photons are routed to three independent parties (Alice, Bob, and Charlie), which can manipulate them, where the rotation of the qubit on the Bloch sphere is performed by means of a MZI and two phase shifts [75].

As a first step, similarly to what we did in the previous Chapter, we can devise a correspondence between bulk optical elements used to manipulate polarization states and integrated optical elements necessary to manipulate path-encoded states. Such correspondence is shown in Fig. 6.4. As customary in the path-encoding scheme (see Section 1.1) we imagine to employ two waveguides, or *paths*, for each photon route in the optical circuit. We assign the state $|1\rangle$ or $|0\rangle$

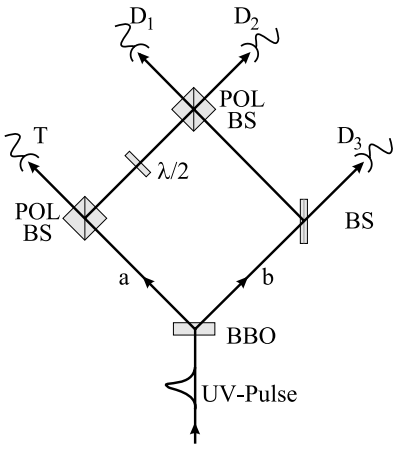

Figure 6.2: Optical scheme used by Bouwmeester et al. [150] for the first generation of polarization-entangled GHZ states .

to a photon when it travels in one waveguide or the other, which we graphically depict as dotted and dashed, respectively, in Fig. 6.4.

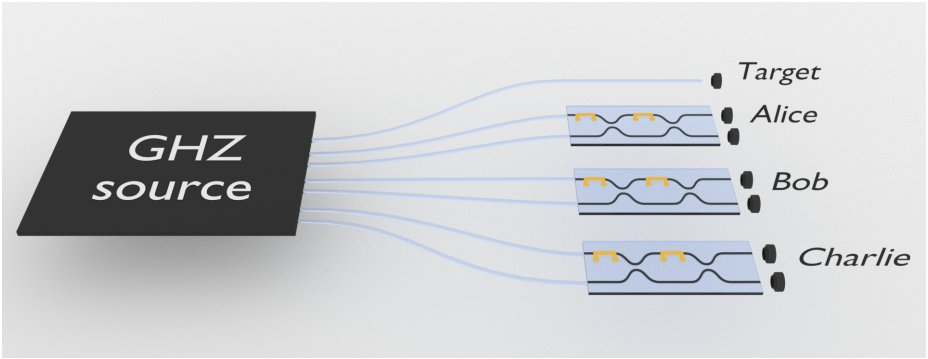

Figure 6.3: Sketch of the general scheme for the preparation and distribution of path-encoded GHZ states.

This convention is kept consistent throughout the whole circuit.

The rotation of polarization states is performed in bulk optics by using a $\lambda/2$ plate, while the corresponding evolution of path states is effected with a 50:50 DC connecting the two waveguides associated with the $|1\rangle$ and $|0\rangle$ states. Photons in a bulk optical circuit can be routed depending on their polarization using a PBS; the same can be done for the path-encoded states by properly connecting the waveguides of the input ports to the waveguides of the output ports (see Fig. 6.4). Finally, photons in a bulk optical circuit can be spatially separated regardless their polarization state using a BS, and the corresponding

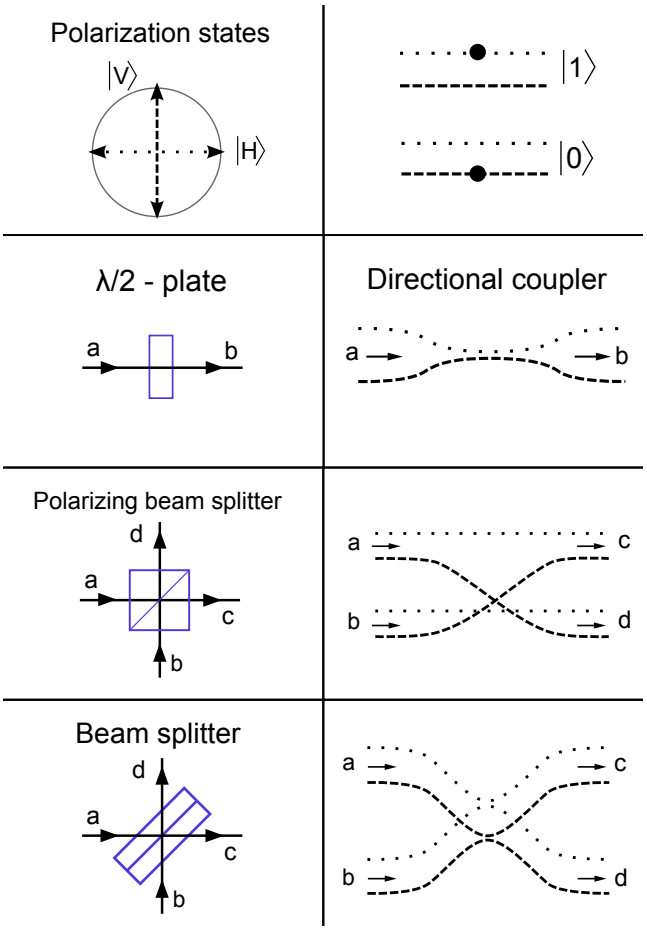

Figure 6.4: Analogies between optical elements employed in bulk optics for schemes involving polarization-entangled states (on the left) and the corresponding integrated optical elements for the scheme introduced here involving path-encoded states (on the right). Dotted and dashed lines indicate waveguides associated with $|1\rangle$ and $|0\rangle$, respectively. The shaded boxes mark the coupling points between waveguides.

operation on path-encoded states is performed in integrated optics using two 50:50 DCs.

Two remarks regarding path states and their manipulation are necessary: First, we note that the generation of a meaningful path-encoded state for a photon pair requires a source more complicated than a single-bus-waveguide ring resonator [174, 175, 176]. Second, some of the integrated optical elements used to manipulate path states (see Fig. 6.4) display a waveguide crossing that seems problematic in a planar geometry, which is usually the choice for PICs. However, we will see that proper sources can be designed, and a waveguide rearrangement can avoid the problematic waveguide crossing.

Considering a generic parametric source, in the approximation of undepleted pump pulses described classically, the state of the generated photons is of the usual form [104]

$$\begin{aligned}|\psi\rangle &= e^{\beta C_{II}^{\dagger} - H.c.} |\text{vac}\rangle \\ &= \left(1 + \mathcal{O}(|\beta|^2)\right) |\text{vac}\rangle + \beta C_{II}^{\dagger} |\text{vac}\rangle + \frac{1}{2}\left[\beta C_{II}^{\dagger}\right]^2 |\text{vac}\rangle + \dots \\ &\equiv \left(1 + \mathcal{O}(|\beta|^2)\right) |\text{vac}\rangle + \beta |\text{II}\rangle + \frac{1}{2}\left[\beta C_{II}^{\dagger}\right]^2 |\text{vac}\rangle + \dots, \quad (6.2)\end{aligned}$$

where $|\text{II}\rangle$ is the normalized two-photon state. In the limit of interest where $|\beta|^2 \ll 1$, we can truncate the expansion (6.2) at the quadratic term in β , which corresponds to the generation of two pairs. The properties of the four-photon state contribution to (6.2), resulting from the generation of two photon pairs, are directly related to the those of the creation operator $C_{II}^{\dagger}$. Hence, once this has been calculated, the output state of two or more pairs can be obtained immediately. For this reason, we begin with a discussion of the generation of a single photon pair.

The structure we propose can be divided in two parts: a nonlinear integrated source, which generates a path-encoded initial state, and a linear optical circuit to manipulate it. The full calculation of the output state is reported in Appendix B.1.

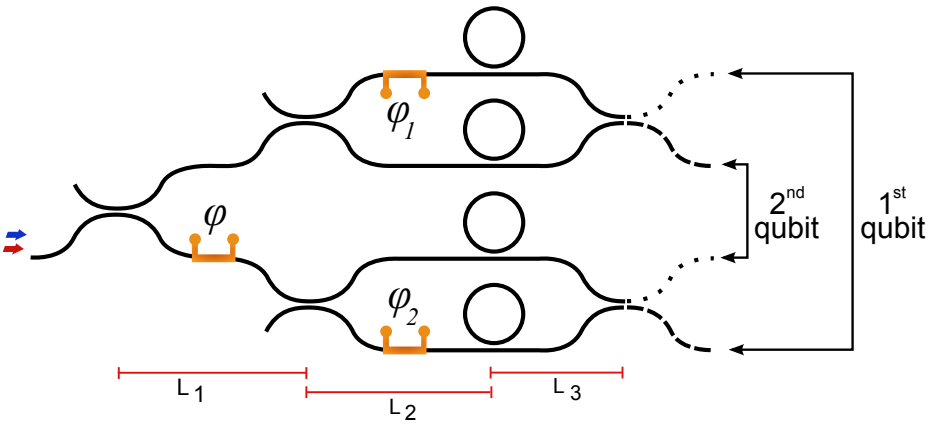

Figure 6.5: Sketch of the nonlinear integrated source of path-entangled states (6.3). Waveguides associated with single qubits are grouped together, phase shifters and relevant lengths are also shown.

The nonlinear integrated source (see Fig. 6.5) consists of four identical ring resonators arranged in two blocks, each of which is a MZI unbalanced by a phase ϕ_i, with one ring resonator per arm. The two blocks are coherently pumped using a 50:50 directional coupler, which splits the pump amplitude into two waveguides, with ϕ being the pump phase difference between the two blocks. Although this is not strictly necessary, here we consider degenerate SFWM [32], for which we require a dual-pump scheme, where the 50:50 split ratio can be guaranteed by choosing an appropriate length of the directional coupler [177]. Since the field enhancement inside the rings is much larger than that in the waveguides, we assume that the generation of photons occurs only in the resonators.

It should be noticed that although the use of four identical microring resonators might pose some constraints, the fabrication technique for multiple integrated elements on SOI platforms has constantly improved in recent years, up to the realization of several hundred coupled microrings [178]. Moreover, it is possible to tune each resonator almost independently via heaters: this enables the control of the position of its resonances with great precision [179]. If one considers silicon ring resonators, the large nonlinearity ($\gamma \approx 200\ W^{-1}m^{-1}$) guarantees high generation efficiencies with mW pump powers and $Q \approx 10000$ [136], which relaxes the constraints on the ring tunability. Finally, the two blocks in Fig. 6.5 have already been used for the generation of deterministically split photons by the reverse HOM effect, yielding high-visibility quantum interference [75]. Indeed, when $\phi_i = \pi/2[2\pi]$ one observes deterministic splitting of the photon pair exiting the MZI [175]. But when the two blocks are pumped with a relative phase shift $\phi = \pi$ (or odd multiple), the two-photon state generated by the

source is the Bell state (see Appendix B.1)

$$|\Psi^-\rangle = \frac{1}{\sqrt{2}}\left(|1\rangle|0\rangle - |0\rangle|1\rangle\right), \tag{6.3}$$

where we use the first and fourth waveguide for the first path-encoded qubit and we use the second and the third waveguide for the second path-encoded qubit as depicted in Fig. 6.5. This situation is analogous to that considered by Bouwmeester et al. [150], where the nonlinear crystal generates photon pairs in the corresponding polarization-encoded entangled state.

We now consider the simultaneous generation of two pairs of photons, described by the effect of $(C_{II}^\dagger)^2$ on the vacuum state. This leads to the four-photon state

$$\begin{aligned}|\mathrm{IV}\rangle = -\frac{1}{2\sqrt{3}}\int dk_1' dk_2' dk_1 dk_2 \phi_{\mathrm{ring}}(k_1,k_2)\phi_{\mathrm{ring}}(k_1',k_2') \\ \times e^{i(\psi(k_1,k_2)+\psi'(k_1,k_2))}(b_{k_1,1}^\dagger b_{k_2,2}^\dagger - b_{k_1,3}^\dagger b_{k_2,4}^\dagger) \\ \times (b_{k_1',1}^\dagger b_{k_2',2}^\dagger - b_{k_1',3}^\dagger b_{k_2',4}^\dagger)|\mathrm{vac}\rangle,\end{aligned} \tag{6.4}$$

where $\phi_{\mathrm{ring}}(k_1,k_2)$ is the BWF of a pair generated in a single ring, $\psi(k_1,k_2)$ and $\psi'(k_1,k_2)$ are phase factors associated with propagation in the channel (which can be assumed constant) defined in (B.23), and $b_{k_i,j}^\dagger$ is the operator associated with the creation of a photon having wave vector k_i and exiting the structure in Fig. 6.5 from the channel j. The state $|\mathrm{IV}\rangle$ is normalized under the assumption that the BWF $\phi_{\mathrm{ring}}(k_1,k_2)$ is separable (see below).

We now turn to the manipulation of the state $|\mathrm{IV}\rangle$, which is done following a strategy similar to the one proposed by Bouwmeester et al. [150] for polarization-encoded entangled states, but implemented for path-encoded entangled states using the correspondence between polarization bulk elements and the path integrated components illustrated in Fig. 6.4. Note that we have avoided the waveguide overlapping in the integrated analogue of a beam splitter (see Fig. 6.4) by a rearrangement of the circuit waveguides as shown in Fig. 6.6.

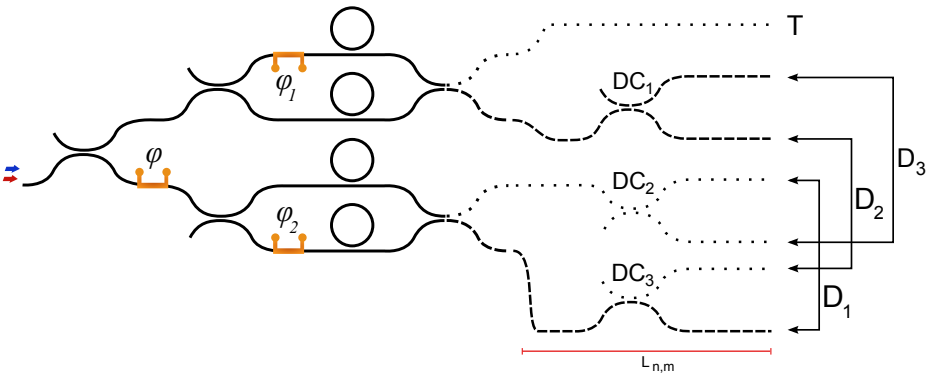

Figure 6.6: Sketch of the complete integrated circuit for the generation of path-encoded GHZ states. We can identify a schematic representation of the source of path-encoded entangled states in the form (6.3), and a realistic implementation of the full circuit obtained by rearranging some of the channels and the detectors. Waveguides associated with single qubits are grouped together.

In analogy with Bouwmeester et al. [150], post-selecting on a three-fold coincidence in detectors D_1, D_2, and D_3 in Fig. 6.6, conditioned on the detection of a photon in the target detector T, identifies that a GHZ state was generated. Care must be taken to ensure that the generated GHZ state is pure. As in the generation of pairs of photons for heralded photon applications, this requires the function $\phi_{\text{ring}}(k_1, k_2)$ to be separable. Indeed, whenever this is not the case, the partial trace over the herald photon Hilbert space reveals a mixed heralded photon state. We have proposed two schemes for obtaining nearly uncorrelated or truly uncorrelated photon pairs in Chapter 3 and 4, respectively, by adjusting the pump pulse duration and the coupling geometry.

Following the asymptotic fields approach (see Section (1.3)and Appendix (B.1)) we can rewrite the complete output state as:

$$|\psi\rangle = \left(1 + \mathcal{O}(|\beta|^2)\right)|\text{vac}\rangle + \beta\,|\text{II}\rangle + \frac{\sqrt{3}}{2}\beta^2\left[|\Phi\rangle - \frac{1}{2\sqrt{3}}\,|\psi_{\text{GHZ}}\rangle\right], \tag{6.5}$$

where $|\Phi\rangle$ includes other contributions that are second order in β but would not lead to a four-fold coincidence event, while

$$|\psi_{\text{GHZ}}\rangle = \int dk_1 dk_2 dk_1' dk_2' \phi_{\text{ring}}(k_1, k_2)\phi_{\text{ring}}(k_1', k_2') \times e^{i\Gamma}\,|\text{T}\rangle\,|\text{GHZ}\rangle\,, \tag{6.6}$$

with Γ a phase factor and

$$\begin{aligned} |\mathrm{GHZ}\rangle &= \frac{1}{\sqrt{2}}\Big[b^\dagger_{k_1,D_{1,1}} b^\dagger_{k_2,D_{2,1}} b^\dagger_{k'_2,D_{3,0}} \\ &\quad + e^{i\Theta(k_2,k'_1,k'_2)} b^\dagger_{k_2,D_{1,0}} b^\dagger_{k'_2,D_{2,0}} b^\dagger_{k_1,D_{3,1}}\Big]|\mathrm{vac}\rangle \\ &= \frac{1}{\sqrt{2}}\left[|110\rangle + e^{i\Theta}|001\rangle\right], \\ |T\rangle &= b^\dagger_{k'_1,T}|\mathrm{vac}\rangle\,. \end{aligned} \tag{6.7}$$

Here $\Theta(k_2, k'_1, k'_2)$ is a relative phase between the two GHZ state components and depends on the relative positions of the detectors (see (B.28)), which cannot be longer than the coherence length of the photons. Such a coherence length can always be increased by filtering, although for typical resonance widths achievable at telecom wavelengths in silicon and silicon nitride resonators it already ranges from centimeters to meters [90, 44, 176].

As expected, any four-fold coincidence event results in a GHZ state, where the probability of such an event is $\left|\beta^2/4\right|^2$, when propagation losses are neglected. The magnitude of β depends on the pump power, the ring radius and the quality factor of the resonators, and it can vary depending on the device under consideration. Yet values of $|\beta|^2 \approx 0.1$ have been demonstrated in PICs [75], and assuming MHz pump repetition rates, this would allow for the preparation of path-encoded GHZ states with kHz generation rates with mW pump powers and quality factors of the order of 10^4. Although our theoretical estimate does not account for any loss, device imperfection, and detector efficiencies, we still expect a large improvement on the generation rate with respect to the present results reported in the literature.

In conclusion, we can identify a one-to-one correspondence between components operating in a path encoding scheme and bulk optical elements operating in a polarization encoding scheme. On this premise, we investigated the possibility to generate of path-encoded tripartite GHZ states. It should be noticed that, although the generation of the desired state is revealed only in post-selection — destroying the quantum state — many protocols involving GHZ states are based on this condition [56, 170, 171]. Our approach is suitable for the generation of multipartite states in quantum photonic integrated devices, as it overcomes the difficulties related to the use of the polarization degree of freedom. To demonstrate this, we designed and studied an integrated structure relying on the generation of photon pairs by SFWM in ring resonators, showing the potential of this approach in terms of source footprint and brightness.

Chapter 7

Conclusions and Perspectives

In this work, we presented and analyzed different solutions for the generation of nonclassical states of light in integrated structures, specifically conceived for the production of entangled or completely unentangled photon pairs and tripartite entangled states. The study of similar sources is of central importance for the development of quantum integrated photonics, which is one of the most promising platforms for the implementation of quantum protocols for communications, sensing/metrology, simulation, and computation.

While Chapter 1 was devoted to a brief introduction of the basic concepts of quantum photonics and integrated nonlinear optics, the first innovative contribution comes with Chapter 2, where we investigated the possibility to use porous silicon as a low-cost χ_3 material for integrated nonlinear optics, with the long-term goal of demonstrating parametric fluorescence. Even though this last objective has proved to be experimentally out of our reach owing to the exceedingly high propagation and coupling losses displayed by our samples, pSi has nonetheless revealed a remarkably intense nonlinear response, such that it was possible to observe photon pairs generated by stimulated FWM even with a CW low-power pump, and estimate a waveguide nonlinear parameter $\gamma = (20 \pm 2)\ m^{-1}W^{-1}$.

The source was analyzed both theoretically and experimentally and it was composed of a side-coupled microring resonator, whose cross section was a ridge waveguide obtained by controlling the silicon fraction in the porous material. The samples were fabricated at the Vanderbilt University, in a collaboration with the group led by Prof. Sharon Weiss. From the measured transmission spectra it was then possible to estimate the pSi microring quality factor which, for the resonances involved in the experiment, was found close to $Q \approx 5{\cdot}10^3$. This information, together with the geometrical and pumping parameters allowed us to determine the parameter γ, showing that pSi has a nonlinear response intermediate between that of semiconductors and oxides. Moreover, thanks to the estimate of the refractive index of pSi in the ridge and substrate region, we could numerically compute the mode effective area A_{eff}, both with a FDE

solver and an effective index approach. From such estimate we eventually determined the nonlinear refractive index of pSi, finding $n_2 = 4.26 \cdot 10^{-18}\ m^2/W$, in a good agreement with previous works in the literature. Finally, leveraging the correspondence between stimulated and spontaneous nonlinear phenomena, we could predict the generation rate of photon pairs by SFWM in our source, and determine the coupled pump power required for observing kHz generation rates. Despite the intrinsic roughness responsible for high propagation losses (estimated, in our case, in 2.75 dB/mm), the quality factor of our ring was sufficiently high to observe stimulated FWM at low CW pump power. Such a remarkable nonlinearity, together with the distinctive properties of pSi such as the large internal surface area and the possibility to infiltrate with other materials, boosts the interest for applications in low-power integrated nonlinear optics.

In Chapters 3 and 4 we moved from the pSi to the SOI platform, which is today well-established and guarantees lower losses and a higher nonlinear parameter. In these Chapters we focused on the spectral correlations of the photon pairs generated by SFWM in integrated microring resonators. In particular, in Chapter 3 we examined theoretically and experimentally the case of a standard side-coupled crystalline silicon microring, and discussed the possibility to tailor the quantum correlations between the frequency-converted photons by adjusting the pump pulse duration. To this end, by taking advantage of the asymptotic field approach, we could compute the JSD and the Schmidt Number in the so-called short and long pump pulse regime. The comparison between the numerical simulations and the experimental measurements in the short pump pulse regime showed a good agreement, with a predicted Schmidt Number of $K_{Theory} = 1.09$ and the experimental bound at $K_{bound} = 1.03 \pm 0.1$. The same comparison could not be performed in the case of the long pump pulse regime, for the experimental value is strongly limited by the measurement resolution. Yet, it should be noticed that the reconstruction of the JSD was achieved with unprecedented accuracy in literature, thanks to the use of the stimulated emission tomography technique. As expected from the theoretical description, the photon pairs generated by SFWM in the long pump pulse regime showed high quantum correlations with an estimated Schmidt Number $K = 37038$, while the photon pairs generated by SFWM in the short pump pulse regime displayed vanishing correlations. As we recalled in the present work, this last condition is crucial for the design of an heralded single photon source, and in this regard integrated microring resonators are often considered valid implementations. However, even with the shortest pump pulse, the the separability of the BWF of a photon pair generated in a side-coupled microring cannot be complete, and the the presence of residual quantum correlations is responsible for the heralding of partially mixed quantum states.

We addressed this problem in Chapter 4, where we discussed the impact of an interferometric coupling scheme on the spectral properties of the photon pairs generated by parametric fluorescence in a ring resonator. Devising a simplified expression for the BWF we showed that the lack of separability of photon pairs generated in a conventional ring is due to the absence of a frequency-

dependent coupling scheme; indeed, when the ratio between the quality factors $\max(Q_S, Q_I)/Q_P$ can be tuned, the purity of the resulting heralded output state varies between 0 and 1 (totally mixed to pure) accordingly. The quality factors can in turn be adjusted by designing a frequency-dependent coupling between the bus waveguide and the microring resonator. In this work, we adopted a double interferometric coupling scheme based on a MZI, whose frequency response can be tuned by unbalancing one of the interferometer arms using microheaters, to couple light in an add-drop microring resonator. To theoretically characterize this source, we produced a insightful, yet approximate, theoretical estimate of its performance, together with a comprehensive numerical calculation of the output state and the single photon purity. We showed that, as expected, for low Q_{SI}/Q_P ratios the purity of the output state is scarce, while upon increasing the Q ratio till unity we could reproduce the behavior of a side-coupled microring, where all the resonances have approximately the same quality factor, yielding a purity $\gamma = 91.7\%$. More interestingly, increasing the Q_{SI}/Q_P ratio above unity we could predict the generation of high-purity heralded single photons, with $\gamma \sim 99.9\%$. Although for lower Q_{SI}/Q_P ratios the agreement between the quick theoretical model and the full numerical calculation is slightly decreases, it is nonetheless remarkably high for the larger ratios, the regime in which the source is meant to operate.

The works presented in Chapters 5 and 6 deal with the generation of tripartite entangled states of light, specifically W states and GHZ states. Multipartite entangled states have been extensively investigated in the last decades and have attracted the researcher's interest for their possible use in protocols for quantum teleportation, QKD and dense coding. These states are typically produced in bulk optics setups, exploiting nonlinear crystals to generate polarization-encoded photon pairs. Here, we presented their implementation on-chip, taking advantage of alternative degrees of freedom for the qubit encoding which better suited the integrated design.

In Chapter 5 we focused on the generation of W states exploiting the energy correlations of photon pairs generated by SFWM in microring resonators. To this end, we first devised a direct correspondence between the optical elements used for the manipulation on polarization-entangled states and their integrated counterparts in energy-encoding, emphasizing the absence of an equivalent implementation of the HWP in integrated linear optics. Despite this lack, we could design an integrated source of W states and even devise a general strategy for achieving the full tomography of the energy-entangled tripartite state, in a fully passive integrated circuit. The photons required for the construction of the W state are generated in a side-coupled microring resonator by short pump pulses, similarly to what we did in Chapter 3 and 4, yet here we necessarily considered the less frequent events in which two photon pairs per pulse are produced, allowing us to access much higher pump intensities. The device we proposed in our work is based on post-selection of the events: the generation of a W state is announced by a four-fold coincidence in the target and the three output channels, and occurs with probability $(\frac{3\sqrt{2}}{8}|\beta|^2)^2$.

The second part of Chapter 5 is devoted to the description of the tomographic

procedure necessary for the reconstruction of the output state, and can be used for confirming the actual generation of a W state. We took advantage of the reduced density matrix tomography approach to limit our analysis to a bicolored photon pair at each time, and finally devised a feasible optical circuit for performing a complete tomography on the photon pair using only linear elements. Although we presented the tomographic scheme in a bulk optical setup, a similar approach can be straightforwardly implemented in an integrated optical circuit.

In the last Chapter of this work we moved our attention to a different class of tripartite entangled states, namely the GHZ state. In this case the energy-encoding does not apply, and we proposed the use of path-encoding of photons for the implementation of an integrated source. Similarly to the previous Chapter, we devised an analogy between the optical elements used to manipulate polarization-encoded states and those required in the path-encoding scheme, finding that a perfect correspondence can be outlined. When photon pairs are generated by type-II SPDC in a bulk nonlinear crystal, their emission is not collinear, a crucial condition for the implementation of path-encoding, where the information is carried by the photon spatial mode. However, this scheme cannot be emulated using a single side-coupled microring resonator. To address this issue, we proposed a novel design for an integrated source of path-encoded $|\Psi^-\rangle$ states comprised of four identical side-coupled microrings in two paralleled MZI configurations. Taking advantage of the quantum interference of the generation probability amplitudes in each microring, and adjusting three phase shifters to exploit the reverse Hong-Ou-Mandel effect, we could demonstrate the effectiveness of our design in producing the desired output states. When two photon pair are simultaneously generated by our source upon a sufficiently intense pump pulse, they are manipulated in a linear integrated circuit we engineered for the production of path-encoded GHZ states upon post-selection of four-fold coincidences. Even though the correspondence between optical elements we outlined in the opening of the Chapter generally entails a few waveguide crossings, our scheme managed to avoid this lossy elements by conveniently rearranging the output detectors. Considering typical performances of SOI microrings and pumping schemes, we predicted a generation rate for path-encoded GHZ states of the order of kHz, several orders of magnitude higher that those achieved in bulk solutions.

In conclusion, this thesis convenes the author's efforts in contributing to the field of quantum technologies through the proposal and the theoretical study of different sources of nonclassical states of light, ranging from heralded single photons to entangled photon pairs, and from tripartite W states to tripartite GHZ states. We hope that the ideas we discussed and the source design we proposed in this document can be further developed for the realization of more elaborate quantum experiments, as a benchmark for future quantum technologies to come. These results confirm that nonlinear integrated optics is a valuable approach for the realization of sources of quantum states of light based on parametric fluorescence, and for their implementation in full lab-on-a-chip quantum experiments. We finally want to recall that part of the work has been done in a collaboration with the J. E. Sipe group at the University of Toronto, where the author carried

on six months of his PhD program. The results we presented here have been published both in peer-reviewed journals and as contributions to conferences, as referenced in the conclusion of the present work.

Appendix A

Generation of energy-entangled W states

A.1 Normalization of the output states $|II\rangle$ and $|IV\rangle$

In this Appendix we deal with the normalization of the output states defined in Eq. (5.7). We adopt a very general approach, starting from the definition of the creation operator for a photon pair $C^{\dagger}_{II}$, in Eq. (1.74) assuming single-mode waveguides,

$$C^{\dagger}_{II} = \frac{1}{\sqrt{2}} \sum_{I_1,I_2} \int dk_1 dk_2 \; \phi_{n_1,n_2}(k_1,k_2) b^{\dagger}_{n_1,I_1,k_1} b^{\dagger}_{n_2,I_2,k_2}, \tag{A.1}$$

where p and q run over all the output channels, $\phi_{p,q}$ is the amplitude of the BWF that is associated with the photon pair exiting from channels p and q and

$$\sum_{p,q} \int \; dk_1 dk_2 \, |\phi_{p,q}(k_1,k_2)|^2 = 1. \tag{A.2}$$

Normalization of the photon pair state $|II\rangle$

Let us consider the unnormalized two-photon state

$$|\mathrm{II}\rangle = \frac{1}{\sqrt{N}} C^{\dagger}_{II} \, |\mathrm{vac}\rangle = \frac{1}{\sqrt{2N}} \sum_{p,q} \int dk_1 dk_2 \; \phi_{p,q}(k_1,k_2) b^{\dagger}_{k_1,p} b^{\dagger}_{k_2,q} \, |\mathrm{vac}\rangle \tag{A.3}$$

where N is a normalization constant, and we assume that the photons can exit the system from channels p and q with wave vectors k_1 and k_2, respectively. Imposing the normalization condition on Eq. (A.3)

$$\langle \mathrm{II}|\mathrm{II}\rangle = 1, \tag{A.4}$$

we obtain

$$\begin{aligned}\langle \mathrm{II}|\mathrm{II}\rangle = &\frac{1}{2N}\sum_{p,q}\sum_{p'q'}\int dk_1 dk_2 dk_1' dk_2'\ \phi_{p,q}(k_1,k_2)\phi^*_{p',q'}(k_1',k_2') \\ &\times \langle \mathrm{vac}|\, b_{k_1',p'} b_{k_2',q'} b^\dagger_{k_1,p} b^\dagger_{k_2,q}\,|\mathrm{vac}\rangle \\ =&\frac{1}{2N}\sum_{p,q}\int dk_1 dk_2\ \phi_{p,q}(k_1,k_2)\phi^*_{q,p}(k_2,k_1) \\ +&\frac{1}{2N}\sum_{p,q}\int dk_1 dk_2\ \phi_{p,q}(k_1,k_2)\phi^*_{p,q}(k_1,k_2) = 1\end{aligned} \tag{A.5}$$

and, given the symmetric nature of $\phi_{p,q}(k_1,k_2)$, we have

$$\frac{1}{N}\sum_{p,q}\int dk_1 dk_2\ |\phi_{p,q}(k_1,k_2)|^2 = 1, \tag{A.6}$$

which, in conjunction with (A.2), implies $N = 1$. Therefore the normalized photon pair state is

$$|II\rangle = C^\dagger_{II}\,|vac\rangle = \frac{1}{\sqrt{2}}\sum_{p,q}\int dk_1 dk_2\ \phi_{p,q}(k_1,k_2) b^\dagger_{k_1,p} b^\dagger_{k_2,q}\,|\mathrm{vac}\rangle \tag{A.7}$$

and this result holds for any source geometry.

Normalization of the four-photon state $|IV\rangle$ — General case

Let us define the unnormalized state $|IV\rangle$ as

$$\begin{aligned}|\mathrm{IV}\rangle = &\frac{1}{\sqrt{N}}(C^\dagger_{II})^2\,|\mathrm{vac}\rangle \\ =&\frac{1}{2\sqrt{N}}\sum_{p,q}\sum_{r,s}\int dk_1 dk_2 dk_3 dk_4\ \phi_{p,q}(k_1,k_2)\phi_{r,s}(k_3,k_4) \\ &\times b^\dagger_{k_1,p} b^\dagger_{k_2,q} b^\dagger_{k_3,r} b^\dagger_{k_4,s}\,|vac\rangle\,,\end{aligned} \tag{A.8}$$

N being a normalization constant. Imposing the normalization condition

$$\langle \mathrm{IV}|\mathrm{IV}\rangle = 1, \tag{A.9}$$

we have

$$\begin{aligned}\langle \mathrm{IV}|\mathrm{IV}\rangle =&\frac{1}{4N}\sum_{p,q}\sum_{r,s}\sum_{p',q'}\sum_{r',s'}\int dk_1 dk_2 dk_3 dk_4 dk'_1 dk'_2 dk'_3 dk'_4 \\ &\times\phi_{p,q}(k_1,k_2)\phi_{r,s}(k_3,k_4)\phi^*_{p',q'}(k'_1,k'_2)\phi^*_{r',s'}(k'_3,k'_4) \\ &\times\langle vac|\, b_{k'_1,p'} b_{k'_2,q'} b_{k'_3,r'} b_{k'_4,s'} b^\dagger_{k_1,p} b^\dagger_{k_2,q} b^\dagger_{k_3,r} b^\dagger_{k_4,s}\,|vac\rangle \\ &=1\end{aligned} \tag{A.10}$$

which, after a few manipulations, gives

$$\begin{aligned}\frac{1}{4N}\sum_{p,q}\sum_{r,s}\int dk_1 dk_2 dk_3 dk_4\ \phi_{p,q}(k_1,k_2)\phi_{r,s}(k_3,k_4) \\ \times\sigma_{ijkl}[\phi^*_{i,j}(k_1,k_2)\phi^*_{k,l}(k_3,k_4)] = 1,\end{aligned} \tag{A.11}$$

where $\sigma_{ijkl}[\dots]$ accounts for all the possible permutations of p, q, r, and s, which are 24 (the wave vectors follow accordingly).

At this point, the state normalization depends on

1. The number of non-vanishing terms in $\sigma_{ijkl}[\dots]$;
2. The separability of $\phi_{p,q}(k_1,k_2)$.

Both the previous points depend at least on the source geometry. So, without going into details on the source characteristics, we can state

$$N = \frac{\sum_{p,q}\sum_{r,s}\int dk_1 dk_2 dk_3 dk_4\ \phi_{p,q}(k_1,k_2)\phi_{r,s}(k_3,k_4)\sigma_{ijkl}[\phi^*_{i,j}(k_1,k_2)\phi^*_{k,l}(k_3,k_4)]}{4} \tag{A.12}$$

In the following we will provide some examples to clarify the dependence on the source geometry; moreover, they are instrumental in deriving other results throughout this thesis.

Normalization of the four-photon state $|IV\rangle$ — Side-coupled ring resonators

When we consider a single side-couple microring resonator and we assume the full separability of the BWF, a simple expression for the normalization constant N can be achieved. Indeed, now $p = q = 1$ and the permutations in (A.12) lead to 24 identical elements. This is actually the case encountered in Chapter 5, for the generation of energy-entangled W states.

Under these conditions, Eq. (A.12) can be recast in the form

$$N = \frac{24\int dk_1 dk_2 |\phi(k_1,k_2)|^2 \int dk_3 dk_4 |\phi(k_3,k_4)|^2}{4}, \tag{A.13}$$

which, together with the normalization condition on the BWF (A.2), gives $N = 6$. In conclusion, the normalized four-photon state $|IV\rangle$ is expressed as

$$|IV\rangle = \frac{1}{2\sqrt{6}} \int dk_1 dk_2 dk_3 dk_4 \ \phi(k_1,k_2)\phi(k_3,k_4) b^\dagger_{k_1} b^\dagger_{k_2} b^\dagger_{k_3} b^\dagger_{k_4} |vac\rangle \qquad \text{(A.14)}$$
$$= \frac{1}{\sqrt{6}} (C^\dagger_{II})^2 |vac\rangle \, .$$

A.2 Calculation of the output state

In this Appendix we derive equation (5.11) starting from the expression of the input state in (5.10). To this end, we apply the asymptotic field formalism of Section 1.3, and we recall that for each directional coupler the scattering matrix is given by

$$S_{DC} = \begin{bmatrix} ir & t \\ t & ir \end{bmatrix} \tag{A.15}$$

where r and t are the real reflection and transmission coefficients with $r^2+t^2=1$, while the linear propagation in a waveguide with length L simply introduces for a phase factor e^{ikL}. For instance, the input state after the first directional coupler DC_1 can be written as (see Fig. (5.5))

$$\begin{aligned} |\psi\rangle &= \frac{1}{2}\beta^2 e^{2iL_0(k_R+k_B)}[(t_1 b^\dagger_{R,1'} - ir_1 b^\dagger_{R,1})(t_1 b^\dagger_{B,1'} - ir_1 b^\dagger_{B,1})]^2 |vac\rangle \qquad \text{(A.16)} \\ &= \frac{1}{2}\beta^2 e^{2iL_0(k_R+k_B)}[(-ir_1 e^{ik_R L_1} b^\dagger_{R,1} + t_1 e^{ik_R L_{1'}} b^\dagger_{R,1'}) \\ &\times \ (-ir_1 e^{ik_B L_1} b^\dagger_{B,1} + t_1 e^{ik_B L_{1'}} b^\dagger_{B,1'})]^2 |vac\rangle\,, \end{aligned}$$

and then throughout the rest of the circuit, we have

$$\begin{aligned} |\psi\rangle &= \frac{1}{2}\beta^2 e^{2iL_0(k_R+k_B)}[(-ir_1 e^{ik_R L_1} b^\dagger_{R,1} + t_1 e^{ik_R L_{1'}} b^\dagger_{R,1'}) \qquad \text{(A.17)} \\ &\times \ (-ir_1 e^{ik_B L_1} b^\dagger_{B,1} + t_1 e^{ik_B L_{1'}} b^\dagger_{B,1'})]^2 |vac\rangle \\ &= \frac{1}{2}\beta^2 e^{2iL_0(k_R+k_B)}[(-ir_1 e^{ik_R L_1} b^\dagger_{R,1} - it_1 r_2 e^{ik_R(L_{1'}+L_2)} b^\dagger_{R,2} \\ &- \ it_1 t_2 r_3 e^{ik_R(L_{1'}+L_{2'}+L_3)} b^\dagger_{R,3} + t_1 t_2 t_3 e^{ik_R(L_{1'}+L_{2'}+L_4)} b^\dagger_{R,4}) \\ &\times \ (-ir_1 e^{ik_B L_1} b^\dagger_{B,1} - it_1 r_2 e^{ik_B(L_{1'}+L_2)} b^\dagger_{B,2} - it_1 t_2 r_3 e^{ik_B(L_{1'}+L_{2'}+L_3)} b^\dagger_{B,3} \\ &+ \ t_1 t_2 t_3 e^{ik_B(L_{1'}+L_{2'}+L_4)} b^\dagger_{B,4})]^2 |vac\rangle\,. \end{aligned}$$

where r_2 and r_3 are real reflection coefficients of DC_2 and DC_3, t_2 and t_3 being their correspondent transmission coefficients. Grouping in $|\Phi\rangle$ all the terms that are not leading to a single photon per channel we have

$$\begin{aligned} |\psi\rangle &= \frac{1}{2}\beta^2 e^{2iL_0(k_R+k_B)} |\Phi\rangle \qquad \text{(A.18)} \\ &+ \ 2ir_1 t_1^3 r_2 t_2^2 r_3 t_3 \beta^2 e^{2iL_0(k_R+k_B)}[e^{ik_R(L_1+L_{1'})} e^{ik_B(2L_{1'}+L_{2'})} b^\dagger_{R,1} \\ &\times \ \Big(e^{ik_R(L_{2'}+L_4)} e^{ik_B(L_2+L_3)} b^\dagger_{B,2} b^\dagger_{B,3} b^\dagger_{R,4} + e^{ik_R(L_{2'}+L_3)} e^{ik_B(L_2+L_4)} b^\dagger_{B,2} b^\dagger_{R,3} b^\dagger_{B,4} \\ &+ \ e^{ik_R L_2} e^{ik_B(L_{2'}+L_3+L_4)} b^\dagger_{R,2} b^\dagger_{B,3} b^\dagger_{B,4}\Big) + e^{ik_R(2L_{1'}+L_{2'})} e^{ik_B(L_1+L_{1'})} b^\dagger_{B,1} \\ &\times \ \Big(e^{ik_R(L_2+L_3)} e^{ik_B(L_{2'}+L_4)} b^\dagger_{R,2} b^\dagger_{R,3} b^\dagger_{B,4} + e^{ik_R(L_2+L_4)} e^{ik_B(L_{2'}+L_3)} b^\dagger_{R,2} b^\dagger_{B,3} b^\dagger_{R,4} \\ &+ \ e^{ik_R(L_{2'}+L_3+L_4)} e^{ik_B L_2} b^\dagger_{B,2} b^\dagger_{R,3} b^\dagger_{R,4}\Big)] |vac\rangle\,. \end{aligned}$$

We can express the output state as

$$\begin{aligned}
|\psi\rangle &= \eta\,|\Phi\rangle + 2\sqrt{3}ir_1t_1^3r_2t_2^2r_3t_3\beta^2e^{2iL_0(k_R+k_B)} \\
&\times [e^{ik_R(L_1+L_{1'}+L_{2'}+L_4)}e^{ik_B(2L_{1'}+L_2+L_{2'}+L_3)}b^\dagger_{R,1} \\
&\times \frac{1}{\sqrt{3}}(b^\dagger_{B,2}b^\dagger_{B,3}b^\dagger_{R,4} + e^{-i\Delta k\Delta L_{34}}b^\dagger_{B,2}b^\dagger_{R,3}b^\dagger_{B,4} + e^{-i\Delta k\Delta L_{22'4}}b^\dagger_{R,2}b^\dagger_{B,3}b^\dagger_{B,4}) \\
&+ e^{ik_R(2L_{1'}+L_2+L_{2'}+L_3)}e^{ik_B(L_1+L_{1'}+L_{2'}+L_4)}b^\dagger_{B,1} \\
&\times \frac{1}{\sqrt{3}}(b^\dagger_{R,2}b^\dagger_{R,3}b^\dagger_{B,4} + e^{i\Delta k\Delta L_{34}}b^\dagger_{R,2}b^\dagger_{B,3}b^\dagger_{R,4} + e^{i\Delta k\Delta L_{22'4}}b^\dagger_{B,2}b^\dagger_{R,3}b^\dagger_{R,4})]\,|vac\rangle\,,
\end{aligned} \tag{A.19}$$

where $\eta = \frac{1}{2}\alpha\beta^2e^{2iL_0(k_R+k_B)}$ is the probability amplitude of obtaining a different output than a W state, and

$$\begin{aligned}
\Delta k &= k_B - k_R \\
\Delta L_{34} &= L_3 - L_4 \\
\Delta L_{22'4} &= L_2 - L_{2'} - L_4.
\end{aligned} \tag{A.20}$$

In short, the output state is finally given by

$$\begin{aligned}
|\psi\rangle &= \eta\,|\Phi\rangle + 2\sqrt{3}ir_1t_1^3r_2t_2^2r_3t_3\beta^2e^{2iL_0(k_R+k_B)} \\
&\times [e^{i\Gamma_1}b^\dagger_{R,1}\,|W_{T_1}\rangle + e^{i\Gamma_2}b^\dagger_{B,1}\,|W_{T_2}\rangle]
\end{aligned} \tag{A.21}$$

where

$$\begin{aligned}
&|W_{T_1}\rangle = \\
&\frac{1}{\sqrt{3}}(b^\dagger_{B,2}b^\dagger_{B,3}b^\dagger_{R,4} + e^{-i\Delta k\Delta L_{34}}b^\dagger_{B,2}b^\dagger_{R,3}b^\dagger_{B,4} + e^{-i\Delta k\Delta L_{22'4}}b^\dagger_{R,2}b^\dagger_{B,3}b^\dagger_{B,4})\,|vac\rangle \\
&\equiv \frac{1}{\sqrt{3}}(|BBR\rangle + e^{-i\Delta k\Delta L_{34}}\,|BRB\rangle + e^{-i\Delta k\Delta L_{22'4}}\,|RBB\rangle),
\end{aligned} \tag{A.22}$$

$$\begin{aligned}
&|W_{T_2}\rangle = \\
&\frac{1}{\sqrt{3}}(b^\dagger_{R,2}b^\dagger_{R,3}b^\dagger_{B,4} + e^{i\Delta k\Delta L_{34}}b^\dagger_{R,2}b^\dagger_{B,3}b^\dagger_{R,4} + e^{i\Delta k\Delta L_{22'4}}b^\dagger_{B,2}b^\dagger_{R,3}b^\dagger_{R,4})\,|vac\rangle \\
&\equiv \frac{1}{\sqrt{3}}(|RRB\rangle + e^{i\Delta k\Delta L_{34}}\,|RBR\rangle + e^{i\Delta k\Delta L_{22'4}}\,|BRR\rangle),
\end{aligned} \tag{A.23}$$

are normalized energy-entangled W states and

$$\begin{aligned}
\Gamma_1 &= k_R(L_1 + L_{1'} + L_{2'} + L_4) + k_B(2L_{1'} + L_2 + L_{2'} + L_3), \\
\Gamma_2 &= k_R(2L_{1'} + L_2 + L_{2'} + L_3) + k_B(L_1 + L_{1'} + L_{2'} + L_4).
\end{aligned} \tag{A.24}$$

A.3 X, Y , and Z measurements for the tomography of ρ_{34}

Here we are interested in expressing the diagonal elements of ρ_{56} as a function of the elements of the reduced density matrix ρ_{34}. Recalling Eq. (5.32), we can look at the first diagonal term

$$\begin{aligned}
&\tau_{11}\left|R_5B_5\right\rangle\left\langle R_5B_5\right| = \qquad\qquad (A.25)\\
&\Big|S_{11}(R)\Big|^2\Big|S_{11}(B)\Big|^2\left|R_3B_3\right\rangle\left\langle R_3B_3\right| + \Big|S_{11}(R)\Big|^2 S_{11}(B)S_{12}^*(B)\left|R_3B_3\right\rangle\left\langle R_3B_4\right|\\
&+S_{11}(R)S_{12}^*(R)\Big|S_{11}(B)\Big|^2\left|R_3B_3\right\rangle\left\langle R_4B_3\right| + S_{11}(R)S_{12}^*(R)S_{11}(B)S_{12}^*(B)\left|R_3B_3\right\rangle\left\langle R_4B_4\right|\\
&+\Big|S_{11}(R)\Big|^2 S_{12}(B)S_{11}^*(B)\left|R_3B_4\right\rangle\left\langle R_3B_3\right| + \Big|S_{11}(R)\Big|^2\Big|S_{12}(B)\Big|^2\left|R_3B_4\right\rangle\left\langle R_3B_4\right|\\
&+S_{11}(R)S_{12}^*(R)S_{12}(B)S_{11}^*(B)\left|R_3B_4\right\rangle\left\langle R_4B_3\right| + S_{11}(R)S_{12}^*(R)\Big|S_{12}(B)\Big|^2\left|R_3B_4\right\rangle\left\langle R_4B_4\right|\\
&+S_{12}(R)S_{11}^*(R)\Big|S_{11}(B)\Big|^2\left|R_4B_3\right\rangle\left\langle R_3B_3\right| + S_{12}(R)S_{11}^*(R)S_{11}(B)S_{12}^*(B)\left|R_4B_3\right\rangle\left\langle R_3B_4\right|\\
&+\Big|S_{12}(R)\Big|^2\Big|S_{11}(B)\Big|^2\left|R_4B_3\right\rangle\left\langle R_4B_3\right| + \Big|S_{12}(R)\Big|^2 S_{11}(B)S_{12}^*(B)\left|R_4B_3\right\rangle\left\langle R_4B_4\right|\\
&+S_{12}(R)S_{11}^*(R)S_{12}(B)S_{11}^*(B)\left|R_4B_4\right\rangle\left\langle R_3B_3\right| + S_{12}(R)S_{11}^*(R)\Big|S_{12}(B)\Big|^2\left|R_4B_4\right\rangle\left\langle R_3B_4\right|\\
&+\Big|S_{12}(R)\Big|^2 S_{12}(B)S_{11}^*(B)\left|R_4B_4\right\rangle\left\langle R_4B_3\right| + \Big|S_{12}(R)\Big|^2\Big|S_{12}(B)\Big|^2\left|R_4B_4\right\rangle\left\langle R_4B_4\right|
\end{aligned}$$

which, in terms of the ρ_{34} matrix coefficients, becomes

$$\begin{aligned}
&\tau_{11}\left|R_5B_5\right\rangle\left\langle R_5B_5\right| = \qquad\qquad (A.26)\\
&\Big|S_{11}(R)\Big|^2\Big|S_{11}(B)\Big|^2\rho_{11} + \Big|S_{11}(R)\Big|^2 S_{11}(B)S_{12}^*(B)\rho_{12} + S_{11}(R)S_{12}^*(R)\Big|S_{11}(B)\Big|^2\rho_{13}\\
&+S_{11}(R)S_{12}^*(R)S_{11}(B)S_{12}^*(B)\rho_{14} + \Big|S_{11}(R)\Big|^2 S_{12}(B)S_{11}^*(B)\rho_{12}^*\\
&+\Big|S_{11}(R)\Big|^2\Big|S_{12}(B)\Big|^2\rho_{22} + S_{11}(R)S_{12}^*(R)S_{12}(B)S_{11}^*(B)\rho_{23}\\
&+S_{11}(R)S_{12}^*(R)\Big|S_{12}(B)\Big|^2\rho_{24} + S_{12}(R)S_{11}^*(R)\Big|S_{11}(B)\Big|^2\rho_{13}^*\\
&+S_{12}(R)S_{11}^*(R)S_{11}(B)S_{12}^*(B)\rho_{23}^* + \Big|S_{12}(R)\Big|^2\Big|S_{11}(B)\Big|^2\rho_{33}\\
&+\Big|S_{12}(R)\Big|^2 S_{11}(B)S_{12}^*(B)\rho_{34} + S_{12}(R)S_{11}^*(R)S_{12}(B)S_{11}^*(B)\rho_{14}^*\\
&+S_{12}(R)S_{11}^*(R)\Big|S_{12}(B)\Big|^2\rho_{24}^* + \Big|S_{12}(R)\Big|^2 S_{12}(B)S_{11}^*(B)\rho_{34}^*\\
&+\Big|S_{12}(R)\Big|^2\Big|S_{12}(B)\Big|^2(1-\rho_{11}-\rho_{22}-\rho_{33}).
\end{aligned}$$

The coefficient τ_{11} corresponds to the probability of detecting both the red and the blue photon in channel 5; we shall refer to this measurement as an $X[S(R), S(B)]$ measurement. Rearranging the terms it easier to see the dependence on the 15 elements of the original density matrix,

$$
\begin{aligned}
X[S(R),S(B)] = \qquad\qquad (A.27)\\
\Big|S_{11}(R)\Big|^2\Big|S_{11}(B)\Big|^2 a_{11} + \Big|S_{11}(R)\Big|^2\Big|S_{12}(B)\Big|^2 a_{22} + \Big|S_{12}(R)\Big|^2\Big|S_{11}(B)\Big|^2 a_{33}\\
+\Big|S_{12}(R)\Big|^2\Big|S_{12}(B)\Big|^2(1-a_{11}-a_{22}-a_{33})\\
+2\Big|S_{11}(R)\Big|^2 Re[S_{11}(B)S_{12}^*(B)]a_{12}^R - 2\Big|S_{11}(R)\Big|^2 Im[S_{11}(B)S_{12}^*(B)]a_{12}^I\\
+2Re[S_{11}(R)S_{12}^*(R)]\Big|S_{11}(B)\Big|^2 a_{13}^R - 2Im[S_{11}(R)S_{12}^*(R)]\Big|S_{11}(B)\Big|^2 a_{13}^I\\
+2Re[S_{11}(R)S_{12}^*(R)S_{11}(B)S_{12}^*(B)]a_{14}^R - 2Im[S_{11}(R)S_{12}^*(R)S_{11}(B)S_{12}^*(B)]a_{14}^I\\
+2Re[S_{11}(R)S_{12}^*(R)S_{12}(B)S_{11}^*(B)]a_{23}^R - 2Im[S_{11}(R)S_{12}^*(R)S_{12}(B)S_{11}^*(B)]a_{23}^I\\
+2Re[S_{11}(R)S_{12}^*(R)]\Big|S_{12}(B)\Big|^2 a_{24}^R - 2Im[S_{11}(R)S_{12}^*(R)]\Big|S_{12}(B)\Big|^2 a_{24}^I\\
+2\Big|S_{12}(R)\Big|^2 Re[S_{11}(B)S_{12}^*(B)]a_{34}^R - 2\Big|S_{12}(R)\Big|^2 Im[S_{11}(B)S_{12}^*(B)]a_{34}^I
\end{aligned}
$$

A similar reasoning applies to the other terms in the diagonal of ρ_{56}. We can define the a $Y[S(R), S(B)]$ measurement as that corresponding to the probability τ_{22} of finding a red photon in channel 5 and a blue photon in channel 6. Such measurement is related to the elements of ρ_{34} by

$$
\begin{aligned}
Y[S(R),S(B)] = \qquad\qquad (A.28)\\
\Big|S_{11}(R)\Big|^2\Big|S_{12}(B)\Big|^2 a_{11} + \Big|S_{11}(R)\Big|^2\Big|S_{11}(B)\Big|^2 a_{22} + \Big|S_{12}(R)\Big|^2\Big|S_{12}(B)\Big|^2 a_{33}\\
+\Big|S_{12}(R)\Big|^2\Big|S_{11}^*(B)\Big|^2(1-a_{11}-a_{22}-a_{33})\\
-2\Big|S_{11}(R)\Big|^2 Re[S_{11}(B)S_{12}^*(B)]a_{12}^R + 2\Big|S_{11}(R)\Big|^2 Im[S_{11}(B)S_{12}^*(B)]a_{12}^I\\
+2Re[S_{11}(R)S_{12}^*(R)]\Big|S_{12}(B)\Big|^2 a_{13}^R - 2Im[S_{11}(R)S_{12}^*(R)]\Big|S_{12}(B)\Big|^2 a_{13}^I\\
-2Re[S_{11}(R)S_{12}^*(R)S_{11}(B)S_{12}^*(B)]a_{14}^R + 2Im[S_{11}(R)S_{12}^*(R)S_{11}(B)S_{12}^*(B)]a_{14}^I\\
-2Re[S_{11}(R)S_{12}^*(R)S_{11}^*(B)S_{12}(B)]a_{23}^R + 2Im[S_{11}(R)S_{12}^*(R)S_{11}^*(B)S_{12}(B)]a_{23}^I\\
+2Re[S_{11}(R)S_{12}^*(R)]\Big|S_{11}(B)\Big|^2 a_{24}^R - 2Im[S_{11}(R)S_{12}^*(R)]\Big|S_{11}(B)\Big|^2 a_{24}^I\\
-2\Big|S_{12}(R)\Big|^2 Re[S_{11}(B)S_{12}^*(B)]a_{34}^R + 2\Big|S_{12}(R)\Big|^2 Im[S_{11}(B)S_{12}^*(B)]a_{34}^I,
\end{aligned}
$$

Finally, we define a $Z[S(R), S(B)]$ measurement as that corresponding to the probability τ_{33} of finding a red photon in channel 6 and a blue photon in channel 5. Once more, this measurement is related to the elements of ρ_{34} by

$$
\begin{aligned}
Z[S(R),S(B)] = \qquad\qquad & (A.29)\\
\Big|S_{12}(R)\Big|^2\Big|S_{11}(B)\Big|^2 a_{11} + \Big|S_{12}(R)\Big|^2\Big|S_{12}(B)\Big|^2 a_{22} + \Big|S_{11}(R)\Big|^2\Big|S_{11}(B)\Big|^2 a_{33}&\\
+\Big|S_{11}(R)\Big|^2\Big|S_{12}(B)\Big|^2(1-a_{11}-a_{22}-a_{33})&\\
+2\Big|S_{12}(R)\Big|^2 Re[S_{11}(B)S_{12}^*(B)]a_{12}^R - 2\Big|S_{12}(R)\Big|^2 Im[S_{11}(B)S_{12}^*(B)]a_{12}^I&\\
-2Re[S_{11}(R)S_{12}^*(R)]\Big|S_{11}(B)\Big|^2 a_{13}^R + 2Im[S_{11}(R)S_{12}^*(R)]\Big|S_{11}(B)\Big|^2 a_{13}^I&\\
-2Re[S_{11}(R)S_{12}^*(R)S_{11}(B)S_{12}^*(B)]a_{14}^R + 2Im[S_{11}(R)S_{12}^*(R)S_{11}(B)S_{12}^*(B)]a_{14}^I&\\
-2Re[S_{11}(R)S_{12}^*(R)S_{11}^*(B)S_{12}(B)]a_{23}^R + 2Im[S_{11}(R)S_{12}^*(R)S_{11}^*(B)S_{12}(B)]a_{23}^I&\\
-2Re[S_{11}(R)S_{12}^*(R)]\Big|S_{12}(B)\Big|^2 a_{24}^R + 2Im[S_{11}(R)S_{12}^*(R)]\Big|S_{12}(B)\Big|^2 a_{24}^I&\\
+2\Big|S_{11}(R)\Big|^2 Re[S_{11}(B)S_{12}^*(B)]a_{34}^R - 2\Big|S_{11}(R)\Big|^2 Im[S_{11}(B)S_{12}^*(B)]a_{34}^I.&
\end{aligned}
$$

The last term τ_{44} can be ignored, since from the unit trace condition it follows that $\tau_{44} = 1 - \tau_{11} - \tau_{22} - \tau_{33}$.

The real coefficients X, Y, and Z depend on the initial density matrix parameters, as well as on the elements of the scattering matrices $S(R)$ and $S(B)$. The basic strategy we devise in Chapter 5 for the complete reconstruction of ρ_{34} is to perform the coincidence measurements X, Y, and Z, subject to a few selected scattering matrices.

Appendix B

Generation of path-encoded GHZ states

B.1 Calculation of the output state

Referring to the schematic representation in Fig. 6.5, the photon pair creation operator $C_{II}^{\dagger}$ can be expressed very generally as

$$C_{II}^{\dagger} = \frac{1}{\sqrt{2}} \sum_{p,q} \int dk_1 dk_2 \phi_{p,q}\left(k_1, k_2\right) b_{k_1,p}^{\dagger} b_{k_2,q}^{\dagger}, \tag{B.1}$$

where p and q run over all the output channels, $\phi_{p,q}$ is the amplitude of the BWF that is associated with the photon pair exiting from channels p and q,

$$\begin{aligned} \phi_{p,q}(k_1,k_2) = & \frac{3\sqrt{2}i\pi\alpha^2\hbar}{4\beta\epsilon_0} \int dk_3 \ \phi_P(k_3)\phi_P(k_1+k_2-k_3) \\ & \times \sqrt{\omega(k_1)\omega(k_2)\omega(k_3)\omega(k_1+k_2-k_3)} \\ & \times \sum_n A_n(k_3)A_n(k_1+k_2-k_3)B_{n,p}(k_1)B_{n,q}(k_2) \\ & \times \int dr \ \Gamma_3 D_{n,k_1}^{asy-in}(r) D_{n,k_2}^{asy-in}(r) D_{n,k_3}^{asy-in}(r) D_{n,k_1+k_2-k_3}^{asy-in}(r) \end{aligned} \tag{B.2}$$

where $A_n(k)$ are the complex coefficients linking the field propagating linearly from the input channel to the field immediately before the coupling point of the n-th ring, while $B_{n,p(q)}(k)$ are the complex coefficients relating the field right after the coupling point of the n-th ring to the field in the output channel $p(q)$. The BWF if Eq. (B.2) is normalized according to

$$\sum_{p,q} \int \ dk_1 dk_2 \left|\phi_{p,q}(k_1,k_2)\right|^2 = 1. \tag{B.3}$$

We are now interested in comparing the efficiency of our source with that of a single microring resonator. To this end, we introduce the average number of generated photons for a side-coupled microring, β_{ring}, pumped with the same average number of photons α^2 as our source, and Eq. (B.2) becomes

$$\begin{aligned}\phi_{p,q}(k_1,k_2) = &\sum_n B_{n,p}(k_1)B_{n,q}(k_2)\frac{\beta_{ring}}{\beta} \\ &\times\frac{3\sqrt{2}i\pi\alpha^2\hbar}{4\beta_{ring}\epsilon_0}\int dk_3\ \phi_P(k_3)\phi_P(k_1+k_2-k_3) \\ &\times\sqrt{\omega(k_1)\omega(k_2)\omega(k_3)\omega(k_1+k_2-k_3)}A_n(k_3)A_n(k_1+k_2-k_3) \\ &\times\int dr\ \Gamma_3\tilde{D}^{asy-in}_{n,k_1}(r)\tilde{D}^{asy-in}_{n,k_2}(r)\tilde{D}^{asy-in}_{n,k_3}(r)\tilde{D}^{asy-in}_{n,k_1+k_2-k_3}(r)\end{aligned} \tag{B.4}$$

The normalization condition (B.3) requires that

$$\begin{aligned}&\sum_{p,q}\int dk_1dk_2|\phi_{p,q}(k_1,k_2)|^2 \\ =&-\left|\frac{\beta_{ring}}{\beta}\right|^2\sum_{p,q}\int dk_1dk_2\sum_{nn'}B_{n,p}(k_1)B_{n,q}(k_2)B^*_{n',p}(k_1)B^*_{n',q}(k_2) \\ &\times\frac{3\sqrt{2}i\pi\alpha^2\hbar}{4\beta_{ring}\epsilon_0}\int dk_3\ \phi_P(k_3)\phi_P(k_1+k_2-k_3) \\ &\times\sqrt{\omega(k_1)\omega(k_2)\omega(k_3)\omega(k_1+k_2-k_3)}A_n(k_3)A_n(k_1+k_2-k_3) \\ &\times\int dr\ \Gamma_3\tilde{D}^{asy-in}_{n,k_1}(r)\tilde{D}^{asy-in}_{n,k_2}(r)\tilde{D}^{asy-in}_{n,k_3}(r)\tilde{D}^{asy-in}_{n,k_1+k_2-k_3}(r) \\ &\times\frac{3\sqrt{2}i\pi\alpha^2\hbar}{4\beta^*_{ring}\epsilon_0}\int dk'_3\ \phi^*_P(k'_3)\phi^*_P(k_1+k_2-k'_3) \\ &\times\sqrt{\omega(k_1)\omega(k_2)\omega(k'_3)\omega(k_1+k_2-k'_3)}A^*_{n'}(k'_3)A^*_{n'}(k_1+k_2-k'_3) \\ &\times\int dr\ \Gamma_3[\tilde{D}^{asy-in}_{n',k_1}(r)]^*[\tilde{D}^{asy-in}_{n',k_2}(r)]^*[\tilde{D}^{asy-in}_{n',k'_3}(r)]^*[\tilde{D}^{asy-in}_{n',k_1+k_2-k'_3}(r)]^* \\ =&1\end{aligned} \tag{B.5}$$

and we shall compare this expression to the normalization condition of the BWF for photon pairs generated in the side-coupled microring resonator. To this end, we note that the field amplitudes should satisfy two conditions:

- **Condition 1:** $A_n(k)A_n(k_1+k_2-k) \equiv \mathbb{A}^2_n(k_1,k_2)$, i.e. the product of the input coefficients does not depend on k. When this condition is met, we

can extract such contribution from the integral in Eq. (B.5) and obtain

$$
\begin{aligned}
&\sum_{p,q}\int dk_1dk_2|\phi_{p,q}(k_1,k_2)|^2 \qquad\qquad (B.6)\\
=&-\Big|\frac{\beta_{ring}}{\beta}\Big|^2\sum_{p,q}\int dk_1dk_2\sum_{nn'}B_{n,p}(k_1)B_{n,q}(k_2)B^*_{n',p}(k_1)B^*_{n',q}(k_2)\\
&\times\mathbb{A}^2_n(k_1,k_2)(\mathbb{A}^*_{n'}(k_1,k_2))^2\frac{3\sqrt{2}i\pi\alpha^2\hbar}{4\beta_{ring}\epsilon_0}\\
&\times\int dk_3\ \phi_P(k_3)\phi_P(k_1+k_2-k_3)\sqrt{\omega(k_1)\omega(k_2)\omega(k_3)\omega(k_1+k_2-k_3)}\\
&\times\int dr\ \Gamma_3\tilde{D}^{asy-in}_{n,k_1}(r)\tilde{D}^{asy-in}_{n,k_2}(r)\tilde{D}^{asy-in}_{n,k_3}(r)\tilde{D}^{asy-in}_{n,k_1+k_2-k_3}(r)\\
&\times\frac{3\sqrt{2}i\pi\alpha^2\hbar}{4\beta^*_{ring}\epsilon_0}\int dk'_3\ \phi^*_P(k'_3)\phi^*_P(k_1+k_2-k'_3)\\
&\times\sqrt{\omega(k_1)\omega(k_2)\omega(k'_3)\omega(k_1+k_2-k'_3)}\\
&\times\int dr\ \Gamma_3[\tilde{D}^{asy-in}_{n',k_1}(r)]^*[\tilde{D}^{asy-in}_{n',k_2}(r)]^*[\tilde{D}^{asy-in}_{n',k'_3}(r)]^*[\tilde{D}^{asy-in}_{n',k_1+k_2-k'_3}(r)]^*\\
=&\Big|\frac{\beta_{ring}}{\beta}\Big|^2\sum_{p,q}\int dk_1dk_2\sum_{nn'}B_{n,p}(k_1)B_{n,q}(k_2)B^*_{n',p}(k_1)B^*_{n',q}(k_2)\\
&\times\mathbb{A}^2_n(k_1,k_2)(\mathbb{A}^*_{n'}(k_1,k_2))^2|\phi_{ring}(k_1,k_2)|^2
\end{aligned}
$$

- **Condition 2:**
  $B_{n,p}(k_1)B_{n,q}(k_2)B^*_{n',p}(k_1)B^*_{n',q}(k_2)\equiv\mathbb{B}^2_{n,p,q}(k_1,k_2)\mathbb{B}^2_{n',p,q}(k_1,k_2)\equiv\mathfrak{B}^4_{n,n',p,q}$ and $\mathbb{A}^2_n(k_1,k_2)(\mathbb{A}^*_{n'}(k_1,k_2))^2\equiv\mathfrak{A}^4_{n,n'}$. Thus, both the product of the input coefficients and the product of the output coefficients is a constant. Therefore, Eq. (B.5) becomes

$$
\begin{aligned}
&\sum_{p,q}\int dk_1dk_2|\phi_{p,q}(k_1,k_2)|^2 \qquad\qquad (B.7)\\
=&\Big|\frac{\beta_{ring}}{\beta}\Big|^2\sum_{p,q}\int dk_1dk_2\sum_{nn'}\mathbb{B}^2_{n,p,q}(k_1,k_2)\mathbb{B}^2_{n',p,q}(k_1,k_2)\\
&\times\mathbb{A}^2_n(k_1,k_2)(\mathbb{A}^*_{n'}(k_1,k_2))^2|\phi_{ring}(k_1,k_2)|^2\\
=&\Big|\frac{\beta_{ring}}{\beta}\Big|^2\sum_{p,q}\sum_{nn'}\mathfrak{A}^4_{n,n'}\mathfrak{B}^4_{n,n',p,q}\int dk_1dk_2|\phi_{ring}(k_1,k_2)|^2\\
=&\Big|\frac{\beta_{ring}}{\beta}\Big|^2\sum_{p,q}\sum_{nn'}\mathfrak{A}^4_{n,n'}\mathfrak{B}^4_{n,n',p,q}=1,
\end{aligned}
$$

given the normalization condition on $\phi_{ring}(k_1,k_2)$. This allows us to recover the relation between β and β_{ring} once the coefficients $A_n(k)$ and $B_{n,p(q)}(k)$ are

calculated. Hence,

$$\left|\frac{\beta_{ring}}{\beta}\right|^2 = \frac{1}{\sum_{p,q}\sum_{nn'}\mathfrak{A}^4_{n,n'}\mathfrak{B}^4_{n,n',p,q}} \tag{B.8}$$

Let us now focus on our particular source geometry, as in Fig. 6.6. The $A_n(k)$ and $B_{n,p(q)}(k)$ coefficients are given by

$$\begin{aligned} A_1(k) &= -t_1 t_{2U} e^{i\phi_1} e^{ik(L_1+L_2)} \\ A_2(k) &= i t_1 r_{2U} e^{ik(L_1+L_2)} \\ A_3(k) &= r_1 r_{2D} e^{i\phi} e^{ik(L_1+L_2)} \\ A_4(k) &= i r_1 t_{2D} e^{i(\phi+\phi_2)} e^{ik(L_1+L_2)} \end{aligned} \tag{B.9}$$

and

$$\begin{aligned} B_{1,1}(k) &= r_{3U} e^{-ikL_3} & B_{3,4}(k) &= i t_{3D} e^{-ikL_3} \\ B_{1,2}(k) &= i t_{3U} e^{-ikL_3} & B_{4,3}(k) &= i t_{3D} e^{-ikL_3} \\ B_{2,1}(k) &= i t_{3U} e^{-ikL_3} & B_{4,4}(k) &= r_{3D} e^{-ikL_3} \\ B_{2,2}(k) &= r_{3U} e^{-ikL_3} & B_{1,3}(k) &= B_{1,4}(k) = B_{2,3}(k) = B_{2,4} = 0 \\ B_{3,3}(k) &= r_{3D} e^{-ikL_3} & B_{3,1}(k) &= B_{3,2}(k) = B_{4,1}(k) = B_{4,2} = 0 \end{aligned} \tag{B.10}$$

where r_1 and t_1 are the real reflection and transmission coefficients of the first DC, and $r_{2U(D)}$ and $r_{3U(D)}$ are the real reflection coefficients of the upper and lower directional couplers before and after the ring resonators, respectively, $t_{2U(D)}$ and $t_{3U(D)}$ being their corresponding transmission coefficients.

Hence, the first condition, namely $A_n(k)A_n(k_1+k_2-k) \equiv \mathbb{A}^2_n(k_1,k_2)$, is easily verified since

$$\begin{aligned} &A_1(k_3)A_1(k_1+k_2-k_3) = \\ &t_1^2 t_{2U}^2 e^{2i\phi_1} e^{2i(k_1+k_2)(L_1+L_2)} \equiv \mathbb{A}^2_1(k_1,k_2) \end{aligned} \tag{B.11}$$

$$\begin{aligned} &A_2(k_3)A_2(k_1+k_2-k_3) = \\ &-t_1^2 r_{2U}^2 e^{2i(k_1+k_2)(L_1+L_2)} \equiv \mathbb{A}^2_2(k_1,k_2) \end{aligned} \tag{B.12}$$

$$\begin{aligned} &A_3(k_3)A_3(k_1+k_2-k_3) = \\ &r_1^2 r_{2D}^2 e^{2i\phi} e^{2i(k_1+k_2)(L_1+L_2)} \equiv \mathbb{A}^2_3(k_1,k_2) \end{aligned} \tag{B.13}$$

$$\begin{aligned} &A_4(k_3)A_4(k_1+k_2-k_3) = \\ &-r_1^2 t_{2D}^2 e^{2i(\phi+\phi_2)} e^{2i(k_1+k_2)(L_1+L_2)} \equiv \mathbb{A}^2_4(k_1,k_2) \end{aligned} \tag{B.14}$$

and the second condition, namely
$B_{n,p}(k_1)B_{n,q}(k_2)B^*_{n',p}(k_1)B^*_{n',q}(k_2) \equiv \mathbb{B}^2_{n,p,q}(k_1,k_2)\mathbb{B}^2_{n',p,q}(k_1,k_2) \equiv \mathfrak{B}^4_{n,n',p,q}$
and $\mathbb{A}^2_n(k_1,k_2)(\mathbb{A}^*_{n'}(k_1,k_2))^2 \equiv \mathfrak{A}^4_{n,n'}$, is verified too, since

$$\begin{aligned}
\mathbb{A}^2_1(k_1,k_2)(\mathbb{A}^*_1(k_1,k_2))^2 &= t_1^4 t_{2U}^4 \equiv \mathfrak{A}^4_{1,1} \\
\mathbb{A}^2_1(k_1,k_2)(\mathbb{A}^*_2(k_1,k_2))^2 &= -t_1^4 t_{2U}^2 r_{2U}^2 e^{2i\phi_1} \equiv \mathfrak{A}^4_{1,2} = (\mathfrak{A}^4_{2,1})^* \\
\mathbb{A}^2_1(k_1,k_2)(\mathbb{A}^*_3(k_1,k_2))^2 &= t_1^2 r_1^2 t_{2U}^2 r_{2D}^2 e^{2i(\phi_1-\phi)} \equiv \mathfrak{A}^4_{1,3} = (\mathfrak{A}^4_{3,1})^* \\
\mathbb{A}^2_1(k_1,k_2)(\mathbb{A}^*_4(k_1,k_2))^2 &= -t_1^2 r_1^2 t_{2U}^2 t_{2D}^2 e^{2i(\phi_1-\phi-\phi_2)} \equiv \mathfrak{A}^4_{1,4} = (\mathfrak{A}^4_{4,1})^* \\
\mathbb{A}^2_2(k_1,k_2)(\mathbb{A}^*_2(k_1,k_2))^2 &= -t_1^4 r_{2U}^4 \equiv \mathfrak{A}^4_{2,2} \\
\mathbb{A}^2_2(k_1,k_2)(\mathbb{A}^*_3(k_1,k_2))^2 &= -t_1^2 r_1^2 r_{2U}^2 r_{2D}^2 e^{-2i\phi} \equiv \mathfrak{A}^4_{2,3} = (\mathfrak{A}^4_{3,2})^* \\
\mathbb{A}^2_2(k_1,k_2)(\mathbb{A}^*_4(k_1,k_2))^2 &= t_1^2 r_1^2 r_{2U}^2 t_{2D}^2 e^{-2i(\phi+\phi_2)} \equiv \mathfrak{A}^4_{2,4} = (\mathfrak{A}^4_{4,3})^* \\
\mathbb{A}^2_3(k_1,k_2)(\mathbb{A}^*_3(k_1,k_2))^2 &= r_1^4 r_{2D}^4 \equiv \mathfrak{A}^4_{3,3} \\
\mathbb{A}^2_3(k_1,k_2)(\mathbb{A}^*_4(k_1,k_2))^2 &= -r_1^4 r_{2D}^2 t_{2D}^2 e^{2i(\phi-\phi-\phi_2)} \equiv \mathfrak{A}^4_{3,4} = (\mathfrak{A}^4_{4,3})^* \\
\mathbb{A}^2_4(k_1,k_2)(\mathbb{A}^*_4(k_1,k_2))^2 &= r_1^4 t_{2D}^4 \equiv \mathfrak{A}^4_{4,4}
\end{aligned} \tag{B.15}$$

and all the coefficients $B_{n,p(q)}(k_{1(2)})$ are of the form

$$\begin{aligned}
B_{n,p}(k_1) &= b_{n,p} e^{-ik_1 L_3} \\
B_{n,q}(k_2) &= b_{n,q} e^{-ik_2 L_3}
\end{aligned} \tag{B.16}$$

leading to

$$\begin{aligned}
B_{n,p}(k_1)B_{n,q}(k_2) &= b_{n,p}b_{n,q}e^{-i(k_1+k_2)L_3} \equiv \mathbb{B}^2_{n,p,q}(k_1,k_2) \\
B^*_{n',p}(k_1)B^*_{n',q}(k_2) &= b^*_{n',p}b^*_{n',q}e^{i(k_1+k_2)L_3} \equiv \mathbb{B}^2_{n',p,q}(k_1,k_2) \\
\mathbb{B}^2_{n,p,q}(k_1,k_2)\mathbb{B}^2_{n',p,q}(k_1,k_2) &= b_{n,p}b_{n,q}b^*_{n',p}b^*_{n',q} \equiv \mathfrak{B}^4_{n,n',p,q}.
\end{aligned} \tag{B.17}$$

In conclusion, using Eqs. (B.9) and(B.10) in Eq. (B.8), we have

$$\left|\frac{\beta_{ring}}{\beta}\right|^2 = \frac{1}{\sum_{p,q}\sum_{nn'}\mathfrak{A}^4_{n,n'}\mathfrak{B}^4_{n,n',p,q}} = 4, \tag{B.18}$$

thus, our structure is capable of generating the photon pair state with 1/4 of the average number of generated photons of a single side-coupled ring resonator under the same pumping rate.

We can now move on to reconstruct the two-photon state at the output of our source of the Bell state from (6.3). Once more, from the coefficients $A_n(k)$ and $B_{n,p(q)}(k)$, we observe that

$$\phi_{1,1}(k_1,k_2) = \phi_{2,2}(k_1,k_2) = \phi_{3,3}(k_1,k_2) = \phi_{4,4}(k_1,k_2) = 0 \tag{B.19}$$

due to the reverse Hong Ou Mandel effect,

$$\phi_{1,3}(k_1,k_2)=\phi_{1,4}(k_1,k_2)=\phi_{2,3}(k_1,k_2)=\phi_{2,4}(k_1,k_2)=0 \tag{B.20}$$
$$\phi_{3,1}(k_1,k_2)=\phi_{3,2}(k_1,k_2)=\phi_{4,1}(k_1,k_2)=\phi_{4,2}(k_1,k_2)=0$$

due to the geometry of the waveguides. Then,

$$\begin{aligned}\phi_{1,2}(k_1,k_2)=&\frac{\beta_{ring}}{\beta}\sum_n A_n(k_3)A_n(k_1+k_2-k_3)B_{n,1}(k_1)B_{n,2}(k_2) \\ &\times\frac{3\sqrt{2}i\pi\alpha^2\hbar}{4\beta_{ring}\epsilon_0}\int dk_3\ \phi_P(k_3)\phi_P(k_1+k_2-k_3) \\ &\times\sqrt{\omega(k_1)\omega(k_2)\omega(k_3)\omega(k_1+k_2-k_3)} \\ &\times\int dr\ \Gamma_3\tilde{D}^{asy-in}_{n,k_1}(r)\tilde{D}^{asy-in}_{n,k_2}(r)\tilde{D}^{asy-in}_{n,k_3}(r)\tilde{D}^{asy-in}_{n,k_1+k_2-k_3}(r) \\ =&\frac{\beta_{ring}}{\beta}\phi_{ring}(k_1,k_2) \\ &\times[A_1(k_3)A_1(k_1+k_2-k_3)B_{1,1}(k_1)B_{1,2}(k_2) \\ &+A_2(k_3)A_2(k_1+k_2-k_3)B_{2,1}(k_1)B_{2,2}(k_2)] \\ =&\frac{\beta_{ring}}{\beta}\phi_{ring}(k_1,k_2)[it_1^2t_{2U}^2r_{3U}t_{3U}e^{2i\phi_1}e^{i(k_1+k_2)(2L_1+2L_2-L_3)} \\ &-it_1^2r_{2U}^2t_{3U}r_{3U}e^{i(k_1+k_2)(2L_1+2L_2-L_3)}]\end{aligned} \tag{B.21}$$

and with $\phi_1=\pi/2$, $r_i=t_i=1/\sqrt{2}$, and $\beta_{ring}/\beta=2$ we have

$$\phi_{1,2}(k_1,k_2)=-\frac{\beta_{ring}}{\beta}\frac{i}{4}e^{i\Psi(k_1,k_2)}\phi_{ring}(k_1,k_2)=-\frac{i}{2}e^{i\Psi(k_1,k_2)}\phi_{ring}(k_1,k_2) \tag{B.22}$$

where

$$\Psi(k_1,k_2)=(k_1+k_2)(2L_1+2L_2-L_3) \tag{B.23}$$

Similarly,

$$\phi_{3,4}(k_1,k_2)=\frac{\beta_{ring}}{\beta}\sum_n A_n(k_3)A_n(k_1+k_2-k_3)B_{n,3}(k_1)B_{n,4}(k_2)\phi_{ring}(k_1,k_2) \tag{B.24}$$

$$\begin{aligned}=&\frac{\beta_{ring}}{\beta}\phi_{ring}(k_1,k_2) \\ &\times[A_3(k_3)A_3(k_1+k_2-k_3)B_{3,3}(k_1)B_{3,4}(k_2) \\ &+A_4(k_3)A_4(k_1+k_2-k_3)B_{4,3}(k_1)B_{4,4}(k_2)] \\ =&\frac{\beta_{ring}}{\beta}\phi_{ring}(k_1,k_2)[ir_1^2r_{2D}^2r_{3D}t_{3D}e^{2i\phi}e^{i(k_1+k_2)(2L_1+2L_2-L_3)} \\ &-ir_1^2t_{2D}^2t_{3D}r_{3D}e^{2i(\phi+\phi_2)}e^{i(k_1+k_2)(2L_1+2L_2-L_3)}]\end{aligned}$$

and with $\phi = \pi$, $\phi_2 = \pi/2$, $r = t = 1/\sqrt{2}$, and $\beta_{ring}/\beta = 2$ we have

$$\phi_{3,4}(k_1,k_2) = \frac{\beta_{ring}}{\beta}\frac{i}{4}e^{i\Psi(k_1,k_2)}\phi_{ring}(k_1,k_2) = \frac{i}{2}e^{i\Psi(k_1,k_2)}\phi_{ring}(k_1,k_2) \quad \text{(B.25)}$$

Note also that $\phi_{2,1}(k_1,k_2) = \phi_{1,2}(k_1,k_2)$ and $\phi_{4,3}(k_1,k_2) = \phi_{3,4}(k_1,k_2)$.

The state $|II\rangle$ is finally given by

$$\begin{aligned}
|II\rangle =& \frac{1}{\sqrt{2}}\int_{\Omega_{SI}} dk_1dk_2(\phi_{1,2}(k_1,k_2)b^\dagger_{1,k_1}b^\dagger_{2,k_2} + \phi_{2,1}(k_1,k_2)b^\dagger_{2,k_1}b^\dagger_{1,k_2} \quad \text{(B.26)}\\
&+\phi_{3,4}(k_1,k_2)b^\dagger_{3,k_1}b^\dagger_{4,k_2} + \phi_{4,3}(k_1,k_2)b^\dagger_{4,k_1}b^\dagger_{3,k_2})\,|vac\rangle\\
=& \frac{2}{\sqrt{2}}\int_{\Omega_{SI}} dk_1dk_2(\phi_{1,2}(k_1,k_2)b^\dagger_{1,k_1}b^\dagger_{2,k_2} + \phi_{3,4}(k_1,k_2)b^\dagger_{3,k_1}b^\dagger_{4,k_2})\,|vac\rangle\\
=& -\frac{i}{\sqrt{2}}\int_{\Omega_{SI}} dk_1dk_2e^{i\Psi(k_1,k_2)}\phi_{ring}(k_1,k_2)(b^\dagger_{1,k_1}b^\dagger_{2,k_2} - b^\dagger_{3,k_1}b^\dagger_{4,k_2})\,|vac\rangle\,.
\end{aligned}$$

For the generation of GHZ states we are interested in the simultaneous generation of two photon pairs (B.26), and thus we focus on the next term in the expansion (6.2), which involves the four-photon state $|\text{IV}\rangle$; with the help of Eq. (B.26), we obtain Eq. (6.4). Referring to Fig. 6.6 and following the notation [180] for directional couplers, we can express the photon creation operators in (6.4) in terms of the photon creation operators in each detector channel $D_{n,m}$ as

$$\begin{aligned}
b^\dagger_{k_1,1} &= e^{-ik_1L_T}b^\dagger_{k_1,T} \quad \text{(B.27)}\\
b^\dagger_{k_2,2} &= -it_1e^{-ik_2L_{3,0}}b^\dagger_{k_2,D_{3,0}} + r_1e^{-ik_2L_{2,0}}b^\dagger_{k_2,D_{2,0}}\\
b^\dagger_{k_1,3} &= -it_2e^{-ik_1L_{3,1}}b^\dagger_{k_1,D_{3,1}} + r_2e^{-ik_1L_{1,1}}b^\dagger_{k_1,D_{1,1}}\\
b^\dagger_{k_2,4} &= -it_3e^{-ik_2L_{2,1}}b^\dagger_{k_2,D_{2,1}} + r_3e^{ik_2L_{1,0}}b^\dagger_{k_2,D_{1,0}}
\end{aligned}$$

where $L_{n,m}$ is the distance between the appropriate output directional coupler in the source and the detector $D_{n,m}$, and L_T is the length between the upper directional coupler in the source and the target detector T. Using Eq. (B.27) in (B.26), and referring to the output state expansion (6.2) we find that the state at the detectors is (6.5)-(6.7), with the relative phase between the terms in the GHZ given by

$$\begin{aligned}
\Theta =& k_1(L_{1,1} - L_{3,1}) + k_2(L_{2,1} - L_{1,0}) \quad \text{(B.28)}\\
&+ k_2'(L_{3,0} - L_{2,0}) + \frac{\pi}{2}.
\end{aligned}$$

B.2 Normalization of the output states $|II\rangle$ and $|IV\rangle$

Similarly to what we have discussed in Appendix A.1, here we provide the correct normalization of the states appearing in Eq. (6.2).

There is no need to discuss the normalization of the photon pair state $|II\rangle$, for we have already demonstrated that it is geometry-independent, and thus Eq. (A.7) holds identical in this context. On the contrary, the normalization of the state $|IV\rangle$ depends on the specific geometry of the source. Similarly to what we did in Appendix A.1, we begin from the unnormalized four-photon state

$$|IV\rangle = \frac{1}{\sqrt{N}}(C_{II}^{\dagger})^2 \,|vac\rangle\,, \tag{B.29}$$

where we have introduced the usual normalization constant N. Since we have already calculated the photon pair state in Eq. (B.26), we can use it in the previous expression to obtain

$$\begin{aligned} |IV\rangle &= \frac{1}{\sqrt{N}}(C_{II}^{\dagger})^2 \,|vac\rangle \\ &= -\frac{1}{2\sqrt{N}}\int_{\Omega_{SI}} dk_1 dk_2 dk_3 dk_4 e^{i\Psi(k_1,k_2)} e^{i\Psi(k_3,k_4)} \phi_{ring}(k_1,k_2)\phi_{ring}(k_3,k_4) \\ &\times (b_{1,k_1}^{\dagger} b_{2,k_2}^{\dagger} - b_{3,k_1}^{\dagger} b_{4,k_2}^{\dagger})(b_{1,k_3}^{\dagger} b_{2,k_4}^{\dagger} - b_{3,k_3}^{\dagger} b_{4,k_4}^{\dagger})\,|vac\rangle\,. \end{aligned} \tag{B.30}$$

From the normalization condition $\langle IV|IV\rangle = 1$ we get

$$\begin{aligned} \langle IV|IV\rangle = &-\frac{1}{2\sqrt{N}}\int_{\Omega_{SI}} dk_1' dk_2' dk_3' dk_4' e^{-i\Psi(k_1',k_2')} e^{-i\Psi(k_3',k_4')} \phi_{ring}^{*}(k_1',k_2') \\ &\times \phi_{ring}^{*}(k_3',k_4')\,\langle vac|\,(b_{1,k_1'} b_{2,k_2'} - b_{3,k_1'} b_{4,k_2'})(b_{1,k_3'} b_{2,k_4'} - b_{3,k_3'} b_{4,k_4'}) \\ &\times [-\frac{1}{2\sqrt{N}}\int_{\Omega_{SI}} dk_1 dk_2 dk_3 dk_4 e^{i\Psi(k_1,k_2)} e^{i\Psi(k_3,k_4)} \phi_{ring}(k_1,k_2)\phi_{ring}(k_3,k_4) \\ &\times (b_{1,k_1}^{\dagger} b_{2,k_2}^{\dagger} - b_{3,k_1}^{\dagger} b_{4,k_2}^{\dagger})(b_{1,k_3}^{\dagger} b_{2,k_4}^{\dagger} - b_{3,k_3}^{\dagger} b_{4,k_4}^{\dagger})\,|vac\rangle] \\ = &\frac{12}{4N}\int_{\Omega_{SI}} dk_1 dk_2 |\phi_{ring}(k_1,k_2)|^2 \int_{\Omega_{SI}} dk_3 dk_4 |\phi_{ring}(k_3,k_4)|^2 = 1, \end{aligned} \tag{B.31}$$

and since the BWF is already properly normalized, we conclude $N = 3$. Finally, the normalized four-photon state $|IV\rangle$ becomes

$$|IV\rangle = \frac{1}{\sqrt{3}}(C_{II}^{\dagger})^2 \,|vac\rangle \tag{B.32}$$

or, in the specific case of our source of path-entangled GHZ states,

$$\begin{aligned} |IV\rangle = &-\frac{1}{2\sqrt{3}}\int_{\Omega_{SI}} dk_1 dk_2 dk_3 dk_4 e^{i\Psi(k_1,k_2)} e^{i\Psi(k_3,k_4)} \phi_{ring}(k_1,k_2)\phi_{ring}(k_3,k_4) \\ &\times (b_{1,k_1}^{\dagger} b_{2,k_2}^{\dagger} - b_{3,k_1}^{\dagger} b_{4,k_2}^{\dagger})(b_{1,k_3}^{\dagger} b_{2,k_4}^{\dagger} - b_{3,k_3}^{\dagger} b_{4,k_4}^{\dagger})\,|vac\rangle\,. \end{aligned} \tag{B.33}$$

Bibliography

[1] from "the quantum manifesto on quantum technologies".

[2] Jonathan P Dowling and Gerard J Milburn. Quantum technology: the second quantum revolution. *Philosophical Transactions of the Royal Society of London A: Mathematical, Physical and Engineering Sciences*, 361(1809):1655–1674, 2003.

[3] Charles H Bennett and Gilles Brassard. Quantum cryptography: Public key distribution and coin tossing. *Proceedings of IEEE International Conference on Computers, Systems and Signal Processing*, 175:8, 1984.

[4] Artur K Ekert. Quantum cryptography based on bell's theorem. *Physical review letters*, 67(6):661, 1991.

[5] Juan Yin, Yuan Cao, Yu-Huai Li, Sheng-Kai Liao, Liang Zhang, Ji-Gang Ren, Wen-Qi Cai, Wei-Yue Liu, Bo Li, Hui Dai, et al. Satellite-based entanglement distribution over 1200 kilometers. *Science*, 356(6343):1140–1144, 2017.

[6] Sheng-Kai Liao, Hai-Lin Yong, Chang Liu, Guo-Liang Shentu, Dong-Dong Li, Jin Lin, Hui Dai, Shuang-Qiang Zhao, Bo Li, Jian-Yu Guan, et al. Long-distance free-space quantum key distribution in daylight towards inter-satellite communication. *Nature Photonics*, 11(8):nphoton–2017, 2017.

[7] E. Knill, R. Laflamme, and G.J. Milburn. A scheme for efficient quantum computation with linear optics. *Nature*, 409(6816):46–52, 2001. cited By 3287.

[8] Alberto Politi, Jonathan CF Matthews, and Jeremy L O'brien. Shor's quantum factoring algorithm on a photonic chip. *Science*, 325(5945):1221–1221, 2009.

[9] Jeremy L O'brien. Optical quantum computing. *Science*, 318(5856):1567–1570, 2007.

[10] Vittorio Giovannetti, Seth Lloyd, and Lorenzo Maccone. Advances in quantum metrology. *Nature photonics*, 5(4):222–229, 2011.

[11] J Aasi, J Abadie, BP Abbott, R Abbott, MR Abernathy, RX Adhikari, P Ajith, SB Anderson, K Arai, MC Araya, et al. Enhanced sensitivity of the ligo gravitational wave detector by using squeezed states of light. *Nature Photonics*, 7(8):613–619, 2013.

[12] Michel H Devoret and Robert J Schoelkopf. Superconducting circuits for quantum information: an outlook. *Science*, 339(6124):1169–1174, 2013.

[13] Andrew A Houck, Hakan E Türeci, and Jens Koch. On-chip quantum simulation with superconducting circuits. *Nature Physics*, 8(4):292, 2012.

[14] Rainer Blatt and Christian F Roos. Quantum simulations with trapped ions. *Nature Physics*, 8(4):277, 2012.

[15] L-M Duan, JI Cirac, and P Zoller. Geometric manipulation of trapped ions for quantum computation. *Science*, 292(5522):1695–1697, 2001.

[16] Jelena Vučković, Jeremy L O'Brien, Akira Furusawa, and Jelena Vučković. Photonic quantum technologies. *Nature photonics*, 3(12):687–695, 2009.

[17] H.J. Kimble. The quantum internet. *Nature*, 453(7198):1023–1030, 2008. cited By 1541.

[18] Dik Bouwmeester, Jian-Wei Pan, Klaus Mattle, Manfred Eibl, Harald Weinfurter, and Anton Zeilinger. Experimental quantum teleportation. *Nature*, 390(6660):575–579, 1997.

[19] Michael A Nielsen and Isaac L Chuang. *Quantum computation and quantum information*. Cambridge university press, 2010.

[20] Jaewoo Joo, William J Munro, and Timothy P Spiller. Quantum metrology with entangled coherent states. *Physical review letters*, 107(8):083601, 2011.

[21] Sean D Huver, Christoph F Wildfeuer, and Jonathan P Dowling. Entangled fock states for robust quantum optical metrology, imaging, and sensing. *Physical Review A*, 78(6):063828, 2008.

[22] Pieter Kok, W. J. Munro, Kae Nemoto, T. C. Ralph, Jonathan P. Dowling, and G. J. Milburn. Linear optical quantum computing with photonic qubits. *Rev. Mod. Phys.*, 79:135–174, Jan 2007.

[23] Terry Rudolph. Why i am optimistic about the silicon-photonic route to quantum computing. *APL Photonics*, 2(3):030901, 2017.

[24] Rodney Loudon. *The quantum theory of light*. OUP Oxford, 2000.

[25] Andrew J Shields. Semiconductor quantum light sources. *Nature photonics*, 1(4):215–223, 2007.

[26] P Michler, A Kiraz, C Becher, WV Schoenfeld, PM Petroff, Lidong Zhang, E Hu, and A Imamoglu. A quantum dot single-photon turnstile device. *science*, 290(5500):2282–2285, 2000.

[27] N. Somaschi, V. Giesz, L. De Santis, J.C. Loredo, M.P. Almeida, G. Hornecker, S.L. Portalupi, T. Grange, C. Antón, J. Demory, C. Gómez, I. Sagnes, N.D. Lanzillotti-Kimura, A. Lemaítre, A. Auffeves, A.G. White, L. Lanco, and P. Senellart. Near-optimal single-photon sources in the solid state. *Nature Photonics*, 10(5):340–345, 2016. cited By 112.

[28] I. Aharonovich and E. Neu. Diamond nanophotonics. *Advanced Optical Materials*, 2(10):911–928, 2014. cited By 66.

[29] E. Neu, D. Steinmetz, J. Riedrich-Möller, S. Gsell, M. Fischer, M. Schreck, and C. Becher. Single photon emission from silicon-vacancy colour centres in chemical vapour deposition nano-diamonds on iridium. *New Journal of Physics*, 13, 2011. cited By 155.

[30] L.J. Rogers, K.D. Jahnke, T. Teraji, L. Marseglia, C. Müller, B. Naydenov, H. Schauffert, C. Kranz, J. Isoya, L.P. McGuinness, and F. Jelezko. Multiple intrinsically identical single-photon emitters in the solid state. *Nature Communications*, 5, 2014. cited By 70.

[31] Darrick E Chang, Vladan Vuletić, and Mikhail D Lukin. Quantum nonlinear optics [mdash] photon by photon. *Nature Photonics*, 8(9):685–694, 2014.

[32] Bin Fang, Offir Cohen, Jamy B. Moreno, and Virginia O. Lorenz. State engineering of photon pairs produced through dual-pump spontaneous four-wave mixing. *Opt. Express*, 21(3):2707–2717, Feb 2013.

[33] LG Helt, Zhenshan Yang, Marco Liscidini, and J E Sipe. Spontaneous four-wave mixing in microring resonators. *Optics letters*, 35(18):3006–3008, 2010.

[34] T. Onodera, Marco Liscidini, J. E. Sipe, and L. G. Helt. Parametric fluorescence in a sequence of resonators: An analogy with dicke superradiance. *Phys. Rev. A*, 93:043837, Apr 2016.

[35] TB Pittman, BC Jacobs, and JD Franson. Heralding single photons from pulsed parametric down-conversion. *Optics communications*, 246(4):545–550, 2005.

[36] Peter J Mosley, Jeff S Lundeen, Brian J Smith, Piotr Wasylczyk, Alfred B U'Ren, Christine Silberhorn, and Ian A Walmsley. Heralded generation of ultrafast single photons in pure quantum states. *Physical Review Letters*, 100(13):133601, 2008.

[37] Matthew J Collins, Chunle Xiong, Isabella H Rey, Trung D Vo, Jiakun He, Shayan Shahnia, Christopher Reardon, Thomas F Krauss, MJ Steel,

Alex S Clark, et al. Integrated spatial multiplexing of heralded single-photon sources. *Nature communications*, 4, 2013.

[38] Evan Meyer-Scott, Nicola Montaut, Johannes Tiedau, Linda Sansoni, Harald Herrmann, Tim J Bartley, and Christine Silberhorn. Limits on the heralding efficiencies and spectral purities of spectrally filtered single photons from photon-pair sources. *Physical Review A*, 95(6):061803, 2017.

[39] Z Vernon, M Menotti, CC Tison, JA Steidle, ML Fanto, PM Thomas, SF Preble, AM Smith, PM Alsing, M Liscidini, et al. Truly unentangled photon pairs without spectral filtering. *arXiv preprint arXiv:1703.10626*, 2017.

[40] Brian J Smith, P Mahou, Offir Cohen, JS Lundeen, and IA Walmsley. Photon pair generation in birefringent optical fibers. *Optics express*, 17(26):23589–23602, 2009.

[41] Zhenshan Yang, Marco Liscidini, and J. E. Sipe. Spontaneous parametric down-conversion in waveguides: A backward heisenberg picture approach. *Phys. Rev. A*, 77:033808, Mar 2008.

[42] M Liscidini, L G Helt, and J E Sipe. Asymptotic fields for a hamiltonian treatment of nonlinear electromagnetic phenomena. *Physical Review A*, 85(1):013833, 2012.

[43] Farid A Harraz. Porous silicon chemical sensors and biosensors: A review. *Sensors and Actuators B: Chemical*, 202:897–912, 2014.

[44] Davide Grassani, Stefano Azzini, Marco Liscidini, Matteo Galli, Michael J. Strain, Marc Sorel, J. E. Sipe, and Daniele Bajoni. Micrometer-scale integrated silicon source of time-energy entangled photons. *Optica*, 2(2):88–94, Feb 2015.

[45] Davide Grassani, Angelica Simbula, Stefano Pirotta, Matteo Galli, Matteo Menotti, Nicholas C Harris, Tom Baehr-Jones, Michael Hochberg, Christophe Galland, Marco Liscidini, et al. Energy correlations of photon pairs generated by a silicon microring resonator probed by stimulated four wave mixing. *Scientific reports*, 6:23564, 2016.

[46] Marco Liscidini and JE Sipe. Stimulated emission tomography. *Physical review letters*, 111(19):193602, 2013.

[47] Cale M. Gentry, Gil Triginer, Xiaoge Zeng, and Miloš Popović. Tailoring of individual photon lifetimes as a degree of freedom in resonant quantum photonic sources. In *Conference on Lasers and Electro-Optics*, page JTu5A.17. Optical Society of America, 2016.

[48] Long Chen, Nicolás Sherwood-Droz, and Michal Lipson. Compact bandwidth-tunable microring resonators. *Optics letters*, 32(22):3361–3363, 2007.

[49] Wolfgang Dür, Guifre Vidal, and J Ignacio Cirac. Three qubits can be entangled in two inequivalent ways. *Physical Review A*, 62(6):062314, 2000.

[50] Takashi Yamamoto, Kiyoshi Tamaki, Masato Koashi, and Nobuyuki Imoto. Polarization-entangled w state using parametric down-conversion. *Physical Review A*, 66(6):064301, 2002.

[51] Manfred Eibl, Nikolai Kiesel, Mohamed Bourennane, Christian Kurtsiefer, and Harald Weinfurter. Experimental realization of a three-qubit entangled w state. *Physical Review Letters*, 92(7):077901, 2004.

[52] Nikolai Kiesel, Mohamed Bourennane, Christian Kurtsiefer, Harald Weinfurter, D Kaszlikowski, W Laskowski, and Marek Zukowski. Three-photon w-state. *Journal of Modern Optics*, 50(6-7):1131–1138, 2003.

[53] Menas Kafatos. *Bell's theorem, quantum theory and conceptions of the universe*, volume 37. Springer Science & Business Media, 2013.

[54] N. Bergamasco, M. Menotti, J. E. Sipe, and M. Liscidini. Generation of path-encoded greenberger-horne-zeilinger states. 04 2017.

[55] Jian-Wei Pan, Dik Bouwmeester, Matthew Daniell, Harald Weinfurter, and Anton Zeilinger. Experimental test of quantum nonlocality in three-photon greenberger-horne-zeilinger entanglement. *Nature*, 403(6769):515–519, 02 2000.

[56] Xing-Ri Jin, Xin Ji, Ying-Qiao Zhang, Shou Zhang, Suc-Kyoung Hong, Kyu-Hwang Yeon, and Chung-In Um. Three-party quantum secure direct communication based on ghz states. *Physics Letters A*, 354(1):67–70, 2006.

[57] K Zyczkowski. Geometry of entangled states. *arXiv preprint quant-ph/0006068*, 2000.

[58] Charles H Bennett and Stephen J Wiesner. Communication via one-and two-particle operators on einstein-podolsky-rosen states. *Physical review letters*, 69(20):2881, 1992.

[59] John S Bell. On the einstein podolsky rosen paradox. *Physics*, 1:195–200, 1964.

[60] Daniel FV James, Paul G Kwiat, William J Munro, and Andrew G White. Measurement of qubits. *Physical Review A*, 64(5):052312, 2001.

[61] Joseph B Altepeter, Daniel FV James, and Paul G Kwiat. 4 qubit quantum state tomography. In *Quantum state estimation*, pages 113–145. Springer, 2004.

[62] G Mauro D'Ariano, Martina De Laurentis, Matteo GA Paris, Alberto Porzio, and Salvatore Solimeno. Quantum tomography as a tool for the characterization of optical devices. *Journal of Optics B: Quantum and Semiclassical Optics*, 4(3):S127, 2002.

[63] Zdeněk Hradil and Jaroslav Řeháček. Efficiency of maximum-likelihood reconstruction of quantum states. *Fortschritte der Physik*, 49(10-11):1083–1088, 2001.

[64] Paul G Kwiat, Edo Waks, Andrew G White, Ian Appelbaum, and Philippe H Eberhard. Ultrabright source of polarization-entangled photons. *Physical Review A*, 60(2):R773, 1999.

[65] T Chaneliere, DN Matsukevich, SD Jenkins, TAB Kennedy, MS Chapman, and A Kuzmich. Quantum telecommunication based on atomic cascade transitions. *Physical review letters*, 96(9):093604, 2006.

[66] Max Born and Emil Wolf. *Principles of optics: electromagnetic theory of propagation, interference and diffraction of light*. Elsevier, 2013.

[67] Andrew G White, Daniel FV James, Philippe H Eberhard, and Paul G Kwiat. Nonmaximally entangled states: Production, characterization, and utilization. *Physical review letters*, 83(16):3103, 1999.

[68] Nobuyuki Matsuda, Hanna Le Jeannic, Hiroshi Fukuda, Tai Tsuchizawa, William John Munro, Kaoru Shimizu, Koji Yamada, Yasuhiro Tokura, and Hiroki Takesue. A monolithically integrated polarization entangled photon pair source on a silicon chip. *Scientific Reports*, 2:817 EP –, 11 2012.

[69] D. Pérez-Galacho, R. Halir, A. Ortega-Mo nux, C. Alonso-Ramos, R. Zhang, P. Runge, K. Janiak, H.-G. Bach, A. G. Steffan, and Í. Molina-Fernández. Integrated polarization beam splitter with relaxed fabrication tolerances. *Opt. Express*, 21(12):14146–14151, Jun 2013.

[70] Peter P Rohde. Simple scheme for universal linear-optics quantum computing with constant experimental complexity using fiber loops. *Physical Review A*, 91(1):012306, 2015.

[71] S Ramelow, L Ratschbacher, A Fedrizzi, N K Langford, and A Zeilinger. Discrete tunable color entanglement. *Physical Review Letters*, 103(25):253601, 2009.

[72] Steven Rogers, Daniel Mulkey, Xiyuan Lu, Wei C Jiang, and Qiang Lin. High visibility time-energy entangled photons from a silicon nanophotonic chip. *ACS Photonics*, 3(10):1754–1761, 2016.

[73] Alexander S Solntsev and Andrey A Sukhorukov. Path-entangled photon sources on nonlinear chips. *Reviews in Physics*, 2:19–31, 2017.

[74] Alberto Politi, Martin J Cryan, John G Rarity, Siyuan Yu, and Jeremy L O'brien. Silica-on-silicon waveguide quantum circuits. *Science*, 320(5876):646–649, 2008.

[75] J. W. Silverstone, R. Santagati, D. Bonneau, M. J. Strain, M. Sorel, J. L. O'Brien, and M. G. Thompson. Qubit entanglement between ring-resonator photon-pair sources on a silicon chip. *Nature Communications*, 6:7948 EP –, 08 2015.

[76] Frank Setzpfandt, Alexander S Solntsev, James Titchener, Che Wen Wu, Chunle Xiong, Roland Schiek, Thomas Pertsch, Dragomir N Neshev, and Andrey A Sukhorukov. Tunable generation of entangled photons in a nonlinear directional coupler. *Laser & Photonics Reviews*, 10(1):131–136, 2016.

[77] Jianwei Wang, Damien Bonneau, Matteo Villa, Joshua W. Silverstone, Raffaele Santagati, Shigehito Miki, Taro Yamashita, Mikio Fujiwara, Masahide Sasaki, Hirotaka Terai, Michael G. Tanner, Chandra M. Natarajan, Robert H. Hadfield, Jeremy L. O'Brien, and Mark G. Thompson. Chip-to-chip quantum photonic interconnect by path-polarization interconversion. *Optica*, 3(4):407–413, Apr 2016.

[78] James G Titchener, Alexander S Solntsev, and Andrey A Sukhorukov. Two-photon tomography using on-chip quantum walks. *Optics letters*, 41(17):4079–4082, 2016.

[79] Ling-An Wu, HJ Kimble, JL Hall, and Huifa Wu. Generation of squeezed states by parametric down conversion. *Physical review letters*, 57(20):2520, 1986.

[80] Ulrik L Andersen, Tobias Gehring, Christoph Marquardt, and Gerd Leuchs. 30 years of squeezed light generation. *Physica Scripta*, 91(5):053001, 2016.

[81] Lawrence E Myers and Walter R Bosenberg. Periodically poled lithium niobate and quasi-phase-matched optical parametric oscillators. *IEEE Journal of Quantum Electronics*, 33(10):1663–1672, 1997.

[82] S Tanzilli, W Tittel, H De Riedmatten, H Zbinden, P Baldi, M DeMicheli, Da B Ostrowsky, and N Gisin. Ppln waveguide for quantum communication. *The European Physical Journal D-Atomic, Molecular, Optical and Plasma Physics*, 18(2):155–160, 2002.

[83] RA Ganeev, IA Kulagin, AI Ryasnyansky, RI Tugushev, and T Usmanov. Characterization of nonlinear optical parameters of kdp, linbo 3 and bbo crystals. *Optics communications*, 229(1):403–412, 2004.

[84] John D Bierlein and Herman Vanherzeele. Potassium titanyl phosphate: properties and new applications. *JOSA B*, 6(4):622–633, 1989.

[85] DN Nikogosyan. Beta barium borate (bbo). *Applied Physics A: Materials Science & Processing*, 52(6):359–368, 1991.

[86] L Lanco, S Ducci, J-P Likforman, X Marcadet, JAW Van Houwelingen, Hugo Zbinden, G Leo, and V Berger. Semiconductor waveguide source of counterpropagating twin photons. *Physical review letters*, 97(17):173901, 2006.

[87] S Mariani, A Andronico, A Lemaître, I Favero, S Ducci, and G Leo. Second-harmonic generation in algaas microdisks in the telecom range. *Optics letters*, 39(10):3062–3065, 2014.

[88] Radhakrishnan Nagarajan, Charles H Joyner, Richard P Schneider, Jeffrey S Bostak, Timothy Butrie, Andrew G Dentai, Vincent G Dominic, Peter W Evans, Masaki Kato, Mike Kauffman, et al. Large-scale photonic integrated circuits. *IEEE Journal of Selected Topics in Quantum Electronics*, 11(1):50–65, 2005.

[89] Satoshi Kako, Charles Santori, Katsuyuki Hoshino, Stephan Götzinger, Yoshihisa Yamamoto, and Yasuhiko Arakawa. A gallium nitride single-photon source operating at 200 k. *Nature materials*, 5(11):887, 2006.

[90] David J. Moss, Roberto Morandotti, Alexander L. Gaeta, and Michal Lipson. New cmos-compatible platforms based on silicon nitride and hydex for nonlinear optics. *Nat Photon*, 7(8):597–607, 08 2013.

[91] Jacob S Levy, Mark A Foster, Alexander L Gaeta, and Michal Lipson. Harmonic generation in silicon nitride ring resonators. *Optics express*, 19(12):11415–11421, 2011.

[92] Francesco Martini and Alberto Politi. Four wave mixing in 3c sic ring resonators. *arXiv preprint arXiv:1707.03645*, 2017.

[93] Xiyuan Lu, Jonathan Y Lee, Steven Rogers, and Qiang Lin. Optical kerr nonlinearity in a high-q silicon carbide microresonator. *Optics express*, 22(25):30826–30832, 2014.

[94] Paveen Apiratikul, Andrea M Rossi, and Thomas E Murphy. Nonlinearities in porous silicon optical waveguides at 1550 nm. *Optics express*, 17(5):3396–3406, 2009.

[95] Fryad Z Henari, Kai Morgenstern, Werner J Blau, Vladimir A Karavanskii, and Vladimir S Dneprovskii. Third-order optical nonlinearity and all-optical switching in porous silicon. *Applied physics letters*, 67(3):323–325, 1995.

[96] A Simbula, GA Rodriguez, M Menotti, S De Pace, SM Weiss, M Galli, M Liscidini, and D Bajoni. Low-power four-wave mixing in porous silicon microring resonators. *Applied Physics Letters*, 109(2):021106, 2016.

[97] Robert W Boyd. *Nonlinear optics*. Academic press, 2003.

[98] John D Joannopoulos, Steven G Johnson, Joshua N Winn, and Robert D Meade. *Photonic crystals: molding the flow of light*. Princeton university press, 2011.

[99] Amnon Yariv and Pochi Yeh. *Photonics: optical electronics in modern communications*, volume 6. Oxford University Press New York, 2007.

[100] Z Vernon, M Liscidini, and JE Sipe. No free lunch: the trade-off between heralding rate and efficiency in microresonator-based heralded single photon sources. *Optics letters*, 41(4):788–791, 2016.

[101] G Breit and HA Bethe. Ingoing waves in final state of scattering problems. *Physical Review*, 93(4):888, 1954.

[102] Z Vernon and JE Sipe. Spontaneous four-wave mixing in lossy microring resonators. *Physical Review A*, 91(5):053802, 2015.

[103] Lukas G. Helt, Marco Liscidini, and John E. Sipe. How does it scale? comparing quantum and classical nonlinear optical processes in integrated devices. *J. Opt. Soc. Am. B*, 29(8):2199–2212, Aug 2012.

[104] Samuel L Braunstein. Squeezing as an irreducible resource. *Physical Review A*, 71(5):055801, 2005.

[105] RRA Syms. Silica-on silicon integrated optics. In *Advances in Integrated Optics*, pages 121–150. Springer, 1994.

[106] S Ambran, HL Rogers, AS Webb, JC Gates, C Holmes, PGR Smith, and JK Sahu. A loss comparison of flat-fibre and silica-on-silicon direct uv written waveguides using a novel bragg grating measurement technique. 2010.

[107] A Mito, K Hagimoto, and C Takahashi. Determination of the third-order optical nonlinear susceptibility of fused silica using optical harmonic generation methods. *NONLINEAR OPTICS-READING-*, 13:3–18, 1995.

[108] TimurdoganE., PoultonC. V., ByrdM. J., and WattsM. R. Electric field-induced second-order nonlinear optical effects in silicon waveguides. *Nat Photon*, 11(3):200–206, 03 2017.

[109] M Cazzanelli, F Bianco, E Borga, G Pucker, M Ghulinyan, E Degoli, E Luppi, V Véniard, S Ossicini, D Modotto, et al. Second-harmonic generation in silicon waveguides strained by silicon nitride. *Nature materials*, 11(2):148, 2012.

[110] M Dinu, F Quochi, and H Garcia. Third-order nonlinearities in silicon at telecom wavelengths. *Applied physics letters*, 82(18):2954–2956, 2003.

[111] Alexander W Fang, Hyundai Park, Oded Cohen, Richard Jones, Mario J Paniccia, and John E Bowers. Electrically pumped hybrid algainas-silicon evanescent laser. *Optics express*, 14(20):9203–9210, 2006.

[112] Kazuhiro Ikeda, Robert E Saperstein, Nikola Alic, and Yeshaiahu Fainman. Thermal and kerr nonlinear properties of plasma-deposited silicon nitride/silicon dioxide waveguides. *Optics express*, 16(17):12987–12994, 2008.

[113] Sven Ramelow, Alessandro Farsi, Stéphane Clemmen, Daniel Orquiza, Kevin Luke, Michal Lipson, and Alexander L Gaeta. Silicon-nitride platform for narrowband entangled photon generation. *arXiv preprint arXiv:1508.04358*, 2015.

[114] Simeon Bogdanov, MY Shalaginov, Alexandra Boltasseva, and Vladimir M Shalaev. Material platforms for integrated quantum photonics. *Optical Materials Express*, 7(1):111–132, 2017.

[115] Shuyue Liu, Minghao Fang, Zhaohui Huang, Juntong Huang, Haipeng Ji, Haitao Liu, Yan-gai Liu, and Xiaowen Wu. Fe (no3) 3-assisted large-scale synthesis of si3n4 nanobelts from quartz and graphite by carbothermal reduction–nitridation and their photoluminescence properties. *Scientific reports*, 5:8998, 2015.

[116] Jacob S Levy, Alexander Gondarenko, Mark A Foster, Amy C Turner-Foster, Alexander L Gaeta, and Michal Lipson. Cmos-compatible multiple-wavelength oscillator for on-chip optical interconnects. *Nature photonics*, 4(1):37–40, 2010.

[117] Jared F Bauters, Martijn JR Heck, Demis John, Daoxin Dai, Ming-Chun Tien, Jonathon S Barton, Arne Leinse, René G Heideman, Daniel J Blumenthal, and John E Bowers. Ultra-low-loss high-aspect-ratio si 3 n 4 waveguides. *Optics express*, 19(4):3163–3174, 2011.

[118] Daoxin Dai, Zhi Wang, Jared F Bauters, M-C Tien, Martijn JR Heck, Daniel J Blumenthal, and John E Bowers. Low-loss si 3 n 4 arrayed-waveguide grating (de) multiplexer using nano-core optical waveguides. *Optics express*, 19(15):14130–14136, 2011.

[119] Xingchen Ji, Felippe AS Barbosa, Samantha P Roberts, Avik Dutt, Jaime Cardenas, Yoshitomo Okawachi, Alex Bryant, Alexander L Gaeta, and Michal Lipson. Ultra-low-loss on-chip resonators with sub-milliwatt parametric oscillation threshold. *Optica*, 4(6):619–624, 2017.

[120] Leigh Canham. *Handbook of porous silicon*. Springer, 2014.

[121] A Loni, LT Canham, MG Berger, R Arens-Fischer, H Munder, H Luth, HF Arrand, and TM Benson. Porous silicon multilayer optical waveguides. *Thin solid films*, 276(1-2):143–146, 1996.

[122] Guoguang Rong, Ali Najmaie, John E Sipe, and Sharon M Weiss. Nanoscale porous silicon waveguide for label-free dna sensing. *Biosensors and Bioelectronics*, 23(10):1572–1576, 2008.

[123] Gilberto A Rodriguez, Shuren Hu, and Sharon M Weiss. Porous silicon ring resonator for compact, high sensitivity biosensing applications. *Optics express*, 23(6):7111–7119, 2015.

[124] Thomas Edward Murphy, Jeffrey Todd Hastings, and Henry I Smith. Fabrication and characterization of narrow-band bragg-reflection filters in silicon-on-insulator ridge waveguides. *Journal of lightwave technology*, 19(12):1938, 2001.

[125] M Khardani, M Bouaïcha, and B Bessaïs. Bruggeman effective medium approach for modelling optical properties of porous silicon: comparison with experiment. *physica status solidi (c)*, 4(6):1986–1990, 2007.

[126] Jinan Xia, Andrea M Rossi, and Thomas E Murphy. Laser-written nanoporous silicon ridge waveguide for highly sensitive optical sensors. *Optics letters*, 37(2):256–258, 2012.

[127] Morio Takahashi and Nobuyoshi Koshida. Fabrication and characteristics of three-dimensionally buried porous silicon optical waveguides. *Journal of applied physics*, 86(9):5274–5278, 1999.

[128] Parastesh Pirasteh, Joël Charrier, Yannick Dumeige, Séverine Haesaert, and Pierre Joubert. Optical loss study of porous silicon and oxidized porous silicon planar waveguides. *Journal of applied physics*, 101(8):083110, 2007.

[129] P Ferrand and R Romestain. Optical losses in porous silicon waveguides in the near-infrared: Effects of scattering. *Applied Physics Letters*, 77(22):3535–3537, 2000.

[130] G Vincent. Optical properties of porous silicon superlattices. *Applied Physics Letters*, 64(18):2367–2369, 1994.

[131] L Pavesi. Porous silicon dielectric multilayers and microcavities. *La Rivista del Nuovo Cimento (1978-1999)*, 20(10):1–76, 1997.

[132] Jarkko J Saarinen, Sharon M Weiss, Philippe M Fauchet, and JE Sipe. Optical sensor based on resonant porous silicon structures. *Optics Express*, 13(10):3754–3764, 2005.

[133] Fryad Zeki Henari. Two-photon absorption of porous silicon. *Laser physics*, 15(12):1634–1636, 2005.

[134] Marco Liscidini. Surface guided modes in photonic crystal ridges: the good, the bad, and the ugly. *JOSA B*, 29(8):2103–2109, 2012.

[135] Peter Bienstman, S Selleri, L Rosa, HP Uranus, WCL Hopman, R Costa, A Melloni, LC Andreani, JP Hugonin, P Lalanne, et al. Modelling leaky photonic wires: A mode solver comparison. *Optical and quantum electronics*, 38(9-11):731–759, 2006.

[136] Stefano Azzini, Davide Grassani, Michael J. Strain, Marc Sorel, L. G. Helt, J. E. Sipe, Marco Liscidini, Matteo Galli, and Daniele Bajoni. Ultra-low power generation of twin photons in a compact silicon ring resonator. *Opt. Express*, 20(21):23100–23107, Oct 2012.

[137] M Ferrera, L Razzari, D Duchesne, R Morandotti, Z Yang, M Liscidini, JE Sipe, S Chu, BE Little, and DJ Moss. Low-power continuous-wave nonlinear optics in doped silica glass integrated waveguide structures. *Nature photonics*, 2(12):737–740, 2008.

[138] Li He, Yang Liu, Christophe Galland, Andy Eu-Jin Lim, Guo-Qiang Lo, Tom Baehr-Jones, and Michael Hochberg. A high-efficiency nonuniform grating coupler realized with 248-nm optical lithography. *IEEE Photonics Technology Letters*, 25(14):1358–1361, 2013.

[139] JH Eberly. Schmidt analysis of pure-state entanglement. *Laser physics*, 16(6):921–926, 2006.

[140] Artur Ekert and Peter L Knight. Entangled quantum systems and the schmidt decomposition. *American Journal of Physics*, 63(5):415–423, 1995.

[141] Ryszard Horodecki, Paweł Horodecki, Michał Horodecki, and Karol Horodecki. Quantum entanglement. *Rev. Mod. Phys.*, 81:865–942, Jun 2009.

[142] Iman Jizan, Bryn Bell, LG Helt, Alvaro Casas Bedoya, Chunle Xiong, and Benjamin J Eggleton. Phase-sensitive tomography of the joint spectral amplitude of photon pair sources. *Optics letters*, 41(20):4803–4806, 2016.

[143] Daniel R. Blay, M. J. Steel, and L. G. Helt. Effects of filtering on the purity of heralded single photons from parametric sources. *Phys. Rev. A*, 96:053842, 2017.

[144] Jesper B Christensen, Jacob G Koefoed, Karsten Rottwitt, Colin McKinstrie, et al. Engineering spectrally unentangled photon pairs from nonlinear microring resonators through pump manipulation. *arXiv preprint arXiv:1711.02401*, 2017.

[145] CK Law and JH Eberly. Analysis and interpretation of high transverse entanglement in optical parametric down conversion. *Physical review letters*, 92(12):127903, 2004.

[146] J Sperling and W Vogel. The schmidt number as a universal entanglement measure. *Physica Scripta*, 83(4):045002, 2011.

[147] Martin B Plenio and Shashank Virmani. An introduction to entanglement measures. *Quantum Inf. Comput.*, 7(1):001–051, 2007.

[148] Paul G. Kwiat, Klaus Mattle, Harald Weinfurter, Anton Zeilinger, Alexander V. Sergienko, and Yanhua Shih. New high-intensity source of polarization-entangled photon pairs. *Phys. Rev. Lett.*, 75:4337–4341, Dec 1995.

[149] E Hagley, X Maitre, G Nogues, C Wunderlich, M Brune, Jean-Michel Raimond, and Serge Haroche. Generation of einstein-podolsky-rosen pairs of atoms. *Physical Review Letters*, 79(1):1, 1997.

[150] Dik Bouwmeester, Jian-Wei Pan, Matthew Daniell, Harald Weinfurter, and Anton Zeilinger. Observation of three-photon greenberger-horne-zeilinger entanglement. *Physical Review Letters*, 82(7):1345, 1999.

[151] Mehul Malik, Manuel Erhard, Marcus Huber, Mario Krenn, Robert Fickler, and Anton Zeilinger. Multi-photon entanglement in high dimensions. *Nat Photon*, 10(4):248–252, 04 2016.

[152] K Schwaiger, D Sauerwein, M Cuquet, J I de Vicente, and B Kraus. Operational multipartite entanglement measures. *Physical Review Letters*, 115(15):150502, 2015.

[153] Hideharu Mikami, Yongmin Li, Kyosuke Fukuoka, and Takayoshi Kobayashi. New high-efficiency source of a three-photon w state and its full characterization using quantum state tomography. *Physical review letters*, 95(15):150404, 2005.

[154] Christian F. Roos, Mark Riebe, Hartmut Häffner, Wolfgang Hänsel, Jan Benhelm, Gavin P. T. Lancaster, Christoph Becher, Ferdinand Schmidt-Kaler, and Rainer Blatt. Control and measurement of three-qubit entangled states. *Science*, 304(5676):1478–1480, 2004.

[155] LF Wei, Yu-xi Liu, and Franco Nori. Generation and control of greenberger-horne-zeilinger entanglement in superconducting circuits. *Physical review letters*, 96(24):246803, 2006.

[156] L. DiCarlo, M. D. Reed, L. Sun, B. R. Johnson, J. M. Chow, J. M. Gambetta, L. Frunzio, S. M. Girvin, M. H. Devoret, and R. J. Schoelkopf. Preparation and measurement of three-qubit entanglement in a superconducting circuit. *Nature*, 467(7315):574–578, 09 2010.

[157] F Bodoky and M Blaauboer. Production of multipartite entanglement for electron spins in quantum dots. *Physical Review A*, 76(5):052309, 2007.

[158] M Menotti, L Maccone, JE Sipe, and M Liscidini. Generation of energy-entangled w states via parametric fluorescence in integrated devices. *Physical Review A*, 94(1):013845, 2016.

[159] Jaewoo Joo, Jinhyoung Lee, Jingak Jang, and Young-Jai Park. Quantum secure communication via w states. *arXiv preprint quant-ph/0204003*, 2002.

[160] Pankaj Agrawal and Arun Pati. Perfect teleportation and superdense coding with w states. *Physical Review A*, 74(6):062320, 2006.

[161] Bao-Sen Shi and Akihisa Tomita. Teleportation of an unknown state by w state. *Physics Letters A*, 296(4):161–164, 2002.

[162] Christian Reimer, Michael Kues, Piotr Roztocki, Benjamin Wetzel, Fabio Grazioso, Brent E Little, Sai T Chu, Tudor Johnston, Yaron Bromberg, Lucia Caspani, et al. Generation of multiphoton entangled quantum states by means of integrated frequency combs. *Science*, 351(6278):1176–1180, 2016.

[163] Davide Grassani, Stefano Azzini, Marco Liscidini, Matteo Galli, Michael J Strain, Marc Sorel, JE Sipe, and Daniele Bajoni. Micrometer-scale integrated silicon source of time-energy entangled photons. *Optica*, 2(2):88–94, 2015.

[164] John Heebner, Rohit Grover, Tarek Ibrahim, and Tarek A Ibrahim. *Optical microresonators: theory, fabrication, and applications*. Springer Science & Business Media, 2008.

[165] Nicolás Quesada and J E Sipe. Effects of time ordering in quantum nonlinear optics. *Physical Review A*, 90(6):063840, 2014.

[166] Nicholas C Harris, Davide Grassani, Angelica Simbula, Mihir Pant, Matteo Galli, Tom Baehr-Jones, Michael Hochberg, Dirk Englund, Daniele Bajoni, and Christophe Galland. Integrated source of spectrally filtered correlated photons for large-scale quantum photonic systems. *Physical Review X*, 4(4):041047, 2014.

[167] Lukas Knips, Christian Schwemmer, Nico Klein, Marcin Wieśniak, and Harald Weinfurter. Multipartite entanglement detection with minimal effort. *Physical review letters*, 117(21):210504, 2016.

[168] Tao Xin, Dawei Lu, Joel Klassen, Nengkun Yu, Zhengfeng Ji, Jianxin Chen, Xian Ma, Guilu Long, Bei Zeng, and Raymond Laflamme. Quantum state tomography via reduced density matrices. *Physical Review Letters*, 118(2):020401, 2017.

[169] Antonio Acin, Dagmar Bruß, Maciej Lewenstein, and Anna Sanpera. Classification of mixed three-qubit states. *Physical Review Letters*, 87(4):040401, 2001.

[170] Jiu-Cang Hao, Chuan-Feng Li, and Guang-Can Guo. Controlled dense coding using the greenberger-horne-zeilinger state. *Physical Review A*, 63(5):054301, 2001.

[171] Xiaolong Su, Caixing Tian, Xiaowei Deng, Qiang Li, Changde Xie, and Kunchi Peng. Quantum entanglement swapping between two multipartite entangled states. *Phys. Rev. Lett.*, 117:240503, Dec 2016.

[172] Long Chen, Christopher R Doerr, and Young-Kai Chen. Compact polarization rotator on silicon for polarization-diversified circuits. *Optics letters*, 36(4):469–471, 2011.

[173] J.C.F. Matthews, A. Politi, A. Stefanov, and J.L. O'Brien. Manipulation of multiphoton entanglement in waveguide quantum circuits. *Nature Photonics*, 3(6):346–350, 2009.

[174] C. Cinelli, G. Di Nepi, F. De Martini, M. Barbieri, and P. Mataloni. Parametric source of two-photon states with a tunable degree of entanglement and mixing: Experimental preparation of werner states and maximally entangled mixed states. *Phys. Rev. A*, 70:022321, Aug 2004.

[175] J. W. Silverstone, D. Bonneau, K. Ohira, N. Suzuki, H. Yoshida, N. Iizuka, M. Ezaki, C. M. Natarajan, M. G. Tanner, R. H. Hadfield, V. Zwiller, G. D. Marshall, J. G. Rarity, J. L. O'Brien, and M. G. Thompson. On-chip quantum interference between silicon photon-pair sources. *Nature Photonics*, 8:104–108, February 2014.

[176] S. F. Preble, M. L. Fanto, J. A. Steidle, C. C. Tison, G. A. Howland, Z. Wang, and P. M. Alsing. On-Chip Quantum Interference from a Single Silicon Ring-Resonator Source. *Physical Review Applied*, 4(2):021001, August 2015.

[177] Wei-Ping Huang. Coupled-mode theory for optical waveguides: an overview. *JOSA A*, 11(3):963–983, 1994.

[178] Michael L Cooper, Greeshma Gupta, Mark A Schneider, William MJ Green, Solomon Assefa, Fengnian Xia, Dawn K Gifford, and Shayan Mookherjea. Waveguide dispersion effects in silicon-on-insulator coupled-resonator optical waveguides. *Optics letters*, 35(18):3030–3032, 2010.

[179] John E Cunningham, Ivan Shubin, Xuezhe Zheng, Thierry Pinguet, Attila Mekis, Ying Luo, Hiren Thacker, Guoliang Li, Jin Yao, Kannan Raj, et al. Highly-efficient thermally-tuned resonant optical filters. *Optics Express*, 18(18):19055–19063, 2010.

[180] John E. Heebner, Philip Chak, Suresh Pereira, John E. Sipe, and Robert W. Boyd. Distributed and localized feedback in microresonator sequences for linear and nonlinear optics. *J. Opt. Soc. Am. B*, 21(10):1818–1832, Oct 2004.

List of Publications

Articles

1. M. Menotti and M. Liscidini, "*Optical resonators based on Bloch surface waves,*" J. Opt. Soc. Am. B **32**, 431-438 (2015).

2. D. Grassani, A. Simbula, S. Pirotta, M. Galli, M. Menotti, N. C. Harris, T. Baehr-Jones, M. Hochberg, C. Galland, M. Liscidini, and D. Bajoni, "*Energy correlations of photon pairs generated by a silicon microring resonator probed by Stimulated Four Wave Mixing,*" Sci. Reports **6**, (2016).

3. M. Menotti, L. Maccone, J.E. Sipe, and M. Liscidini, "*Generation of energy- entangled W states via parametric fluorescence in integrated devices*," Physcal Review A **94** (1), 013845 (2016).

4. A. Simbula, G. A. Rodriguez, M. Menotti, S. De Pace, S. M. Weiss, M. Galli, M. Lisicidini, and D. Bajoni, "*Low-power four-wave mixing in porous silicon microring resonators,*" Applied Physics Letters **109** (2), 021106 (2016).

5. N. R. Fong, M. Menotti, E. Lisicka-Skrzek, H. Northfield, A. Olivieri, N. Tait, M. Liscidini, and P. Berini, "*Bloch Long-Range Surface Plasmon Polaritons on Metal Stripe Waveguides on a Multilayer Substrate,*" ACS Photonics **4** (3), 593-599 (2017).

6. Z. Vernon, M. Menotti, C. C. Tison, J. A. Steidle, M. L. Fanto, P. M. Thomas, S. F. Preble, A. M. Smith, P. M. Alsing, M. Liscidini, and J. E. Sipe, "*Truly unentangled photon pairs without spectral filtering,*" Optics Letters **42** (18) 3638-3641 (2017).

7. N. Bergamasco, M. Menotti, J. E. Sipe, and M. Liscidini, "*Generation of path-encoded Greenberger-Horne-Zeilinger states,*" Physical Review Applied (in press).

Contributions to Conferences and Proceedings

1. "*Bloch surface wave ring resonators,*" CLEO 2016 – San Jose, California, June 5-11, 2016 (JTh2A.104).

2. "*Four-Wave Mixing in porous silicon microring resonators,*" CLEO 2016 – San Jose, California, June 5-11, 2016 (SW4E.7).

3. "*Four-Wave Mixing in porous silicon microring resonators*" Transparent Optical Networks (ICTON), 2016

4. "*Bloch long-range surface plasmon polaritons in metallic stripe waveguides,*" CLEO 2017 – San Jose, California, 5/14/2017 (SM3N.3).

5. "*Generation and characterization of energy-entangled W states,*" CLEO 2017 – San Jose, California, 5/14/2017 (FW4E.7).

6. "*An approach to the generation of GHZ states by interference of multiple integrated sources on a single chip,*" CLEO 2017 – San Jose, California, 5/14/2017 (JW2A. 22).

7. "*Generation of energy-entangled W states*" Transparent Optical Networks (ICTON), 2017

8. "*Guided Bloch long-range surface plasmon polaritons*" Transparent Optical Networks (ICTON), 2017

9. "*Generation of path-encoded GHZ states*" FisMat 2017 – Trieste, Italy, October 1-5, 2017

Acknowledgments

It is clear in my mind that concluding my PhD course and writing this thesis wouldn't have been possible without the support and the patience of many, inside and outside the Department of Physics. While I understand that these few lines can never do proper justice, I nonetheless would like to try to acknowledge all those precious colleagues and friends. This work is dedicated to all of them.

First of all, I would like to express my gratitude to my supervisor, Prof. Marco Liscidini. By looking back at our first meeting as an undergraduate student I can realize how much of his competence and passion for physics he managed to patiently instill into me during the last years. It is safe to say that most of this work would have never been possible without his many creative ideas and his dedication to work, providing suggestions, new approaches, and a unique care in the dissemination of the results. I certainly owe him a sound work ethic and an attitude to teamwork, both local and international, which helped me in forming a more comprehensive viewpoint on scientific research worldwide.

In the framework of these collaborations, I have had the possibility to spend six months at the University of Toronto in the group led by Prof. John E. Sipe, who I sincerely thank for the warm welcome, the support, and all the advices he promptly provided, always with such a natural kindness. During our collaboration I could appreciate and learn the importance of a wide, interdisciplinary background, and a great attention to every small detail.

I want to express my gratitude to Prof. Sara Ducci from the LMPQ at the Université Paris Diderot and Dr. Luke Helt from Queen's University for the critical reading of my thesis; thanks to your meticulous analysis I believe the quality of this document has greatly improved, both in the substance and in the form.

I am particularly thankful to Prof. Lucio Andreani, for his support throughout the PhD course and beyond, as well as to all the other professors in the Nanophotonics group in Pavia. In particular, thanks to the collaboration with Prof. Matteo Galli and Prof. Daniele Bajoni I had the possibility to acquire a more profound insight into the complexities and the charm of experimental quantum optics, which they pursue with great passion and dedication. I also wish to acknowledge Prof. Lorenzo Maccone for the collaboration and the useful

discussions on theoretical quantum optics.

During the last three years, Room 249 of the Department of Physics was just like a second home for me, a place to work in harmony and to have fun during the breaks. If this was the case, the credit goes to the amazing colleagues and friends I met during my PhD. Therefore, I wish to sincerely thank Daniele Aurelio, Salvatore Del Sorbo, Nicola Bergamasco, Federico Sabattoli, and the "unofficial" member of Room 249, Emma Lomonte. I am equally thankful to all my colleagues in the lab, including Angelica Simbula, Marco Clementi, Francesco Garrisi, and Micol Previde Massara, as well as all the other students and friends in the nanophotonics group, among the others Marco Passoni, Francesco Tacchino, and Saeid Rafizadeh. A special debt of gratitude goes also to all the students and post-docs in the University of Toronto, and particularly to Zachary Vernon, for the warm welcome and the useful tips on the city. The coffee/tea breaks, the stimulating discussions, the nights spent on board games and wine: every moment contributed to making this positive experience forever sculpted into my memory, and to create friendships that I hope will endure in the future.

I left the Collegio Don Bosco in Pavia prior to beginning my PhD course, yet I truly cannot miss to thank my sincere friends from the college, who I've always considered as a second family right from the early days together. In particular, I'd like to thank Spina, Macchio and Charly, Berry, Polpa, Teo, Meloz, Alby, Giorgio, Paddy and Fede for sharing some memorable years together in the *Ala*, as well as all the other great mates and friends, whose list would be too long and inevitably incomplete. A special thanks goes to Donga, for his passion and dedication to creating the right spirit for having great fun while respecting at least the majority of the college rules. Although I feel terribly sorry for not having dedicated enough time to many of these friends during the PhD years, I constantly preserve in my mind every single second of the great time we spent together, and all the crazy episodes we shared and which we love to recall in our reunions. I'd like to thank you all, for I have no doubts that such friendships will last, unaffected by distance or time.

A special thank from the bottom of my heart goes to my girlfriend Maria Elena, for the moral support she provided me during the PhD years. It's impossible to imagine such goal accomplished without your prompt and loving encouragements in every moment of despair, as much as without the cheerful celebrations for every achievement. No physical distance can really separate us.

Finally, but I really should have mentioned this in the first place, I want to thank my family for the constant support they have always provided me, never questioning my choices while, instead, encouraging me to pursue what I love to do in my life. I owe them a debt of gratitude I most certainly can never pay back.